Title
III-V Nanostructures on Dissimilar Substrates for Optoelectronic Applications

Author
Ng, Kar Wei

Publication Date
2013

Peer reviewed|Thesis/dissertation

III-V Nanostructures on Dissimilar Substrates for Optoelectronic Applications

by

Kar Wei Ng

A dissertation submitted in partial satisfaction of the

requirements for the degree of

Doctor of Philosophy

in

Engineering – Electrical Engineering and Computer Sciences

and the Designated Emphasis

in

Nanoscale Science and Engineering

in the

Graduate Division

of the

University of California, Berkeley

Committee in charge:

Professor Constance J. Chang-Hasnain
Professor Ming C. Wu
Professor Ronald Gronsky

Fall 2013

III-V Nanostructures on Dissimilar Substrates for Optoelectronic Applications

by

Kar Wei Ng

Abstract

III-V Nanostructures on Dissimilar Substrates for Optoelectronic Applications

by

Kar Wei Ng

Doctor of Philosophy in Engineering – Electrical Engineering and Computer Sciences

And the Designated Emphasis in Nanoscale Science and Engineering

University of California, Berkeley

Professor Constance J. Chang-Hasnain, Chair

The heterogeneous integration of optoelectronic and electronic circuits is poised to transform personal electronics because it will not only enable a vast range of otherwise unattainable capabilities, but will also reduce power consumption, weight and size. Monolithic integrations of high-quality III-V materials with single and poly-crystalline silicon are therefore highly desirable. Direct growth of III-V on silicon substrates has been very challenging because of high epitaxy temperatures that are incompatible with CMOS circuits. Moreover, the large mismatches of lattice constants and thermal expansion coefficients between III-V compounds and silicon cause compromises in reliability and performance. As for poly-silicon, the lack of long-range crystalline coherency in the substrate makes high-quality III-V epitaxial deposition impossible. As such, there has been a focus on growing three-dimensional nanostructures, which show great promise to overcome these difficulties.

In this dissertation, a novel growth mechanism that yields catalyst-free, self-assembled, single-crystalline nanoneedles and nanopillars on dissimilar substrates will be presented. At CMOS-compatible growth temperatures (400 ~ 455 ^{o}C), single-crystalline InGaAs and InP nanostructures are grown on silicon and poly-silicon substrates via metalorganic chemical vapor deposition. Unlike nanowires synthesized with vapor-liquid-solid or selective area growth, the nanostructures expand in both axial and radial directions simultaneously. On top of silicon, these core-shell nanostructures can scale beyond a micron in diameter while maintaining pure wurtzite crystal phase. This high-quality growth is very unusual considering over 6% lattice mismatch between III-V and silicon. More surprisingly, single crystalline InGaAs nanopillars with base diameter far exceeding the substrate crystal grain size can be grown directly on poly-silicon. We study these seemingly impossible heterogeneous growths extensively by examining the crystal lattice at the hetero-interfaces via high-resolution transmission electron microscopy. Discussions on stress-relaxing mechanism, nanostructure nucleation schemes as well as alloy composition uniformity will be presented.

With the excellent crystalline quality, InGaAs and InP nanostructures exhibit extraordinary optical properties. Lasing is achieved, for the first time, in *as-grown* InGaAs and InP nanopillars monolithically synthesized on silicon and poly-silicon. Nanopillar-based devices with respectable diode ideality factor and extremely low dark currents are developed directly on top of silicon. Demonstrations of optoelectronic functionalities including light emission, detection and photovoltaics will be presented. The findings in this work open up a new chapter in the heterogeneous integration of lattice-mismatched materials and their device structure design.

To my beloved family

Table of Contents

List of Figures

Acknowledgements

Like the nanostructure growth mode presented in this dissertation, my PhD life has not been conventional. I have experienced the deepest valley in my life during the first year of my study. I am very thankful to have a very supportive family which brings me out of the darkness. I am very grateful to my parents and sister, who put down their work and came to US immediately after my injury. Without their continuous love, care and encouragements in these five and a half years, I would not be able to stay strong and tough for all the challenges. Losing one eye's vision is indeed a misfortune. But I am glad that the family bonds have become stronger than ever.

I have to express my deepest gratitude towards my thesis supervisor, Professor Connie Chang-Hasnain, for her continuous guidance to my research. I am very grateful that she has given me such a great opportunity to work on nano-science and to explore my research interest in transmission electron microscopy. In addition to technical knowledge, Professor Chang-Hasnain has also inspired me with her life experience. I am truly impressed by her passion, diligence and optimistic altitude towards research. I would also like to thank Professor Ming Wu, Professor Eli Yablonovitch and Professor Ronald Gronsky for serving on my qualifying exam committee. Their insightful advice has been very useful to my research and dissertation writing.

I am truly grateful to my best friends and labmates in Berkeley, Weijian Yang and Yi Rao, for taking great care of me through all my surgeries over these many years. I will never forget the support you gave me, both physically and mentally, during the most difficult time of my life.

Being a grower who cannot do process, I am really indebted to my co-workers Wai Son (Wilson) Ko, Fanglu Lu, Thai Truong Du Tran and Dr. Roger Chen. I would not have been able to make any achievements in research without their help and input. I owe much to Dr. Linus C. Chuang, who not only mentored my research work, but also helped my family a lot when we were living in UC Village. I am very grateful to Dr. Forrest Sedgwick for enlightening me out of deep depression in front of Tang Center. At the same time, it has been my pleasure to work with Linda Li, April Sun, Indrasen Bhattacharya and Dr. Stephon Ren. I appreciate the fruitful discussions we had that led to all the wonderful work in the group. Finally, I would like to thank the rest of the optoelectronic group members for their intellectual support and friendship that makes my life colorful inside and outside Cory Hall.

My gratitude also goes to my collaborators outside UC Berkeley. I have to thank Professor Vladimir Dubrovskii and Dr. Maxim Nazarenko for developing such a beautiful model for the core-shell nanopillar growth. I feel particularly indebted to Professor Martin Kamp and Professor Alfred Forchel for getting excellent preliminary results on high-resolution transmission electron microscopic studies, which later become the major topic of this dissertation.

I would not have been able to carry out my work on microscopy without the support from the national center for electron microscopy (NCEM). I have to extend my sincere gratitude to Dr. Peter Ercius, Chenyu Song, Dr. Colin Ophus, Dr. Marissa Mancuso, Dr. Christian Kisielowski and John Turner for their guidance and training. Special thanks goes to Mary Scott for her intellectual input to the 3D tomography project. I truly enjoy the time spending with all the NCEM scientists over the past two years.

For financially supporting my work, I thank MARCO IFC, DoE Sunshot (DE-EE0005316) and E3S (NSF Award 0939514).

These five and a half years have not been easy to me. Thank you all for being on my side.

Chapter 1 Introduction

The integration of optoelectronic and electronic circuits is poised to transform personal electronics because it will not only enable a vast range of otherwise unattainable capabilities, but will also reduce power consumption, weight and size. In spite of all the wonderful electrical properties, silicon, the backbone material for transistor technologies, cannot interact with light efficiently because of its indirect band gap. III-V compound semiconductors, on the other hand, have been an important building block in optoelectronics due to their excellent optical and electrical properties. The synergy of III-V with silicon inexpensively is therefore highly desirable.

Direct growth of III-V on top of silicon is seemingly the easiest way to merge the two materials together. However, owing to mismatches in lattice constants and thermal coefficients, high-quality epitaxial growth is actually very difficult [1-3]. Wafer bonding is thus developed to mitigate these issues. In this technique, an intermediate layer, usually composed of metal, epoxy or solder balls, is used to 'glue' the III-V epi-wafers onto silicon substrates [4-9]. Devices with respectable electrical and optical performances have been reported. However, the diverse terrain in complementary-metal-oxide-semiconductor (CMOS) circuits poses great challenge in the intact fusion of the two materials. Moreover, the precision required for patterning and alignment can become very difficult to achieve when the bonding area increases. Scalability therefore becomes an issue for this approach.

To facilitate scalable manufacturing, monolithic integration of single-crystalline III-V with silicon is of paramount importance. Among all the III-V materials, GaP has a lattice constant that is closest to that of silicon. Much effort has therefore been put on the synthesis and fabrication of thin-film devices based on the GaP material system. A very complicated alloy Ga(NAsP) is developed as the active material for light emission [10-11]. While low temperature operation of electrically pumped laser has been demonstrated on silicon, the high growth temperature ~ 700^{o}C is detrimental to CMOS transistors. This incompatibility therefore poses a major roadblock to the monolithic synergy of III-V and CMOS technology via epitaxial growth.

Instead of traditional thin film, a lot of research work focuses on the growth of three-dimensional nanostructures. With growth temperature considerably lower than that in conventional epitaxial growth, nanostructures show great promise in overcoming the incompatibility issue. In addition, the extra dimension of freedom along the lateral direction facilitates stretching of bonds elastically to accommodate for stress due to lattice mismatch without creating misfit defects (see Figure 1-1). Single crystalline III-V nanowires can thus be grown monolithically on top of silicon.

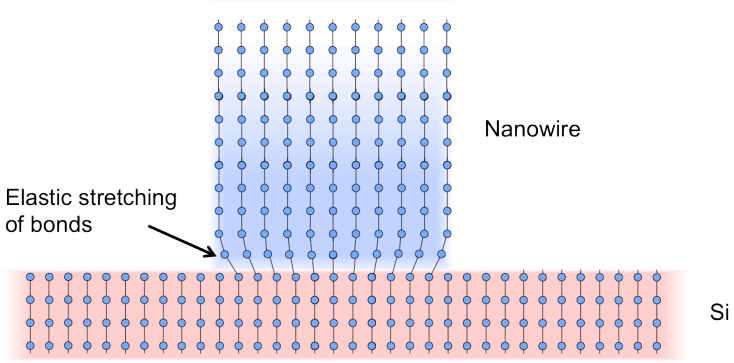

Figure 1-1 Elastic stress relaxation at the III-V/Si interface in nanowires

There are two major techniques for the synthesis of nanowires – vapor-liquid-solid (VLS) growth [12-14] and selective area growth (SAG) [15-17]. In the former case, nano-scale metal droplets (e.g. Au or In) are used as the catalyst for nanowire growth. At elevated temperature, the metal catalysts melt into liquid droplets and dissolve reactants from the surrounding vapor. Solid III-V crystal is subsequently deposited onto the substrate upon super-saturation, as illustrated in the schematic in Figure 1-2(a). In the latter case, a mask layer is deposited on top of the substrate. SiO_2 or SiN_x are the common material choices for the mask layer, which serves to confine the growth at specific areas. Nanowires are then grown at the pre-defined openings via normal epitaxial deposition, as depicted in Figure 1-2(b). Using these techniques, III-V nanowires with outstanding optical and electrical properties have been demonstrated on silicon.

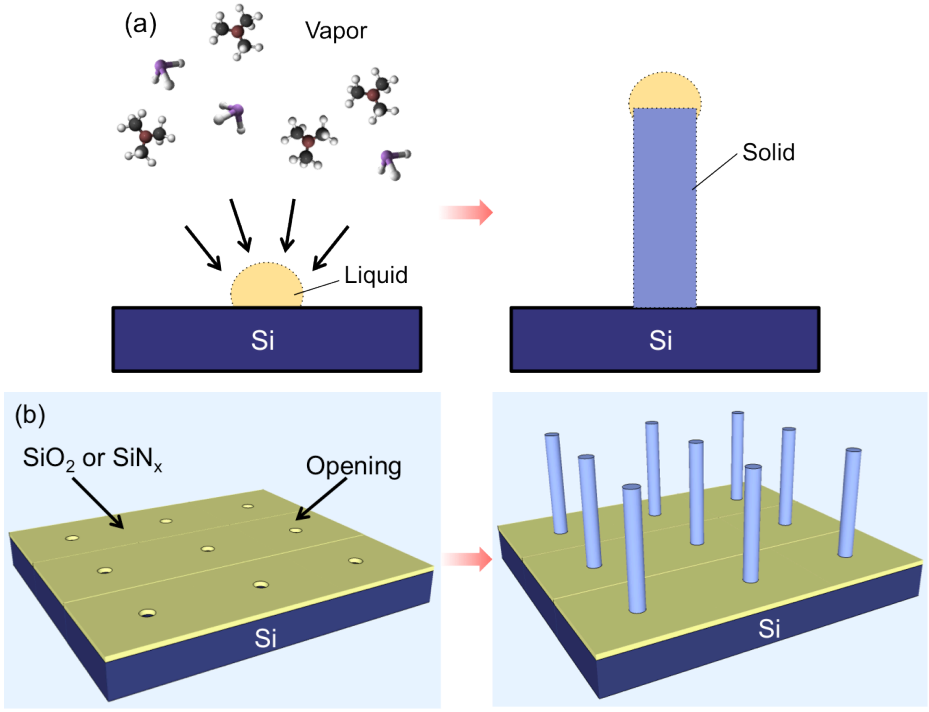

Figure 1-2 Schematic illustrations of (a) VLS growth (b) Selective area growth

Although III-V nanowires on silicon show promising optoelectronic performances, there are limitations with the growth mechanisms. Au particles used in VLS growth are considered as 'toxic' contaminants to CMOS fabrication since the inert metal can create deep traps in transistors [18]. While the nanowire length along the axial direction can be tailored by varying the growth time, the diameter is pretty much pre-defined by the nanoparticle size in VLS or by the mask opening size in SAG. Unfortunately, there exists a critical diameter in these techniques above which the nanostructure turns into polytypic or even polycrystalline phase [19-20]. Thus, nanowires synthesized with VLS or SAG usually have diameters < 300 nm. The small lateral dimension increases the surface-to-volume ratio, making the nanowires more vulnerable to irradiative surface recombination. In addition, light confinement is poor in nanowires with small diameters. Consequently, lasing is never achieved in as-grown nanowires on top of silicon. Hence, an alternative technology that enables the synthesis of micron-sized high quality III-V structures on silicon is highly desirable.

Recently, we discovered a novel growth mechanism that yields self-assembled, single crystalline nanoneedles and nanopillars. The nanostructures consist of (Al, In)GaAs core-shell heterostructures and can be monolithically grown on silicon substrate *via* metal-organic chemical vapor deposition (MOCVD) [21-23]. The growth temperature is as low as 400 ^{o}C, which we consider to be CMOS compatible. Unlike nanowires synthesized by VLS and SAG, our nanostructure size scales linearly with growth time in both axial and lateral directions, thanks to the characteristic core-shell growth mode. In particular, the nanostructure base diameter can be increased to beyond a micron while still maintaining excellent crystal quality, despite more than 4% lattice mismatch between III-V and silicon. This amazing growth mode is also applicable to the synthesis of GaAs nanoneedles on sapphire in which the lattice mismatch is as high as 46% [24]. With size much larger than conventional nanowires, nanopillars exhibit superior optical cavity quality factor. Room-temperature operation of as-grown nanopillar-based lasers on silicon by optical pulsed pumping is consequently demonstrated. In addition, we reported room-temperature operation of (Al, In)GaAs light-emitting diodes and avalanche photodiodes grown on silicon substrates and processed by standard fabrication techniques [5]. These exciting results motivate detailed studies of this unique growth mechanism.

This dissertation devotes to the material studies of III-V nanostructures grown on dissimilar substrates via the novel growth mechanism. Basic crystallography and principles of transmission electron microscopy are introduced in Chapter 2 to facilitate the subsequent discussion on crystal phase purity and defects. Chapter 3 details the investigation on how single crystalline InGaAs nanopillars can be grown on mismatched (111)-Si substrates. Explanations will be given on how misfit stress is relaxed via the formation of tapered root and what initiates the nucleation of nanopillars. Moreover, how the nanopillars can grow into wurtzite phased metastable state will also be discussed. The chapter ends with the demonstration of devices with respectable electrical and optical performances, showing the potential of the nanopillar structures to bridge the gap between optoelectronics and Si-based CMOS technologies.

In addition to single crystalline silicon, polycrystalline silicon is also a very important platform for a vast variety of applications including sensing, nanofludidics, thin film transistor, photovoltaics and so on. Chapter 4 focuses on how nanopillar growth on poly-silicon can enable the integration of optoelectronics with these many applications. In particular, we will discuss how the tapered root can enable the growth of single crystalline nanopillar with base diameter far exceeding the substrate crystal grain size. The demonstration of the first random lasing in arsenide-based nanostructures will also be included.

With the success in the synthesis of arsenide-based nanostructure devices on silicon, we extend the unique core-shell growth mechanism to another III-V material system, InP. Owing to its superior surface properties, lasing is achieved in unpassivated InP nanopillars under optical pump. Chapter 5 discusses the similarities and differences between the growth of InP and InGaAs nanostructures on silicon in terms of crystal phase purity, stress relaxing mechanism and nucleation model. We will also investigate how regrowth and site-controlled growth can facilitate direct device fabrications on silicon. The studies presented in this dissertation underscore a possible pathway for the monolithic integration of opto-electronics and many other possible technologies, with single and polycrystalline silicon as the bridging platform.

Chapter 2 Crystallography and Electron Microscopy

As discussed in chapter 1, a large portion of this dissertation focuses on the study of crystal growth of III-V nanostructures on Si substrates. Transmission electron microscopy (TEM) is a powerful tool in examining the crystal quality and phase purity of nanostructures. We can also deduce the possible growth mechanism by identifying the type of defects present and how the defects propagate. Understanding the basics, e.g. how images are formed and what the limits are, is of great importance in interpreting the microscopic images. This chapter is going to briefly discuss basic crystallography of III-V materials, followed by a succinct introduction to fundamentals of coherent and incoherent transmission electron microscopy.

2.1 Zincblende and Wurtzite Crystal Structures

Simply speaking, a crystal is an ensemble of well-ordered closely packed atoms linked together with chemical bonds. The closely packed structure can be considered as layers of atoms stacking on top of each other to form a bulk lattice. In III-V crystals, the atoms are all in sp^3 hybridization. Each III- (or V-) atom is bonded to four V- (or III-) atoms, resulting in a tetrahedral configuration, as illustrated in Figure 2-1(a)[**]. Each bond is a single bond formed by overlapping of sp^3 orbitals. With the absence of π-electron overlap, the two groups linked together by a single bond can rotate freely with respect to each other. Two rotational 'eigenstates', namely staggered and eclipsed states, are of particular interest, as depicted in Figure 2-1(b) and (c). In staggered conformation, the separation between an atom and its 3rd nearest neighboring atom is the farthest, thus minimizing the repulsion between the pair. On the other hand, eclipsed conformation exhibits mirror symmetry and allows maximum attraction for the aforementioned pair. In a III-V crystal, the 3rd nearest neighbor of a III-atom must be a V-atom, and vice versa. It seems that eclipsed state would be more energy favorable as it maximizes the attraction between the 3rd closest neighbors. However, this is not always true, depending on the ionicity of the bond. If the compound involves elements with high electronegativity, the bond becomes highly polarized with electrons pulled towards that element (e.g. N in a GaN crystal). This polarization induces attractions between the 3rd nearest neighbors and thus favors the eclipsed state. However, if the bond is highly covalent (e.g. Ga-As and In-As bonds), electrons are more fairly shared between the two elements and thus more confined within the bond. Attraction between the third nearest neighbors is negligible. In this case, a staggered conformation is preferred to lower repulsion between the neighboring bonds.

[**] The 3D molecular models are generated with Jmol: an open-source Java viewer for chemical structures in 3D

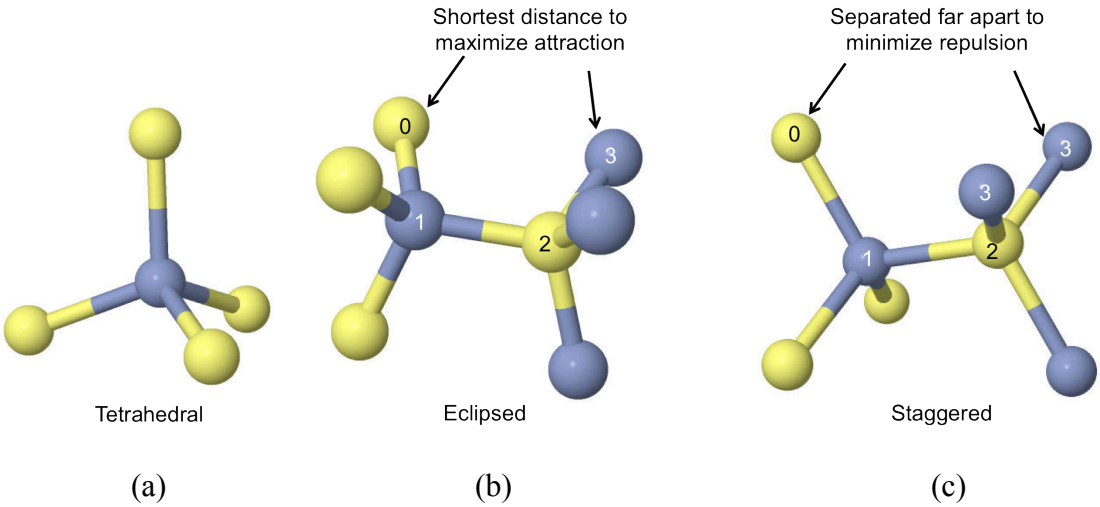

Figure 2-1 Schematic diagrams of (a) tetrahedral unit cell with atoms in sp^3 hybridizations (b) eclipsed and (c) staggered rotational 'eigenstates'. The numbers on the atoms indicates how we count the proximity of the neighboring atoms. Atom #0 is the atom of concern and while atom #3 is the 3rd nearest neighbor.

Theoretically, each covalent bond in an sp^3 hybridized system can be either staggered or eclipsed. To form a closely packed atomic layer, 3 of the 4 covalent bonds have to be in staggered state. The remaining covalent bond, which is responsible for inter-layer linking, can be either staggered or eclipsed. This freedom subsequently gives rise to the two most common crystal phases in III-V materials – zincblende (ZB) and wurtzite (WZ) structures. ZB structure, consisting of purely staggered bonds, is usually more energy favorable due to its higher degree of symmetry. On the other hand, WZ structure is considered asymmetric due to the presence of an eclipsed bond along c-axis or [0001], i.e. the direction in which the atomic layers stack on top of one another. This peculiarity gives rise to many unique properties in WZ crystals, including the presence of spontaneous and piezo- electric fields [25], polarization dependence on crystal orientation [26] and strong 2nd harmonic emission [27]. In addition, WZ crystals usually have energy band properties that are different from those of ZB materials. For example, InP in WZ phase has a bandgap energy 80meV higher than its ZB counterpart. This is exactly the motivation why we are interested in using WZ phased InP nanostructure for photovoltaic applications, which will be discussed in more details in Chapter 5.

As mentioned, the major difference between ZB and WZ structures is how the atomic layers are linked together. The eclipsed bonds in WZ structures along c-axis leads to an ABAB stacking sequence of the atomic layer, while the staggered bonds in ZB results in an ABCABC stacking sequence. Figure 2-2 shows how the staggered and eclipsed bonds affect the stacking in ZB and WZ crystals.

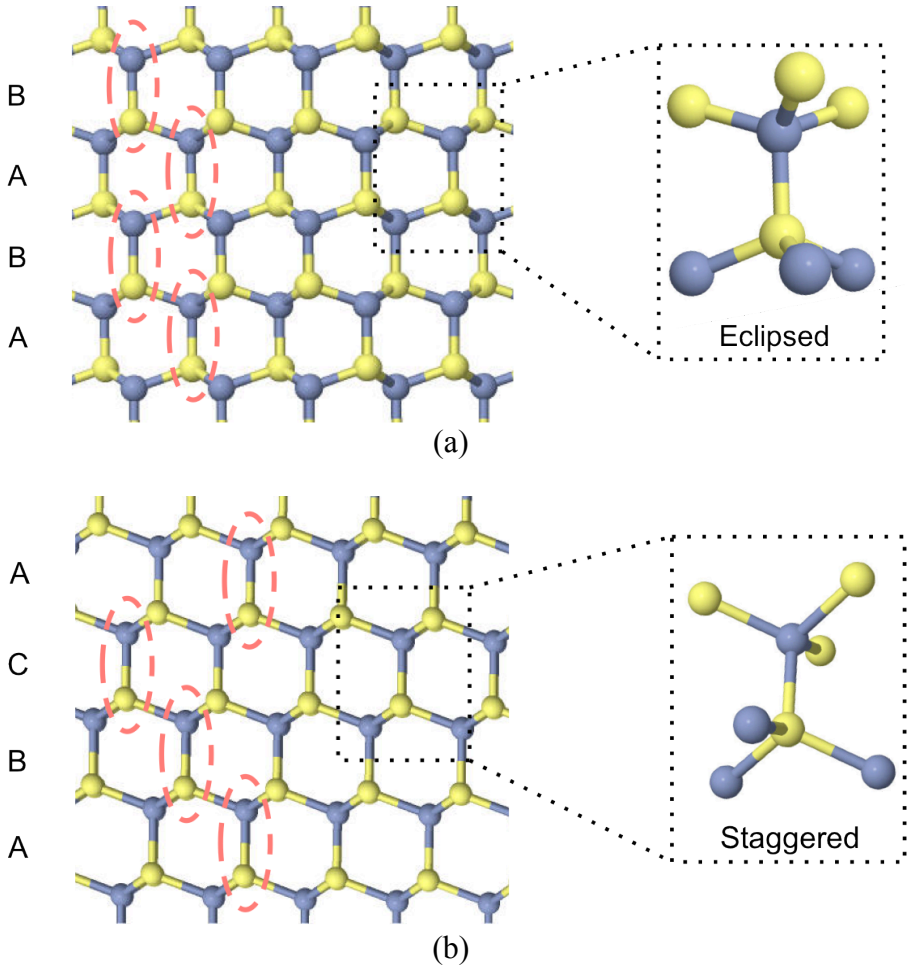

Figure 2-2 Schematics of (a) Wurtzite and (b) Zincblende lattices. Red circles highlight the position of the concerned III-V pair in each layer.

Whether a III-V material prefers WZ or ZB phase can be roughly estimated by the ionicity of the crystal [28]. The higher the ionicity, the more attraction between the 3rd nearest neighbors and thus the more favorable WZ over ZB phase. Ionicity can be determined by the parameter

$$\frac{ZC}{\hbar\omega_p}$$

where Z is the valence, C is Philip's electronegativity difference and $\hbar\omega_p$ is the plasma energy of the valence-electron gas. Higher valence implies a stronger tendency of electron transfer (ionic) rather than electron sharing (covalent). As II-VI materials have higher valence than III-V compounds, II-VI materials are usually more stable in WZ than ZB while III-V are predominantly ZB. Higher electronegativity difference between the III- and V-atoms promote polarization in the III-V pair and thus increases the ionicity of the chemical bond. Nitrogen has a much higher electronegativity than other group V

elements such as phosphorus and arsenic. As a result, all III-N compounds have much stronger tendency to attain WZ phase while all III-P and III-As materials are more stable in ZB phase. However, being too ionic induces excess attraction between the 3rd nearest neighbors and this distorts the original tetrahedral based architecture. This distortion can be estimated by measuring the c/a ratio of the WZ crystal. The more the c/a ratio deviates from the ideal value of 1.633, the greater is the distortion of the lattice and thus the less stable is the crystal phase. For example, MgO, a very ionic II-VI binary compound, exists as rock salt crystal rather than WZ or ZB phase. To have a more accurate estimation on the preferred crystal phase, a more rigorous calculation of energies is needed.

A more accurate way to determine the favorable crystal phase in III-V material is to calculate the free energy difference between the two phases ΔE_{W-ZB}. A negative ΔE_{W-ZB} means that WZ phase is less stable than ZB phase, and vice versa. Figure 2-3 shows the WZ-ZB energy differences ΔE_{W-ZB} calculated using orbital radius model [29]. While nitrides (except BN) prefer WZ phase, all the other III-V compounds are more stable in ZB phase. These results agree with the predictions made based on ionicity estimations.

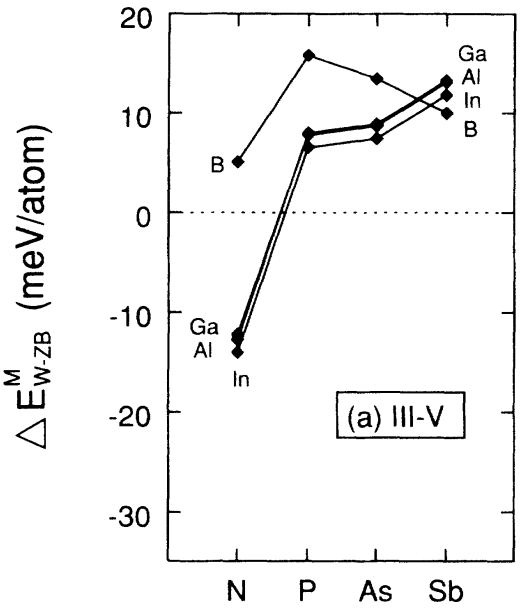

Figure 2-3 Predicted WZ-ZB energy differences ΔE_{W-ZB} for the III-V series (Ref [29])

So far we have been discussing the crystal phase stability in bulk III-V materials. What will happen when the dimensions shrink down to nanometer scale? In general, the feasibility of a reaction depends on the change in free energy ΔF. The more negative the change in total free energy, the more favorable the reaction. The change in free energy by formation of nanowire [30] is given by

$$\Delta F = -\frac{\pi D^2 L}{4\Omega}\Delta\mu + \pi D L \gamma_{S-V}^{l} + \frac{E}{1-\nu}\frac{\pi D^2 L}{4}\frac{\epsilon_o^2}{1+\frac{A_v L}{D}}$$

, where D is the nanowire diameter, L is the length, Ω is the volume of each III-V atomic pair, $\Delta\mu$ is the potential change from vapor to solid, γ_{S-V}^{l} is the solid-vapor surface energy, E is the Young modulus, ϵ_o is the strain and ν is the Poisson ratio. In simple terms, the total free energy change is a sum of crystal formation energy, surface energy and strain energy. In bulk materials, the surface-to-volume ratio is small so that the crystal formation energy dominates over the surface energy. Thus, the crystal phase feasibility is solely dependent on how stable the chemical bonds are within the lattice. Since $\Delta E_{W-ZB} > 0$ in arsenides and phosphides, ZB structure is preferred in their bulk epitaxial films.

In the case of nanostructures, however, surface energy can no longer be neglected. In general, nanostructures grow along [111] in ZB (or [0001] in WZ). The sidewalls of the nanowire, which contribute to most of the surface areas, are composed of planes perpendicular to the growth directions. In ZB, the low energy planes that are perpendicular to [111] are $\{1\bar{1}0\}$ and $\{\bar{2}11\}$. The equivalent planes in WZ crystal are $\{1\bar{1}00\}$ and $\{11\bar{2}0\}$, respectively. Creating a surface can be considered as breaking a set of bonds in an infinite crystal lattice. Surfaces with less dangling bonds possess lower surface energy and thus are more stable. Figure 2-4 illustrates how bonds are broken in creating ZB$\{1\bar{1}0\}$ and $\{\bar{2}11\}$, as well as WZ $\{1\bar{1}00\}$ and $\{11\bar{2}0\}$. Since ZB $\{\bar{2}11\}$ looks exactly the same as WZ $\{1\bar{1}00\}$ (as seen in Fig 2-4 (a) and (b)), the number of dangling bonds on ZB $\{110\}$ and WZ $\{11\bar{2}0\}$ are the same. In other words, ZB $\{1\bar{1}0\}$ has the same surface energy as WZ $\{11\bar{2}0\}$. On the other hand, 4 dangling bonds are created in every 3 layers when exposing ZB $\{\bar{2}11\}$ while only 3 bonds are broken in every 3 layers in creating WZ $\{1\bar{1}00\}$ surface. Therefore, on average, WZ crystal has a lower surface energy than its ZB counterpart.

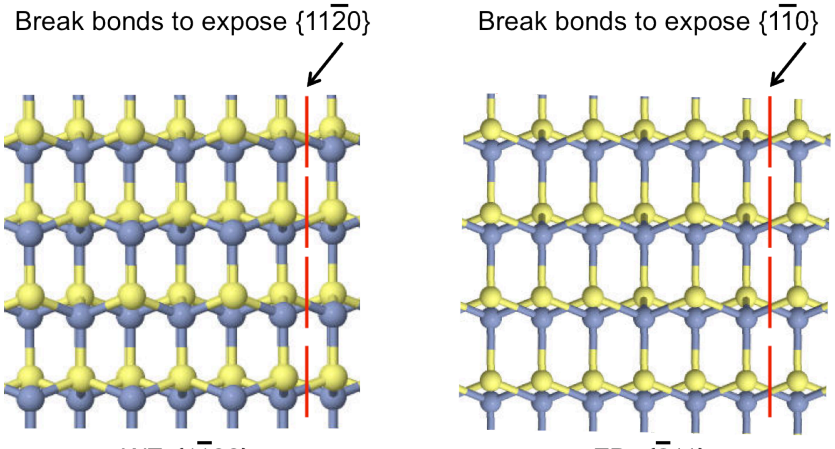

(a) (b)

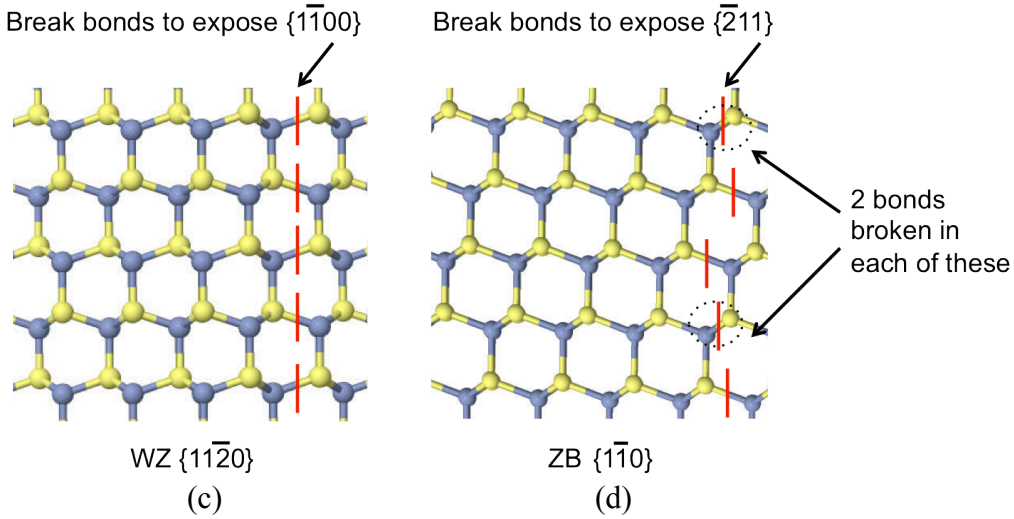

Figure 2-4 Schematic diagrams illustrating the number of dangling bonds created to expose (a) {11$\bar{2}$0} (b) {1$\bar{1}$0} (c) {1$\bar{1}$00} (d) {$\bar{2}$11}

When the surface-to-volume ratio becomes sufficiently large, surface energy can outweigh crystal formation energy and become the most influential factor in ΔF. Having a substantially lower surface energy, WZ structure can become more energy favorable when the nanowire diameter is below a certain critical value, which is usually well below 100 nm. This is actually experimentally observed in many works on nanowire growth via vapor-liquid-solid and selective growth [19, 20]. As the nanowire expands over the critical diameter, the structure loses its crystal purity in WZ phase and evolves into a mixture of WZ and ZB phases. The nanoneedle/nanopillar in this work, however, remain to be pure WZ phase even when the structures scales up to micron size. This unconventional behavior will be described in more details in chapter 3.

2.2 Coherent Imaging with Electrons

To study crystal phase purity and identify defects at hetero-interfaces, the capability to resolve lattice in atomic scale is of great importance. Lattice spacings are usually in the order of Å, or 10^{-10} m, which is well below the diffraction limit of visible light with wavelengths > 400 nm. Thus, an alternative 'light' source with much smaller wavelength is needed. Fast-moving electron beam is an ideal candidate for lattice imaging because its wavelength can be sharply reduced by increasing the accelerating voltage. With the use of de Broglie relation and taking special relativity into account, we can calculate the wavelength of electrons by the equation

$$\lambda = \frac{h}{m_o v}\sqrt{1-\frac{v^2}{c^2}}$$

At 200keV (a common operating voltage in TEM), the wavelength of electrons can be as small as 0.00251 nm, which is 1/100 times the lattice constant. In spite of such a small

wavelength, the state-of-the-art resolution in aberration corrected microscope can only approach 0.1 Å. This is highly related to the imperfections in lenses and mechanical stability of the microscope as well as the sample itself. Nevertheless, such resolution is already making TEM one of a very powerful tool to study crystals and defects.

When an electron beam is incident onto a lattice, each atom acts as a scattering center which 're-radiates' circular waves in all directions. The waves from each atom interact with one another, resulting in constructive and destructive interferences along certain directions, depending on the periodicity of the lattice arrangements. This coherent scattering mechanism is known as diffraction and is governed by the Bragg's law of diffraction

$$2dsin\theta = n\lambda$$

With lattice spacing $d \sim 1$ Å and electron wavelength $\lambda \sim 0.01$ Å, Bragg's law enforces that diffraction can happen only when $sin\theta \sim 0$, i.e. when the planes are oriented almost parallel to the incident beam. After going through the sample, the diffracted beams are focused by the objective lens and subsequently projected onto the screen or camera. There are two planes related to the objective lens, namely the focal plane and the image plane, as illustrated in Figure 2-5.

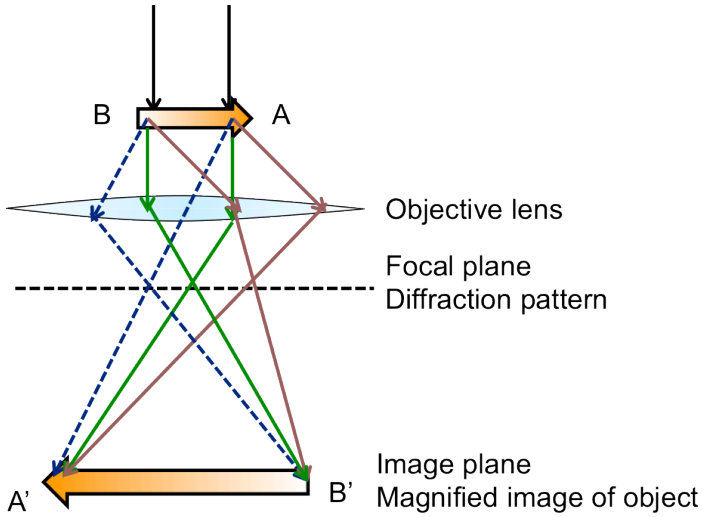

Figure 2-5 Ray diagram illustration of imaging in TEM

At the focal plane, all electrons diffracted to the same direction are focused down by the objective lens to a single spot. For example, the red beams in Figure 2-5 all condense to the same point at the focal plane of the lens. Each spot therefore represents the scattering from a set of plane. This collection of spots on the focal plane is known as the diffraction pattern. By using an aperture to limit the area of interest, selective area diffraction pattern (SADP) can be obtained. SADP is actually the Fourier transform of the lattice, also known as reciprocal lattice, along a particular direction. In order words, SADP is a unique fingerprint that enables us to recognize the crystal structure of the sample being examined. By identifying the features in SADP, we can even deduce the crystal purity of

a sample. Figure 2-6 shows the diffraction patterns of a pure WZ and polytypic (WZ-ZB mixed phase) crystal. The SADP of the WZ sample displays a clear single set of spots, revealing the high crystal purity. On the other hand, the diffraction spots in the polytypic sample are hazy and are connected by streaky lines along the [0001] direction. This indicates a huge amount of stacking disorders in the area of interest. More details of this phenomenon will be discussed in chapter 5. In addition to qualitative determination of crystal phase and purity, SADP also enables quantitative measurements of lattice constants. In fact, the spacing between the diffraction spot and the transmitted beam is inversely proportional to the lattice spacing of the corresponding set of planes. It should be noted that SADP is formed from the diffraction over a relatively large area of the sample. Therefore, the information obtained from an SADP is an average result of the whole area selected. This can be useful when we want to understand the general crystalline property of a nanostructure as a whole.

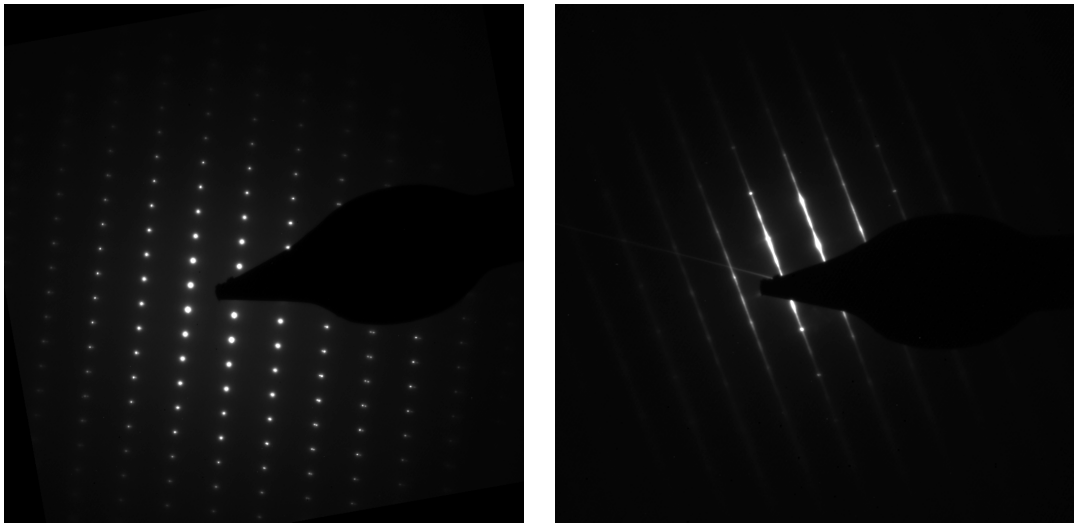

Pure WZ phase WZ/ZB mixed phase

Figure 2-6 Diffraction patterns of pure WZ and WZ/ZB polytypic crystals

While SADP is a useful tool to determine crystal phase and quality over a large area, imaging can provide valuable information on how the lattice varies at highly localized regions, e.g. hetero-interface between different materials. Furthermore, defects like dislocations and stacking faults can be identified via imaging under special alignments such as two-beam condition. At low magnification, imaging is achieved by utilizing amplitude contrast. Areas with more scattering events (e.g. thicker region or border of discontinuous material) usually appear to be darker. In this work, we use amplitude contrast imaging extensively to locate stacking defects in the nanoneedle/nanopillar structure. However, since the mis-stacked layer is very thin (~ 2-3 nm), its appearance is usually unobvious, especially when the structure is thick. In this case, proper sample tilt can help boosting the contrast and increasing the visibility of defects. Figure 2-7 shows a pair of images of the same object with different sample tilts – the 1st image is tilted on-axis along [11$\bar{2}$0] while the 2nd one is slightly off from [11$\bar{2}$0] towards [0001]. While the on-axis image shows a clean nanopillar with no defects, horizontal stacking fault lines

appear clearly in the off-axis image. Tilting the nanopillar away in a direction perpendicular to the mis-stacked layers can increase their effective interaction volume with the incident electron beam. Owing to their different lattice arrangements, the mis-stacked layers scatter electrons in a way that is incoherent with the rest of the crystal. This subsequently results in the contrast observed. Proper alignment of the sample is thus important in boosting up the contrast and displaying defects properly in amplitude contrast imaging and this will be used in the discussion of crystal purity in the following chapters.

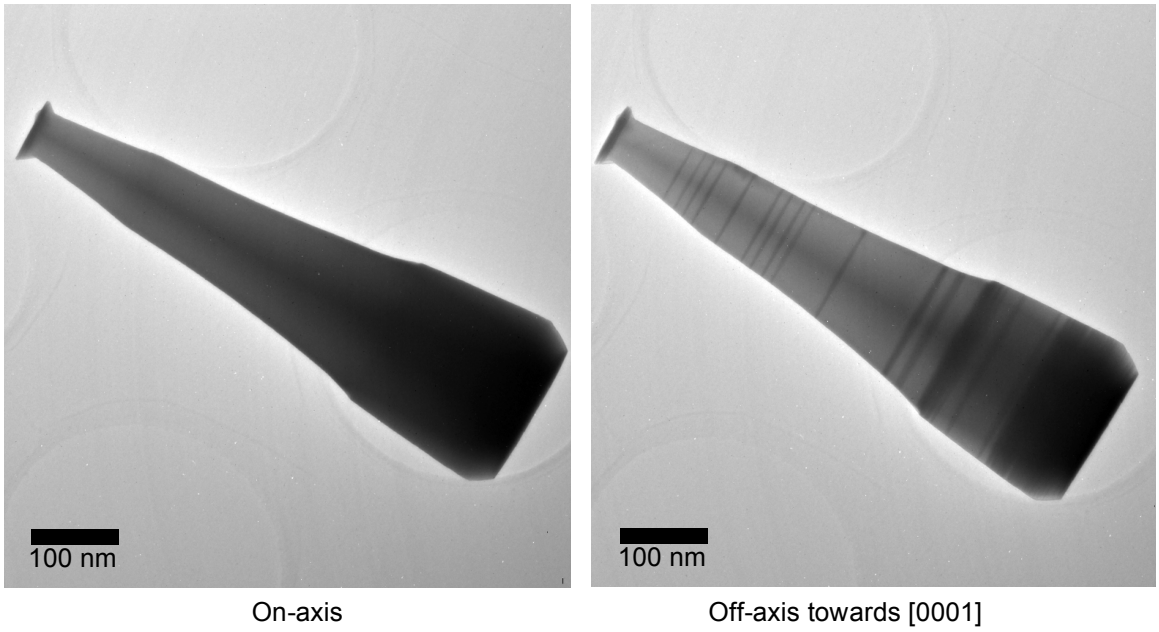

Figure 2-7 TEM images of the same nanopillar with the sample tilted on- and off-axis.

To resolve the crystal lattice in atomic resolution, another imaging mechanism known as phase contrast imaging is utilized. In high resolution TEM (HRTEM), electron beam gets diffracted when it passes through a crystal lattice. At the image plane, the diffracted beams and transmitted beam interfere with one another and the phase difference between the beams results in intensity contrast over the image. Although phase contrast coherent imaging can allow resolution down to sub-angstrom scale, the images formed by this technique are not easily interpretable. When the sample has considerable thickness (i.e. > 10 nm), multiple diffractions can occur when electrons go through the sample. This causes complications in contrast interpretation. In addition, the contrast transfer function (CTF) of the microscope, i.e. the system response in spatial frequency domain, varies as a function of defocus Δf. Atoms can appear as bright dots at one defocus and become dark dots at another defocus. Thus, images taken at different defocuses at the same location can look significantly different. This phenomenon can be observed in the focal series in Figure 2-8 in which a GaAs nanoneedle tip is imaged under various focusing conditions. As Δf increases from -43nm to -13nm, the bright dots in the needle tip change in size and shift in position. Thus, determining atomic position accurately by simple visual judgment is impossible.

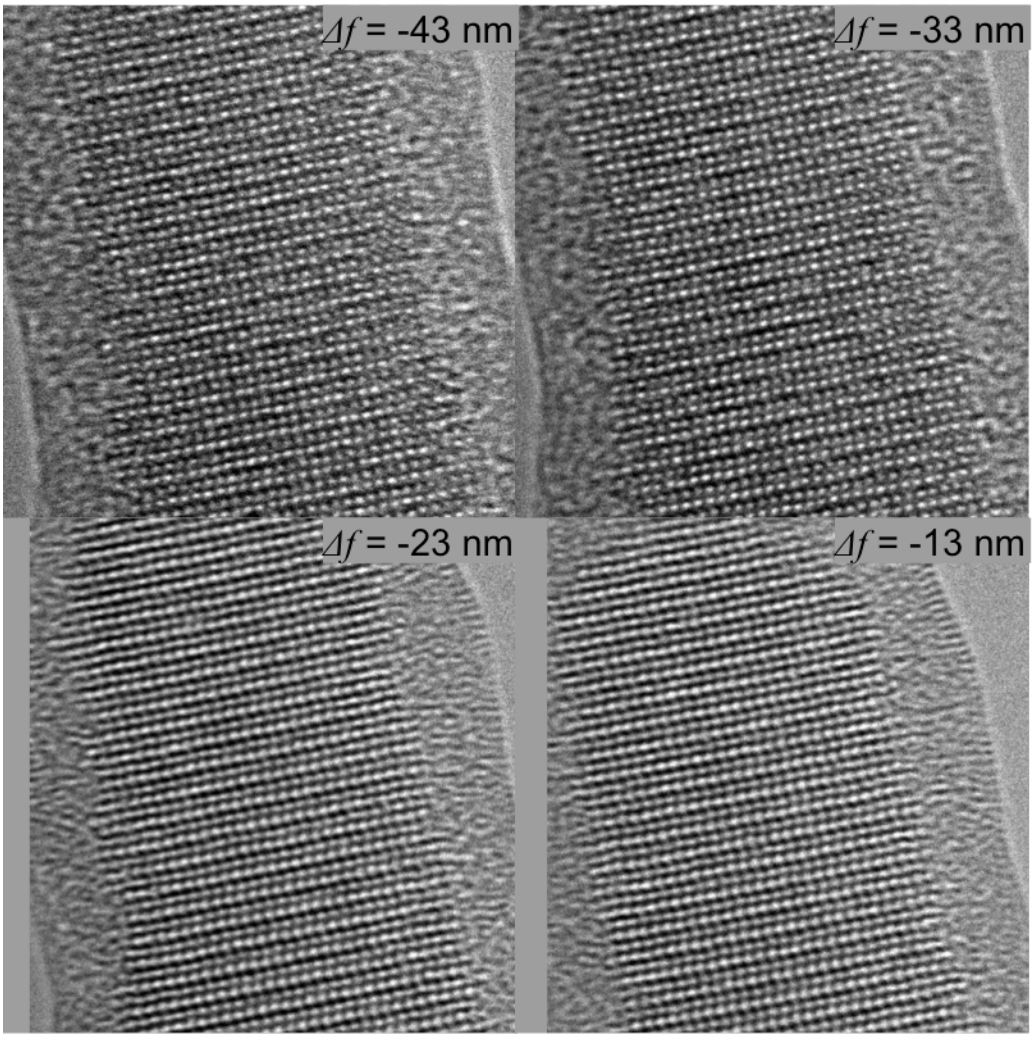

Figure 2-8 Focal series of a GaAs nanoneedle tip

Image processing with proper algorithm is crucial to determine atomic positions precisely with coherent imaging. In normal imaging, only the intensity (and thus amplitude) of the electron wave exiting the sample is detected. However, most of the lattice information is actually embedded in the phase of the exit wave, which is not directly measurable. A technique known as exit wave reconstruction [31] is developed to recover the phase information by back calculating the exit wave function from TEM images. In this process, a focal series of around 20 images are taken under the same microscope settings but with different defocus conditions. If all the microscope parameters like aberrations, beam convergence angles, etc. are known, the CTF of the microscope at each defocus can be computed accurately. Hence, the electron wave exiting the sample can be calculated through iterations. Figure 2-9 shows a reconstructed phase image of the same GaAs nanoneedle tip depicted in Figure 2-8. 20 images with Δf increment step size of 2nm were taken. The characteristic zig-zag lattice arrangement of WZ crystal can clearly be seen in the reconstructed image. A direct interpretation of atomic positions is thus possible. We note that the nanoneedle drifted to the left during the focal series acquisition

and therefore only the right side of the needle tip can be reconstructed. To obtain better reconstruction, improvements in stage/sample mechanical stability are crucial.

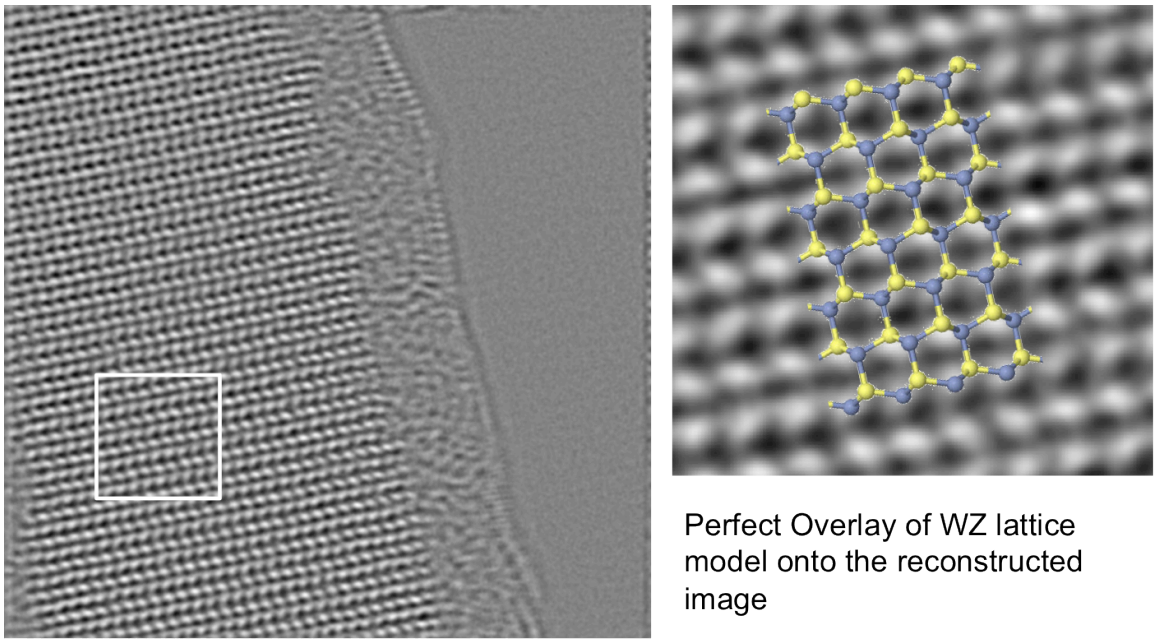

Figure 2-9 Phase image of the GaAs nanoneedle tip obtained by phase contrast reconstruction.

Although atomic positions cannot be read off directly from the as-acquired images, phase contrast imaging does give us an idea how the lattice is like. For example, the ABAB stacking pattern of WZ crystals can be seen clearly from the HRTEM images in Figure 2-8. Any disorder in the lattice can be visible immediately in phase contrast images. In addition, defects like stacking faults or polytypism can be observed easily in HRTEM since any crystal incoherency would result in significant diffraction contrast in the image. Also, HRTEM is more forgiving to the microscope alignment as well as sample tilt. Reasonably high quality HRTEM images can still be obtained even if the alignments are slightly off from perfection. In the following chapters, we are going to study various hetero-interfaces with phase contrast imaging.

2.3 Incoherent imaging with electrons

As discussed in the previous section, direct interpretation of atomic position is difficult with phase contrast imaging. Although exit wave reconstruction can help recover the lost information in phase, intense computation power is necessary for iterative calculation of the exit wave function. Furthermore, a focal series of at least 20 images is needed. The long acquisition time poses a huge challenge on stage and sample stability. An alternative imaging technique with faster acquisition and intuitive interpretation capability is thus desired. Instead of getting contrast as a result of diffraction, imaging can be achieved by detecting incoherently scattered electrons through a crystal lattice. While a parallel beam is incident onto the sample for coherent imaging, the electron beam converges into a small spot in the incoherent technique. The electron probe size can be as small as 0.2 Å

and thus probing single atomic column is possible. The very fine electron probe scans over the entire area of interest for raster imaging, thus giving rise to the name scanning transmission electron microscopy (STEM). Unlike coherent imaging in which the scattered electrons close to the optical axis (i.e. center of the lens) are detected, electrons scattered to specific angles are collected in STEM. Figure 2-10 illustrates the various types of images that can be formed by detecting electrons with different scattering angle α. Since high-energy electron beam has a wavelength much shorter than lattice spacing, Bragg's law enforces that the coherently diffracted beams are scattered at shallow angles. Therefore, bright field and annular dark field images are dominated by phase contrast. Electrons scattered at high angle, however, depend heavily on the scattering power of individual atoms, i.e. interference due to periodic lattice arrangement is negligible. To detect these high angle electrons, a special ring detector with a hollow center is needed. This detection scheme is thus called high angle annular dark field (HAADF) imaging.

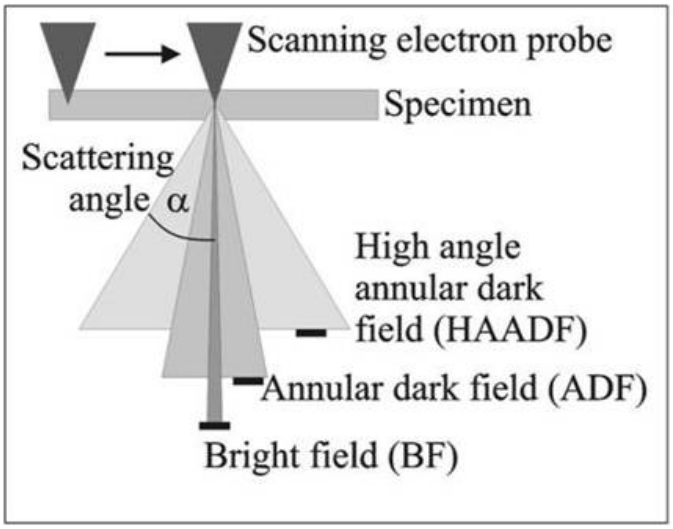

Figure 2-10 Schematic diagram illustrating the working mechanism of STEM [32]

At high angles, Rutherford scattering dominates the scattering mechanism, which is proportional to Z^2 (with Z being the atomic number) [33]. In other words, elements with higher atomic number have higher scattering capability. Therefore, HAADF imaging is also known as Z-contrast imaging – heavier (and thus higher atomic number) elements appear brighter in the image. HAADF-STEM images thus enable intuitive interpretation of the chemical composition variation over the sample. This advantage of HAADF imaging is reflected in Figure 2-11, which shows a cross-section of an InP/InGaAs double quantum well nanopillar structure. Since P-atoms are much lighter than As-atoms, InGaAs appears much brighter than InP in the HAADF image. Parameters like quantum well thickness, interface sharpness, etc. can be read off directly from the image. This information is valuable to device design and growth condition optimization and will be discussed in more details in chapter 5.

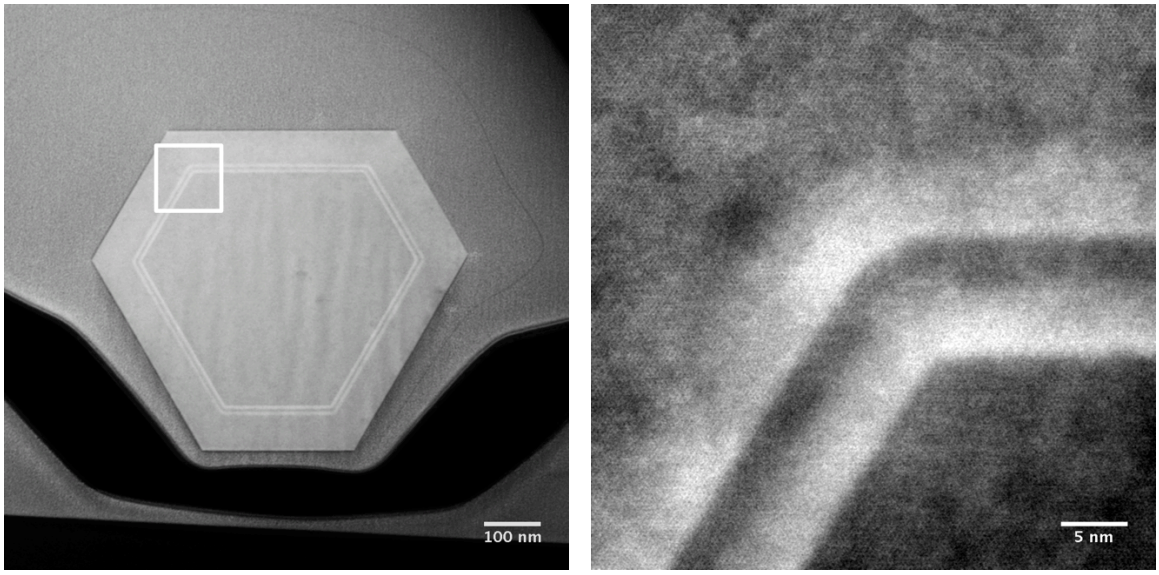

Figure 2-11 HAADF-STEM images of InP-GaAs double quantum well structure

As mentioned, HAADF imaging does not involve diffraction contrast. Therefore, atomic positions can be directly read off from the image – atoms are white while empty spaces are dark. These important properties facilitate the study of lattice in atomic scale. For example, one can investigate the strain present at a hetero-interface by studying how the atoms drift away from their unstrained positions [34]. In addition, z-contrast imaging at atomic scale allows direct identification of elements in a compound semiconductor. For example, since In-atoms are much heavier than P-atoms, In-atoms have much higher intensity in a HAADF-STEM image, as illustrated in Figure 2-12. These powerful properties enable us to determine polarity of a ZB or WZ crystal, which is highly related to the chemical and optical properties of the material.

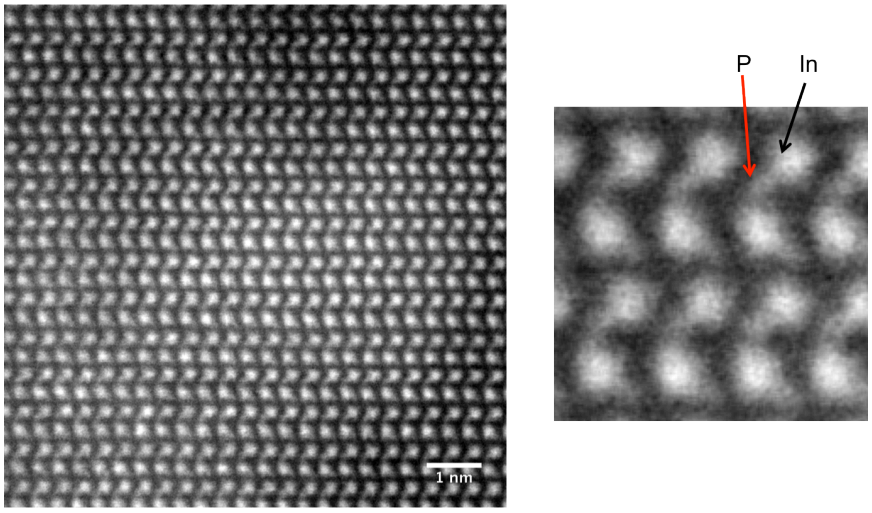

Figure 2-12 HAADF-STEM image of an InP WZ crystal

In spite of the many attractive properties, HAADF-STEM has its own shortcomings. As the electron beam is incident on the sample as a fine probe, a high current dose is delivered to a very small spot. A prolonged exposure can therefore 'burn' a hole on the sample. Moreover, the high current density attracts hydrocarbons, a commonly seen contaminant in TEM samples, to deposit onto the area of interest. The hydrocarbon layer acts as an extra scattering medium and increases the noise in the image. In a dirty sample, amorphous hydrocarbon nanowires can be 'grown' by moving the beam slowly away from the sample, as illustrated in Figure 2-13(a). Carbon contaminants can be removed by oxygen plasma or heating up the sample in vacuum for prolonged period. However, all these steps can cause undesirable damage to the sample. Another difficulty with HAADF-STEM imaging is the intolerance towards sample misalignment. When the crystal has a slight mis-tilt from the zone axis, the atoms from the same column spread themselves out laterally, thus messing up the interpretability of the image (see Figure 2-13(b)).

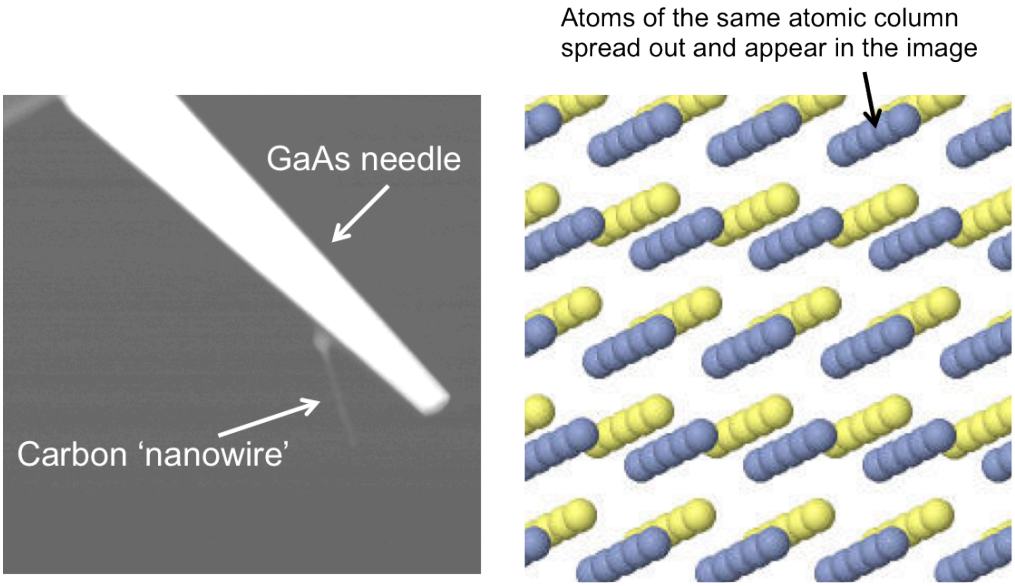

Figure 2-13 (a) Contamination in STEM (b) Effect of a slight mis-tilt from zone axis in incoherent imaging.

With their unique advantages, both coherent and incoherent imaging schemes are utilized to study the mismatched growth of III-V on top of silicon in the following chapters. HRTEM was done with FEI CM-300 at 300KV and Tecnai F20 operating at 200kV. HAADF-STEM imaging was done with Tecnai F20 at 200kV, Titan at 300kV as well as TEAM I at both 80 and 300kV.

2.4 Electron Dispersive X-ray Spectroscopy

When electrons pass through a sample, they can be scattered elastically (as in imaging) or inelastically. In the latter case, electrons can lose energy and excite atoms in the sample

to a higher energy level. Photons are then emitted when the atoms go back to ground state. The photon energy is a quantized entity that is unique to individual elements. Therefore, by quantitatively measuring the intensity and photon energy of the emission, we can deduce the chemical composition of a particular compound. This technique is known as electron dispersive X-ray Spectroscopy (EDS) [35].

Figure 2-14 shows a typical EDS energy spectrum of an InGaAs nanoneedle. The x- and y-axes are photon energy and intensity, respectively. Energy peaks are automatically identified with the responsible elements. With proper fitting to remove the background Bremsstrahlung spectrum [36] and taking into account the Cliff-Lorimer coefficients [37] of the elements, the chemical composition can be determined with respectable accuracy.

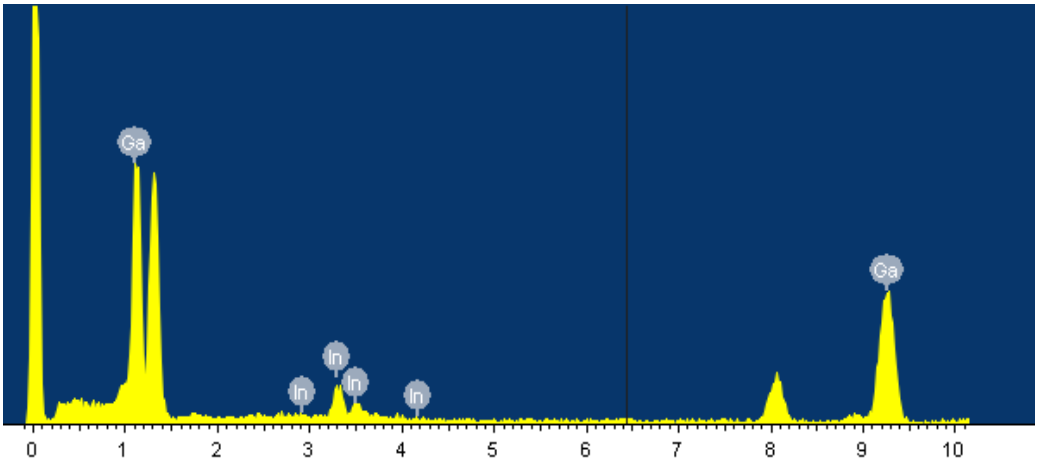

Figure 2-14 Typical EDS spectrum obtained from an InGaAs nanoneedle

With the use of a fine electron probe (the same as that used in STEM), one can not only study the chemical composition of a highly localized region, but also raster to obtain elemental maps of the area of interest. It is therefore possible to study how elements vary spatially, which is important in understanding the abruptness of a heterogeneous interface. In the following chapters, EDS mapping and line profiles are used to quantitatively study composition variations across the InGaAs/GaAs hetero-interfaces, as well as the abnormal indium distribution in (0001) plane of an InGaAs/GaAs nanoneedle.

2.5 Sample Preparation

Sample preparation is the most important part in electron microscopy. A thin sample is always desired for high-resolution imaging as this can suppress multiple scattering within the TEM foil. In general, the thickness of TEM samples should be well below 100 nm. There are multiple ways to prepare ultra-thin TEM foils. Conventional technique usually involves mechanical lapping and polishing to bring the thickness down to ~ 10 μm, followed by ion milling with low energy Ar^+ beams. This technique is not very suitable for III-V nanoneedle/nanopillar since the nanostructure density is not really high. In this work, sample preparation is done in two ways – mechanical removal and liftout with the use of focused ion beam (FIB).

Since the structures of interest are already in nanometer size, they can be directly examined with TEM without any milling step. But of course, the nanostructures have to be detached from the substrate before they can go into the microscope. This can be done by rubbing a TEM grid on the substrate, which mechanically breaks the nanostructures off. Some of the broken structures would then adhere onto the grid by Van der Waal's attractions. The beauty of this wipe-down technique is its simplicity. Besides, multiple needles can be 'wiped' down and examined at the same time. A statistical qualification on the crystal quality can thus be obtained quickly. However, there is no way to verify where a nanoneedle nucleates on – it can be seeding right from the substrate or it can be growing out from a polycrystalline III-V island at a later phase of the growth. Moreover, the base diameter of a nanoneedle can reach over a micron. Such thickness blocks most of the electrons and thus any defects present at the base will not be resolvable. Another problem with wiped-down nanostructures is their mechanical instability. Since they are only held onto the grid by weak Van der Waal's forces, they can roll on the surface freely or even be moved by focused electron beam inside the microscope. Nevertheless, this method does not involve any ion milling and thus the nanostructures can be examined in their most unperturbed state.

To study how III-V nucleates on Si, it is crucial to examine the hetero-interface at atomic resolution. FIB is used to cut through the center of the nanostructure and expose the III-V/Si interface. The FIB used in this work is a Dual Beam FEI scanning electron microscope (SEM). With both electron or ion beams, users can monitor the entire milling and liftout process in real time with SEM. The procedure is outlined as following:

1. Create a pair of markers to register the center of the nanostructure to be extracted (Figure 2-15(a)). This is a crucial step since the nanostructure will be covered completely with Si re-deposition during milling.
2. Pt can be deposited on the nanostructure for passivation. If the region of interest is the III-V/Si interface, the bulk of the nanostructure can passivate itself.
3. Use 30kV Ga^+ ion beam to sputter (i.e. mill) two big holes around the nanostructure to create a thin slice (or lamella) with a thickness of $1 \sim 2$ μm. The slice cannot be too thin or otherwise it would be too fragile for lift-out.
4. Mill the bottom and sides of the lamella to isolate it from the substrate (Figure 2-15(b)). The lamella is hanging freely with only one thin arm attaching to the substrate.
5. Insert the micro-manipulator and glue it to the side of the lamella with Pt. Pt is delivered to the chamber in a gas form via gas insertion system (GIS).
6. Use ion beam to cut the cantilever arm and lift-out the lamella from the substrate (Figure 2-15(c)).
7. Create a slot on the side of a post in the lift-out copper grid.
8. Slide the lamella into the slot until it reaches the bottom. Glue the lamella firmly with Pt (Figure 2-15(d)). Cut the glue connecting the probe tip and the lamella and retract the probe tip (Figure 2-15(e)).
9. Thin the lamella down to < 100 nm (Figure 2-15(f)). Further clean up with Ar^+ beam is necessary to remove the amorphous layers created by high energy Ga^+ ions.

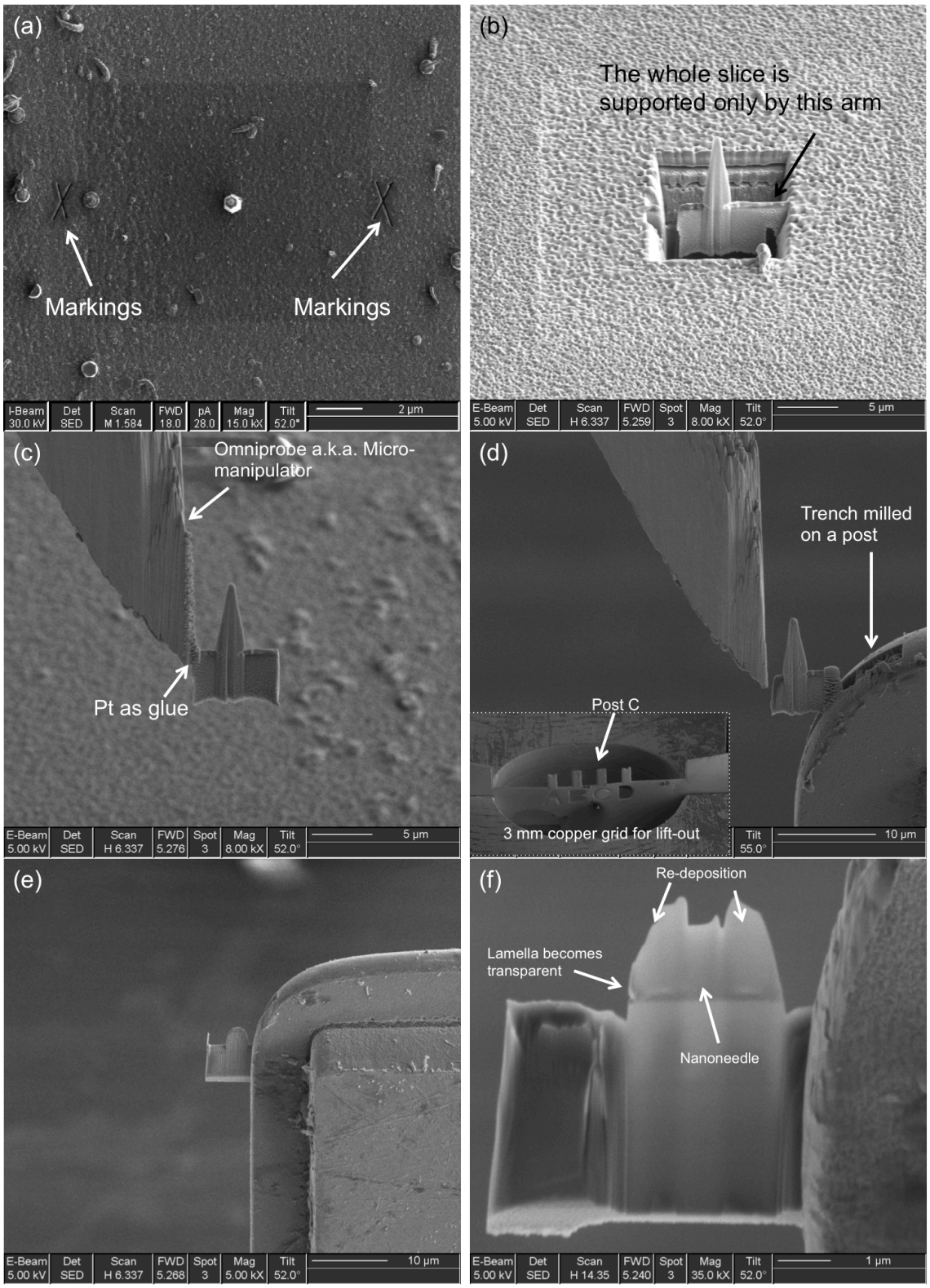

Figure 2-15 Procedures to lift-out a nanoneedle with the use of FIB

With the use of FIB, one can have full control on which part of a particular nanostructure to investigate. This is very useful in the study of hetero-interfaces, which are usually buried deep within the nanostructure and not readily observable in wiped-down samples. However, only one structure can be thinned down for TEM at a time, making this process very time inefficient. Also, milling with high-energy ion beam can cause undesirable damage to the sample. Ga^+ ions can penetrate into the lamella and cause contaminations. This problem is particularly serious on InP – Ga accumulates as balls on the lamella surface and acts as mask in the subsequent milling. Severe curtaining (i.e. highly corrugated surface due to milling artifacts) can occur at the end, leading to a disaster in interpretation of data. Such effect can be observed in Figure 2-16.

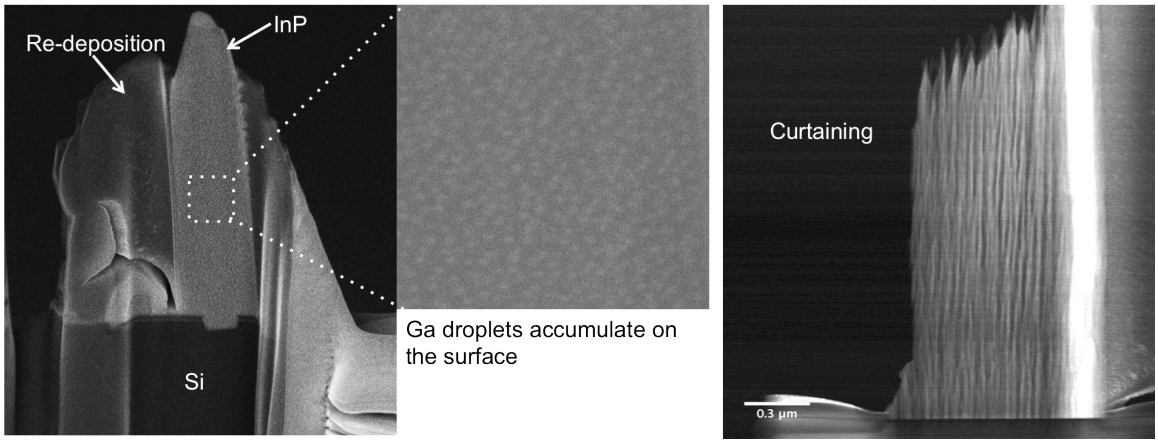

(a) (b)

Figure 2-16 (a) SEM image of an InP lamella with lots of Ga droplets accumulating on the surface. (b) TEM image of a sample with significant curtaining.

2.6 Summary

In this chapter, we introduced the two most important crystal structures in III-V materials – wurtzite and zincblende structures. The stability of the two structures is compared based on ionicity as well as formation energy differences. In addition, we discussed the basic working principles of coherent and incoherent imaging in transmission electron microscopy. Chemical composition can be quantitatively determined by means of energy dispersive X-ray spectroscopy. We also outlined the steps to fabricate TEM thin foils with the use of focused ion beam and simple mechanical break-and-adhere. All of these techniques have their pros and cons, and they are utilized in a way that we can make full use of their advantages.

Chapter 3 Unconventional Growth Mechanism for Monolithic Integration of InGaAs on Silicon

As discussed in Chapter 1, the heterogeneous integration of optoelectronic and electronic circuits is highly desirable. This is because it will not only enable a vast range of otherwise unattainable capabilities, but will also reduce power consumption, weight and size. To facilitate scalable manufacturing, monolithic integration of lattice-mismatched single-crystalline materials is of paramount importance. Direct growth of III-V thin film on silicon substrates has been very challenging because of high epitaxy temperatures that are incompatible with CMOS circuits. In addition, the large mismatches in lattice and thermal coefficients between III-V compounds and silicon can induce high density of defects inside the epilayer. As such, there has been a focus on growing three-dimensional nanostructures, which show great promise to overcome these difficulties [21-23, 38-42].

Recently, we reported a novel growth mechanism that yields catalyst-free, self-assembled, single-crystalline nanoneedles and nanopillars. The nanostructures consist of (Al, In)GaAs core-shell heterostructures and can be monolithically grown on single-crystalline silicon and sapphire at low-temperature (400 ^{o}C), *via* metal-organic chemical vapor deposition (MOCVD) [1-5]. We demonstrated room-temperature operation of (Al, In)GaAs light-emitting diodes and avalanche photodiodes grown on silicon substrates and processed by standard fabrication techniques [3]. Furthermore, we reported room-temperature operation of nanopillar-based lasers on silicon by optical pulsed pumping [4]. These exciting results motivate detailed studies of this unique growth mechanism that enables high-quality growth of micron-sized III-V structures on silicon.

In this chapter, we examine the $In_{0.2}Ga_{0.8}As$/Si interface at the nanopillar roots using high-resolution transmission electron microscopy (HRTEM) by cutting through the center of nanopillars with the use of focused ion beam (FIB). Nanopillars with various growth duration and, hence, base diameters are studied. Nanopillars are found to grow directly on to, and aligned with, the (111)-silicon substrate. The nanopillar root above the silicon interface consists of a transition region in which stacking disorders and defects are confined within. However, above this transition region and up to their full lengths, nanopillars are shown to consist of pure, single wurtzite (WZ) phase without any misfit defects, despite a 6% lattice mismatch between $In_{0.2}Ga_{0.8}As$ and silicon. In the smallest nanopillar with base diameter equal to 50 nm, the transition region is only 3.5 nm thick, *i.e.* ~ 12 monolayers. For nanopillars with over 700 nm base diameter, the transition region is approximately 280 nm thick. The transition region assumes an inverted cone shape in the vertical direction and effectively reduces the InGaAs/silicon contact diameter to about 100 nm. Owing to the unique property of the core-shell growth mode, defects at the base do not propagate upwards and only along the horizontal planes terminating at the sidewall, thus enabling high crystal quality in the bulk material above. In addition, through HRTEM we observe that GaAs, the passivating shell layer for $In_{0.2}Ga_{0.8}As$, grow as much as 15 times larger than the critical thickness in two-

dimensional case without any misfit dislocations emerging at the interface. The nanopillar size scales with growth time and maintains excellent crystalline quality. Lasing is demonstrated under continuous wave (CW) operation when the diameter of the nanopillar base exceeds 1.5 μm. This observation signifies a new concept in heterogeneous growth and device structure design.

3.1 Synthesis of InGaAs Pillars

InGaAs nanopillars are grown on silicon by metal-organic chemical vapor expitaxy (MOCVD). (111) Si substrates are used mainly in this work to yield upright nanopillars. Notably, we can also grow on patterned (110) and (100) Si substrates with slanted nanopillars growing along the degenerate <111> directions. Prior to growth, bare silicon substrates are cleaned with acetone, methanol and water to remove any organic contaminants. After that, the wafers are dipped into 1:10 buffered oxide etchant (BOE) for 3 minutes to remove the native oxide. Complete removal of oxide is indicated by hydrophobicity of the substrate surface. BOE dip not only removes the oxide but also terminates the dangling silicon bonds with hydrogen atoms, thus preventing the surface from oxidation for a short period of time. [43]. We then perform mechanical roughening on this clean silicon surface. Various techniques have been explored to roughen the surface, including tweezer scratching, ion bombardment, wet chemical etching with tetramethylammonium hydroxide (TMAH), etc. There are two purposes with this roughening step.

1. Create bumpiness over the surface which can possibly change the local gas flow pattern around the roughened regions.
2. Open up fresh silicon surfaces for oxidation in air. Oxide is found to be crucial in nanostructure nucleation. In a control experiment, we deoxidized the surface again after mechanical roughening and nanopillars did not nucleate at all. More details will be discussed in the section 3.4.

The roughened substrates are then loaded into an Emcore D75 MOCVD system for material growth. Trimethylindium (TMIn), Triethylgallium (TEGa) and TBAs (tert-butyl arsine) are used as the precursors of In, Ga and As, respectively. The temperature is first raised to ~ 600 ^{o}C to anneal the substrate under a chamber pressure of 70 Torr. TBAs is flown into the chamber during the high-temperature step. The reactor is then cooled down to the growth temperature 400^{o}C. TMIn and TEGa are then flown into the reactor to start the growth. By varying the relative flow rates of TMIn and TEGa, we can control the alloy composition. Nanopillars with heterostructures can thus be synthesized with the characteristic core-shell growth. In this chapter, we focus on the study of two structures – $In_{0.2}Ga_{0.8}As$/GaAs and $In_{0.12}Ga_{0.88}$/$In_{0.2}Ga_{0.8}As$/GaAs. Schematics of these structrures are presented in Figure 3-1. The mole fractions of TEGa and TBAs are kept constant at 1.12×10^{-5} and 5.42×10^{-4}, respectively, during the entire growth process. The mole fractions of TMIn in 12% and 20% InGaAs are 9.86×10^{-7} and 1.73×10^{-6}, respectively.

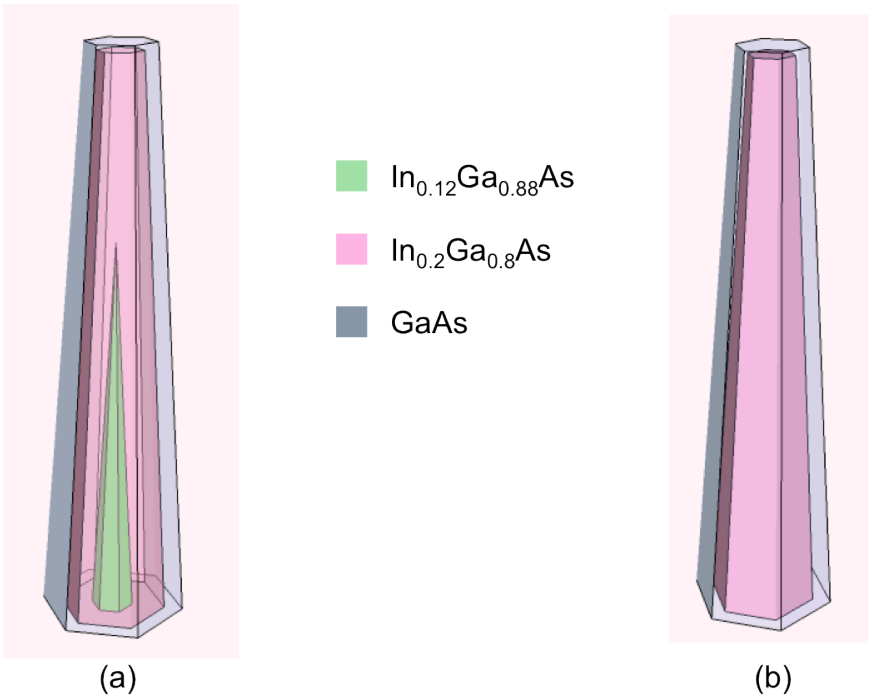

Figure 3-1 The two heterostructures studied in this chapter

Figure 3-2 shows scanning electron microscope (SEM) images of some typical as-grown InGaAs/GaAs core-shell nanopillars grown on (111)-Si. The nanopillars are standing upright on the substrate, showing that they are growing along Si [111] direction. Moreover, the nanostructures exhibit hexagonal shape with clear side facets. This is a first indication that these nanostructures are single crystalline, which is to be further proved by high resolution TEM studies in section 3.3.

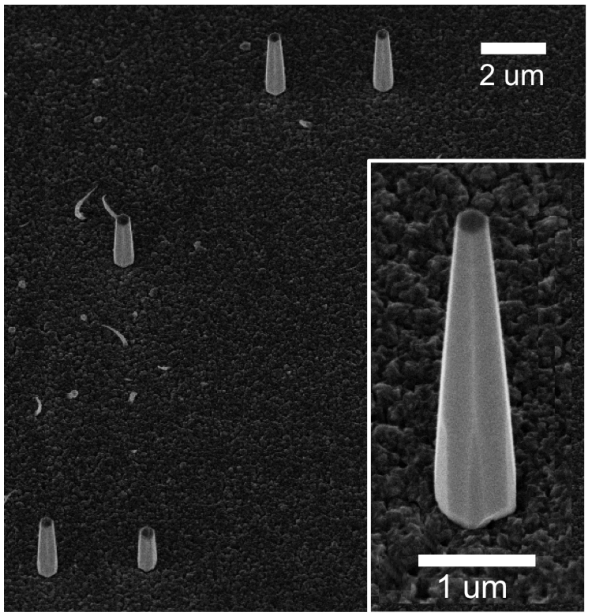

Figure 3-2 SEM images of InGaAs/GaAs nanopillars at 30^{o} tilt

3.2 Growth Evolution of InGaAs/GaAs Core-Shell pillars

To study how the nanostructure evolve, we perform multiple growth runs with increasing growth times. The evolution of the $In_{0.2}Ga_{0.8}As$/GaAs core-shell nanopillars grown on silicon is illustrated by the scanning electron microscope (SEM) images displayed in Figure 3-3 (a), which show that the nanopillar size scales with growth time. Initially, the nanostructure grows into a hexagonal pyramid with an extremely sharp tip – the facet-to-facet taper angle is as small as 5^{o}. Growth then continues in a core-shell manner, with the sharpness well preserved. Vertical growth stops beyond a certain point (in this case after about 42 minutes), while radial growth continues, transforming the originally sharp needle into a hexagonal frustum. This growth mechanism is schematically illustrated in Figure 3-3(b), and is similar to that of GaAs nanoneedles grown on sapphire substrates [**Error! Bookmark not defined.**, 44], with the exception of the abrupt stop to vertical growth. In Figure 3-3(b), we also show an inverted-cone shape root as well as polycrystalline layer surrounding the pillars. Details of how this extraordinary geometry is formed will be discussed in section 3-3.

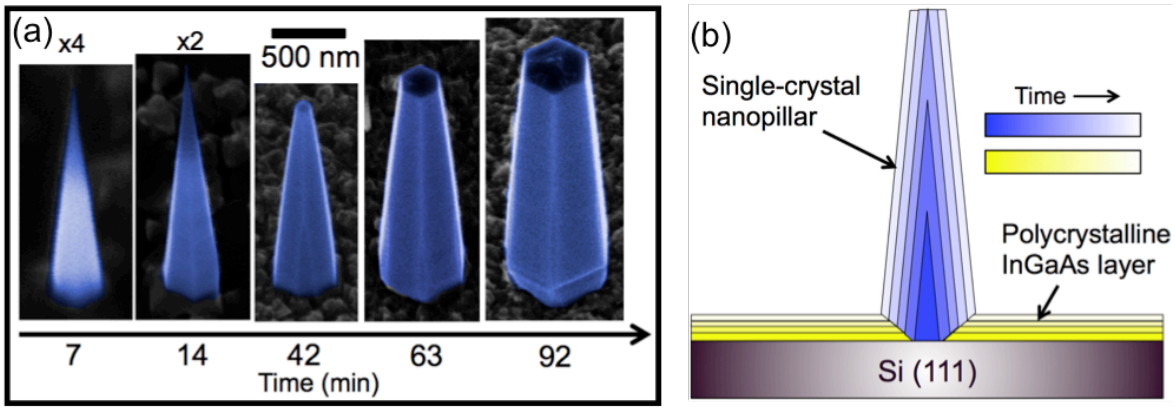

Figure 3-3 (a) Time evolution of the nanostructure from a sharp nanoneedle to a blunt nanopillar (b) Schematic illustrating core-shell growth mode of the nanopillar structure.

A statistical study was performed in which more than 50 nanostructures were measured for each of the six selected growth durations. Figure 3-4 shows the average base diameter and height as a function of growth time, respectively. The base diameter increases linearly with time. In particular, the base diameter can scale up to 1.5 μm while maintaining excellent crystal quality, a distinct difference from other critical dimension-limited nanowire growth [19, 20, 45] The average length also shows a linear dependence on time at the early stage of growth when the nanostructure is still sharp. The length saturates when the growth time reaches ~ 42 minutes, transforming the originally sharp nanoneedle into blunt pillars.

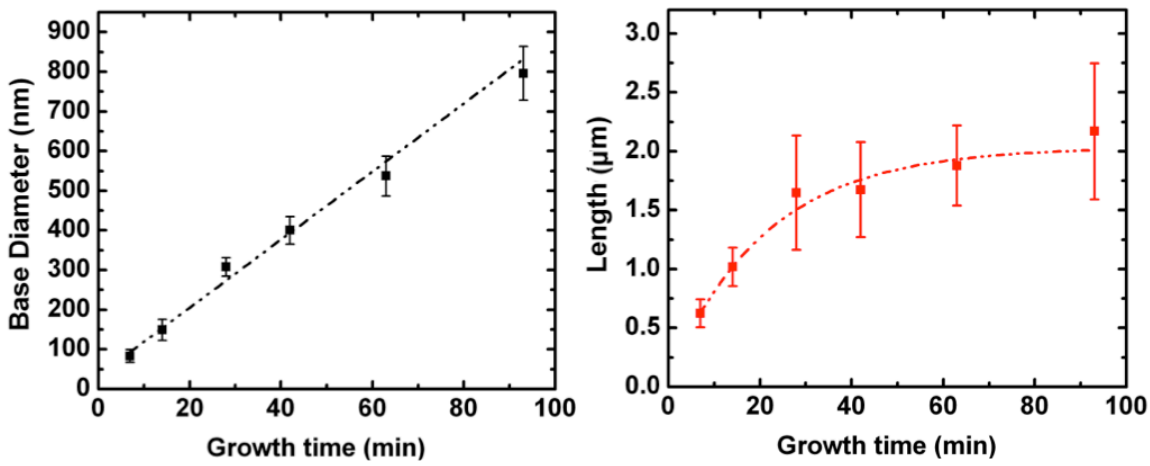

Figure 3-4 Dependences of nanostructure base diameter and length on growth time.

3.3 HRTEM Studies of InGaAs/Si Interfaces

We carried out extensive HRTEM to investigate the origin of the nanopillar growth mechanism. Sample preparation involves the extraction of a lamella from an as-grown nanopillar on (111) silicon with the use of FIB milling and *in-situ* micromanipulations. We cut the nanopillars to expose $(2\bar{1}\bar{1}0)$ facets so that the distinction between WZ and zincblende (ZB) phases can be clearly seen. Over 20 nanopillars have been examined with HRTEM in this work. Details of the sample preparation procedures can be found in chapter 2.5.

Figure 3-5 shows a schematic diagram and the corresponding cross-sectional TEM image of an $In_{0.2}Ga_{0.2}As/GaAs$ nanopillar growing on (111) silicon, respectively. We note that the top part of the pillar is undesirably damaged during the milling process. As a result, only 1.7 μm of the originally 5-μm tall pillar remains intact for this study. Nevertheless, the nanopillar can be clearly seen to directly grow on silicon with a 'footprint' much smaller than the base diameter of the nanopillar, which is 720 nm in this particular lamella. In the many nanopillars examined, the footprint diameter is found to range from 70 to 130 nm. The pillar has an initial section that tapers upwards with an increasing diameter at about 45^{o}, as shown in Figure 3-6. The tapered region has a thickness of 280 nm, which is approximately equal to that of the surrounding layer. Notably, horizontal lines are observed in this inverse-tapered transition region, as seen in Figure 3-6. These features are actually stacking disorders and polytypes, which appear as a result of lattice and thermal mismatches. A range of angles from about 45^{o} to 60^{o} was observed for various TEM samples. The formation of such inverted cone is due to the formation of a polycrystalline layer with slower growth rate. The formation of this poly-InGaAs layer is a result of the low temperature used in the synthesis, which is unfavorable for ZB phase crystal formation. This polycrystalline layer grows instantaneously with the nanopillars and limits the nanopillar base from expanding, as illustrated in Figure 3-3(b).

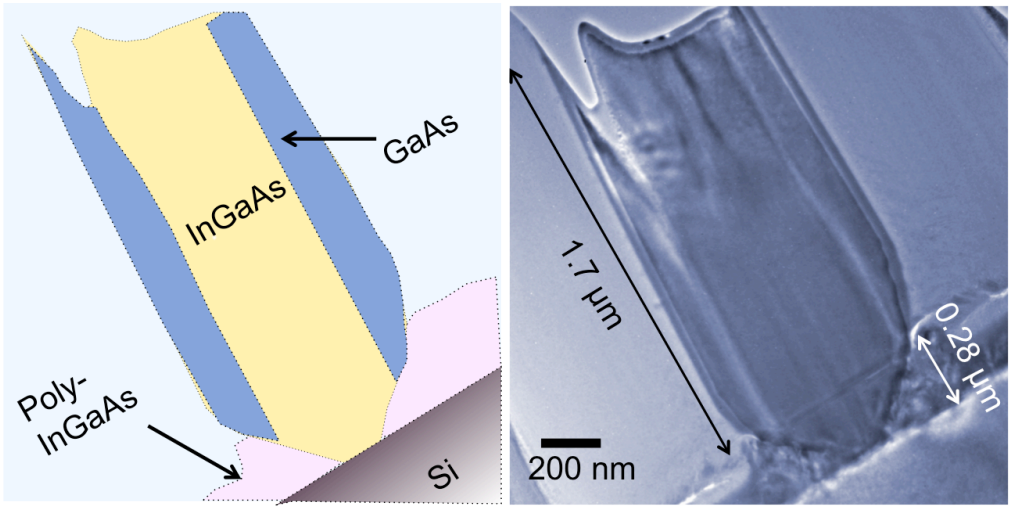

Figure 3-5 Schematic diagram and TEM image of an InGaAs/GaAs core-shell nanopillar grown on silicon

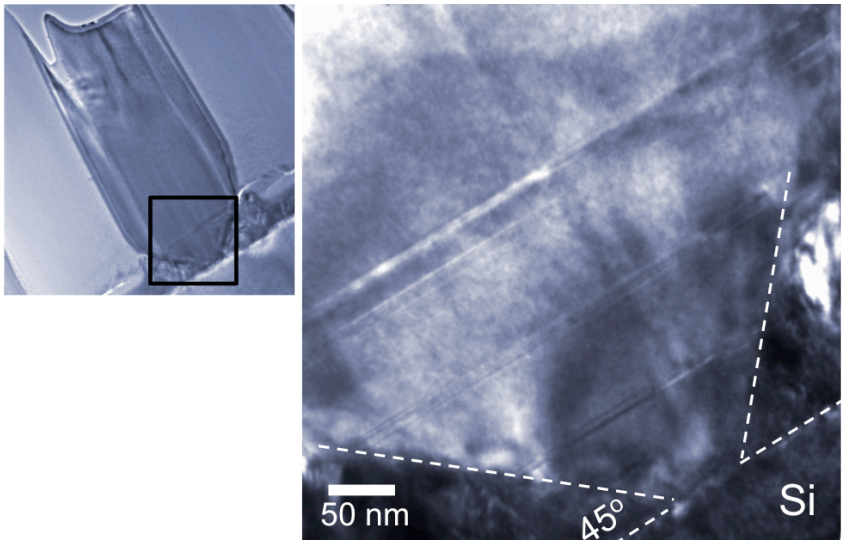

Figure 3-6 Inverse tapering at the base of nanopillar

The polycrystalline layer surrounding the inverted cone pillar root is examined with HAADF-STEM and HRTEM, as shown in Figure 3-7. This material is found covering the entire wafer and forms a rough, continuous layer. The STEM image shows that this material is polycrystalline with many domains, showing short-term ZB crystallinity with random orientations. Stacking faults and dislocations can be seen clearly at the boundary of the crystal domains in the HRTEM image. The origin of this film can be attributed to the coalescence of the randomly formed ZB-phase islands that nucleate during the initial growth stage at low temperature.

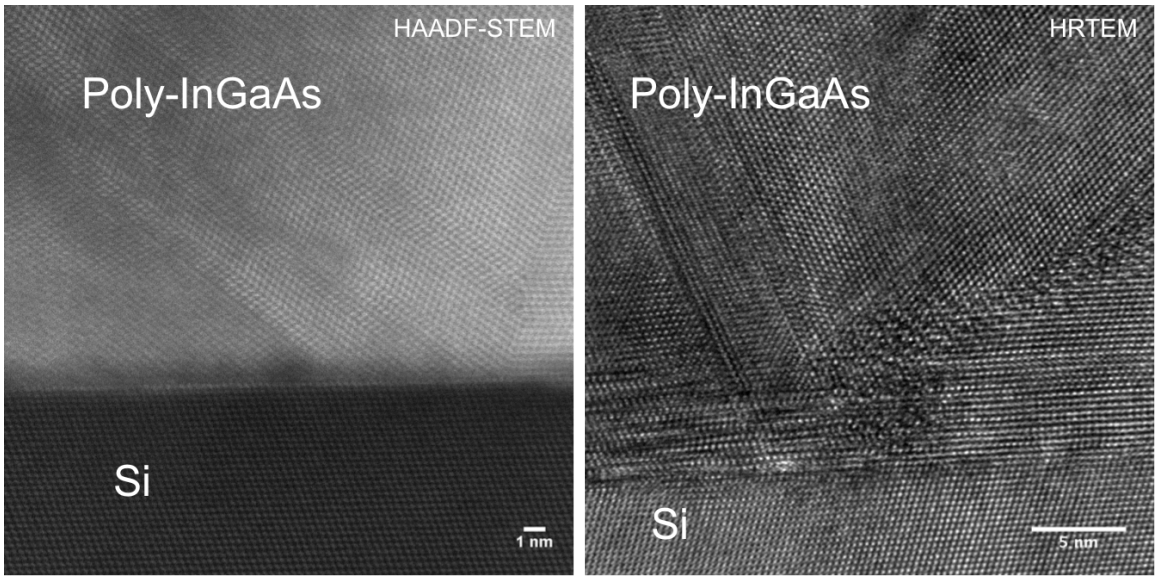

Figure 3-7 HAADF-STEM and HRTEM images of the poly-InGaAs/Si interface.

Above the bottommost tapered-cone region, the bulk material of the nanopillar is pure and single crystalline. No defects or polytypic regimes can be observed for the length above the tapered transition region, as seen in Figure 3-8. We attribute this high-quality growth to the relaxation of misfit strain in the bottom transition region such that the crystal above is essentially stress-free. In this particular TEM sample, the single-crystal bulk material extends 1.7 μm above the root and would continue all the way up to the tip of the nanopillar. Figure 3-9 shows an HRTEM image of $In_{0.2}Ga_{0.2}As$ in the bulk along $[1\bar{2}10]$. The lattice displays a characteristic zig-zag configuration, attesting to the WZ nature of the crystal. Excellent crystal quality is confirmed by the very clear diffraction pattern taken along $[1\bar{2}10]$ in Figure 3-9.

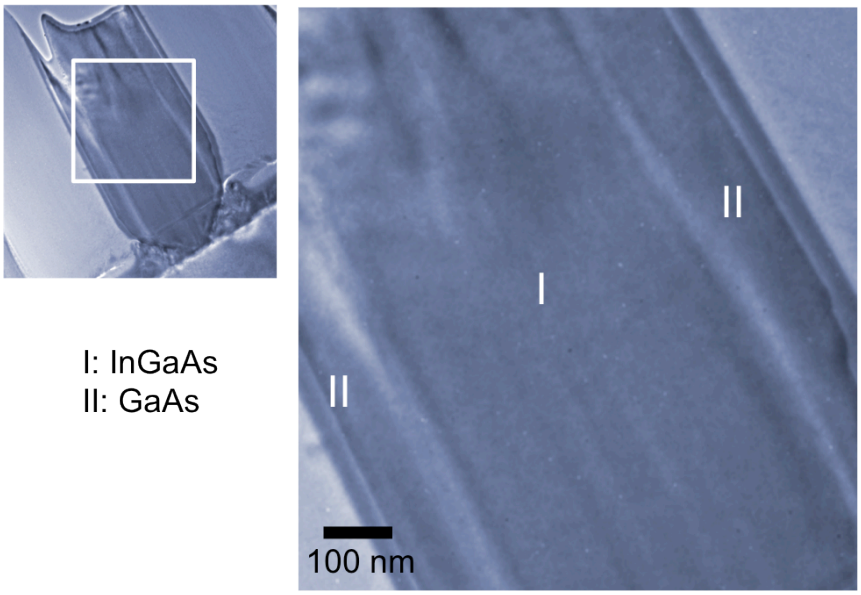

Figure 3-8 TEM image of the bulk material without any noticeable defects.

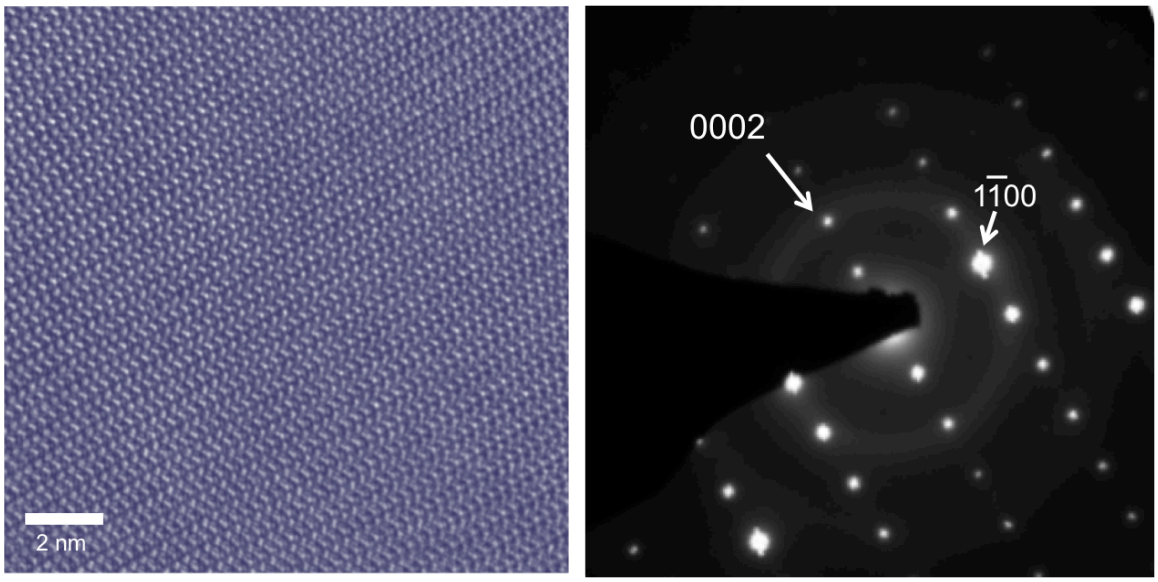

Figure 3-9 HRTEM image and diffraction pattern obtained from the nanopillar bulk. Pure WZ crystal phase can be observed.

While the bulk material is single crystalline, horizontal defect lines are observed at the inversely tapered region at the base. Figure 3-10 shows an HRTEM image of these defects. The originally pure WZ-phased crystal is decorated with stacking disorders, as indicated by the arrows in the figure. We note that the sample thickness at this particular region is above 50 nm. At such thickness, dynamic scattering occurs, i.e. electrons experience multiple diffractions when transmitting through the sample. Scattering from any incoherency in the crystal is amplified, thus resulting in the enhanced contrast.

However, interpretation of lattice positions becomes difficult – the lattice spots become smeared out at the defective regimes.

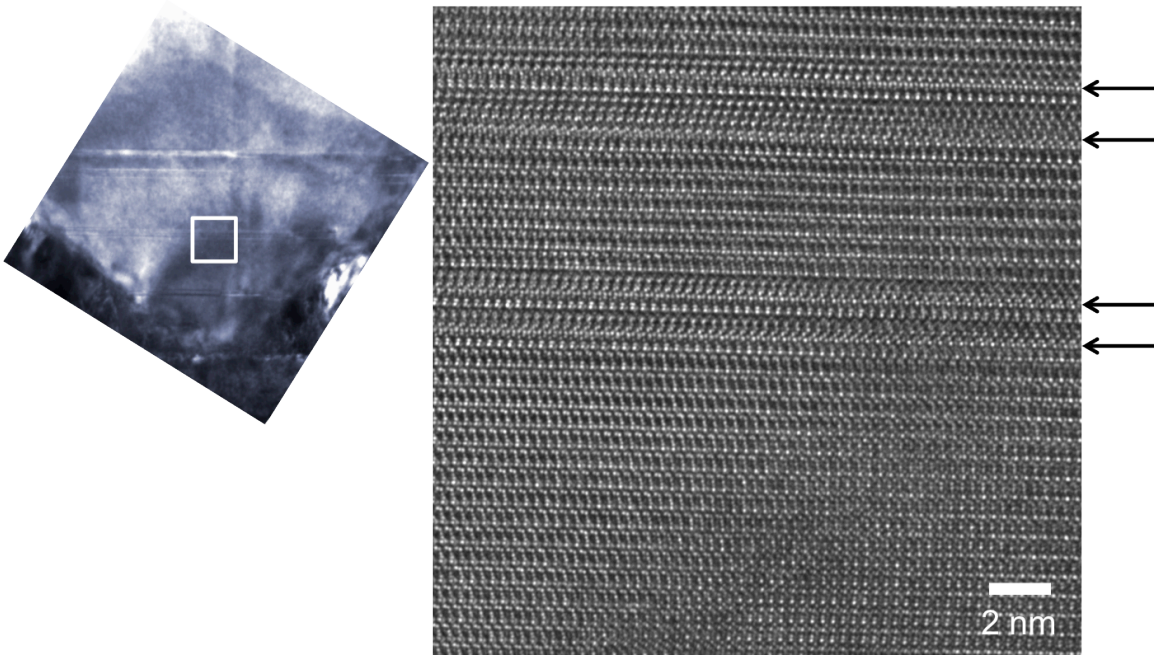

Figure 3-10 HAADF-STEM and HRTEM images of the poly-InGaAs/Si interface.

To study how the atomic layers are mis-stacked, a thinner region of another lamella is imaged with HRTEM, as seen in Figure 3-11. As the foil is much thinner, the stacking disorders do not exhibit extra contrast as in Figure 3-10. However, lattice arrangements can be clearly observed. While a small portion of the crystal is in pure WZ phase, most of the area is in ZB phase. The co-existence of WZ and ZB phases is known as polytypic, as illustrated in the schematic in Figure 3-12. Notably, twinnings and stacking faults (also illustrated in Figure 3-12) are present in the ZB-phased regimes. These stacking defects are usually bounded by partial dislocations, which can relax misfit stress. We believe that the presence of these stacking disorders confined within the inverse cone helps accommodating the mismatch strain between Si and InGaAs. This will be discussed in more details shortly.

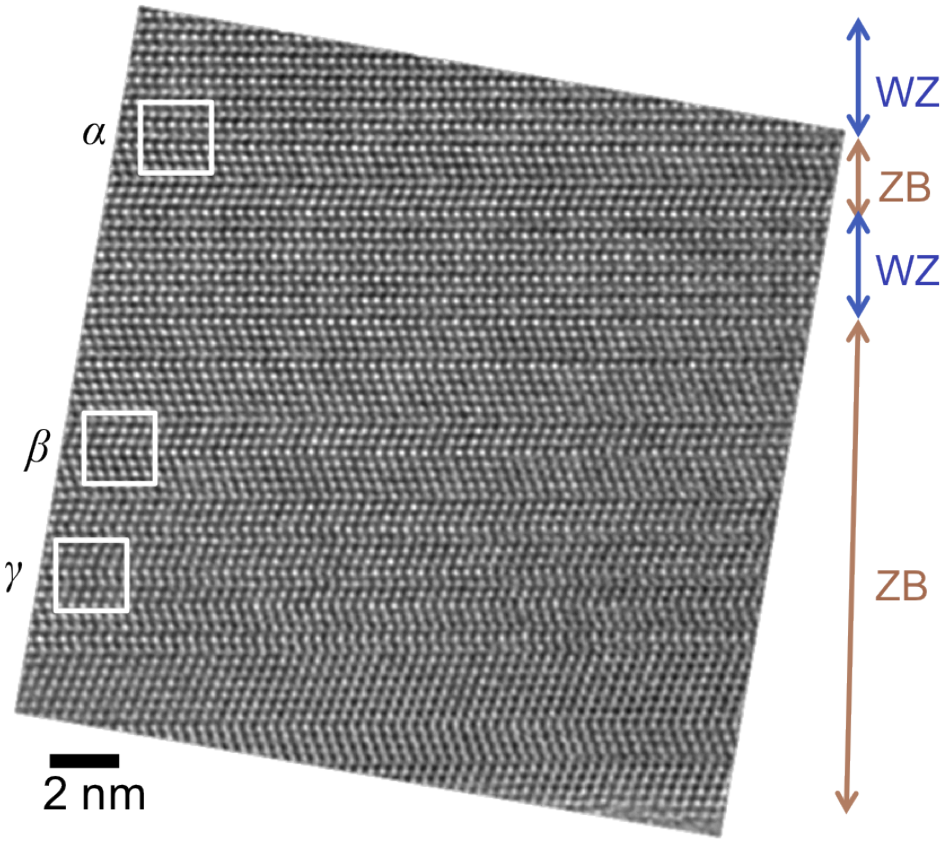

Figure 3-11 Stacking disorders under high resolution

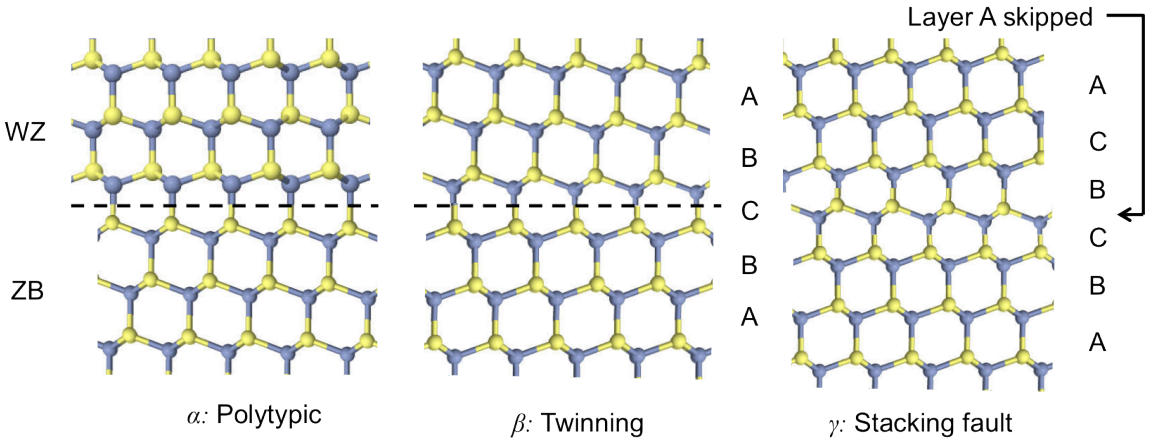

Figure 3-12 Schematic diagrams showing the stacking disorders present in Figure 3-11

To study how stacking disorders develop, we examine the base of nanopillars with different growth times, and hence base diameters. Figure 3-13 shows the TEM images of nanopillars grown for 7, 14 and 68 minutes. As mentioned before, the footprint of InGaAs on silicon is typically 70 ~ 130 nm, which is likely to be the average distance

between islands during initial nucleation. When the nanopillar size is less than 130 nm, the surrounding polycrystalline grains are yet to get close enough and mask the nanopillar growth. Therefore, inverted cone is not observed in Figure 3-13 (a) and (b). Nevertheless, the same phenomenon is observed in all three cases – all stacking faults and defects are well confined within the bottommost region. In particular, when the base diameter is 50 nm, stacking defects only extend 3.5 nm, or ~ 12 monolayers, above silicon, as seen in Figure 3-13 (a). As nanopillar base diameter increases, the disordered region gets thicker to accommodate the extra misfit stress, as seen in Figure 3-13 (b) and (c).

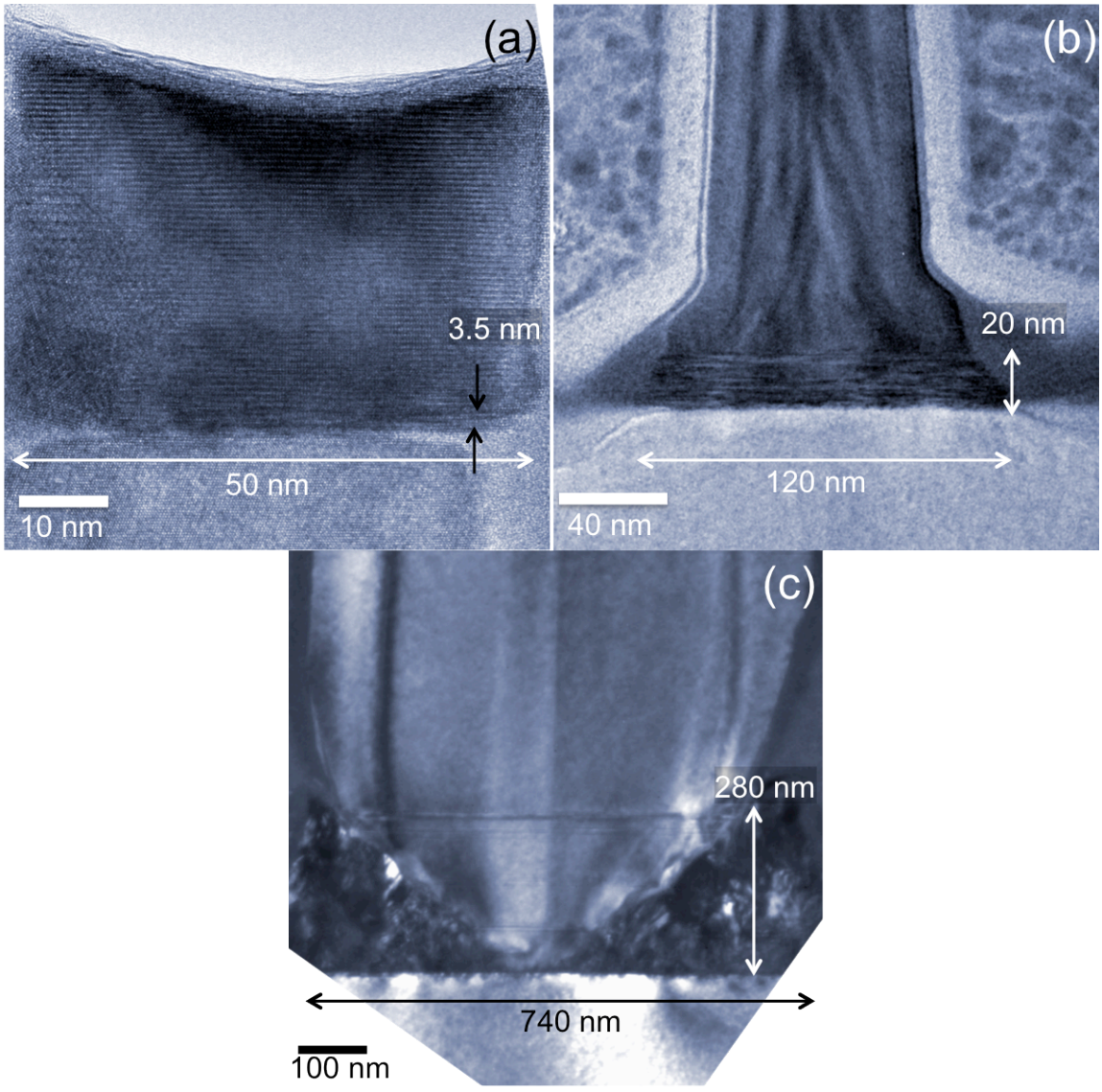

Figure 3-13 InGaAs/Si interface of nanopillars grown for (a) 7 minutes (b) 14 minutes (c) 68 minutes

We note that all defects propagate laterally rather than vertically along [0001]. In other WZ crystals like GaN, threading dislocations propagating along the growth direction are

usually observed. Epitaxial lateral overgrowth (ELOG) is then developed to promote lateral growth so as to bend the dislocations from propagating upward into the active region [46]. The growth mechanism described here, on the other hand, is a pure core-shell growth mode in which growth occurs only in the lateral direction, except the very tip of the structure. Misfit defects therefore propagate horizontally and terminate at the sidewall. Hence, the crystal structure remote from the substrate stabilizes into a single pure WZ phase, which is energetically preferred due to a lower number of dangling bonds on the WZ sidewalls [30]. In addition to stacking disorders, inverted tapering is crucial in stress relaxation. The inverted-cone taper serves to limit the footprint area while the base expands, somewhat similar to the critical diameter observed in nanowires below which misfit strain can be relaxed elastically [**Error! Bookmark not defined.**-45]. Although the footprint (> 70 nm) has already exceeded the theoretical critical value, small contact area and outward tapering still facilitate elastic strain relaxation. As seen in Figure 3-13(c), stacking disorders only appear infrequently in the tapered transition region, suggesting that the special taper geometry is the dominant mechanism in stress relaxation.

To realize electrical devices, it is essential to study how the III-V material is connected to the substrate nanoscopically. Obtaining HRTEM images at the interface, however, is not trivial. To resolve lattices clearly, the area of interest has to be thinned down to below 50 nm. The thickness requirement on hetero-interface is even more challenging since dynamic scattering at the InGaAs/Si interface induces great complications in phase contrast. Multiple millings with Ar^+ ions are therefore required to thin the interface as much as possible. However, we found that the InGaAs/Si interface is very vulnerable to ion/electron damages, possibly because of the strain present. Figure 3-14(a) and (b) show HRTEM images of the hetero-interface with different exposure times to a 300keV electron beam. At the beginning, InGaAs is observed to nucleate directly on Si. As the exposure time increases, however, lattice points can no longer be resolved at the interface. We believe that the high-energy electron beam causes damage to the interface and 'amorphizes' the crystal across the boundary. Ar^+ ion beam is even more effective in amorphizing the hetero-interface. Figure 3-14 (c) shows another InGaAs/Si interface which is completely damaged after prolonged ion milling. Therefore, only interfaces with proper ion and electron doses can yield meaningful information about the vulnerable hetero-interface.

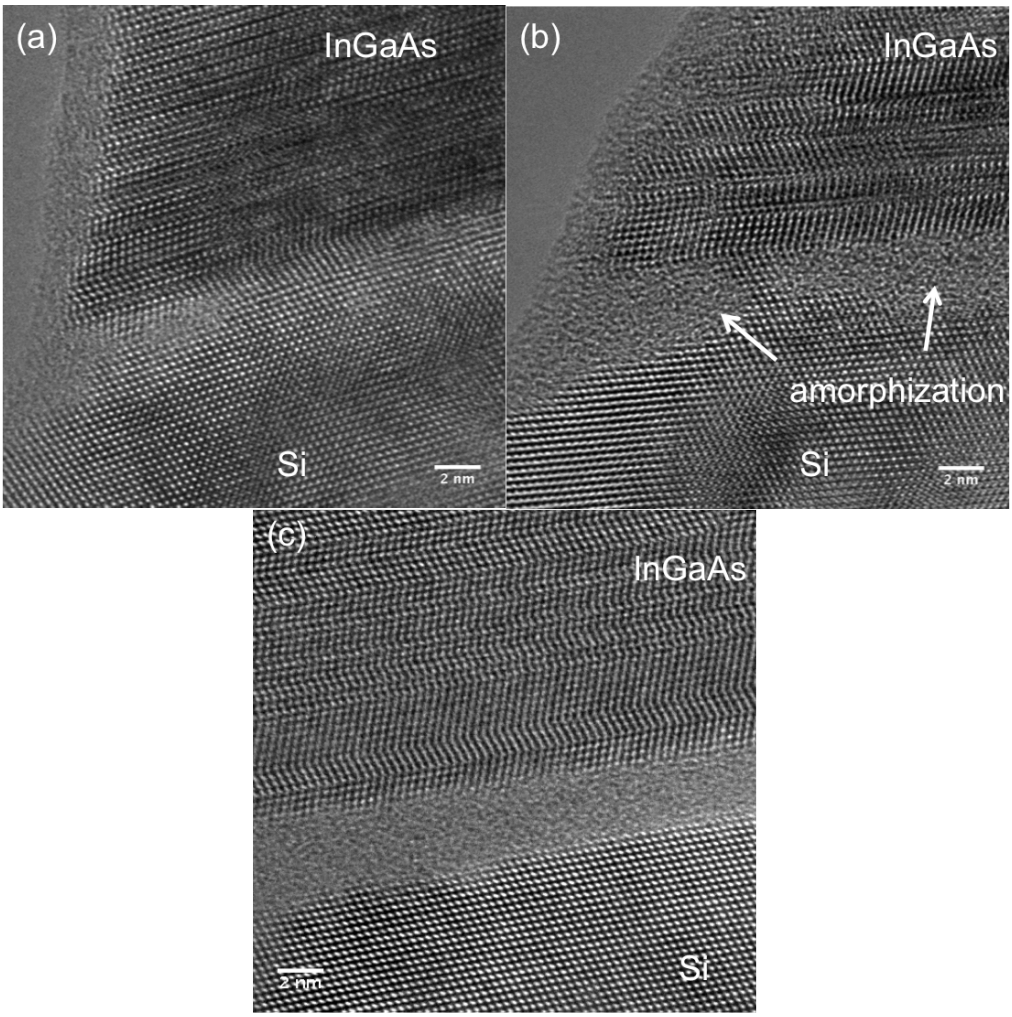

Figure 3-14 InGaAs/Si interface after (a) short and (b) long exposure times to 300keV electron beam. (c) Another sample with interface completely damaged by ion beam.

Figure 3-15 displays the HRTEM images of the exact InGaAs/Si interfaces of the nanopillars shown in Figure 3-13. We note that InGaAs always grows directly on silicon without any amorphous material in between. This is in sharp contrast to many III-V nanowires on silicon, which are observed to stem from thin SiN_x, SiO_2 or SiO_2/Si openings [47-49]. While direct electrical conduction from III-V to silicon is guaranteed, III-V stacking disorders at the root may seem to be a hindrance to excellent electrical performance. However, remarkable diode behavior can still be obtained in the presence of stacking disorders. In particular, the I-V curves obtained from the nanopillar photodetector we reported recently show an ideality factor close to 2 [50], which is a typical value for high quality double heterostructure p-n junction with radiative recombination. We attribute this to the fact that the junction is well embedded in the single-crystalline bulk material and thus the effect of defects is insignificant. This explains the excellent electrical properties observed in the nanopillar devices in our previous work [**Error! Bookmark not defined.**].

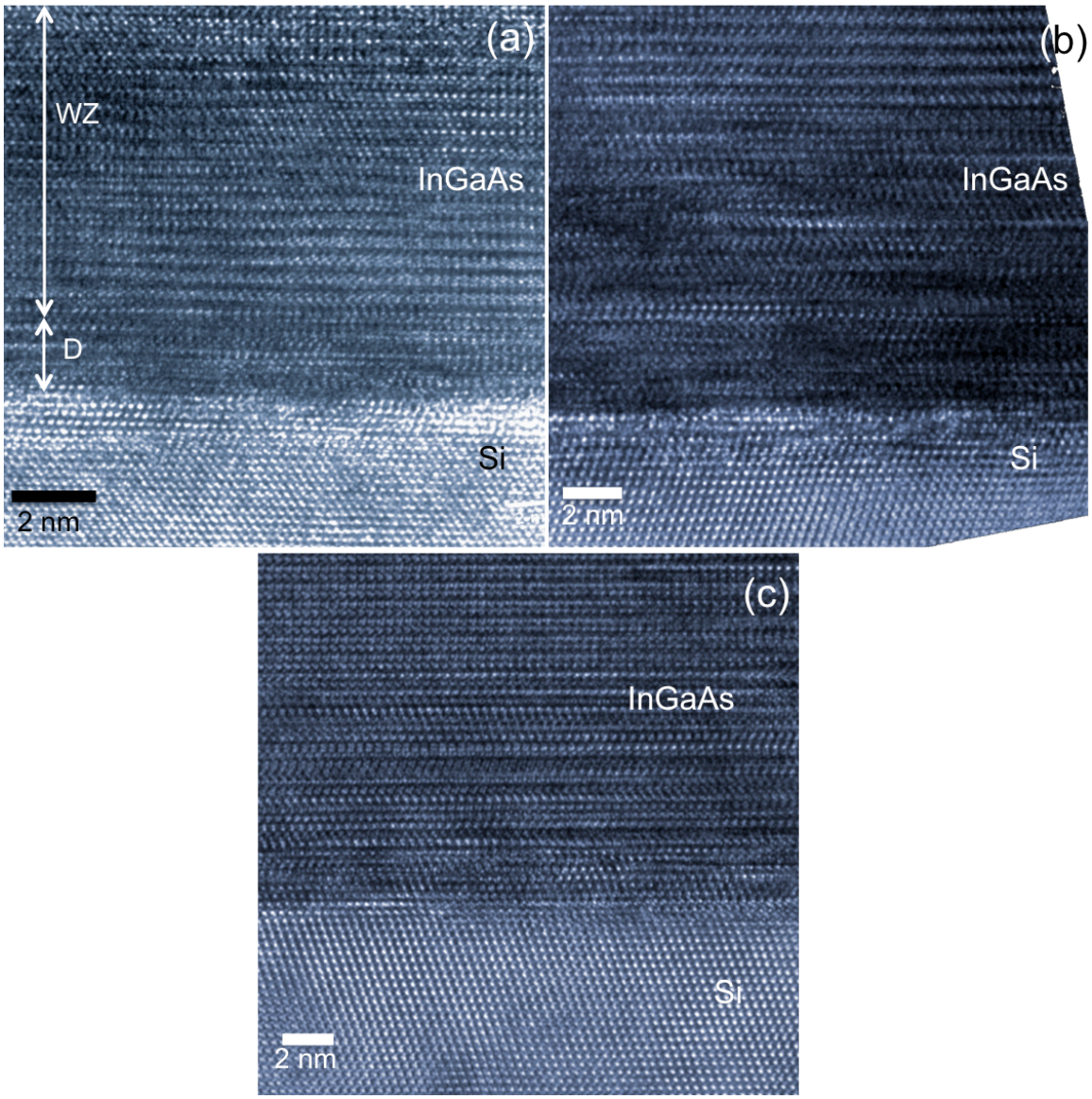

Figure 3-15 HRTEM images of InGaAs/Si interfaces of nanopillars grown for (a) 7 minutes (b) 14 minutes (c) 68 minutes

3.4 Nucleation of Nanopillars on Silicon

In addition to the stress relaxing mechanism, it is also important to understand how nanopillars nucleate. In section 3.3, we observed that InGaAs nucleates directly on silicon without any amorphous materials in between. However, the lattice points are not very well resolved. Is group III or group V forming the first layer on the Si substrate? To answer this question, the best way is to examine the interface with ultra-high resolution HAADF-STEM. However, the fragile InGaAs/Si may get damaged during image

acquisition. An alternative way is to deduce from the polarity of the crystal. As discussed in chapter 2, terminating a crystal can be considered as breaking a set of bonds in an infinite lattice. Along [0001], a facet can be created by cutting the crystal in two ways, as illustrated in Figure 3-16(a). While only one dangling bond is created per atom by cutting through cross-section A, splitting along cross-section B breaks three bonds per atom. To minimize surface energy (i.e. number of dangling bonds), WZ crystal always terminates by cleaving along cross-section A. The exposed facet is known as c-plane and is composed of only either cations or anions. C-plane is therefore a polar plane. If the top facet is terminated with group III monolayer, the bottom facet must be composed of group V atoms, and vice versa. The same polarity phenomenon also applies to ZB (111) planes – group III terminated (111) planes are known as (111)A while group V terminated as (111)B. It is worth noting that there is no (111)A or B in silicon as the elemental diamond structure is purely covalent.

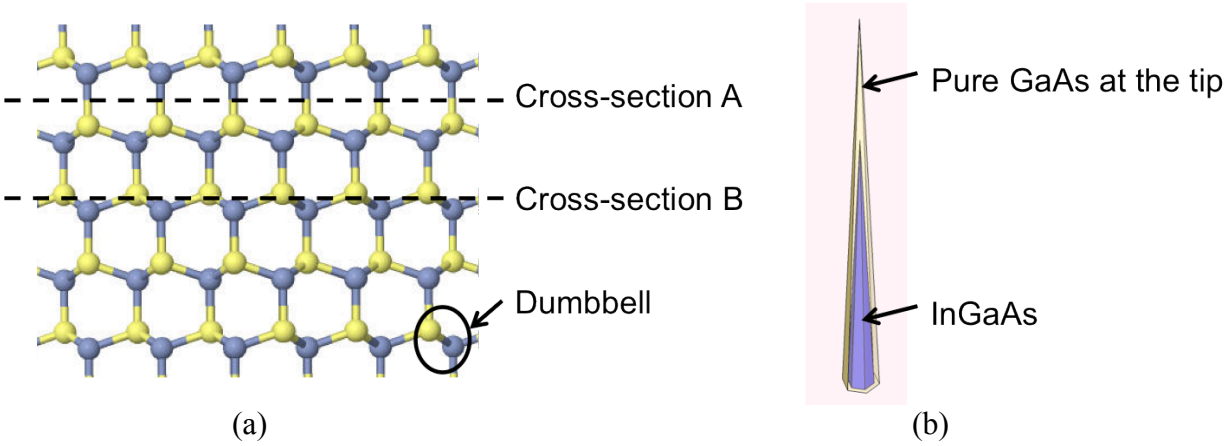

Figure 3-16 Schematic diagrams (a) showing how WZ crystal terminates along [0001] (b) of an InGaAs/GaAs nanoneedle

How does polarity help us to study nucleation? One can consider that the III-V crystal terminates at the III-V/Si interface, forming a polar c-plane at the border. Therefore, by studying the polarity of the crystal, we can deduce which element composes the first layer that covers the substrate. Polarity can be determined by studying the convergent beam electron diffraction (CBED) pattern in TEM [51]. Alternatively, we can also study polarity by identifying group III and V atoms directly in the 'dumbbell', i.e. the III-V atomic pair labeled in Figure 3-16(a). If a group III atom occupies the top site (i.e. the yellow atomic column in Figure 3-16(a)) of the dumbbell, the top facet of the crystal would be group III-terminated, and vice versa. HAADF-STEM imaging can be utilized for this purpose, as it enables direct interpretation of the positions and chemical information of atomic columns.

To study the polarity of the nanostructure, we examine the very tip of an InGaAs/GaAs nanoneedle. The tip of the sharp nanostructure is composed of GaAs only due to the characteristic core-shell growth mechanism, as illustrated in the schematic shown in

Figure 3-16 (b). In this case, two atoms are to be distinguished, namely Ga and As. Being the heavier element, As should appear brighter than Ga in a z-contrast image. However, the contrast can be subtle since the atomic number difference is only 2. Figure 3-17(a) shows a HAADF-STEM image of a nanoneedle wiped down on a copper grid. The image was taken with transmission electron aberration-corrected microscope, TEAM-I, at 80 kV. Clear zig-zag lattice structure can be clearly seen in the 10nm-wide tip. Notably, there is a thin oxide layer wrapping around the whole needle. This 2-nm amorphous layer scatters electrons randomly and increases the noise background of the image. As a result, the two atoms within each dumbbell cannot be resolved clearly at the tip. We therefore took another image at a slightly thicker region to boost the signal-to-noise ratio. Figure 3-17(b) shows a high magnification image of the slightly thicker region which has the same orientation as the image shown in Figure 3-17(a). Two atomic columns can be clearly resolved in each dumbbell, with the top column brighter than the bottom one. This shows that As is occupying the top site in the dumbbell pair. With this atomic configuration, we can deduce that bottom facet of the nanostructure should be group III-terminated.

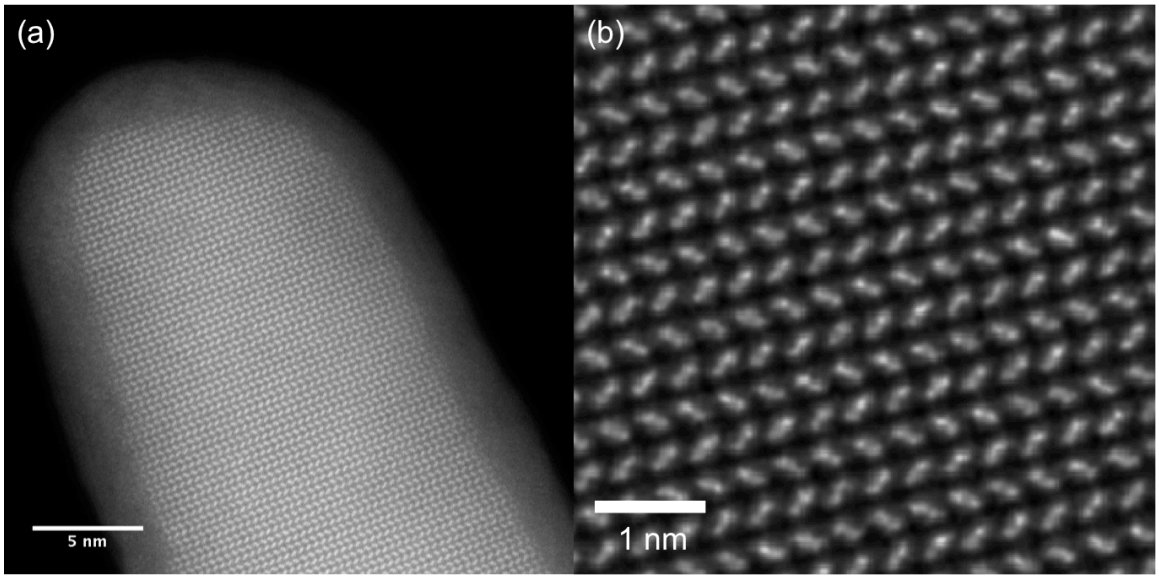

Figure 3-17 HAADF-STEM images of a GaAs nanoneedle tip

As discussed in section 3.3, InGaAs nanopillar base is decorated with stacking disorders which relax misfit stress. Would these defects change the polarity of the crystal? A change in polarity involves the formation of homo-bonds, i.e. Ga-Ga, In-Ga and As-As bonds, over the entire (111) or (0001) planes. This is highly energy unfavorable since homo-bonds are unstable and form usually only at grain boundaries of inversion domains. Therefore, it is very unlikely to have polarity switched across these planar defects. To experimentally verify this, we study the stacking disorders present in the nanoneedle/nanopillar structures under high resolution, as shown in Figure 3-18. In spite of the presence of polytypes and twinning, the polarity of the dumbbells remains the same over the entire lattice – the top site of each dumbbell is occupied with the brighter

atomic column, i.e. arsenic. This is true even at the boundary of polytypes and mirror plane in twinning, as revealed in the three magnified images. Therefore, the polarity observed at the tip should also be valid at the base of the nano-structure.

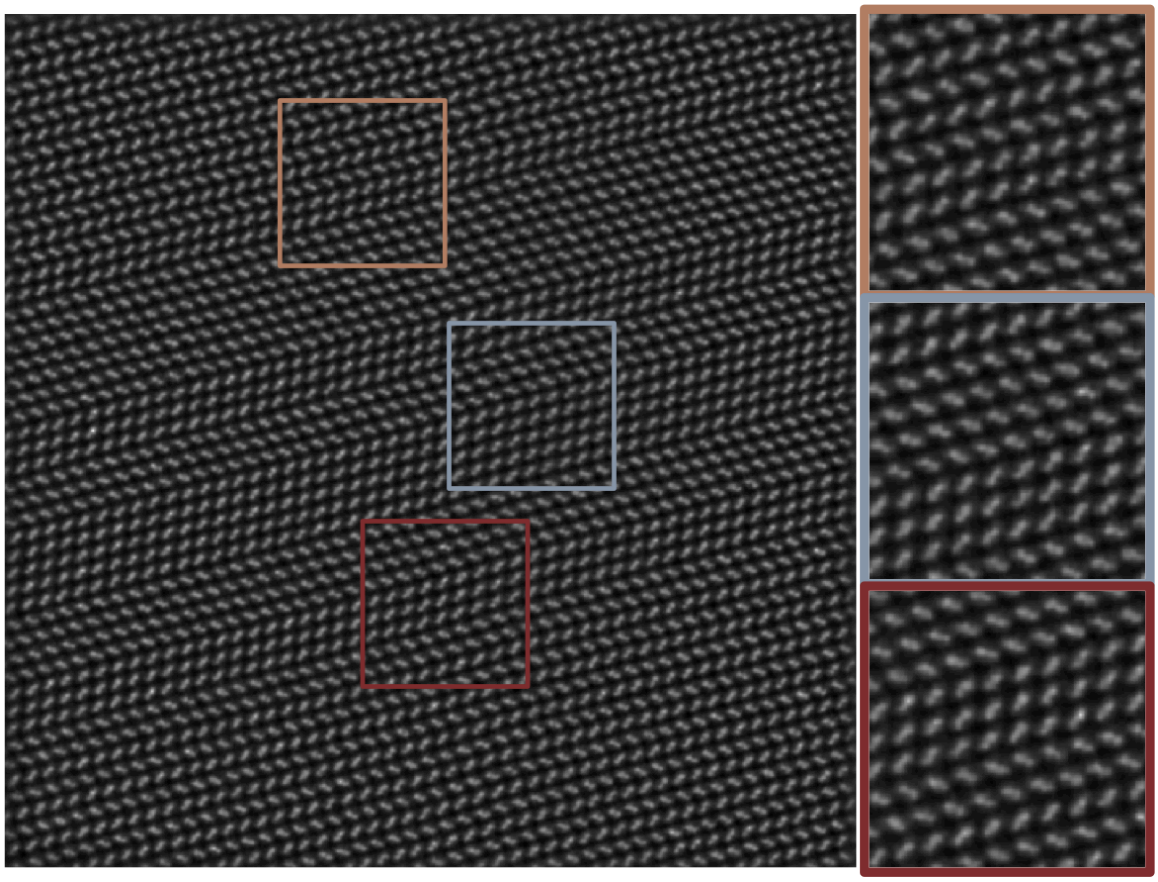

Figure 3-18 HAADF-STEM image of a region with stacking disorders.

Group-V precursor (i.e. TBAs) is pre-flown into the reactor during substrate annealing and temperature stabilization before the start of growth, as discussed in section 3.2. Therefore, one would expect that the growth of nanoneedle/nanopillar should start with a group-V monolayer. The observation in the z-contrast image, however, suggests the opposite. In other words, the nucleation of the InGaAs/GaAs nanostructure is initiated by metal, i.e. Ga and In, rather than their group-V counterpart. This metal initiated growth is not limited to InGaAs – we observe the same polarity in InP nanoneedle grown with the same mechanism. This will be covered in more details in chapter 5. The observation in HAADF-STEM studies leads to the following hypothesis. As mentioned in section 3.1, surface roughening, which opens up fresh silicon surface for oxidation, is a key factor for seeding nanostructure. III-V cannot nucleate on top of native oxide due to the amorphous nature of oxide. As a result, metal adatoms tend to cluster into very small droplets on the oxide layer at the initial phase. These nano-droplets diffuse away from the roughened regions to flat silicon surface and later on evolve into nanoneedle. To verify this hypothesis, we perform growths with different V-III ratios. By lowering the TBAs flow,

we can enhance the diffusion length of group III adatoms, thus increasing the chance for metal droplet formation on the roughened region. This is proven to be true by the drastic soar in nanoneedle density with decreasing V-III ratio, as seen in the SEM images shown in Figure 3-19(a). In addition, nanopillars nucleate at locations much further away from the roughened region under lower TBAs flow, as a result of longer diffusion length of group III droplets. Figure 3-19(b) reveals that nanopillar nucleation extends to over 120 μm away from the roughened region when the TBAs flow is cut down by 20 times. This dependence of density on V-III ratio as well as the observed polarity in z-contrast image substantiate that our nanoneedles/nanopillars are initiated with metal.

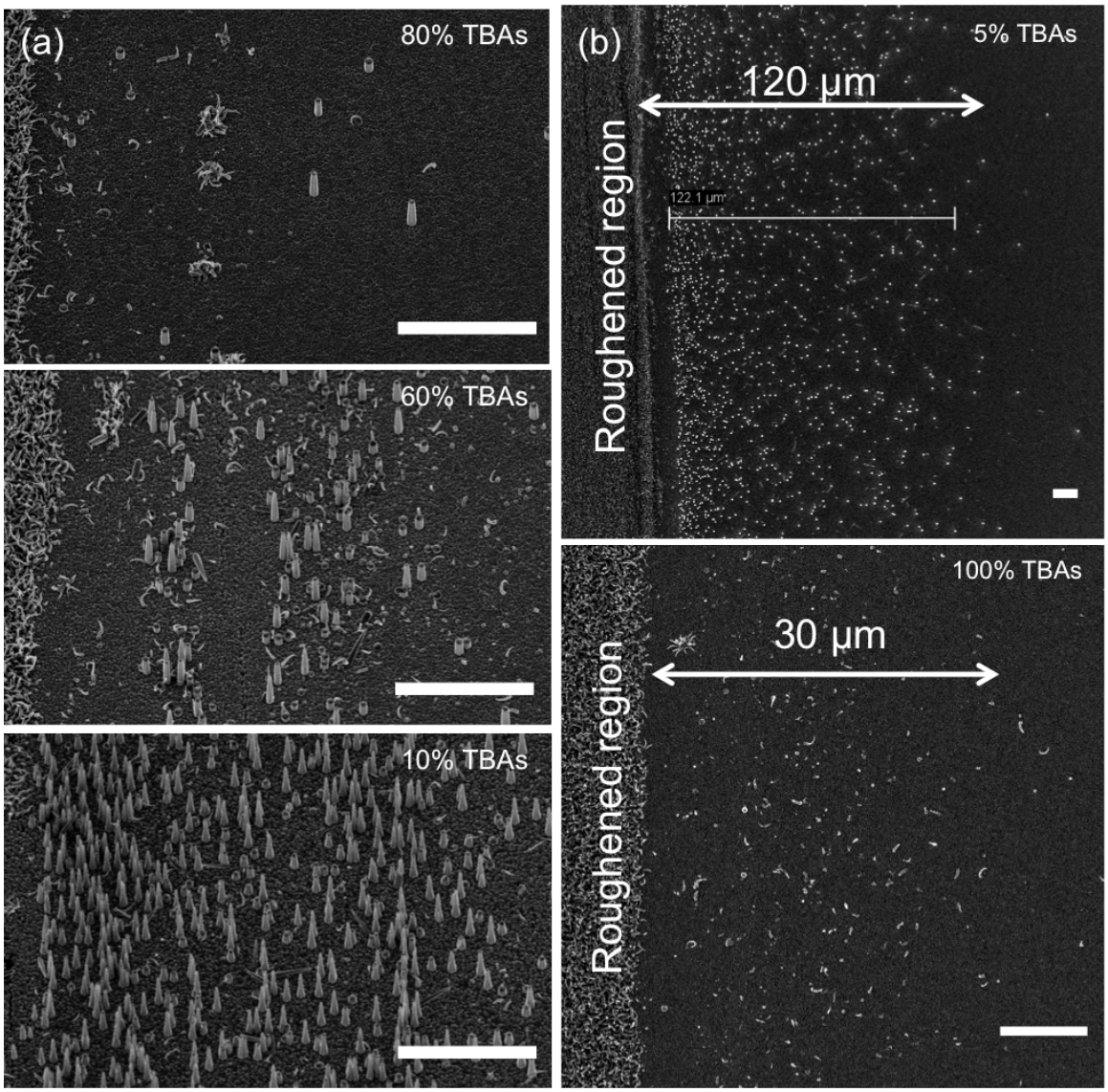

Figure 3-19 (a) Nanopillar density at different TBAs flows (b) Nanopillars nucleate at locations further from the roughened region at lower TBAs flow. All scale bars represent 10 μm.

Although metal is involved in nucleation, we note that the growth mechanism presented in this work is different from conventional vapor-liquid-solid (VLS) growth. In the latter case, a metal catalyst is needed to dissolve the reactants and stays at the tip of the nanowire throughout the entire growth. In our growth mode, however, no metal catalyst is ever observed at the tip of the nanostructure. We believe that the metal seed is completely consumed for nanoneedle formation and the subsequent growth is in a pure core-shell fashion. Another major difference is that the nanowire diameter grown by VLS is pre-defined by the catalyst size. If the catalyst size exceeds the critical diameter, the whole nanowire becomes polytypic. In the nanoneedle growth, however, the base diameter can expand freely while maintaining excellent phase purity except the bottommost tapered region. The metal initiated core-shell growth presented in this work is truly a unique mechanism that enables high-quality and sizable mismatched growth of nanostructures.

3.5 Vertical Growth Termination in InGaAs Nanopillar

In Section 3.2, we observed that vertical growth termination turns the originally sharp nanoneedle into blunt nanopillar. We investigate the origin of the vertical growth termination by examining the tips of sharp and blunt InGaAs/GaAs nanostructures with HRTEM, depicted in Figure 3-20. Sample preparation was done by simple wipe-down of the as-grown nanostructures onto a TEM copper grid. Sharp nanoneedle possesses a pure WZ structure which extends all the way up to the topmost layer as seen in Figure 3-20(a). On the other hand, blunt nanopillar has ZB monolayers sitting on top of pure WZ phase body as the terminating layers, shown in Figure 3-20(b). As mentioned previously, the growth of ZB InGaAs is unfavorable under the growth condition used in this work. Upon formation of ZB crystal, the growth rate at the tip reduces significantly.

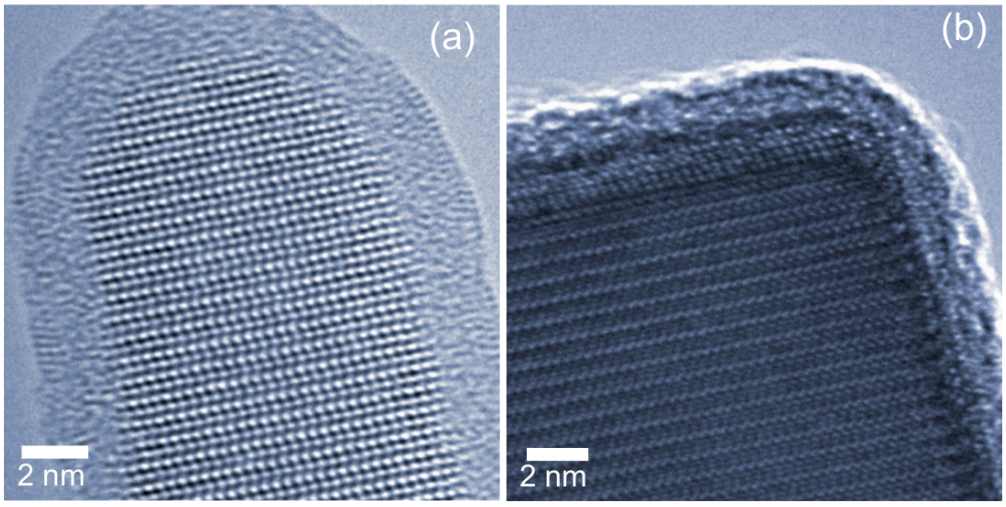

Figure 3-20 HRTEM images at the tip of (a) a sharp needle (b) a blunt pillar.

In some extreme cases, the ZB crystal at the tip evolves into polycrystalline cluster, similar to the ZB InGaAs layer surrounding the nanopillar, as seen in Figure 3-21. This implies that a sudden phase switch at the tip effectively stops the core-shell growth in the vertical direction.

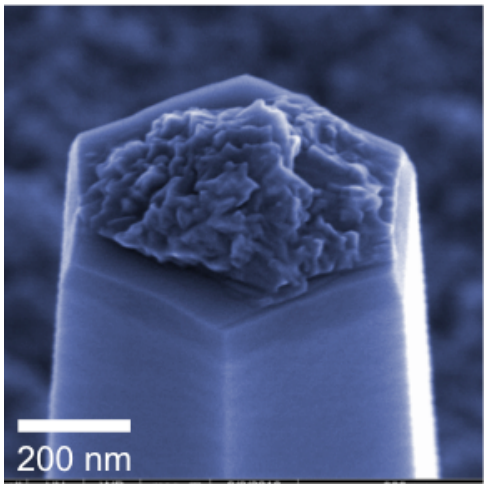

Figure 3-21 Nanopillar tip with poly-InGaAs growing on top.

We note that vertical growth termination is observed in the growth of InGaAs but not observed in binary GaAs grown under the same condition. Figure 3-22 displays the time evolution series of GaAs nanoneedles grown on sapphire and silicon. GaAs nanoneedles remain as sharp pyramids even when the length goes over 8 μm. Such observation suggests that vertical growth termination is highly related to the incorporation of indium.

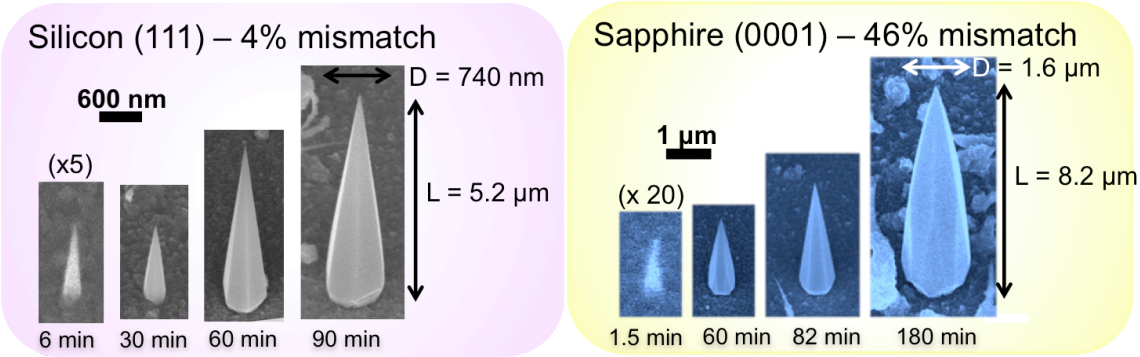

Figure 3-22 Time evolution series of GaAs nanoneedles grown on sapphire and silicon

To study the effect of indium incorporation to the nanostructure shape, a series of typical InGaAs nanostructures with different indium compositions were grown, as shown in

Figure 3-23. We note that the three samples have nearly the same diameters, as illustrated by the white arrows in the figure. Nanopillar length, however, decreases significantly with indium composition. The higher the indium flow, the earlier the onset of truncation. We attribute this truncation to the different diffusion lengths of indium and gallium [52-53]. Since gallium has a shorter diffusion length, the supply of gallium decreases as the nanoneedle length increases. Vertical growth thus becomes slower, triggering the phase transition from WZ to ZB at the tip. This frustrates the characteristic core-shell growth in the vertical direction. On average, nanopillars can reach a length of between 1.7 and 2 μm, as shown in Figure 3-3.

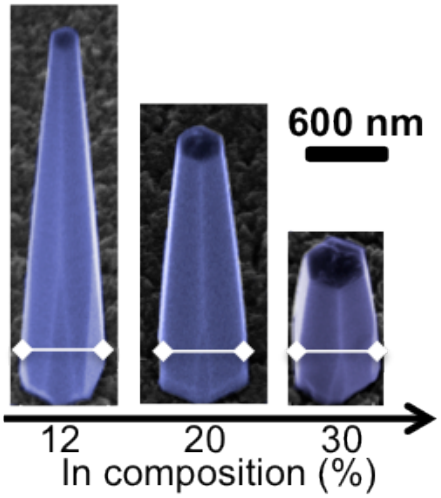

Figure 3-23 Nanopillar length reduction with increasing indium composition

3.6 Wurtzite Phase Stability in InGaAs nanostructures

As discussed in Chapter 2, ZB is the preferred crystal phase in bulk III-V materials. WZ phase is stable only when surface energy becomes the dominant factor in the total free energy, i.e. when surface-to-volume ratio is high. Thus, nanowires with diameters smaller than the critical value can grow into pure WZ-phased crystal. InGaAs nanostructures presented in this work, however, maintain excellent crystal purity in WZ phase while having dimensions far exceeding the critical diameter. We believe that these nanopillars are in a meta-stable state, i.e. a local minimum in energy. This anomalous meta-stable state comes from the characteristic core-shell growth. The growth can be considered as consisting of two components – vertical growth (along c-axis) and lateral growth (perpendicular to c-axis). In section 3.2 we observed that sharp nanoneedles evolve into blunt nanopillars as growth time increases. There are two implications with this phenomenon.

1. The two growth components are relatively independent since lateral growth continues even after vertical growth stops.
2. Vertical growth occurs only at the very tip of the nanostructure. Otherwise, the nanostructure would not have expanded in the horizontal direction only after vertical growth stops.

So which growth component is responsible for the formation of meta-stable wurtzite-phased giant? Both. Lateral growth is a layer-by-layer growth similar to normal thin film epitaxy. The freshly deposited layer simply follows the crystal lattice of the core. Since the core is in WZ phase, the subsequent deposition should also assume a WZ lattice arrangement. In other words, lateral growth effectively increases the volume of wurtzite-phased crystal. As the size increases, the surface-to-volume ratio reduces and the crystal becomes more stable in ZB phase. However, large amount of energy would be needed to break bonds and convert the entire bulk material back into the energy-preferred ZB phase. This energy barrier keeps the nanostructure stable in WZ phase even when the size is well beyond the critical diameter.

Vertical growth, on the other hand, is a completely different story. While lateral growth is simply a copy of the core's lattice, vertical growth creates the core for subsequent horizontal expansion. Growth along c-axis involves the deposition of basal planes whose stacking sequence defines the crystal phase of the freshly deposited material. Since ZB and WZ share the same basal plane, stacking the new layers in ABAB or ABCA can be relatively independent of the crystal underneath. As discussed in the previous section, sharp nanoneedle has pure WZ phase all the way up to the tip. We believe that the extraordinary sharpness of the nanoneedle tip is the driving force for WZ phase to dominate along the vertical direction. The sharpness maintains a large local sidewall-surface-to-volume ratio at the tip. This favors the formation of WZ phase since WZ $\{1\bar{1}00\}$ has lower surface energy than ZB {211}. However, vertical growth slows down as the nanoneedle length increases. While lateral growth remains relatively constant throughout the growth, a slower vertical growth results in thickening of the tip. In other words, the top facet, which is composed of c-plane, increases in diameter. A large top facet, however, does not benefit the growth of WZ crystal, as ZB {111} has the same surface energy as WZ (0001). The net result is that the effective sidewall-surface-to-volume ratio at the thicker tip reduces, making WZ phase less energy favorable. Eventually, when the top facet exceeds certain diameter, ZB phase becomes more energy-stable and the formation of ZB phase lattice terminates the vertical growth, as seen in section 3.5.

In InGaAs nanoneedle, the vertical and lateral growth rates are 4.3 μm/hr and 0.5 μm/hr, respectively. This growth rate anisotropy brings about the extreme sharpness observed in the InGaAs nanostructure. The origin of the ultra fast vertical growth is probably the rich supply of adatoms which diffuse from the substrate and/or nanoneedle sidewall to the tip. To study how vertical growth is affected by adatom diffusion, we grew a series of InGaAs/GaAs core-shell nanostructures under various group V flow rates, as seen in Figure 3-24. While the base diameter (i.e. lateral growth) is not sensitive to group V partial pressure, nanopillar length increases gradually with reducing TBAs flow. At

extremely low TBAs flow, the nanostructure remains as sharp needles with length exceeding 4 microns. Lowering group V flow increases the diffusion length of group III adatoms and thus vertical growth in WZ phase can sustain in taller nanoneedles. These results show that the growth rate along [0001] is indeed highly dependent on diffusion flux of adatoms.

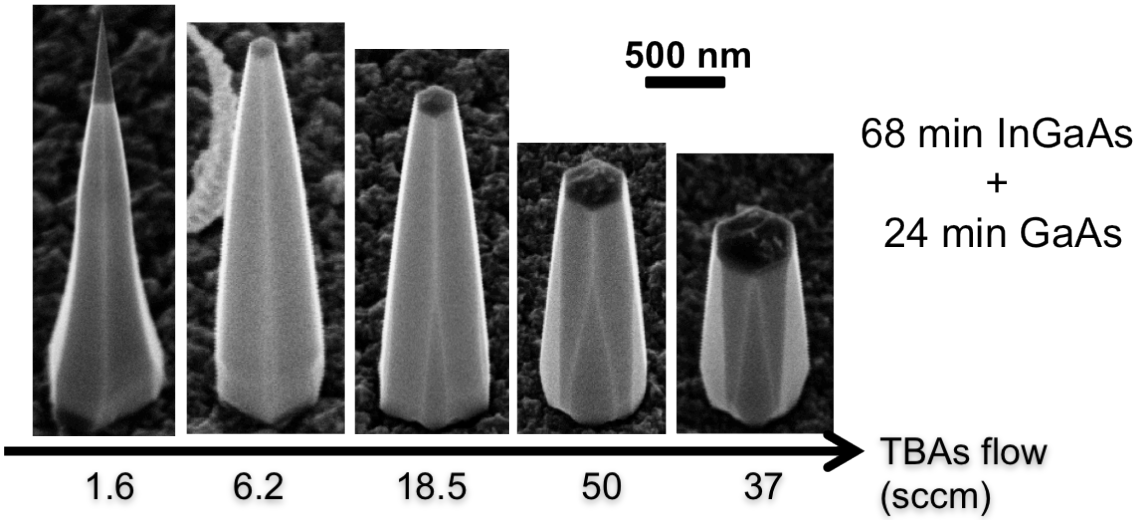

Figure 3-24 Dependence of InGaAs nanostructure length on TBAs flow

So far we have identified the different growth components that enable InGaAs nanostructures to expand in pure WZ phase. Although ZB phase is more energy favorable in the micron-size regime, the large energy barrier prevents bulk WZ lattice from converting into the preferred crystal phase. Theoretically, crystal phase transformation is possible if a huge amount of energy is supplied to the nanopillar. Here, we experimentally demonstrate this transformation *in situ* in a FEI CM-300 TEM. A wiped-down InGaAs nanopillar was first examined carefully with a low current density electron beam to avoid any damage to the nanostructure. Figure 3-25(a)-(c) show bright field TEM images of the InGaAs nanopillar under various magnifications. The pillar is observed to be free of any stacking disorders at the tip. Moreover, HRTEM image at the tip and selective area diffraction pattern in the inset show that the nanopillar is in pure WZ phase. After the low-energy examination, the beam was condensed into a small spot and positioned onto the nanopillar base for several seconds to deliver a high-energy dose. Figure 3-25(d) shows a low magnification TEM image of the nanopillar after the high power dose. One can observe that the tip and the base of the pillar are deformed as a result of the energy blast. Moreover, a hole is 'burnt' near the tip of the pillar at where a small piece of 'junk' is present. We believe that the incident electrons form electric current inside the pillar and discharge at these positions, creating a large amount of heat locally and resulting in the observed deformations. Upon close examination, a lot of defects (mainly stacking disorders) are found at the tip after the local heating process, as seen in Figure 3-25(e). Notably, the defective region extends to ~ 140 nm below the top facet. This is probably the region that experiences most of the heat during electric

discharge. Selective area diffraction patterns in the inset show that the tip transforms from pure WZ phase to ZB phase with significant twinning. The occurrence of phase transformation is further confirmed with high-resolution studies. The original WZ lattice at the tip is completely transformed into ZB stacking, as shown in Figure 3-25(f). We note that the experiment was carried out in a single beam TEM such that the transformation process could not be monitored in real time when the beam was condensed to deliver the power impulse. With a dual-beam system like TEAM 0.5, we may be able to quantitatively evaluate the energy required for the WZ-to-ZB transformation. Nevertheless, this *in situ* experiment is a first demonstration showing that the WZ phase InGaAs nanopillars can be fairly stable and a large amount of energy is needed to transform the meta-stable state into the most energy-preferred ZB phase.

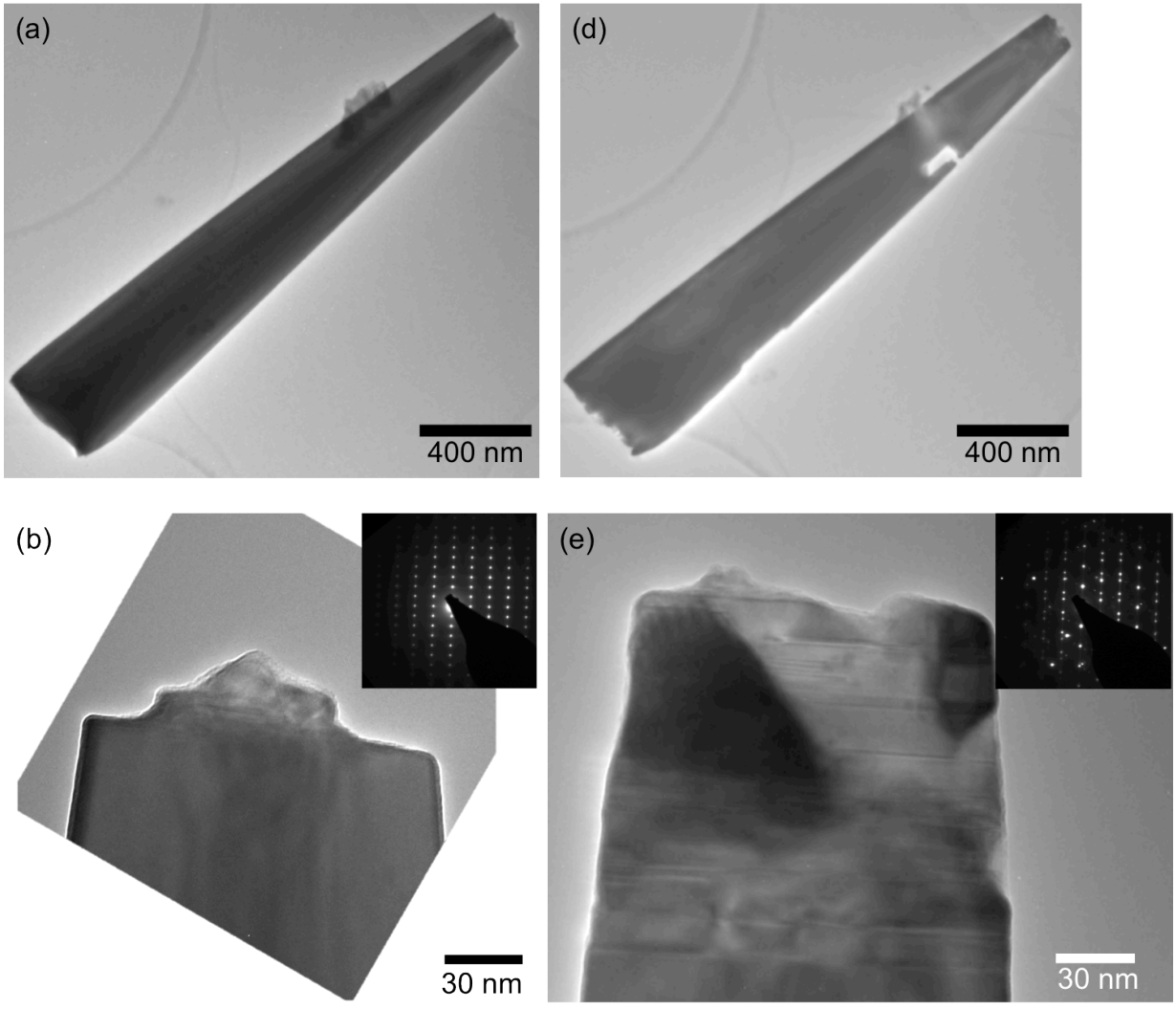

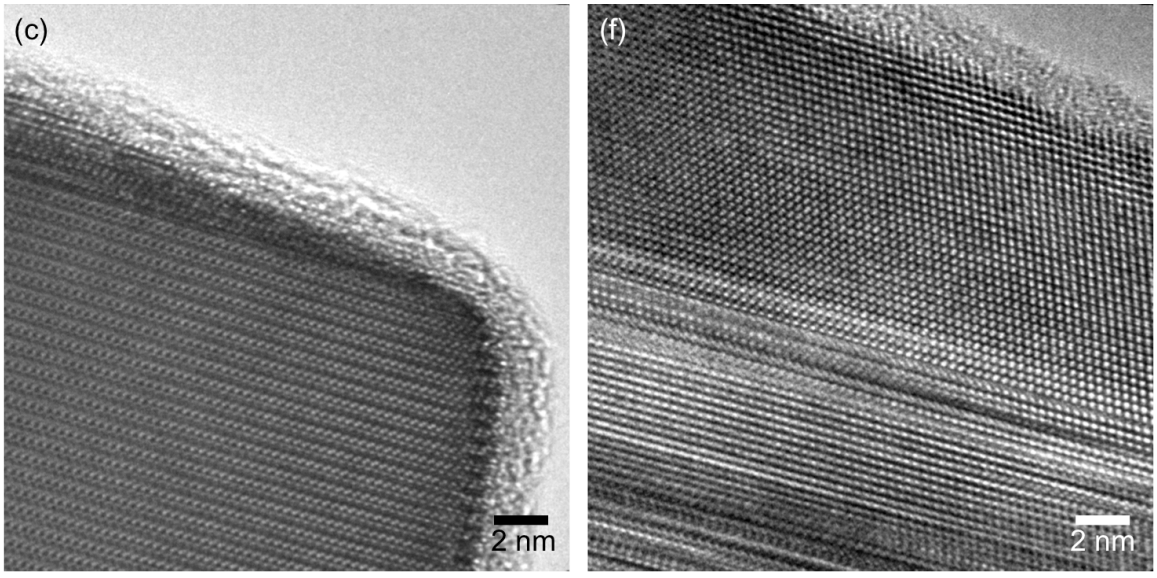

Figure 3-25 Bright field TEM images at different magnifications of an InGaAs nanopillar (a)~(c) before and (d)~(f) after high-energy dose

3.7 High Quality Mismatched Growth of GaAs on $In_{0.2}Ga_{0.8}As$ Beyond Critical Thickness

The core-shell nanopillar growth facilitates thicker growth of lattice-mismatched layers, which is of critical importance for heterojunction device engineering. Previously, the thin-film critical thickness of $In_{0.2}Ga_{0.8}As$ on (100)-GaAs was found to be less than 10 nm (~ 1.5% lattice mismatch) [54]. Given the unique core-shell growth mode and pure WZ phase, it is important to explore if a similar critical thickness exists. A series of samples with various GaAs thicknesses was grown on $In_{0.2}Ga_{0.8}As$ cores, while keeping the same core diameter of 600 nm and growth conditions. No defects were observed for GaAs grown on $In_{0.2}Ga_{0.8}As$ pillars up to a thickness of 150 nm, as shown in Figure 3-26(a). HRTEM images in Figure 3-26(b) and (c) display that GaAs continues seamlessly on $In_{0.2}Ga_{0.8}As$, maintaining the characteristic zig-zag WZ lattice arrangement. In over 20 lamellas examined, no observable misfit defects were found along the entire interface in the bulk of the nanostructure. This limit-breaking coherent growth comes as a consequence of the core-shell growth mode, where the surface area of the shell layer increases almost linearly with its thickness. A large surface area facilitates the elastic relaxation of stress induced at the $In_{0.2}Ga_{0.8}As$/GaAs interface. This unique stress relaxation mechanism enables the growth of mismatched layers to thicknesses far beyond the conventional thin-film limit and could lead to device structures with potentially unprecedented functionalities.

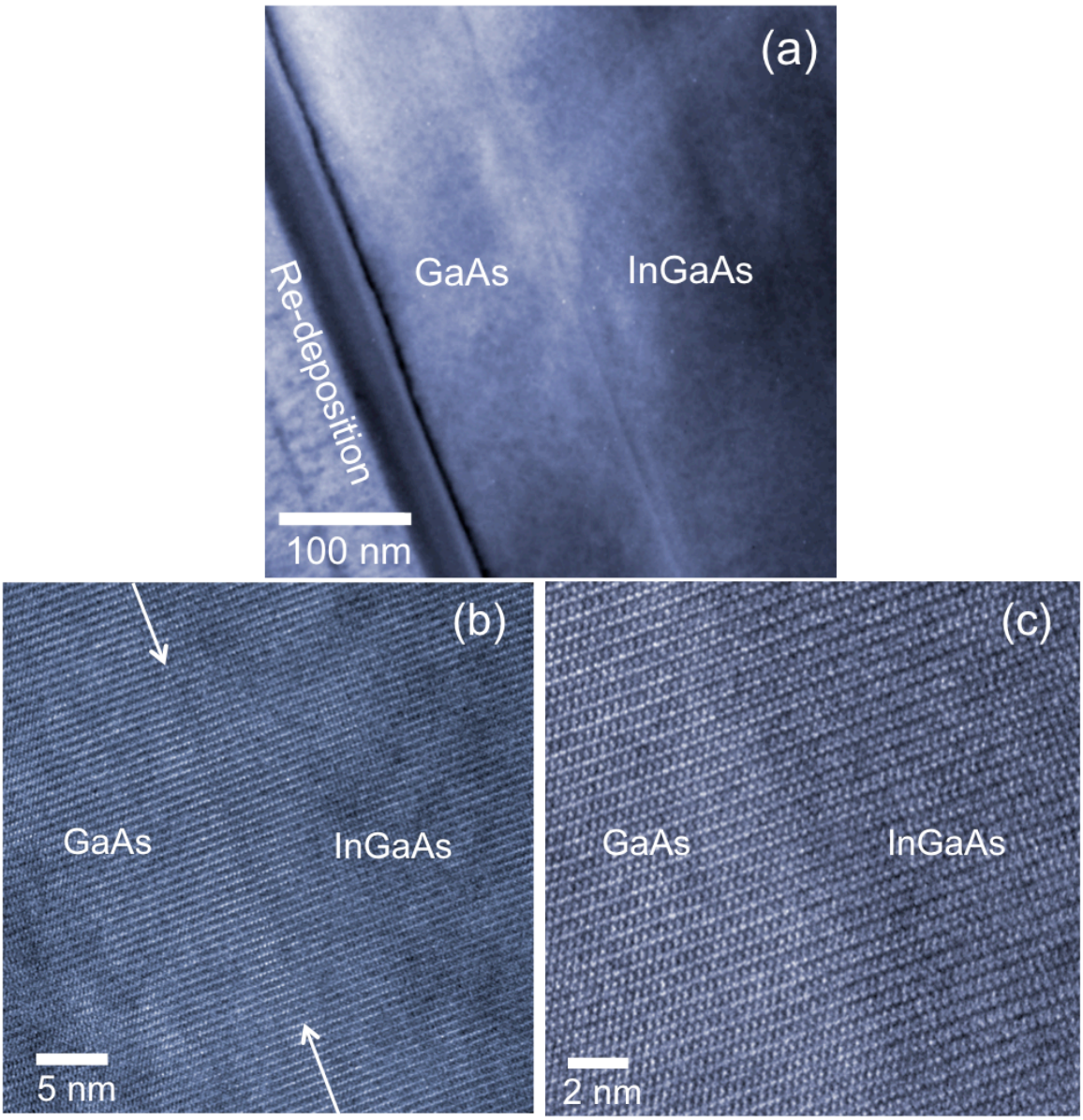

Figure 3-26 InGaAs/GaAs interface under various magnifications

To understand how GaAs thickness can largely exceed the thin film critical thickness, a mathematical model has been developed in collaborations with Dr. Maxim Nazarenko and Professor Vladimir G. Dubrovskii at St. Petersburg Academic University. The goal of the model is to estimate the total elastic energy built up in the core-shell structure and compare it with the dislocation formation energies. In this model, we first consider a simplified case in which the core-shell structure is constituted of two long co-axial cylinders, as illustrated in Figure 3-27. Here, the core and shell thicknesses and cylinder lengths are defined as R_0, Δ and L, respectively.

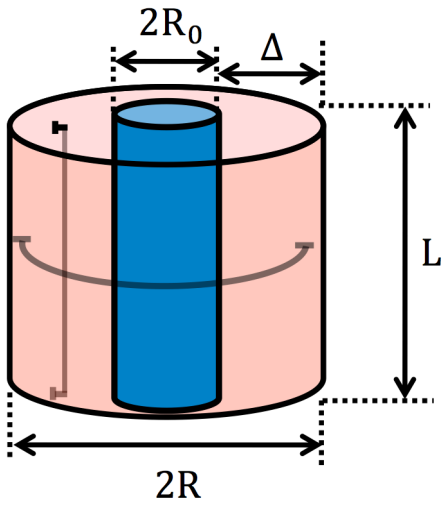

Figure 3-27 Co-axial cylinder model for stress relaxation in core-shell nanopillars

The total elastic energy W can be computed by integrating the product of the strain tensor ε and the corresponding stress tensor σ. Since we are dealing with a structure with co-axial cylinders, cylindrical coordinate system is utilized in the following analysis. Notably, both ε and σ are diagonal matrices due to axial symmetry of the problem. Each tensor contains three non-zero components along the radial (r), azimuthal (φ) and vertical (z) directions. The total elastic energy in cylindrical coordinates can then be expressed as

$$W = \int_0^{\mathrm{L}} \mathrm{d}z \int_0^{2\pi} \mathrm{d}\varphi \int_{R_0}^{R} \frac{\varepsilon_{rr}\sigma_{rr} + \varepsilon_{\varphi\varphi}\sigma_{\varphi\varphi} + \varepsilon_{zz}\sigma_{zz}}{2} r\mathrm{d}r$$

The next step is to find out the expressions for the tensor components of ε and σ. With cylindrical coordinates, the governing equation of linear elasticity theory for the radial displacement field u can be expressed as

$$\frac{\partial^2 u_r}{\partial r^2} + \frac{1}{r}\frac{\partial u_r}{\partial r} - \frac{u_r}{r^2} = \frac{\partial}{\partial r}\left[\frac{1}{r}\frac{\partial}{\partial r}(r u_r)\right] = 0$$

Here, we assume that the core and shell have identical Young's Modulus E and Poisson's ratio ν, and that both the top and base of the cylinders are flat. The boundary conditions can then be given by

$$u_{sr}|_{r=R_0} - u_{cr}|_{r=R_0} = \varepsilon_0 R_0$$
$$u_{sz}|_{z=0} - u_{cz}|_{z=0} = 0$$
$$u_{sz}|_{z=L} - u_{cz}|_{z=L} = \varepsilon_0 L$$

where the indices 's' and 'c' denote shell and core, respectively. ε_0 is the lattice mismatch, and R_0, R, and L are the inner core radius, the outer shell radius and the cylinder length, respectively. By applying these boundary conditions to the results given in Ref. [55] for a single cylinder, the generalized solution for ε and σ in the shell at a given pressure p at the core-shell interface is

$$\varepsilon_{rr} = \frac{(1+\nu)C^2R^2}{E(R^2-R_0^2)}\left\{-\frac{p}{r^2}+(1-2\nu)\frac{p}{R^2}\right\}-\nu\varepsilon_0\frac{R_0^2}{R^2}$$

$$\varepsilon_{\varphi\varphi} = \frac{(1+\nu)R_0^2R^2}{E(R^2-R_0^2)}\left\{\frac{p}{r^2}+(1-2\nu)\frac{p}{R^2}\right\}-\nu\varepsilon_0\frac{R_0^2}{R^2}$$

$$\varepsilon_{zz} = \varepsilon_0\frac{R_0^2}{R^2}$$

$$\sigma_{rr} = \frac{pR_0^2}{R^2-R_0^2}\left(1-\frac{R^2}{r^2}\right)$$

$$\sigma_{\varphi\varphi} = \frac{pR_0^2}{R^2-R_0^2}\left(1+\frac{R^2}{r^2}\right)$$

$$\sigma_{zz} = \frac{2\nu pR_0^2}{R^2-R_0^2}+\varepsilon_0E\frac{R_0^2}{R^2}$$

The core stress and strain are calculated in a similar way. To obtain the final solution, we need to find p by using the boundary condition. The result is obtained in the form

$$p = E\varepsilon_0\frac{R^2-R_0^2}{2(1-\nu)R^2}$$

With all these parameters defined, the total elastic energy W can be computed. W can be expressed as the following simplified form

$$W = \pi E\varepsilon_0^2(1+\nu)R_0^2L+O\left(\frac{R_0}{\Delta}\right)$$

where $O(x)$ denotes a quantity in the order of x. As the shell thickness Δ approaches infinity, the second term in the above expression vanishes and the total elastic energy W saturates at a maximum value. This trend can be observed in Figure 3-28 in which W is plotted as a function of shell thickness. In the calculations, we used the following material parameters for the GaAs/$In_{0.2}Ga_{0.8}As$ heterointerface: E = 86 GPa, $\nu = 0.31$ with $\varepsilon_0 = 2\%$. The nanopillar length L is fixed at 5 μm, and the core radius R_0 is 300 nm. The curve shows that the elastic energy increases sharply at small shell thickness Δ and levels off when the shell thickness reaches around 500 nm. This implies that elastic stress is concentrated near the interface and is almost fully relaxed when the shell thickness

approaches the core radius. This extraordinary behavior comes from the surface area of the shell scaling almost linearly with the shell thickness. An expanding surface effectively accommodates displacement of lattice positions due to lattice mismatch. Misfit stress can then be relaxed elastically as shell thickness increases. As a result, the elastic energy in the core-shell geometry caps at a certain value rather than increasing monotonically with the layer thickness, which is the case of 2-dimensional epitaxial growth.

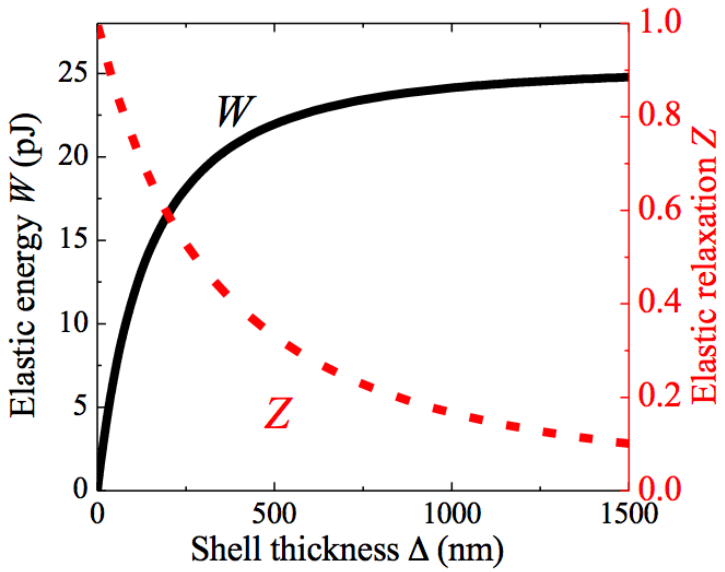

Figure 3-28 Dependence of elastic energy and elastic relaxation on shell thickness

To compare the core-shell geometry with the thin film case, we consider the elastic energy in a uniformly strained 2D layer of the same volume, grown on a semi-infinite substrate with the same lattice mismatch, the Young's modulus and the Poisson's ratio

$$W_{2D} = \pi L(R^2 - R_0^2)L\frac{\varepsilon_0 E}{1-\nu}$$

We then define the relative elastic energy, or elastic relaxation, as

$$Z = W/W_{2D}$$

This parameter Z is a measure of how the stress behavior in the core-shell structure deviates from the normal 2D epitaxial case. Like W, Z can be expressed in a simplified form as

$$\mathrm{Z} = \frac{(1-\nu^2)R_0^2}{\Delta^2} + O\left(\frac{R_0^3}{\Delta^3}\right)$$

Since the surface area remains constant throughout 2-dimensional thin film growth, elastic stress relaxation that exists in the core-shell geometry is impossible. Unlike core-

shell growth, elastic energy keeps building up with the layer thickness in 2D epitaxial growth. Thus, the elastic energy ratio Z reduces monotonically with increasing shell thickness Δ, as one can deduce from the above expression. The same trend can also be seen from the red curve in Figure 3-28. Consequently, mismatched growth of 2D epitaxial layer is limited to thickness well below 50 nm. Above the critical thickness, formation of dislocations becomes energy favorable and defects nucleate to relax the mismatch stress.

To estimate the critical shell thickness in the core-shell geometry, we now consider two types of dislocations: edge dislocation with the Burgers vector pointing along the tangential direction and loop dislocation with the Burgers vector in the axial direction (see Figure 3-27). The dislocation formation would relax either the tangential strain $\varepsilon_{\theta\theta}$ $\varepsilon_{\theta\theta}$ or the edge strain ε_{zz}. With this choice of dislocation types, we compare the total energy of dislocated system with the elastic energy of the same system without dislocation. As in Ref. [56] and [57], this is equivalent to comparing the pure dislocation energy of dislocation $\mathrm{E_{disl}}$ with the elastic energy gain upon the dislocation formation due to the decrease of lattice mismatch ΔW. We use the results presented in Ref. [58] and [59] for the pure dislocation energy E_{disl} for the two dislocation types considered. ΔW is obtained from the results presented above by decreasing the lattice mismatch in horizontal and vertical planes due to nucleation of the edge and loop dislocations, respectively. The critical thickness is then found by setting $E_{\mathrm{disl}} = \Delta W$ separately for the edge and loop dislocations. The results obtained are shown in Figure 3-29. Three major effects can be read off from the plot.

1. The critical thickness $\mathrm{h_c}$ induced by edge and loop dislocations feature a rather similar trend – $\mathrm{h_c}$ increases sharply at low lattice mismatch. This implies that the core-shell geometry can indeed elastically relax lattice mismatch efficiently and disfavor the formation of dislocations at low lattice mismatch.
2. Formation of edge dislocations is energy preferred at very high lattice mismatch. Therefore, the critical thickness is essentially determined by nucleation of loop dislocations.
3. There exists a critical lattice mismatch ε_c below which the critical thickness becomes infinite. In other words, below ε_c, misfit stress can be elastically accommodated completely and the shell can reach any thickness without inducing any dislocations.

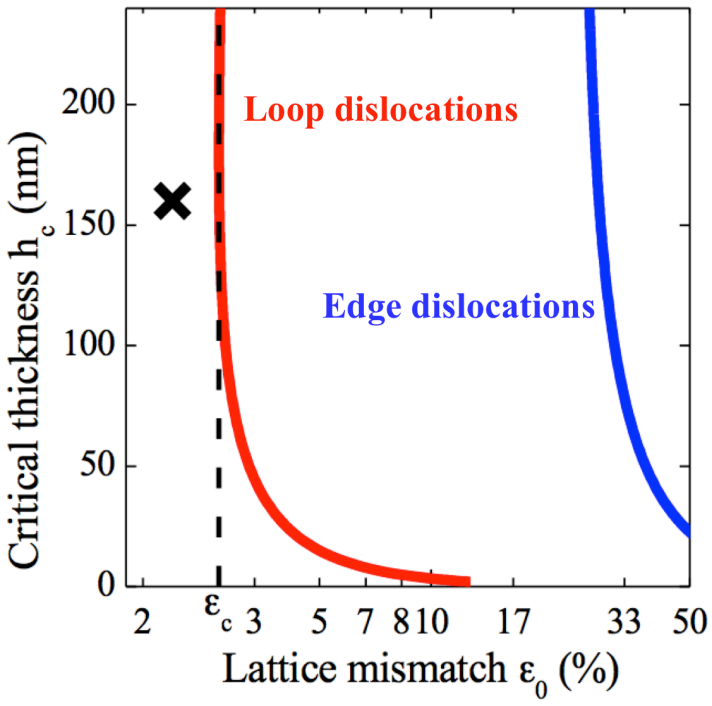

Figure 3-29 Dependence of critical thickness defined by loop and edge dislocations on lattice mismatch

In an InGaAs/GaAs core-shell system with a core radius of 300 nm, the calculated critical lattice mismatch is ~ 2.7%. With a lattice mismatch of ~ 2% in the $In_{0.2}Ga_{0.8}As$/GaAs nanopillar structure, the critical thickness is infinite according to this cylindrical model. This gives a first-order explanation why we can experimentally obtain defect-free growth of GaAs with thickness far exceeding the 2D thin film critical thickness.

So far we have been modeling the elastic energy of a pair of co-axial cylinders. Our real nanostructure, however, is in the shape of a frustum. To develop a more realistic model of a tapered nanopillar, we consider coaxial cone geometry shown in Figure 3-30 in the small slope approximation, where the first order perturbation theory in the taper angle is used. Now, the quantities R_0, p, ε and σ are treated as functions of z. While the analytical expressions are much more complicated in this case, the final results remain qualitatively the same as in the cylindrical case. The major effect regarding the efficient stress relaxation is demonstrated in Figure 3-31(a) and (b). In calculations, we consider a nanopillar with a length of 2 μm and a taper angle of 5°, the core radius of 300 nm at the base, with all other parameters the same as before. Comparing Figure 3-31(a) to Figure 3-28, it can be seen that the elastic energy relaxation in the nanopillar is very close to the cylindrical case. This shows that a tapered geometry has little effect on the stress relaxing properties. Figure 3-31(b) presents the radial strain σ_{rr} depending on the distance from the core $r - R_0$. In this plot, the core radius at the cross-section considered is 220 nm and the shell thickness is 160 nm. The radial stress gradually decreases from over 2% at the core-shell interface down to < 1% at the shell surface. This again agrees with the

experimental observation that GaAs can grow into very thick layer on top of $In_{0.2}Ga_{0.8}As$ in spite of ~ 2% lattice mismatch.

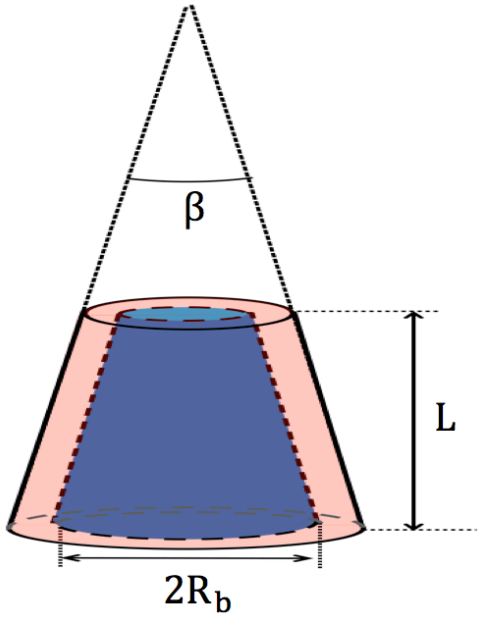

Figure 3-30 Truncated cone model with base core radius R_b, nanopillar length L, and taper angle β

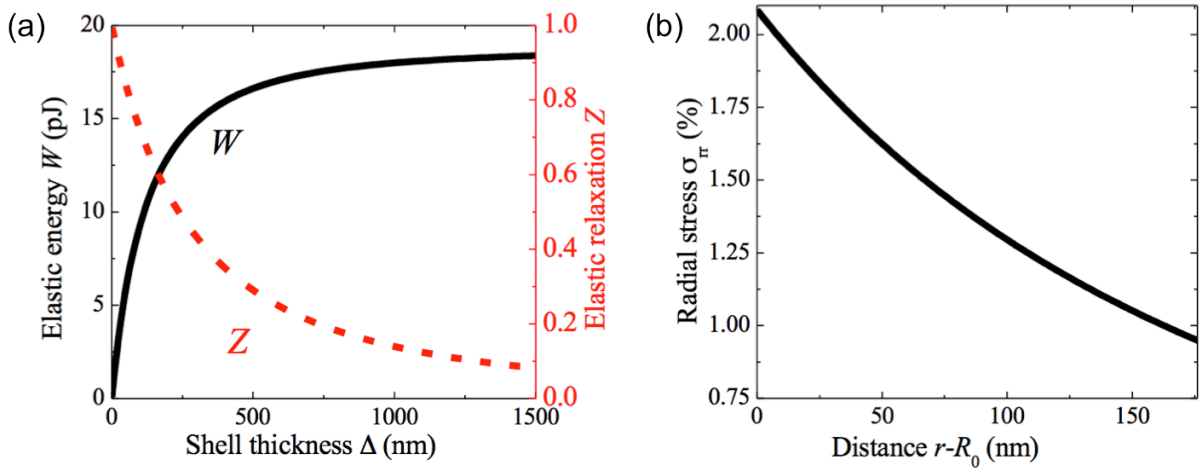

Figure 3-31 (a) Dependence of elastic energy and relaxation on shell thickness (b) Variation of radial stress in the shell as a function of distance from the core-shell interface

While the core-shell geometry enables stress relaxation by expanding the surface area, axial heterostructures can also accommodate misfit strain in freestanding nanowires. Which geometry is more efficient in terms of stress relaxation? To answer this question, we compare the elastic relaxation Z of the two structures. The faster the decay of Z with layer thickness Δ, the more efficient the stress relaxation. While nanowires enable an

infinite coherent growth when the diameter is below the critical value [**Error! Bookmark not defined.**,**Error! Bookmark not defined.**,56,59], Z_{axial} scales inversely proportional only to Δ. In the core-shell case, $Z_{core\text{-}shell}$ scales inversely proportional to Δ^2. Therefore, the core-shell geometry can relax misfit stress much more efficiently, leading to the high-quality mismatched growth of thick capping layer on the InGaAs core.

3.8 Composition Variations in InGaAs/GaAs nanopillars

In addition to crystalline quality, compositional coherence also plays an important role in the electrical and optical properties of nanopillar devices. A sharp alloy interface can provide better carrier confinement and hence more efficient radiative recombination. In this section, we study the composition profile of the $In_{0.12}Ga_{0.88}As/In_{0.2}Ga_{0.8}As/GaAs$ double hetero-structure with HAADF-STEM imaging and EDS analysis. Schematic illustration of the structure is shown in Figure 3-1. There are two main reasons for using double hetero-structure:

1. To reduce the volume of the active region, i.e. $In_{0.2}Ga_{0.8}As$. This lowers the threshold current required for lasing action.
2. To place the active region right at the optical mode. Lasing action in InGaAs-based nanopillars assumes a helically propagating mode [**Error! Bookmark not defined.**], as illustrated in Figure 3-32(a). Finite-difference time-domain (FDTD) simulation shows that the intensity field forms 'hotspot' close to the edge of the pillar, as revealed in Figure 3-32(b). Thus, putting the active region closer to the surface of the nanopillar by using double hetero-structure maximizes the overlap of material gain and optical mode.

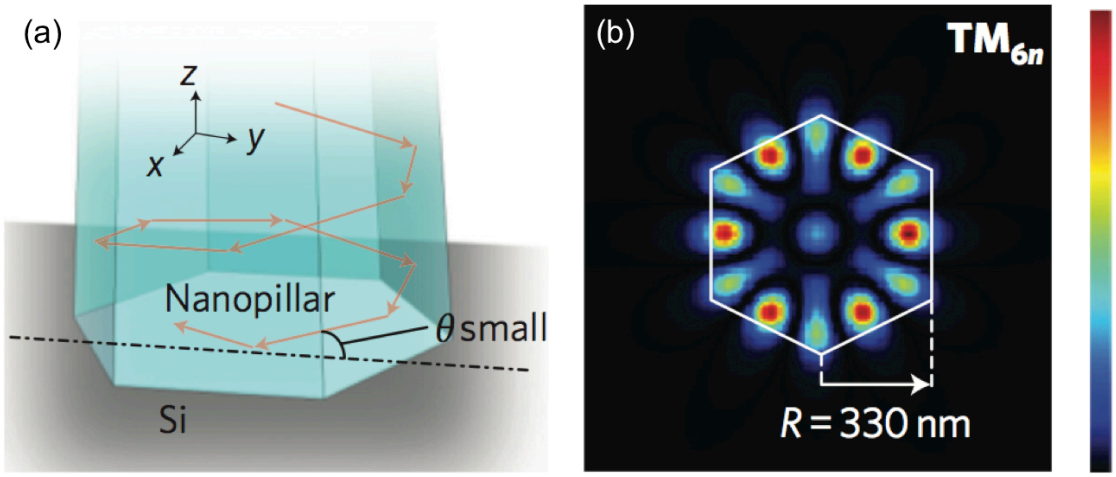

Figure 3-32 (a) Ray diagram illustrating light propagates helically along the nanopillar (b) An FDTD-simulated light intensity distribution of TM_{6n} mode in the transverse plane

HAADF imaging and EDS analysis were carried out in a Titan TEM at 300keV. Compositional variations along both the axial and lateral directions are studied. In the latter case, thin slices of the transverse cross-section are fabricated with FIB. First, we use a micromanipulator to break the pillar *in situ* inside the SEM chamber and let it lie flat on the substrate surface. Pt is then deposited on the area of interest to anchor the loose pillar onto the substrate and provide passivation against ion damage. The subsequent procedures are exactly the same as those used in creating lamella for root study, except that c-plane is exposed now instead of a-plane. Figure 3-33 shows HAADF-STEM images of three transverse cross-sections cut at different locations of a pillar. Since indium has a higher atomic number than gallium and arsenic, layers with more indium appear brighter. Cross-section III consists of a three-layer architecture in which the innermost $In_{0.12}Ga_{0.88}As$ core is embedded within the $In_{0.2}Ga_{0.8}As$ active region and the GaAs shell. In particular, the three regions are completely concentric as a result of core-shell growth. In cross-sections II and III, however, there exists an asymmetric layer that wraps around the GaAs shell. This non-concentric layer is due to ion beam damage during sample preparation and has no relation with the growth. When moving up the pillar, one can notice that the innermost $In_{0.12}Ga_{0.88}As$ core shrinks in size and finally disappears in the topmost cross-section. This is a direct consequence of the characteristic core-shell growth mode in which the $In_{0.12}Ga_{0.88}As$ core is completely embedded inside the active region in all growth directions. This observation agrees well with our core-shell model, which is schematically illustrated in the same figure.

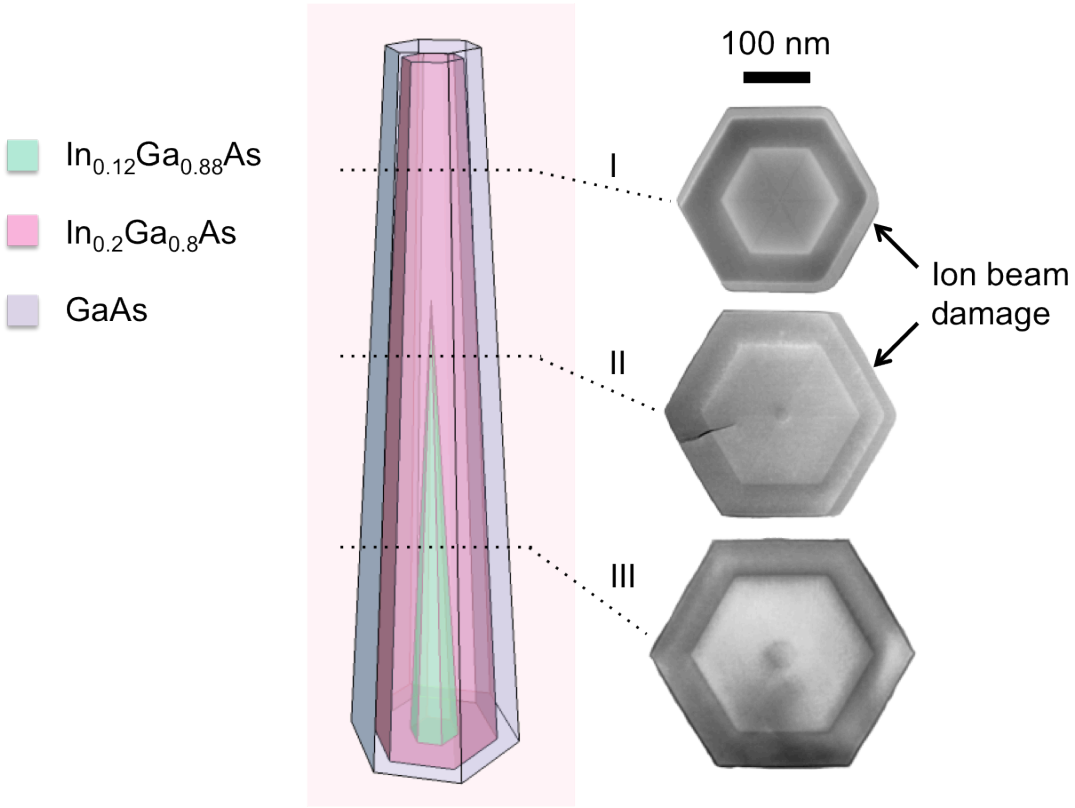

Figure 3-33 Transverse cross-sections cut at different locations of nanopillars

Another important feature observed in the cross-sections in Figure 3-33 is the diametric lines that spread out radially from the center of the hexagons. Figure 3-34(a) shows a magnified image of the central region of cross-section III, which depicts an $In_{0.12}Ga_{0.88}As$ core surrounded by $In_{0.2}Ga_{0.8}As$. The faint dark lines start at the center, propagate through the $In_{0.12}Ga_{0.88}As$ and $In_{0.2}Ga_{0.8}As$ layers and terminate at the $In_{0.2}Ga_{0.8}As$/GaAs interface. Specifically, the dark lines are extending along the degenerate $<11\bar{2}0>$ directions and have a finite width of ~ 7nm. Contrast in an HAADF image comes from two major factors – thickness and compositional variations. The observation that these dark lines are absent at the GaAs shell is a first sign that the observed contrast is due to local indium fluctuations. To find out the origin, we performed EDS analysis on the central region of the area shown in Figure 3-34(a). We scanned a finely condensed electron beam over the entire area of interest, registering the X-ray spectrum at each pixel. By taking into account of the Cliff-Lorimer factor [60] and deconvoluting the signals from unrelated elements (e.g. Pt, Si, etc.), we can quantitatively calculate the relative abundance of each element at each pixel. The spatial distributions of indium, gallium and arsenide are then plotted out as elemental maps, as shown in Figure 3-34(b). The corresponding HAADF image is also included in the same figure. The black dot at the center of the core is an artifact caused by electron beam damage during imaging. While arsenic shows a rather uniform distribution over the entire region, more gallium is detected in the core than the surrounding region, which comes as a natural consequence of the variation in gallium contents. The indium spatial map, on the other hand, is an exact resemble of the HAADF image. Faint dark lines are observed to stretch out from the hexagonal $In_{0.12}Ga_{0.88}As$ core. This indicates that the diametric lines are indium deficient compare to the surrounding $In_{0.2}Ga_{0.8}As$ materials. In other words, the dark lines signify a spontaneous alloy composition ordering along the lateral growth direction.

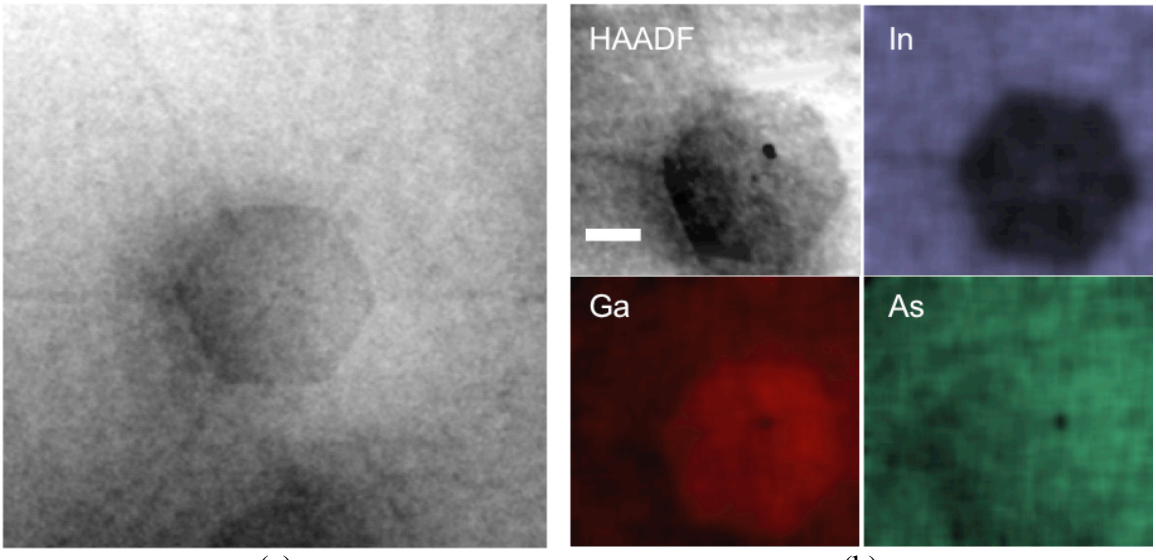

(a) (b)

Figure 3-34 (a) Anomalous diametric dark lines spreading out from the center (b) Spatial distributions of indium, gallium and arsenic

The observed natural alloy composition ordering comes from the difference in diffusion lengths of Ga and In adatoms. In WZ nanostructures growing along c-axis, sidewalls are usually composed of either m-planes (i.e. $\{1\bar{1}00\}$) or a-planes (i.e. $\{11\bar{2}0\}$). Experimentally, we observed in the nanopillars that m-planes are more stable than a-planes when the group III supply is sufficiently high. The growth along $<11\bar{2}0>$ is therefore much faster than $<1\bar{1}00>$. The growth rate anisotropy results in the shrinkage of a-planes and hence minimization of surface energy. The sidewall facet selection mechanism is schematically illustrated in Figure 3-35. The extinction of $\{11\bar{2}0\}$ facets results in the hexagonal shape observed in nanopillars.

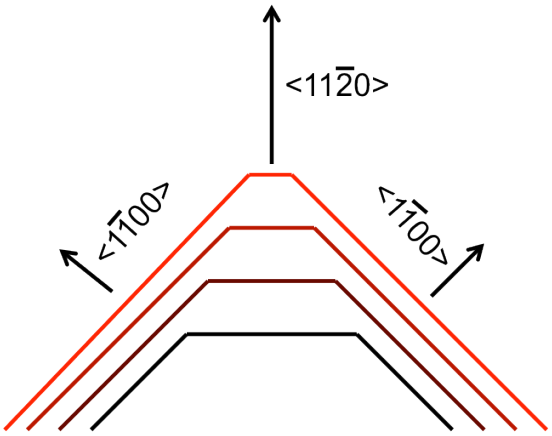

Figure 3-35 Schematic illustrating the extinction of $\{11\bar{2}0\}$ facets due to growth rate anisotropy

As the $\{11\bar{2}0\}$ facets become smaller, the corners of the hexagon become sharper, i.e. surface curvature at the corner increases. This changes the diffusion behavior of adatoms at the hetero surfaces. In general, the adatom diffusion flux **J** can be calculated using the Nernst-Einstein relation

$$\boldsymbol{J} = -\frac{nD_s}{k_B T}\nabla\mu$$

, where μ is the surface chemical potential, n is the surface density of adatoms, D_s is the surface diffusion coefficient, k_B is Boltzmann's constant, and T is the temperature. Simply speaking, diffusion involves the flow of adatoms from high to low surface chemical potential. In a system in which the surface properties change only in one dimension, we can consider μ to vary with three major factors, namely surface stress, surface curvature and entropy of mixing. μ can then be expressed as

$$\mu = \mu_0 + \Delta\mu_{stress} + \Delta\mu_{curvature} + \Delta\mu_{mixing}$$

A reduction in $\{11\bar{2}0\}$ facet area leads to an increase in $\Delta\mu_{curvature}$ and hence its overall surface chemical potential μ. As a result, adatoms tend to diffuse away from the sharp edge. This phenomenon is known as capillarity which describes the tendency of a surface

to minimize the surface energy by smoothing out any roughness [61]. The diffusion of adatoms away from the $\{11\bar{2}0\}$ facets due to capillarity slows down the growth in the $<11\bar{2}0>$ direction. When the growth rate along $<11\bar{2}0>$ finally becomes the same as that of $<1\bar{1}00>$, the $\{11\bar{2}0\}$ facets stop shrinking and reaches an equilibrium size. As discussed in Section 3.5, indium has a higher diffusion length, and thus diffusion coefficient, than gallium. Nernst-Einstein relation enforces that the diffusion flux of indium would be higher than that of gallium. Hence, the growth along $<11\bar{2}0>$ becomes low in indium. This indium-deficient growth with self-limited size along $<11\bar{2}0>$ is exactly the origin for the diametric dark lines observed in Figure 3-34.

Notably, this self-ordering phenomenon is also observed in the growth of zincblende-phased AlGaAs nanowires [62]. Dark lines of high aluminum composition is observed along the <211> due to shorter diffusion length of Al compare to Ga. AlGaAs possesses a direct-to-indirect band gap transition and exhibits strong sensitivity to deep level trap formation depending on Al composition. Therefore, alloy composition fluctuation in these nanowires can have negative impact on the optical performance. In our case, InGaAs is direct bandgap at all alloy composition. Therefore, spontaneous alloy composition ordering is not detrimental to the optical performance of the nanopillars. Since the indium-deficient layer is thin, the misfit stress due to lattice mismatch should be well accommodated by the core-shell growth mode. In other words, such composition ordering would not induce any misfit defects that would act as irradiative recombination centers. Moreover, the indium deficit layer has larger bandgap than the $In_{0.2}Ga_{0.8}As$ active region. The composition variation therefore would not have great impact on the emission wavelength. In the next section, we will show that the pillars can still exhibit excellent optical properties despite the natural compositing ordering.

In addition to the transverse cross-section, we studied the composition coherency along the axial direction. We cut through the center of the nanopillar and expose the a-plane with the use of FIB, similar to what we did for the root study. Figure 3-36(a) shows a HAADF-STEM image of the cross-section. Notably, the cross-section along the axial direction resembles the core-shell structure schematic in Figure 3-33. The very tip of the pillar is damaged during ion milling in spite of Pt passivation. Unlike the transverse cross-sections, z-contrast is not very prominent among the three layers, i.e. $In_{0.12}Ga_{0.88}As$, $In_{0.2}Ga_{0.8}As$ and GaAs. The hetero-interfaces, however, appear much darker than other regions of the pillar. We attribute this to thickness variation across the lamella. The intense misfit stress at the hetero-interfaces weakens the local crystal stability and thus ion milling is faster at that region. The region adjacent to the interface is therefore thinner, leading to the observed contrast. Similar to InGaAs/GaAs core-shell structure studied in the previous section, inverse tapering is observed at the base of the pillar due to the formation of poly-InGaAs. Figure 3-36(b) shows a close-up image of the hetero-interfaces. The innermost $In_{0.12}Ga_{0.88}As$ layer converges into a sharp tip within the nanopillar and is completely surrounded by $In_{0.2}Ga_{0.8}As$ layer in all growth directions. This observation signifies a direct proof of the characteristic core-shell growth mode that we illustrated in Figure 3-3(b).

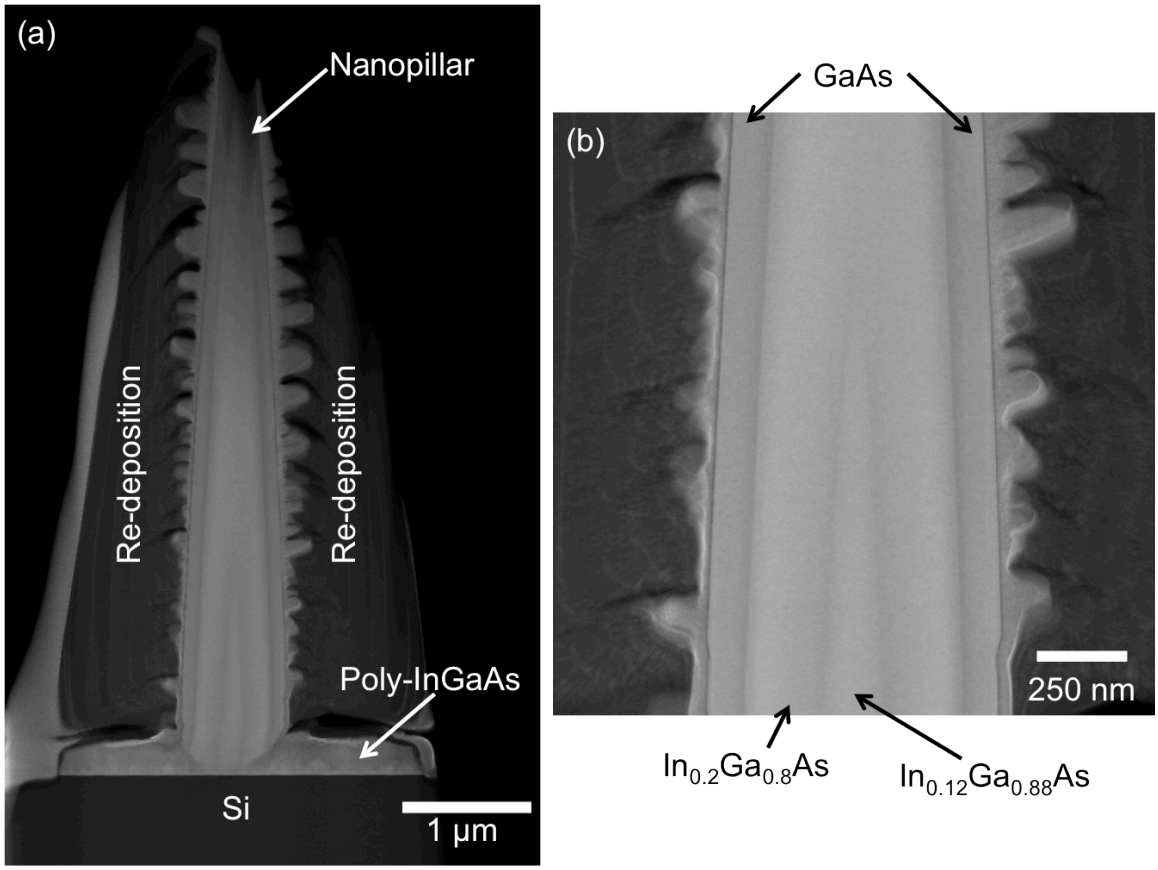

Figure 3-36 HAADF-STEM images of an $In_{0.12}Ga_{0.88}As/In_{0.2}Ga_{0.8}As/GaAs$ nanopillar showing the core-shell growth mechanism

The spatial distributions of the indium, gallium and arsenide are plotted out as elemental maps, as shown in Figure 3-37. The corresponding HAADF image is also included in the same figure. To allow easier interpretation, we cropped away the signals obtained from the re-deposition region. As expected, arsenic shows a fairly uniform distribution over the entire nanopillar since the III-V stoichiometry is independent of group III alloy composition. Indium and gallium, however, show a complementary behavior in distribution because the two group III elements always add up to 50% of the total atomic abundance. From the indium map, we can discern three regimes with different indium compositions, although intensity contrast between $In_{0.12}Ga_{0.88}As$ and $In_{0.2}Ga_{0.8}As$ is a bit subtle to recognize. Interestingly, noticeable signal of indium is detected in the GaAs shell. We attribute this to the trace amount of indium that re-deposits onto the lamella during ion milling. In fact, the measured average atomic abundance of indium is well below 0.5% in the shell region. Notably, the indium map shows uniform intensity over the entire $In_{0.2}Ga_{0.8}As$ active region, which extends for more than 4 μm above the pillar base. This is a first indication that the active region exhibits excellent composition uniformity along the axial direction, which is critical to the optical performance of the nanostructure.

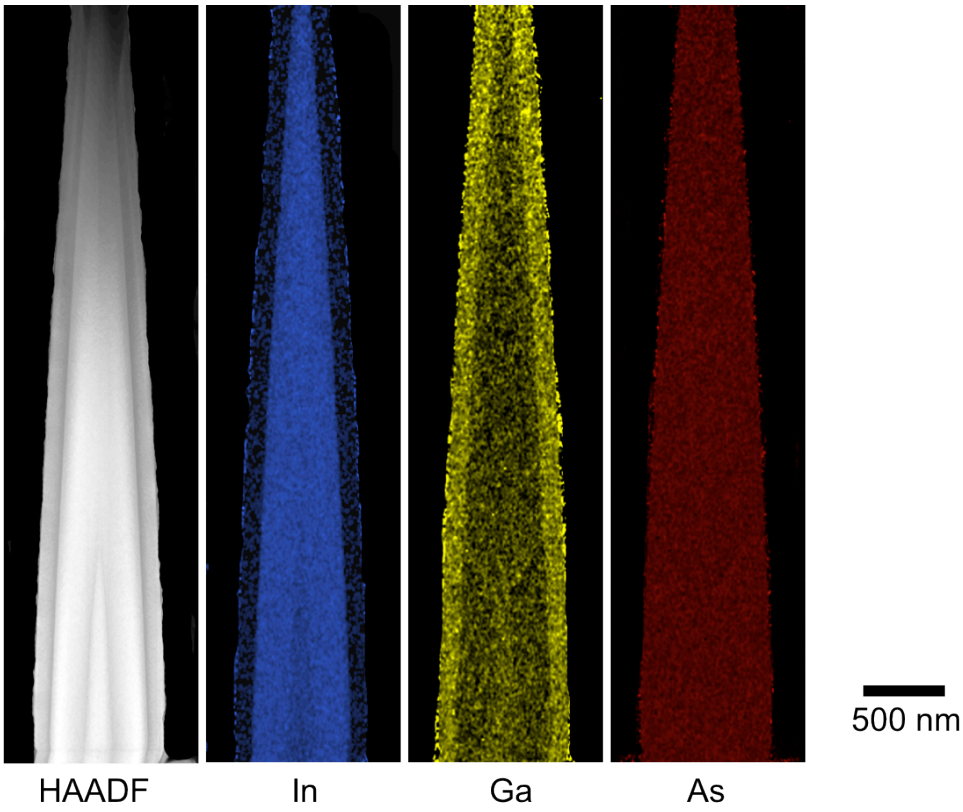

Figure 3-37 Spatial distributions of In, Ga and As in an $In_{0.12}Ga_{0.88}As/In_{0.2}Ga_{0.8}As/GaAs$ nanopillar

To investigate the composition uniformity more quantitatively, we plot the relative abundances of In, Ga and As along the line A-A', as illustrated in Figure 3-38. The line profiles of Ga and As are rather noisy in the plot. We note that the L_α emission energies of Ga and As are 1.098 keV and 1.282 keV, respectively [63]. The energy spacing of the two peaks (< 200 eV) is actually very close to the energy resolution limit of the EDS detector [64]. The small energy gap lowers the accuracy in deconvoluting the emissions from the two elements. One can actually observe that the Ga profile varies 'out of phase' with the As profile – Ga% rises when As% decreases, and vice versa. In spite of the noise, we can observe that Ga and As abundances are fairly constant on average over the entire line-scan. Indium, on the other hand, shows a much stable line profile along the full length, i.e. over 4 μm, of the pillar. These results show that the alloy composition of the active region is indeed very coherent from base to tip. This chemical homogeneity gives rise to excellent optical and electrical performances, which will be discussed in more details in the following sections.

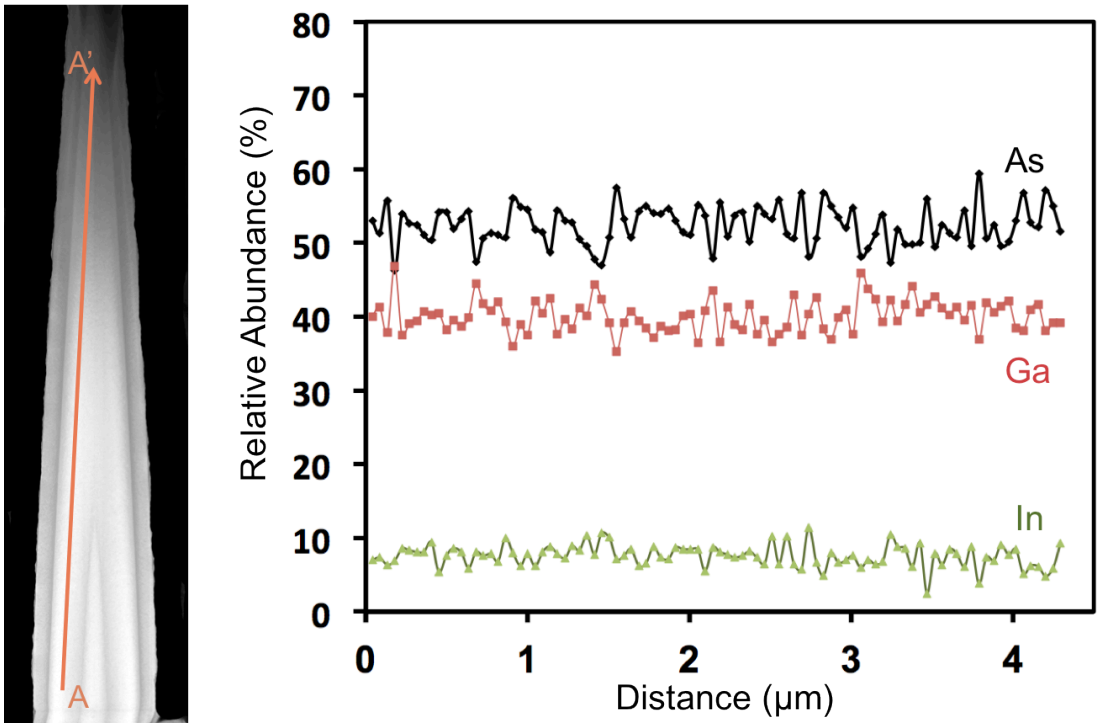

Figure 3-38 Line profiles of In, Ga and As abundances

3.9 Continuous Wave Operation of InGaAs Nanolaser

In the previous sections, we have seen that the InGaAs/GaAs core-shell pillar structure, although grown on highly mismatched Si substrate, exhibits excellent crystal quality as well as superior composition homogeneity along the axial direction. These extraordinary material properties give rise to remarkable optical properties. With the use of a 785-nm diode laser as a CW pumping source, we optically excite $In_{0.2}Ga_{0.8}As$ nanopillars and study the photoluminescence (PL). Remarkably, CW lasing operation is achieved in nanopillars directly grown on silicon under optical pumping at 4 K. Figure 3-39(a) displays the emission spectra under various pump powers. At low pump levels, spontaneous emission is observed with a peak wavelength at 970 nm and a 3-dB bandwidth of approximately 17 nm. As the excitation power increases, we observe the emergence of a cavity mode at 960 nm, at a pump power is as low as 0.25 times the threshold pump power (0.25 P_{th}). The cavity peak finally evolves into laser oscillation. A sideband suppression ratio as high as 10 dB is observed at 4 P_{th}. In particular, clear fractal pattern is observed in the near field image of the nanolaser above threshold, as demonstrated in Figure 3-39(b). Fractal pattern is formed as a result of interferences of highly coherent light being scattered on a rough surface. This indicates that coherent emission is obtained from the nanostructure, which is a signature of lasing action.

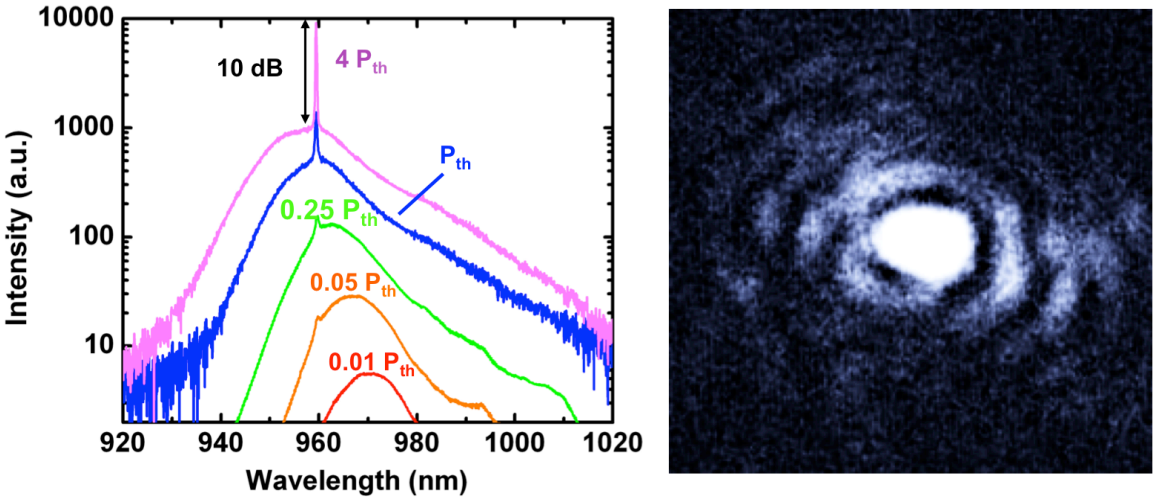

Figure 3-39 (a) CW emission spectra at different pump powers (b) Near field image of the nanolaser above threshold showing fractal pattern

To further prove that the nanopillar is indeed lasing, light output power from the nanopillar emission is plotted against the pump power. The plot is also known as light-light (L-L) curve, which is displayed in Figure 3-40(a). Light output power is obtained by integrating the area under the intensity spectra shown in Figure 3-39(a). Two segments can be observed in the L-L curve. The first segment has a gentle slope and corresponds to the spontaneous emission from the nanopillar. When the pump power reaches ~ 450 μW, the output power shows a sudden increase in slope, indicating the onset of lasing. This two-segment behavior is a clear sign of lasing action.

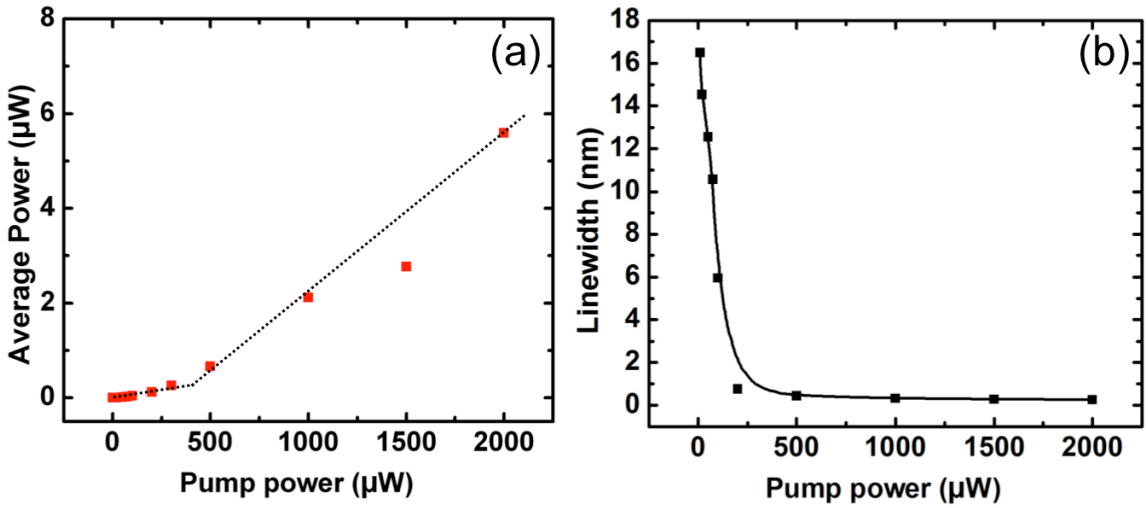

Figure 3-40 (a) Light output power and (b) Linewidth plotted against pump power

Lasing action is also indicated by the prominent linewidth narrowing, as seen in Figure 3-40(b). At a pump power of 1000 μW, the laser linewidth is as narrow as 0.2 nm, which is comparable with the narrowest linewidths observed for existing nanocavity lasers [65-68]. As illustrated in Figure 3-32, the laser assumes a helically-propagating mode and, hence, the output emitted from the top surface is relatively low. Nevertheless, more than 5.5 μW of CW optical power was collected, which is among the highest reported for nanolasers. This underscores the potential usefulness of integrating these nanopillar lasers onto silicon for various applications.

Compare to conventional nanowire work, a major advantage of this growth process is that it enables high quality sub-micron growth of III-V on silicon, as attested by detailed HRTEM studies. The bulk of the structure is in pure wurtzite phase, which is in contrast to most nanowires reported with zincblende/wurtzite polytypism. As our nanostructure can scale up to micron size, lasing from a *single, as-grown* pillar can be achieved. This is yet to be demonstrated in other nanowire work because insufficient optical feedback can be provided by the small-sized cavity. With InGaAs/GaAs core-shell nanopillars, we obtained a density of around 1 per 200 μm^2, similar to that of GaAs nanoneedles grown on silicon reported in our previous work. Since each pillar is large enough, it can be processed and used as a single device, as evident by the optically pumped laser reported here. Hence, different from nanowires, where an ensemble would be required to function as a laser [69], high density may be neither necessary nor desirable. We note that this growth has been repeated for over 500 times and this signifies the potential of this work as an important pathway for heterogeneous integration.

3.9 InGaAs Pillar-based Electrical Devices

With the excellent crystal quality and optical performance, we anticipate that the InGaAs pillars can make good electrical devices. Double hetero-structure, i.e. $In_{0.12}Ga_{0.88}As$/ $In_{0.2}Ga_{0.8}As$/GaAs, is utilized for better carrier confinement. Doping the structure properly is a critical task in order to realize electrical injection. We leave the $In_{0.2}Ga_{0.8}As$ active region undoped to maximize radiative recombination and thus light emission efficiency. The $In_{0.12}Ga_{0.88}As$ core is n-doped to ~ 10^{19} cm^{-3} with Te while the GaAs shell is p-doped to ~ 5×10^{18} cm^{-3} with Zn. However, 50 nm of the core and shell layers that are in direct contact with the active region are kept undoped. These undoped regions act as buffer which blocks any possible dopant diffusion into the active region. FDTD simulations reveal that a larger base diameter can increase the cavity quality factor, or simply cavity Q, of the pillar structure. Therefore, pillars used for device fabrications have diameters as large as 1.6 μm to improve optical feedback via the helically propagating mode. This remarkably gigantic dimensions are enabled by the unique core-shell growth mode and has not been ever achieved with other III-V nanowires grown on silicon substrates.

Prior to actual device fabrications, we verify the optical properties of the micro-pillars by photoluminescence (PL). In spite of the presence of dopants, lasing action can still be

achieved at fairly low pump power that is comparable to the undoped structures. This shows that the crystal quality of the undoped active region is not greatly affected by dopants. Electrical devices are then fabricated with the as-grown micro-pillars. In the following, we are going to focus on devices of two major functionalities – light detection and emission.

As discussed in previous sections, the entire is substrate is covered with polycrystalline InGaAs film which is in direct contact with the single crystalline pillars. This poly-film is conductive and would create a huge shunt path to the silicon substrate. Therefore, it is crucial to remove disconnect the poly-film from the pillar in order to obtain a functional device. This can be done by selective etch in which the top part of the pillar is covered with metal as an etch mask. Wet etching is then performed to remove the surrounding poly-film as well as the p-shell close to the base of the pillar. After this, gold is evaporated at an angle to cover one side of the pillar for electrical contact. The other side is exposed so that light can still reach the active region of the pillar for light detection and photovoltaics. The schematic of a fabricated device is displayed in Figure 3-41(a). Unlike other nanowires with only ~ 100 nm diameter, the micron-sized pillars are strong enough to survive conventional fabrication processes like contact-mode photolithography and wet chemical etching. Figure 3-41(b) shows an array of pillar devices fabricated with conventional means, underlying the possibility of mass production of III-V devices on silicon in the future.

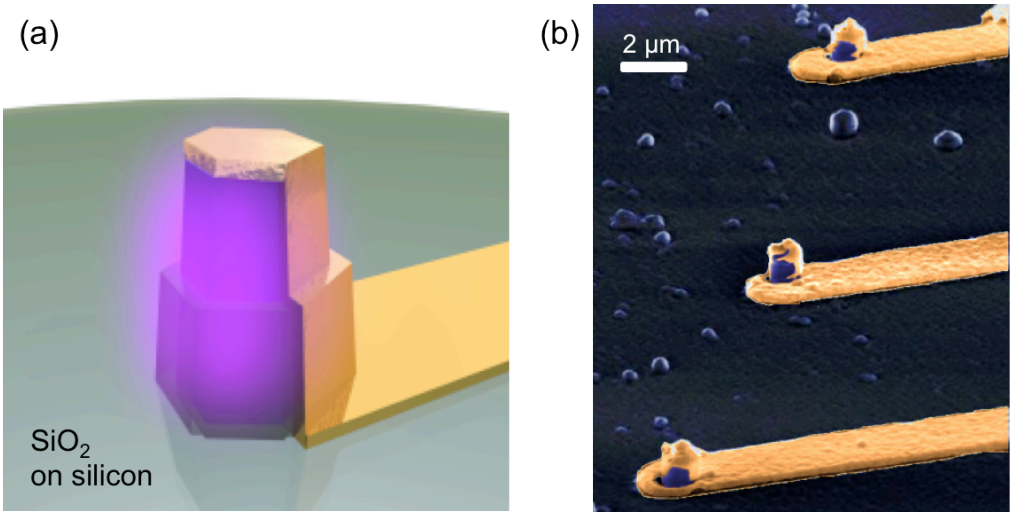

Figure 3-41 (a) Schematic of a micro-pillar device (b) SEM image of an array of pillar devices fabricated with conventional lithography processes

Figure 3-42(a) shows the I-V curve of a typical pillar device in logarithmic scale. In the absence of light, the dark current is as low as only 1.2 pA at 0 V and 45 nA at -1 V. Some devices exhibit dark current as low as 1 nA at -4 V reverse bias. Notably, many pillar devices show ideality factors of nearly 2, which is a typical number in high-quality thin film diodes. The low dark current and respectable ideality factor attest to the decent diode behaviors of the pillar devices. Such promising diode performance suggests that III-V

nanomaterial quality can approach that of epitaxial films with further development. Under illumination, the I-V curve shifts upwards as seen from the red trace in Figure 3-42(a), clearly indicating photocurrent generation. Photovoltaic effect can also be observed in the same graph. Similar to the GaAs-based nanoneedle photodetector reported previously, photocurrent in the present InGaAs-based device increases with reverse bias, revealing avalanche multiplication effects. With unity gain defined by the flat photovoltaic region near 0 V, we obtained a strong avalanche gain as high as 33 at -4.4 V, as demonstrated in Figure 3-42(b). Notably, avalanching occurs at relatively low voltages compared to traditional planar III-V devices. This is probably due to the high doping concentrations, leading to a small depletion region width. Thus, a low bias voltage can create very large electric fields for avalanching effect to occur. In addition to the superior avalanching gain, the pillar detector also exhibit decent frequency response. In particular, the avalanche photodetectors can be used to detect signal with modulation frequency up to 1 Gbps signal. These results signify the potential of the pillar device for high-speed light detection in on-chip optical communications.

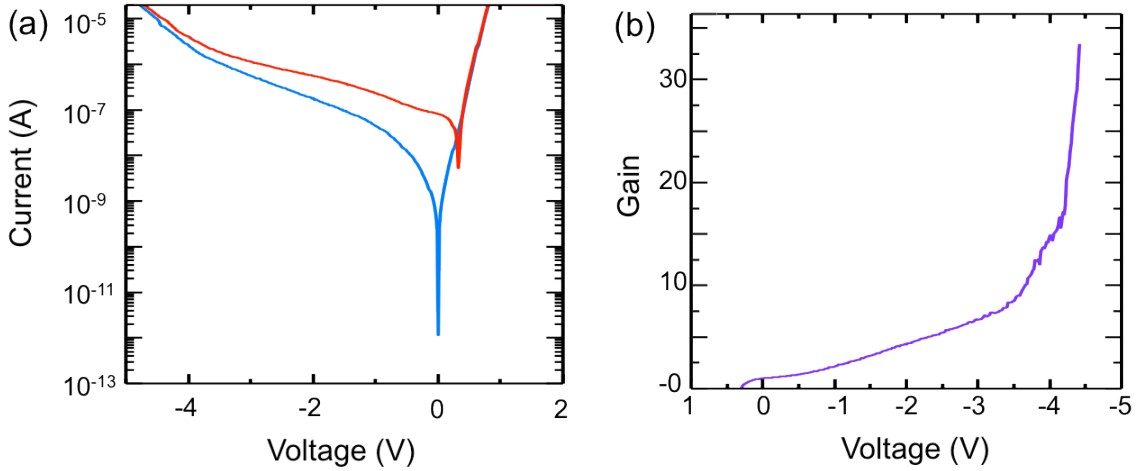

Figure 3-42 (a) I-V characteristics of photodetectors with and without illuminations (b) Avalanche multiplication gain as a function of biasing voltage

While powerful for photodetection, what makes III-V compounds stand out from silicon and germanium is their capability for efficient light emission. In the photodetector described above, we deposit gold on only one side of the pillar for electrical contact so that light can enter from the uncovered side. This asymmetric metal deposition, however, is detrimental to optical cavity Q, as light inside the light would tend leak out from the opened region. To make a laser, we cover the entire nanopillar completely with either gold or silver to create a metal-optic cavity [70-72]. Figure 3-43 shows the schematic and SEM image of an InGaAs nanopillar embedded inside a metal-optic cavity. We note that silver works better than gold as the metal encapsulation due to lower metal loss.

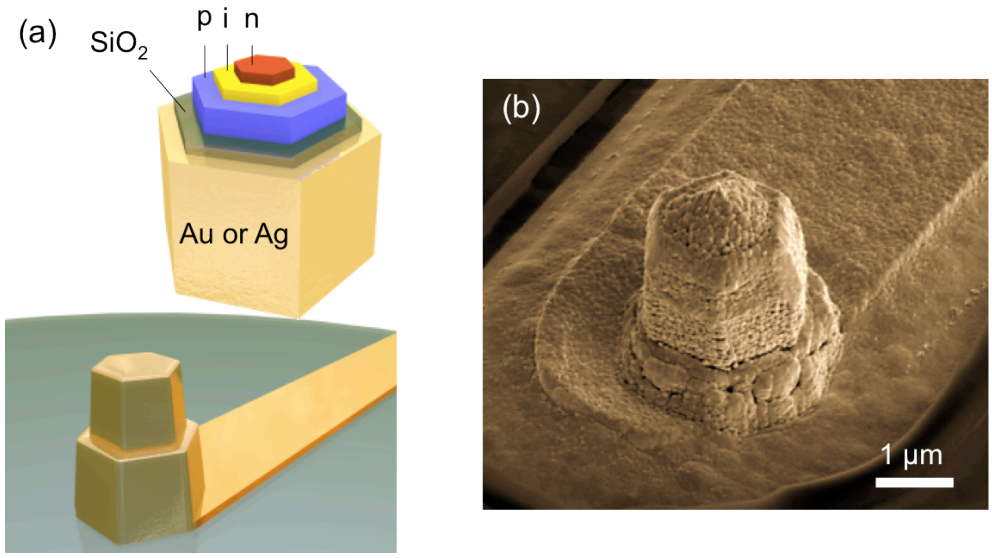

Figure 3-43 (a) Schematic and (b) SEM image of a nanopillar encapsulated in metal-optic cavity

Upon electrical injection, amplified spontaneous emission (ASE) is observed at 4 K, as shown in Figure 3-44(a). Under progressively higher current injection, a prominent emission peak at approximately 1.1 μm emerges and grows before eventually saturating. Additional cavity modes at shorter wavelengths meanwhile continue to amplify as carrier density builds up inside the nanopillar. The inset displays a top-view near field image of light emission from a device. Light intensity shows a specific spatial pattern, which is likely to be the optical mode that forms in the opto-metal cavity. This further suggests that certain modes are indeed amplified and dominate emission. We note that there is a dark spot at the center of the emission. This is due to the thick gold deposited on the top facet which effectively blocks light from emitting along the vertical direction.

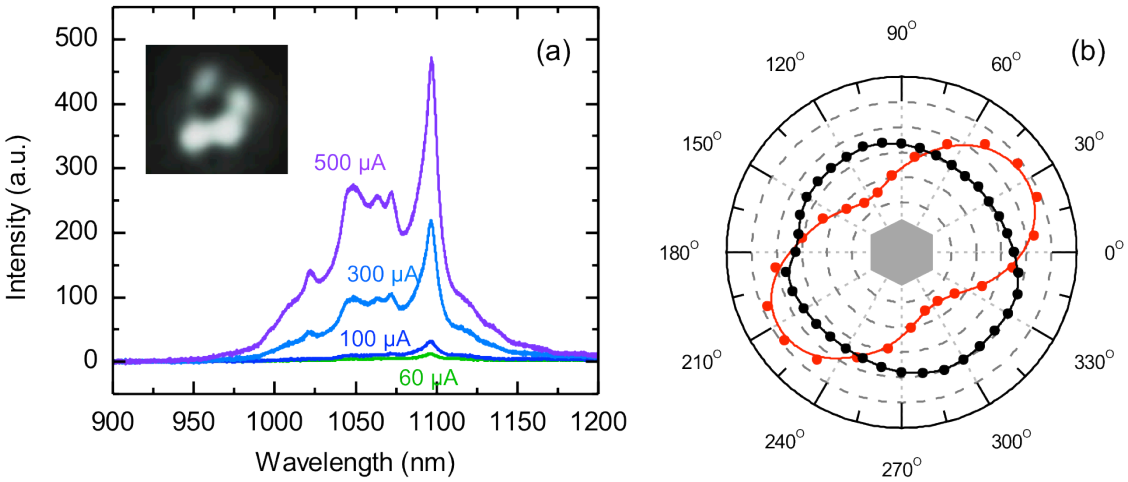

Figure 3-44 (a) Emission spectra under various pump currents. Inset is a top-view near-field image of the emission (b) Polarization dependences of emissions from as-grown nanopillar (red) and micro-pillar devices (black)

To verify that the observed peaks in Figure 3-44(a) are really coming from ASE, we studied the polarization dependence of the light emission. When viewing along the c-axis, WZ crystal has a high degree of symmetry and thus there is no special polarization preference in light emission. This agrees with the polarization dependence of photoluminescence from as-grown pillars, as revealed in the black curve in Figure 3-44(b). Emissions from the metal-optic cavity, however, are linearly polarized, as seen from the red curve of the same figure. This is likely a sign of emission being amplified by polarization-sensitive optical mode inside the cavity.

Though ASE is observed under both CW and pulsed pumping, lasing is yet to be achieved. We attribute this to insufficient optical feedback of the metal-optic cavity. The high refractive index contrast between GaAs and air provides good confinement of light within the pillars, enabling lasing to occur under optical pump even at room temperature. The metal-optic cavity, on the other hand, is more lossy compare to the natural cavity. Optimizing the metal-optic cavity is therefore the major task for realizing electrically-injected monolithic nanolasers on silicon. We estimated the material gain to be as high as 3,400 cm^{-1} in current-injected nanopillars. With this high gain, lasing would occur when the cavity Q can exceed ~100. This is trivial for traditional laser structures, but remains a challenge for nanophotonic cavities. With improved cavity design, an exciting possibility emerges for directly interconnecting nanolasers with CMOS circuits, greatly deepening the marriage of photonic and electronic devices.

3.10 Summary

In this chapter, we investigated the growth mechanisms of high-quality (In)GaAs nanoneedle/nanopillar structures on silicon. Through HRTEM studies, InGaAs is found to nucleate directly on silicon without any amorphous material in between. Misfit strain between silicon and InGaAs is relaxed *via* an interesting inverted-cone shape tapering of the root, which reduces the footprint of the nanostructure and relax misfit strain partially through an elastic mechanism. The remaining stress is accommodated by horizontally terminated stacking disorders, which are well confined within the inverse-cone region. Thus, the bulk material of micron-sized pillars can remain single crystalline in spite of the 6% lattice mismatch between InGaAs and silicon.

In addition, we studied the polarity of the crystal via HAADF imaging. InGaAs nanoneedle is found to terminate with arsenic at the top (0001) facet. This indicates that metal is likely the first monolayer which covers up the silicon substrate. This observation suggests that the growth of nano-structures is metal initiated. Nucleation starts with the formation of metal nano-droplets on the roughened region. These droplets diffuse out to the flat silicon surface and react to form tiny InGaAs crystal seeds which subsequently expand into nanoneedles via core-shell growth. Notably, the nanoneedle growth mechanism is different from conventional VLS growth. While the nanostructures in this work start small and then scales linearly with time, VLS grown nanowire diameter is pre-defined by the size of the metal catalyst. Therefore, the nanostructures presented in this

work can have size far exceeding the nanowire critical diameter while still preserving pure wurtzite crystal phase.

With base diameter far exceeding the critical value for nanowire growth, InGaAs nanoneedles/nanopillars still exist as pure wurtzite phase rather than the energetically favorable zincblende phase. We attribute this to the high-energy barrier which prevents the bulk material to undergo phase transformation. For the first time, we *in situ* convert the wurtzite-phased crystal back into the energy-preferred zincblende phase inside a TEM. This shows that the wurtzite phase exhibited in the nanostructure is indeed a meta-stable state.

In spite of close to 2% lattice mismatch, misfit-defect free GaAs is observed to grow on $In_{0.2}Ga_{0.8}As$, with a thickness exceeding 15 times the critical value in 2-dimensional thin-film. A mathematical model is developed to understand how this happens. It turns out that most of the misfit stress is concentrated close to the hetero-interface and the total elastic energy due to misfit stress saturates as the shell thickness increases. This extraordinary phenomenon is due to the characteristic core-shell growth mode that enables the expansion of surface area as the GaAs shell thickness increases. An increase in surface area at the growth front effectively accommodates misfit stress elastically. The unique stress relaxing mechanism enables the growth of mismatched layers to thicknesses far beyond the conventional thin-film limit and could lead to device structures with potentially unprecedented functionalities.

In addition to crystal quality and stress relaxing mechanism, alloy composition coherence is also studied in the $In_{0.12}Ga_{0.88}As/In_{0.2}Ga_{0.8}As/GaAs$ hetero-structure. Spontaneous alloy composition ordering is observed in the transverse cross-section as a result of diffusion length difference between indium and gallium. However, this variation is not detrimental to the optical performance of the nanostructure since the misfit stress can be accommodated without inducing defects. Along the axial direction, the alloy composition is found to be highly coherent. This is crucial to the emission efficiency of the structure.

With the excellent crystal quality and composition homogeneity, InGaAs based nanopillars exhibit extraordinary optical performance. Continuous wave operation of InGaAs nanolaser is achieved at 4K upon optical pump. We note that this is the first as-grown laser sitting on top of silicon substrate. Although Si is absorptive at the lasing wavelength, the output power and linewidth of the emission are among the best in all available nanolasers. These remarkable results signify the potential for these InGaAs based nanostructures to be used as active light source on silicon.

Photodetector and light emitter are fabricated with the nanopillars as-grown on silicon, using conventional lithography and etching processes. The devices reveal extremely low dark current and ideality factor close to 2, which are comparable to decent thin film diodes. Nanopillar-based photodetectors show strong avalanche gain and can operate up to 1 Gbps. Amplified spontaneous emissions are observed in pillars embedded in metal-optic cavity. With further improvements in device structure and cavity design, electrically pumped nanolasers can be realized with InGaAs based nanopillars monolithically grown

on top of silicon at a CMOS-compatible temperature. This study opens a new chapter in the integration of III-V optoelectronics with CMOS technology for unprecedented functionalities.

Chapter 4 Single Crystalline InGaAs Nanopillar Grown on Polysilicon

III-V compound materials have been an important building block in optoelectronics technology due to their direct bandgaps leading to excellent optical and electrical properties. Conventionally, high-quality epitaxial growth requires the use of III-V substrates, which are usually expensive and fragile. Heterogeneous growth of III-V materials on substrates with lower cost is thus highly desirable. Among various low-cost substrates, polycrystalline silicon (poly-Si) is an excellent choice because of its unique semi-conducting property to facilitate doping into both p- and n-type for various semiconducting device functionalities. Moreover, poly-Si can be deposited and patterned easily on a great variety of carrier substrates, such as glass, polymer, metal, and oxidized silicon substrates, just to name a few. With these unparalleled properties, poly-Si has become one of the most important electronic materials used in a vast variety of applications including CMOS transistor, sensing, nanofluidics, thin film transistor (TFT) in displays, photovoltaics, etc [73-77].

Being able to grow high-quality III-V structures on poly-Si could open up a new pathway for low-cost monolithic integrations of optoelectronics with these many applications. In particular, single-crystalline structures that are micron-sized are critical to reduce surface-to-volume ratios. However, the growth of single crystalline III-V structures on poly-Si remains to be challenging due to the extremely short-range crystalline coherency in poly-Si. There have been previous reports of III-V semiconductor nanowire growth on low-cost amorphous and poly-crystalline substrates [78-81]. In the former case, only nanowires with diameter as small as 50 nm are shown to have high crystal purity. Moreover, the amorphous substrate is electrically insulating, making electrical contact to the nanowire difficult. On poly-crystalline substrates, the diameter of the nanowire is limited to well below 200 nm by the grain size of the substrate to ensure that the nanostructure is not nucleating from multiple substrate crystal grains. Increasing the size of the nanostructure while maintaining high crystal purity thus is a major challenge.

In this chapter, we demonstrate the growth of single crystalline $In_{0.2}Ga_{0.8}As$/GaAs core-shell nanopillar on poly-Si via metalorganic chemical vapor deposition (MOCVD) at a low temperature of 400^{o}C. The base diameter of the nanopillars is over 800 nm, which far exceeds the grain size of the substrate (~100 nm). Nanopillars are randomly oriented due to the polycrystalline nature of the substrate. A density as high as 10^8 cm^{-2} is achieved. With the use of focused ion beam (FIB) and high-resolution transmission electron microscopy (HRTEM), we cut through the center of nanopillars and examine the InGaAs/poly-Si interface. The InGaAs nanopillar is observed to stem directly on a polycrystalline substrate. In addition, the bulk of the pillars is single crystalline with pure wurtzite (WZ) crystal phase. The key to this high-quality mismatched growth is the inverse-cone shape at the base of the nanostructure. This feature reduces the footprint of the nanostructure down to below 40 nm in diameter and ensures that III-V material seeds

on a single Si crystal grain. The vertical growth direction [0001] is found to align with Si [110] rather than the conventional Si [111] direction. This crystalline alignment leads to discrepancy in lattice arrangement across the hetero-interface, facilitating the formation of misfit dislocations which relax stress due to 5.3% lattice mismatch. Photoluminescence is utilized to further verify the crystalline and optical quality of the nanostructures. Lasing is achieved upon optical pump with the *as-grown* nanopillars, attesting their excellent crystalline and optical quality. Notably, this is the first report of as-grown lasers on poly-silicon. These remarkable results are first proof that these nanostructures can potentially be used as high performance devices on top of poly-Si. The study presented here underscores a new methodology for inexpensive integration of materials for various functionalities with high-quality optoelectronic devices.

4.1 Synthesis of InGaAs nanopillars on polysilicon

Similar to the growth of nanostructures on silicon, synthesis of InGaAs nanopillars on polysilicon was carried out by low-temperature (400 ^{o}C) MOCVD. The substrate used in this work is an 800-nm-thick polysilicon layer deposited on top of oxidized silicon substrate, as depicted in the schematic in Figure 4-1. The poly-Si layer was deposited by low-pressure chemical vapor deposition. Prior to the nanopillar growth, the substrate was cleaned and deoxidized with acetone, methanol and buffered oxide etchant, followed by surface mechanical roughening. These procedures are exactly the same ones used in the growth of nanopillar on single crystalline silicon. Surface roughening opens up fresh silicon surface which can be readily oxidized in air. During the growth, metal nano-droplets form on the oxidized region and subsequently migrate to bare silicon for nanopillar nucleation. Other growth parameters like reactant flow rates, pressure, etc. are exactly the same as those used in Chapter 3.

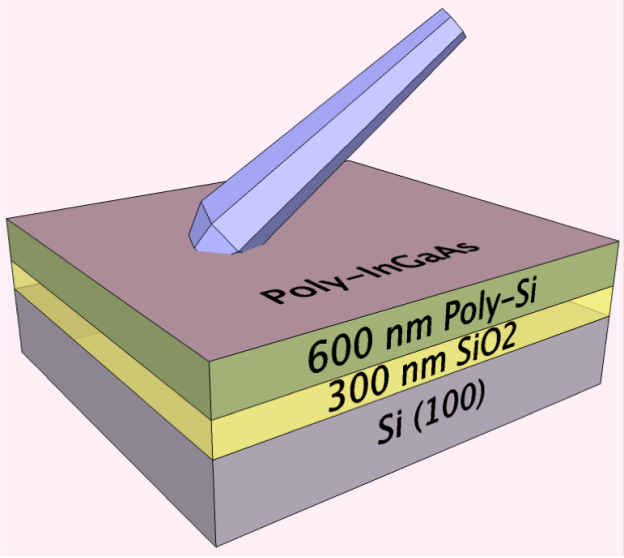

Figure 4-1 Schematic diagram illustrating the growth of InGaAs nanopillars on poly-Si

The growth of InGaAs nanostructures on poly-Si assumes a core-shell growth mechanism, similar to what we discussed in Chapter 3. More details will be discussed in the following sections. In particular, we observed some variations in nanopillar density over 1"-diameter substrate, most likely due to V/III ratio, temperature and surface non-uniformity. In the low-density regions, individual nanopillars can be identified distinctively, as shown in the scanning electron microscope (SEM) image in Figure 4-2(a). The nanopillars are found to orient randomly as a result of the polycrystalline nature of the substrate. Despite being grown on a polycrystalline substrate, the nanopillars possess clear facets, which are first indications that they are crystalline structures. In an 80-min growth, the base diameter and height can reach ~ 800 nm and 4 μm, respectively. On the other hand, in the high-density regions, nanopillars grow into an ensemble with a density as high as 10^8 cm^{-2}, as illustrated in Figure 4-2(b). These densely packed nanostructures have much smaller diameters, ~400 nm, and are randomly oriented such that some of the nanopillars are actually crossing one another. This is a signature of the characteristic core-shell growth mode. In spite of the crossed growth, the nanopillars do exhibit distinctive hexagonal cross-sections and smooth sidewalls, as seen in the close-up image in Figure 4-2(c). The high density and randomly aligned nanopillar ensemble can trap and scatter light effectively, which make them ideal candidates for light sensing and photovoltaic applications [82].

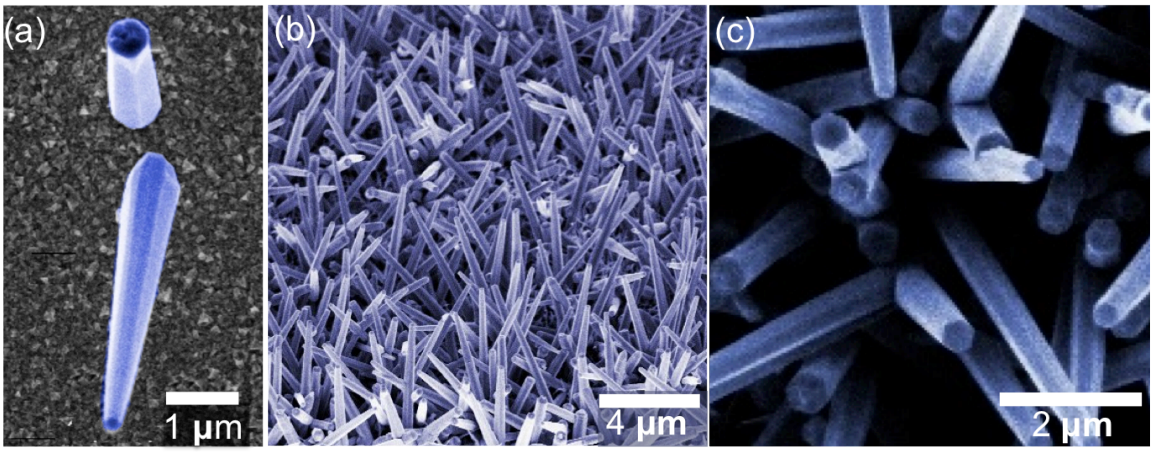

Figure 4-2 SEM images of (a) individually discernable pillars (b) high density nanopillar ensemble with random orientation (c) nanopillar ensemble at high magnifications

4.2 Crystal Quality Characterization with Transmission Electron Microscopy

Given the lack of long-range crystalline coherence in poly-silicon, it is crucial to find out if the nano- or micro- pillars are actually of good quality. Here, we study this topic extensively with high resolution TEM (HRTEM) and scanning transmission electron microscopy (STEM). To have a quick check on the crystal quality of multiple nanopillars, we first examine nanopillars that are mechanically wiped down onto a TEM

copper grid. Figure 4-3(a) shows a bright field (BF) TEM image of a typical InGaAs nanopillar. No noticeable defects can be seen along the entire length (~ 2 μm) of the pillar. At high magnification (see Figure 4-3(b)), we can see the ABAB stacking sequence in the lattice, revealing the wurtzite nature of the crystal. The phase purity of the nanostructure is further confirmed by the clearly discernable diffraction pattern in Figure 4-3(c). This indicates that, in spite of the polycrystalline nature of the substrate, InGaAs nanopillars grow as single crystalline structures.

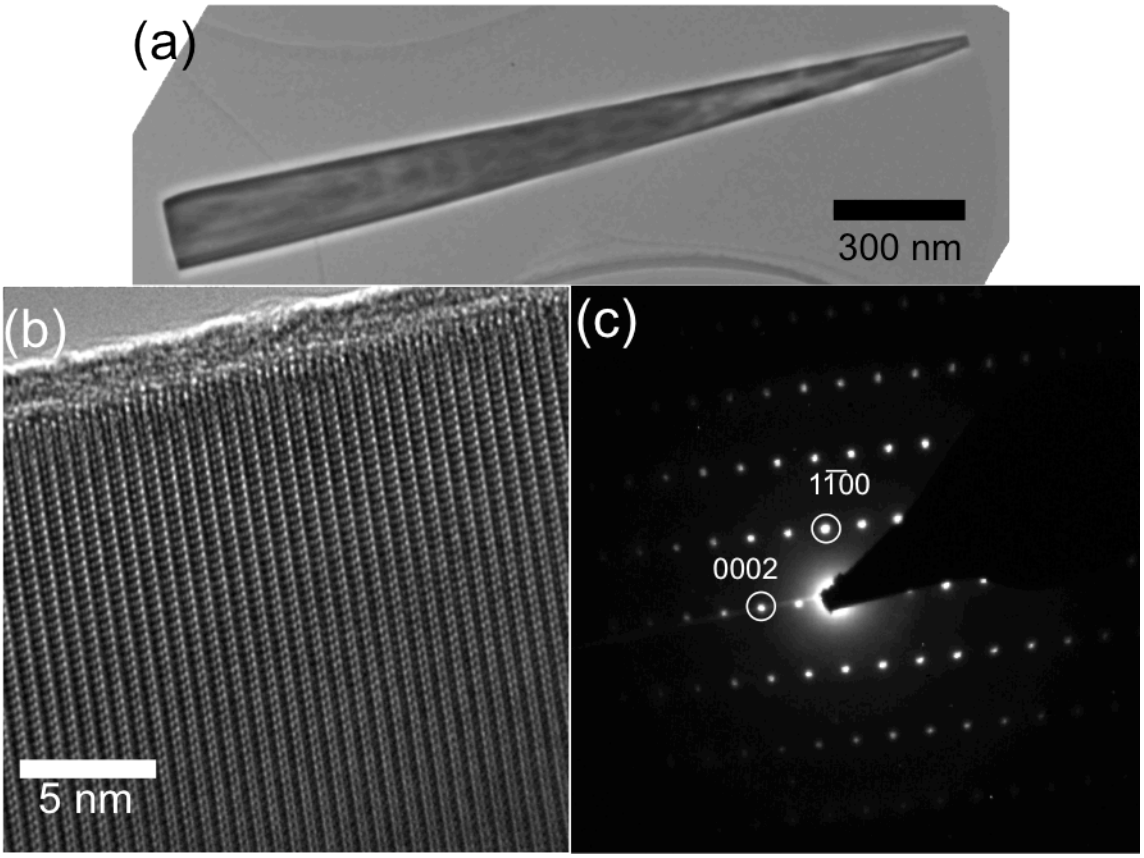

Figure 4-3 (a) BF-TEM image of a wiped-down nanopillar (b) HRTEM image of the crystal revealing wurtzite lattice arrangement (c) Selective area diffraction pattern of the nanopillar

To study how high-quality nanostructure develop on top of a polycrystalline platform, we examine the very center of the nanopillar by cutting across the pillar with FIB and expose the $(2\bar{1}\bar{1}0)$ facets, or a-planes, to clearly disclose the distinction between wurtzite and zincblende (ZB) phases. Details of sample preparation can be found in Chapter 2. More than ten nanopillars growing along different directions were examined in this work to obtain a general qualification of crystalline quality.

Figures 4-4(a) and (b) show a high angle annular dark field (HAADF) STEM image and schematic illustration of a close-to-upright nanopillar grown on poly-Si. We note that poly-Si possesses a rather rough surface being deposited on an oxidized silicon substrate.

Despite the roughness, InGaAs is observed to stem directly from poly-Si without any void in-between, as seen in the bright field TEM image of the pillar base in Figure 4-5(a). As the substrate is polycrystalline, one would expect any crystal nucleating directly on top should have mediocre quality. Surprisingly, the bulk of the 650-nm thick pillar is single crystalline, as attested by the clear diffraction pattern in the inset of Figure 4-5(b). The unique zigzag lattice arrangement in the HRTEM image in Figure 4-5(b) further confirms that the crystal is in pure WZ phase.

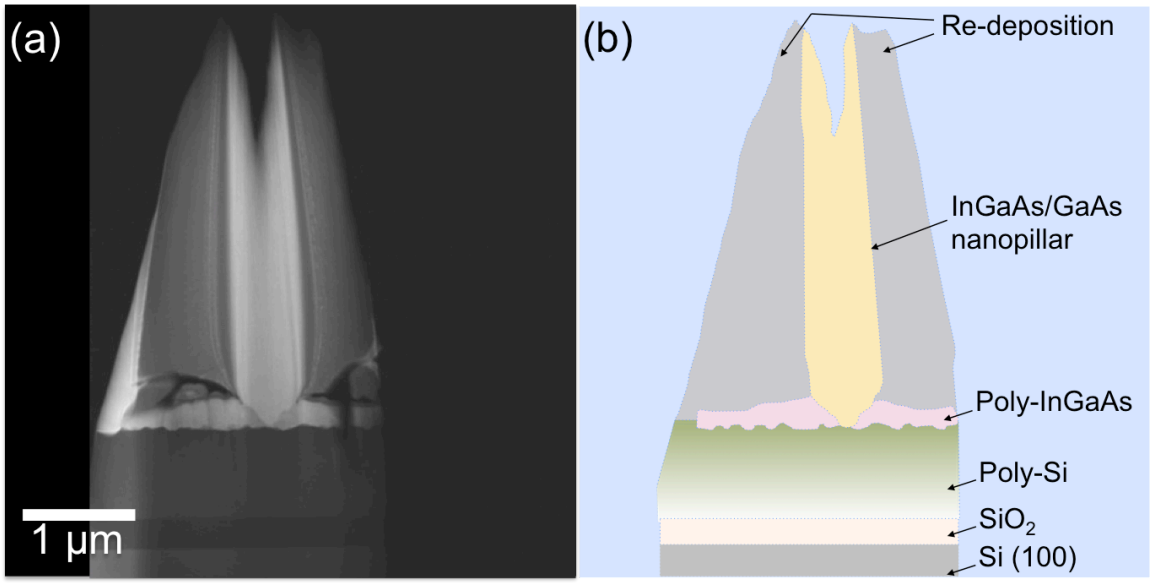

Figure 4-4(a) HAADF image and (b) the corresponding schematic of a close-to-upright nanopillar grown on poly-Si

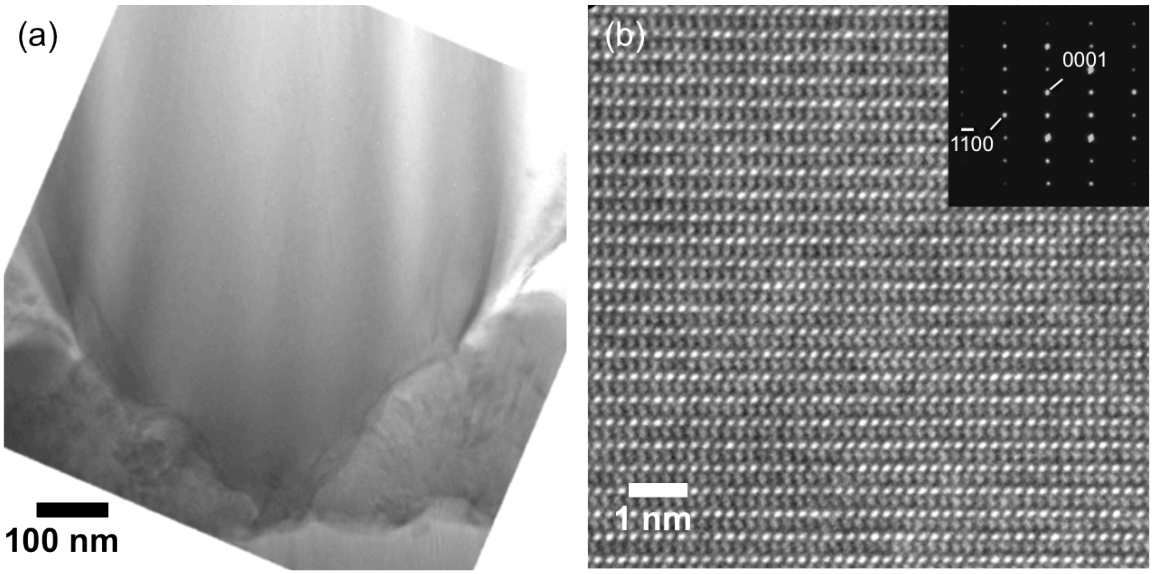

Figure 4-5(a) BF-TEM image of the pillar base and (b) HRTEM image showing the wurtzite crystal lattice of the bulk material. Inset is selective area diffraction pattern

Surrounding the nanopillar, InGaAs evolves into polycrystalline thin film. The same poly-InGaAs layer is also observed in the growth of (In)GaAs nanostructures on (111)-Si and sapphire substrates [24, 83], indicating that the formation of such layer is likely due to the low growth temperature and high lattice mismatch rather than crystallinity of the substrate. This polycrystalline layer grows simultaneously with the single crystalline structure throughout the entire growth process and restricts the pillar base from expanding, thus resulting in inverse tapering at the root, as seen in Figures 4-4 and 4-5. Consequently, the diameter of the bulk can expand to sub-micron (~ 650 nm in this particular TEM sample) while the footprint remains to be < 40 nm. The diameter of nucleation site, and thus the diameter of nanowire grown by VLS or selective area growth, has to be smaller than the Si grain size or otherwise III-V would nucleate on multiple grains and eventually evolve into polycrystalline structures [79]. The cone-shaped base presented in this work thus allows the growth of single crystalline sub-micron sized structures on polycrystalline platforms with grain sizes as small as 40 nm. This relaxes the requirement for the crystal grain size of the substrate, thus potentially simplifies the procedures in poly-Si deposition. This can be beneficial to integrating III-V with materials which are sensitive to temperature and thermal budgets.

The inverse cone geometry at the pillar base reduces stress developed in the nanostructure due to over 5% lattice mismatch. In InGaAs nanopillar grown on (111)-Si, the remaining stress is relaxed via formation of stacking disorders, which are well confined within the inversely tapered region. This is the case as well for some of the nanopillars grown on poly-Si. Figure 4-6 features a slanted nanopillar grown on poly-Si. The top part of the cross section is severely damaged during ion milling. Nevertheless, the tapered root of the pillar can still be identified clearly. Interestingly, unlike the pillar shown in Figure 4-4, the inverse cone at the base is not very symmetric. This is probably due to the bizarre geometry of the nanopillar that causes spatial growth rate fluctuation in the poly-InGaAs film that wraps around the pillar. In addition, some textures aligning almost vertically can be seen in the poly-Si layer. These textures are likely a combination of grain boundaries and curtaining effect due to directional ion milling in which ions always come from the top of the lamella. Despite the asymmetry, most area of the tapered region is still single crystalline, as revealed in the dark-field (DF) TEM image in Figure 4-6(b). The inverse cone is completely wrapped around by poly-InGaAs, similar to what we observed in Chapter 3. Stacking disorders that propagate perpendicular to the growth direction are observed at the bottommost 100 nm of the base for stress relaxation. The footprint, i.e. the exact InGaAs/poly-Si contact area, is less than 30 nm in diameter. This is much smaller than what we observed in InGaAs grown on crystalline silicon, which is > 100 nm in diameter. As discussed in Chapter 3, footprint size is correlated to the average separation between nucleation sites. With the nano-roughness on the surface, poly-Si favors multiple nucleations over short distance, leading to the observed tiny footprint.

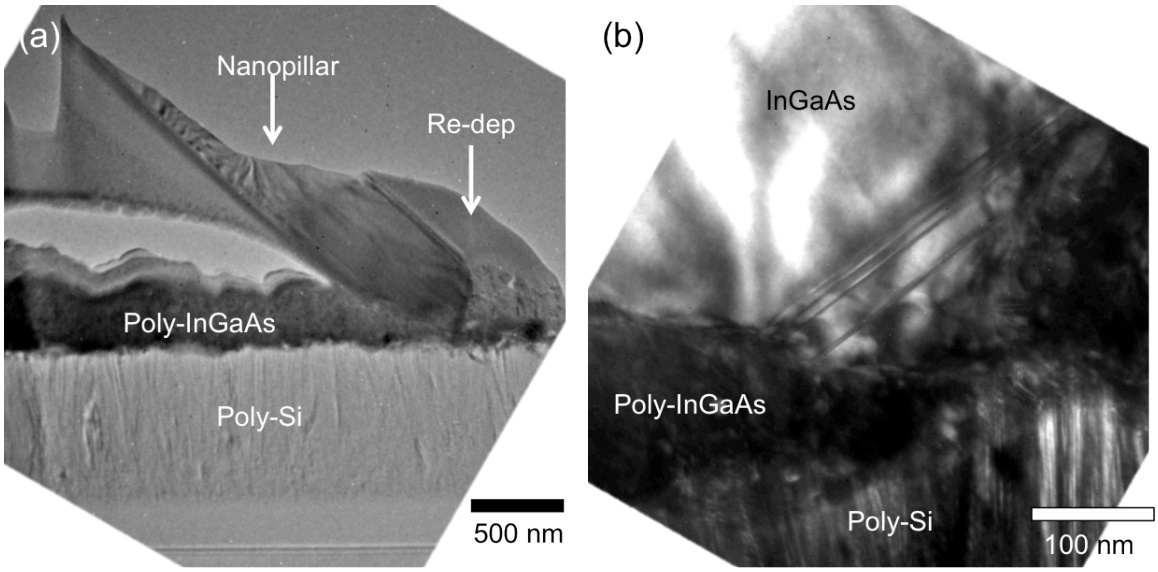

Figure 4-6 (a) BF-TEM of a slanted nanopillar (b) DF-TEM image taken at the tapered base of the pillar, revealing stacking faults at the bottommost 100 nm

4.3 Unconventional Crystalline Alignment at the III-V/Poly-Si interface

While some of the nanopillars there exists nanopillars on poly-Si in which stacking fault is completely absent in the inverse-cone, like the one shown in Figure 4-4. To understand how misfit stress can be relaxed, it is essential to study the InGaAs/poly-Si interface. Figure 4-7 shows an HRTEM image along $[2\bar{1}\bar{1}0]$ zone axis. The poly-Si surface is rough even in nanoscopic scale, resulting in random morphologies along the hetero-interface. We believe that the roughness creates a lot of dangling bonds over the surface and lowers the energy barrier for III-V nucleation on Si, thus enabling the high-density growth observed. The roughness along $[2\bar{1}\bar{1}0]$, i.e. the direction pointing into the paper, causes overlapping of Si and InGaAs lattices and this leads to a blurry hetero-interface in Figure 4-7. Despite the nanoscopic roughness, InGaAs is observed to grow directly on top of the poly-Si layer without any amorphous material in between. The bottommost 3~10 nm is a transition regime composed of ZB/WZ mixed layers. Within the transition regime, we note that the crystal in zone A is in ZB phase while that in zone B is in WZ phase. This is rather subtle as the crystal phase is usually coherent along the lateral direction, i.e. perpendicular to [0001]. One possible reason is that InGaAs nucleated at the two sites separately. Depending on the local surface morphology of poly-Si, InGaAs evolved into either ZB or WZ phase to minimize the interface energy, hence resulting in the observed lateral crystal incoherency. Lattice disordering is observed at where the grains meet, as indicated by an arrow in Figure 4-7. These defects do not propagate upward because the crystal at the base expands in the lateral direction only as a result of the characteristic core-shell growth mode. InGaAs then evolves into pure WZ phase above the transition and this continues up to the tip of the nanopillar. With the unique core-shell growth, high quality single-crystalline nanopillar can be obtained even on a bumpy poly-Si surface.

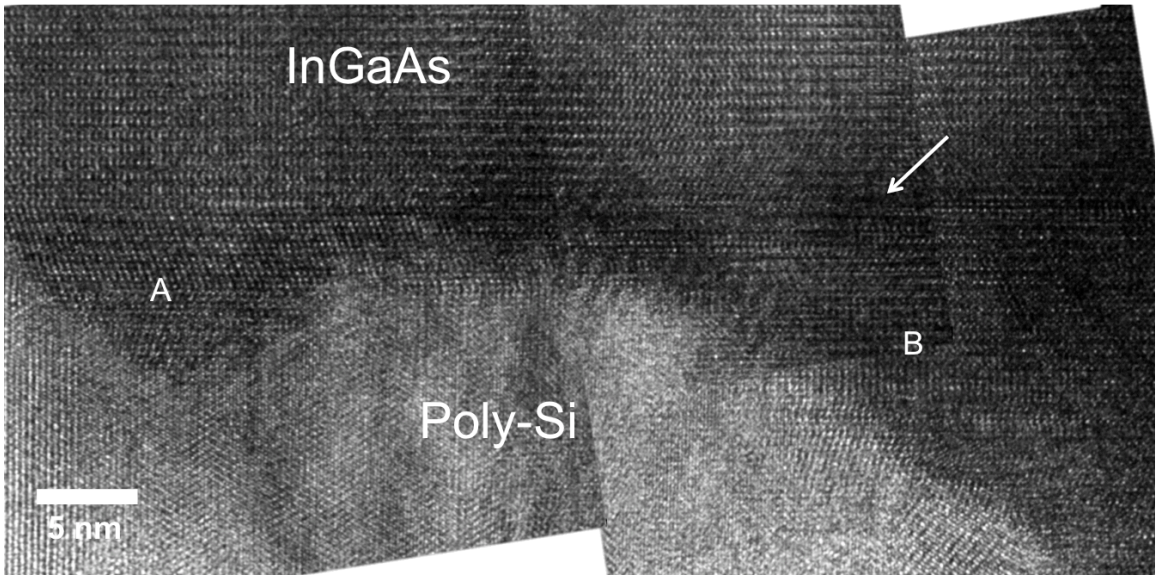

Figure 4-7 HRTEM image taken at the exact poly-Si/InGaAs interface of the pillar shown in Figure 4-4

Although the nanopillar shown above provides much information on the influence of nanoscopic roughness on nucleation, the hetero-interface is undesirably blurry and thus fine details cannot be interpreted clearly. To study the crystalline relation between III-V and the substrate, HRTEM of the hetero-interface of another nanopillar is presented in Figure 4-8(a). The footprint of this particular nanopillar is only 15 nm in diameter. Below the pure WZ phase crystal is a 5nm transition region composed of pure ZB phase crystal. Fast Fourier transforms (FFTs) of the lattices in region I (i.e. WZ phase InGaAs) and region II (i.e. ZB phase poly-Si) are shown in Figures 4-8(b) and (c), respectively. We note that FFT of region II is a bit hazy due to overlap of crystal lattices with slightly different orientations in the poly-Si substrate along the zone axis. Nevertheless, it can be observed that InGaAs [0001] (or [111] in the bottommost ZB transition region) is aligned to Si [110], i.e. InGaAs (111) plane in the transition region is in direct contact with Si (110) at the hetero-interface. In fact, the same crystalline relation is also observed in zone A of Figure 4-7. Compared to Si (111), Si (110) has considerably higher surface energy and is thus more favorable for III-V nucleation [84]. However, this crystalline dependence is rather uncommon as (111) and (110) planes are quite different in lattice arrangements. Such discrepancy in lattice arrangement is actually beneficial as it favors the formation of dislocations and dangling bonds at the InGaAs/Si interface, as illustrated in Figures 4-9. These interfacial defects can effectively relax most of the misfit stress between the substrate and the epitaxial material and this is also observed in the hetero-integration of other material systems [85]. The unconventional crystalline relation, together with the inverse cone geometry at the base, minimize compressive stress induced by over 5% lattice mismatch and enables of the growth of stacking disorder free single crystalline III-V nanopillar on poly-Si.

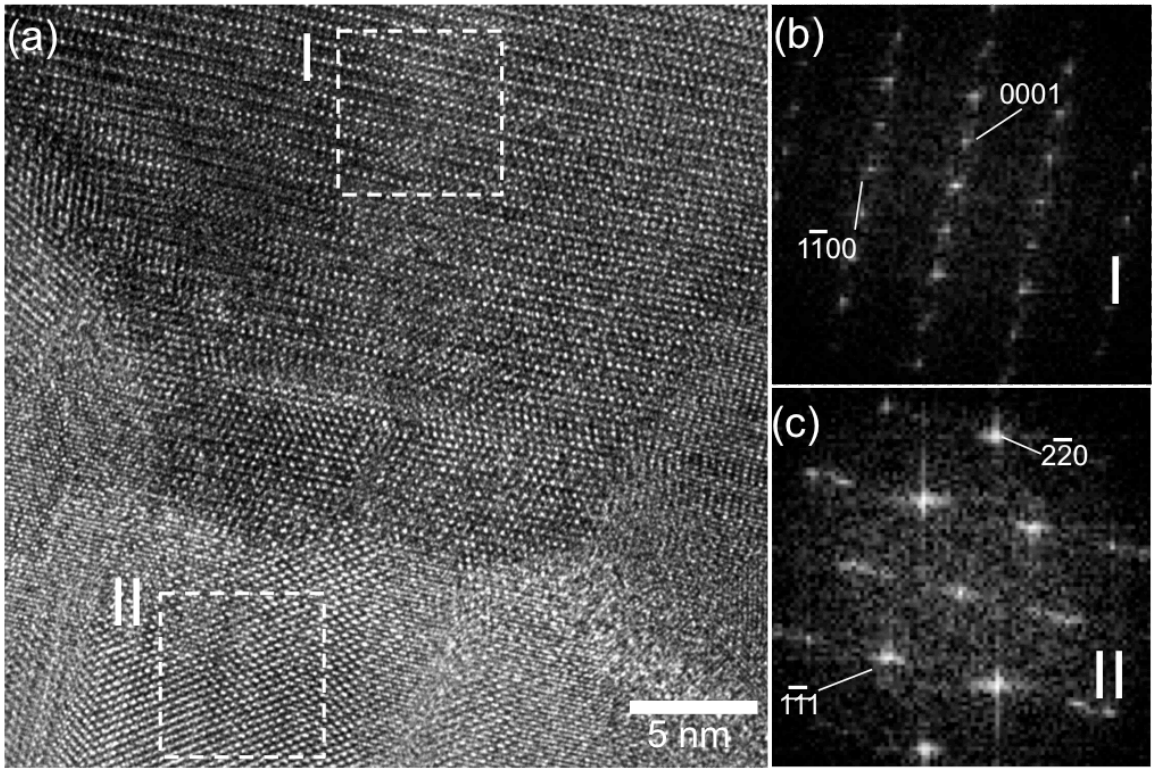

Figure 4-8 (a) HRTEM of an InGaAs/poly-Si interface along [$2\bar{1}\bar{1}0$] zone axis (b) & (c) FFTs of region I (WZ phase InGaAs) and region II (ZB phase poly-Si), respectively

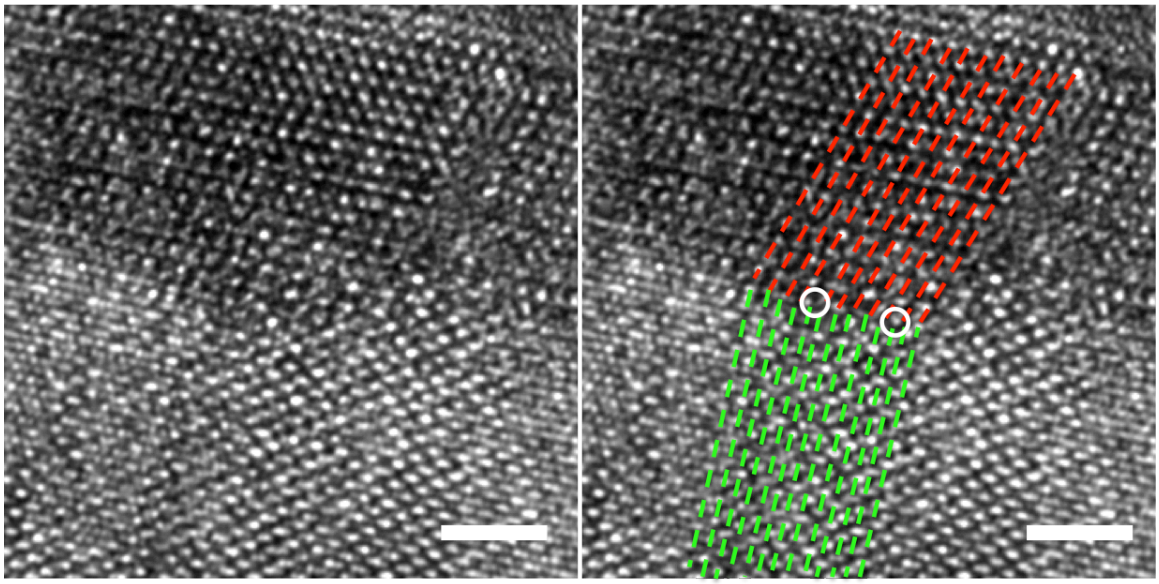

Figure 4-9 Zoom-in image of the exact InGaAs/Si interface with eyeguides for InGaAs ($1\bar{1}1$) and Si (001) planes and interfacial misfit dislocations. Scale bars are 2 nm.

4.4 Alloy Composition Profile at the Core-shell Interface

Similar to nanoneedles grown on sapphire and crystalline Si substrates, InGaAs/GaAs nanopillars grow in a core-shell manner on top of poly-Si. The characteristic core-shell geometry facilitates elastic misfit stress relaxation, enabling the growth of single crystalline GaAs with thickness far beyond the thin film critical limit [86]. To visualize the core-shell growth mode, we cut across a nanopillar horizontally to expose the c-plane, i.e. (0001) plane. HAADF-STEM image and the corresponding schematic illustration of the cross section are shown in Figures 4-10. A clear boundary can be seen at the InGaAs/GaAs interface. While GaAs shell is perfectly hexagonal with sidewalls composed of $\{11\bar{2}0\}$ (i.e. a-planes), InGaAs core is a nonagon bounded by six $\{1\bar{1}00\}$ (i.e. m-planes) and three a-planes. We attribute this asymmetry to non-uniform III-adatom supply around the nanostructure. As the density can be as high as 10^8 cm^{-2}, significant competitions of adatoms occur among neighboring nanopillars. However, since the nanostructures have random orientations, one side of the pillar may experience more crowding effect than the other side, resulting in inhomogeneous growth rate. In the structure shown in Figure 4-10, GaAs is thinner in the lower half of the cross-section, which is likely to be a consequence of asymmetric resource competition. Furthermore, there are studies showing that the formation of m-planes is more energy favorable under high group-III supply while a-planes appear when group III supply is low [87]. A mix of a- and m-planes in the lower half of the core further confirm that group III supply is low on that side the nanopillar. As a result, the uneven group III adatom supply give rise to asymmetry in pillar shape and this can impact the optical cavity properties of the nanostructures.

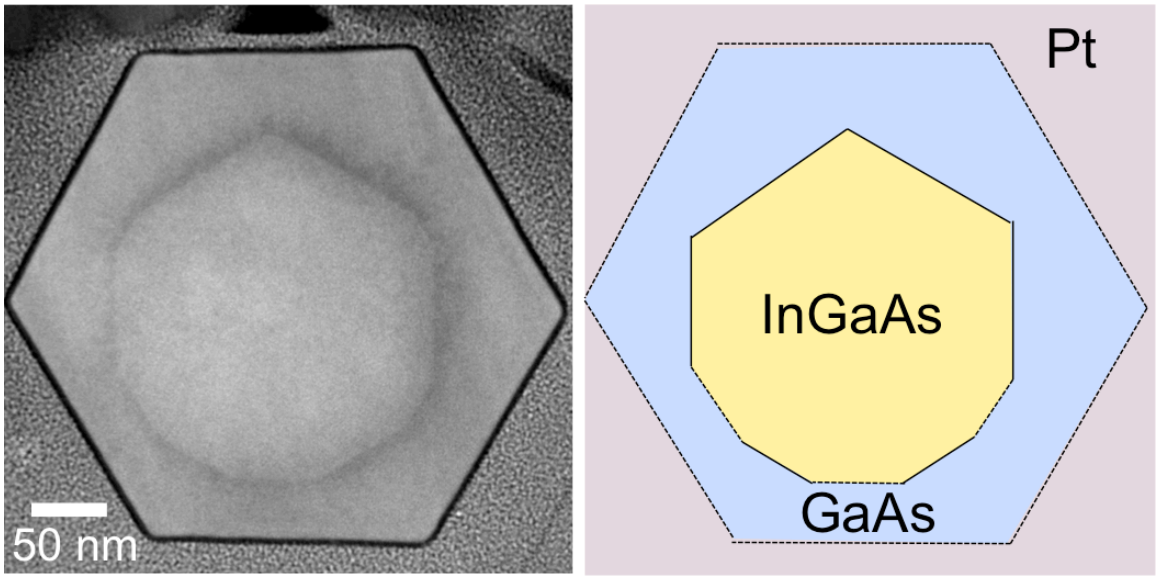

Figure 4-10 HAADF image of the transverse cross-section of a InGaAs/GaAs core-shell structure

Although there is an irregularity in the shape of the core, the quality of the crystal is not compromised. Figure 4-11(a) shows a HR-STEM image of InGaAs core along [0001].

The lattice assumes a honeycomb pattern, which is a distinctive feature of WZ phase crystal along [0001]. The difference in lattice along WZ [0001] and ZB [111] are displayed in Figure 4-12. The clear diffraction pattern in the inset of Figure 4-11(a) further confirms the crystal purity. At the InGaAs/GaAs interface, the honeycomb pattern continues seamlessly across the border without any noticeable misfit defects, as illustrated in Figure 4-11(b). This smooth transition across the hetero-interface is observed in the entire structure, independent of whether the border is an a-plane or m-plane. This observation confirms that the core-shell geometry indeed enables high-quality mismatched growth of layers exceeding the thin film critical thickness, no matter what substrate is being used.

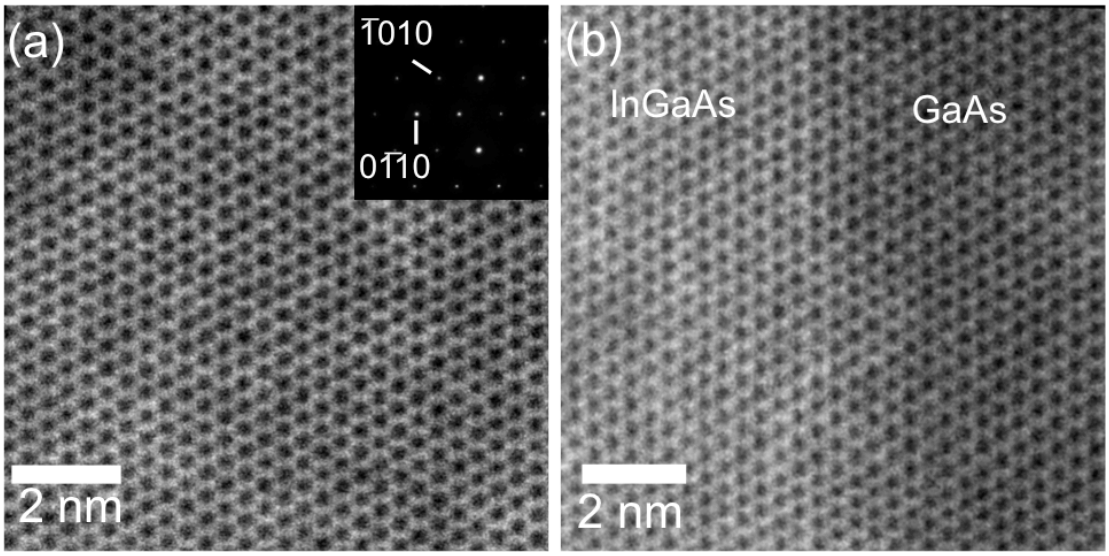

Figure 4-11 (a) HAADF image showing the honeycomb lattice of the wurtzite phase crystal (b) Lattice continues seamlessly across the InGaAs/GaAs interface

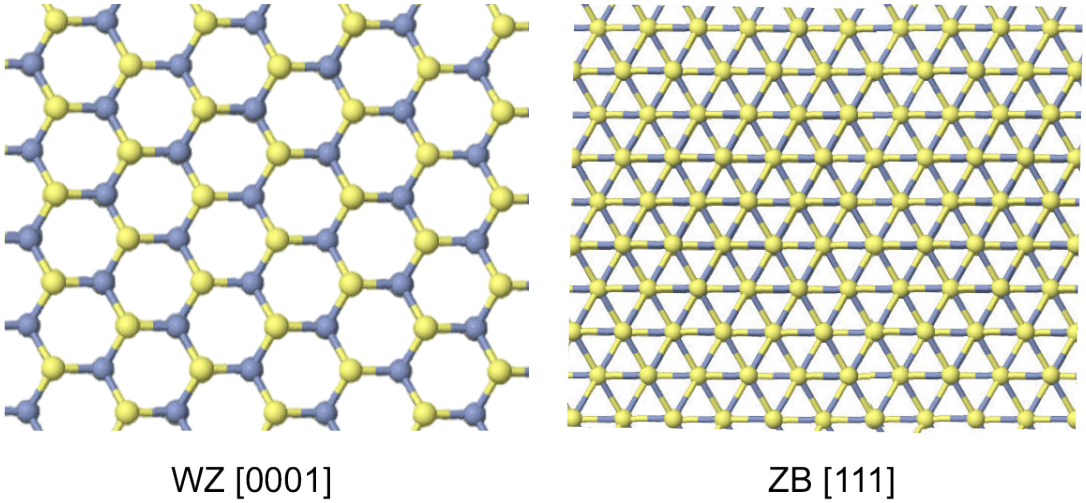

Figure 4-12 Schematics of lattice arrangements viewing along WZ [0001] and ZB [111]

Interface sharpness has significant impact on the optical properties of a nanostructure. We performed energy dispersive x-ray spectroscopy (EDS) to understand the compositional variation at the InGaAs/GaAs interface. Figure 4-13(a) shows the elemental maps of Ga, In and As of the interface depicted in the HAADF-STEM image. While As shows a uniform distribution over the entire area, a sharp cut off is observed in the In map at the hetero-interface. The Ga map also shows a subtle intensity change through the boundary, indicating the rise of Ga abundance from $In_{0.16}Ga_{0.84}As$ to GaAs. Figure 4-13(b) presents the quantitative profiles of the three elements in the area depicted in Figure 4-13(a). Indium composition drops abruptly at the hetero-interface with a transition of around 2 nm. We anticipate that the actual transition region is even thinner as the EDS resolution is limited by electron scattering in the sample. Nevertheless, this is one of the sharpest interfaces as characterized by EDS, to the best of our knowledge. These observations attest to the abruptness of the InGaAs/GaAs interface, which gives rise to excellent crystal quality of the nanostructures.

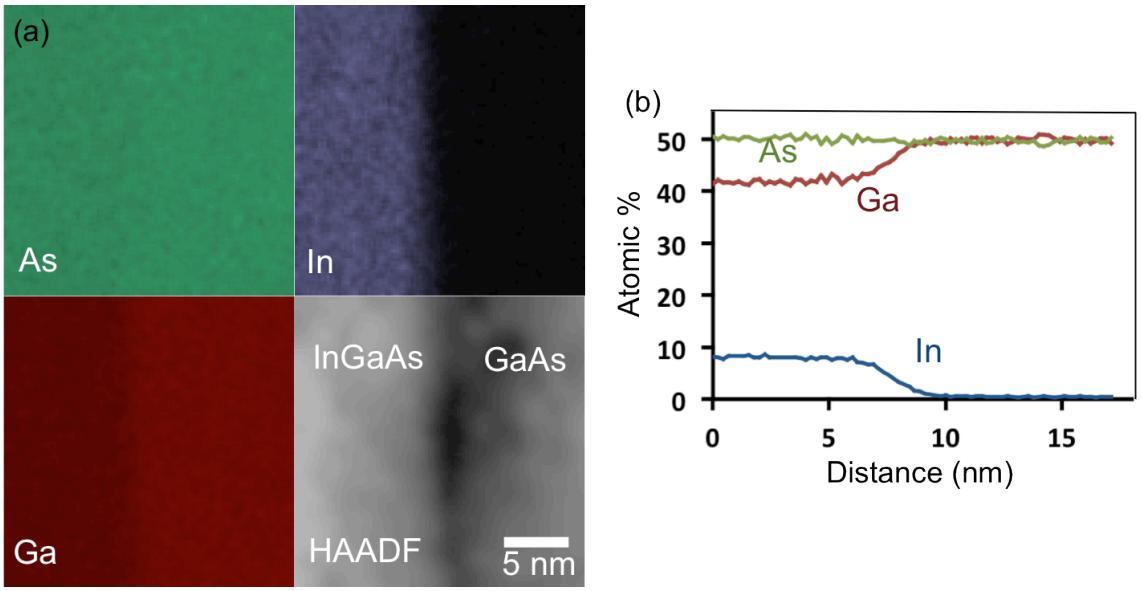

Figure 4-13 (a) Elemental EDS maps and HAADF-STEM image of an InGaAs/GaAs interface. (b) Element concentration line scan profiles across the hetero-interface shown in (a).

4.5 Lasing Action from As-grown Pillars on Poly-Si

With the excellent crystalline quality, lasing is achieved with both individual and ensemble InGaAs/GaAs nanopillars under optical pump at 4K with Ti:sapphire laser. Figure 4-14(a) shows the emission spectra of a standalone nanopillar under various pump powers. At low pump levels, spontaneous emission is observed with a peak wavelength near 920 nm. As the excitation power increases, a cavity mode emerges at around 895 nm, which finally reaches laser oscillation. Near field optical image for a standalone nanopillar laser above threshold is shown in inset. Lasing is attributed to a helically

propagating mode in which light spirals along the well-faceted hexagonal nanopillar [23], similar to what we discussed in Chapter 3. Although there is a detuning between gain and cavity mode, a 13dB side-mode suppression ratio is observed at 1.5 times threshold pump power (P_{th}). Figure 4-14(b) shows the output power and spectra linewidth as a function of pump power. Clear threshold behavior is observed in light output power and linewidth narrowing.

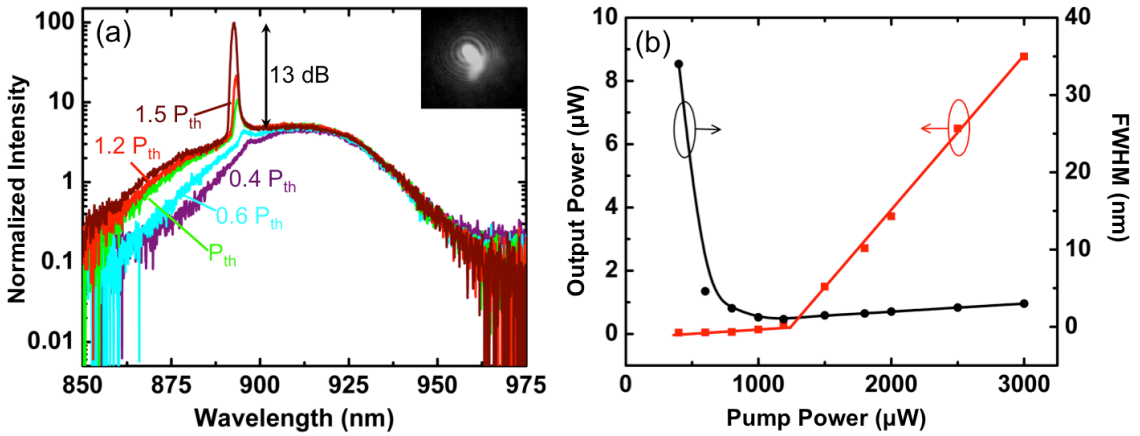

Figure 4-14 (a) Emission spectra from a standalone nanopillar under different pump powers (b) Dependence of output power and linewidth on pump power

Lasing is achieved with nanopillar ensemble for the first time in arsenide material system, as seen in Figure 4-15(a). Unlike single pillar laser, spontaneous emission increases linearly with pump power even above lasing threshold. As the pillar density is high in the ensemble, multiple pillars are excited at the same time upon optical pump. The nanopillars in the ensemble have much smaller diameters and, hence, lower optical quality factors than those of the standalone pillars. Furthermore, the high density results in crossing of nanopillars as seen in Figure 4-2. Helically propagation of light in single needle is likely to be disturbed by the high density. Here, we believe that lasing is attributed to scattered feedback from multiple pillars, similar to the random lasing effect. [88-89] As a result, spontaneous emission is not clamped above threshold. In fact, spontaneous emission increases linearly with pump power, as depicted in Figure 4-15(b). Side mode suppression ratio reaches 12 dB at a rather high pump power level of $4P_{th}$, considerably higher than standalone nanopillar laser. However, the lasing threshold is also significantly lower. Near field optical image of the ensemble laser is shown in the inset. Significant coherent speckle, as seen in Figure 4-15(c), is observed due to scattering from multiple pillars, which is also distinct from that of standalone pillar laser. Clear threshold behavior is observed in the pump power dependence of light output power, as seen in Figure 4-15(d). Linewidth reduces by over 30 times near and above the threshold, attesting the wavelength coherency of the laser emission. These exciting results reveal the excellent optical properties of these nanostructures and underscore their potential usefulness as efficient optical components that can be integrated inexpensively with various substrates or carriers.

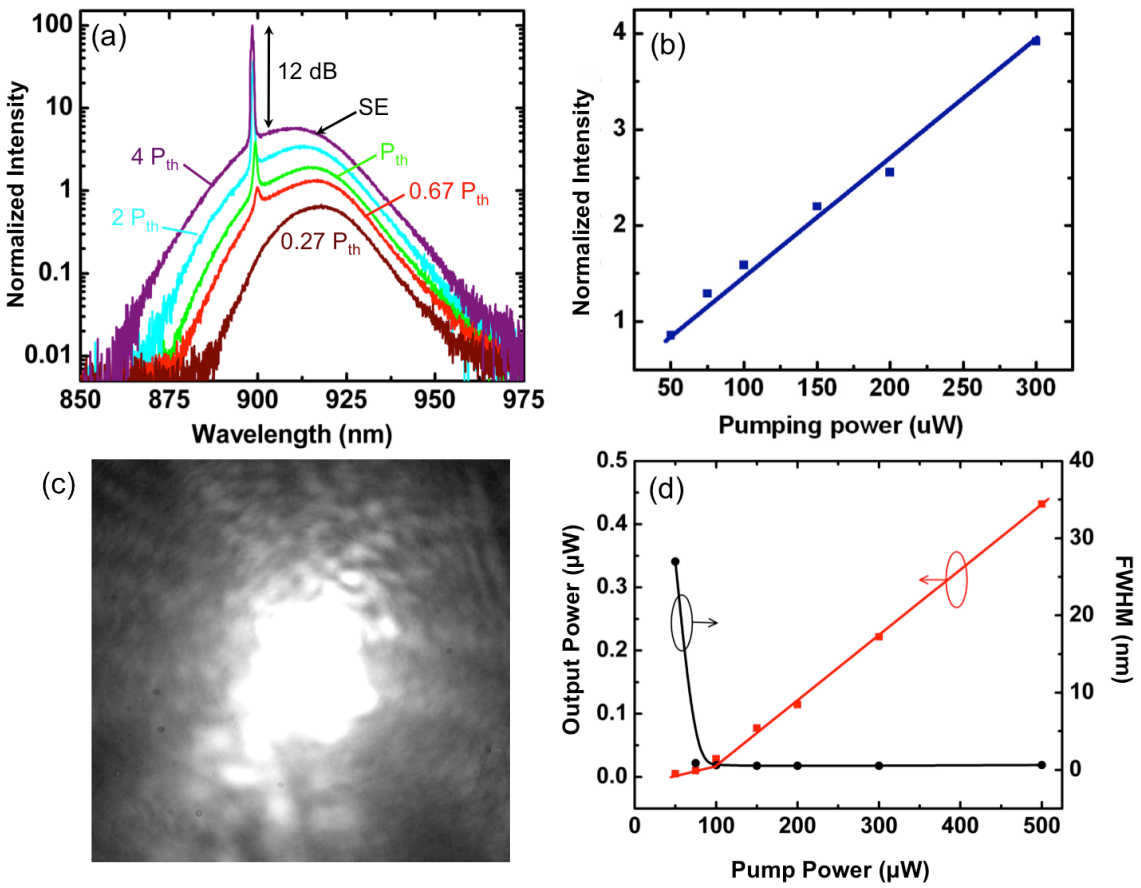

Figure 4-15 (a) Emission spectra from a nanopillar ensemble under different pump powers. Dependences of (b) Spontaneous emission and (d) output power and linewidth on pump power. (c) Speckle pattern observed from near field above threshold

4.6 Summary

In this chapter, we demonstrated the growth of single crystalline InGaAs/GaAs pillars on polycrystalline silicon. The pillar base diameter approaches a micron, which is far greater than the substrate crystal grain size. With the inverse tapering at the base, the effective footprint of the nanostructure is reduced to below 40 nm in diameter. The small contact area prevents the III-V crystal from nucleating on top of multiple grains in the substrate and minimizes stress in the system due to lattice mismatch. In fact, the small footprint lowers the grain size requirement on the poly-Si film or substrate and this can potentially lower the production cost. The special crystal alignment between InGaAs and Si facilitates formation of misfit dislocations at the interface, thus allowing the growth of stacking fault free III-V crystal on poly-Si. Although asymmetry is observed in the core-shell configuration, the lattice is highly coherent across the hetero-interface. In addition, EDS shows that the hetero-interface has an abrupt composition profile, which is crucial to carrier confinement in the structure. Lasing is demonstrated upon optical pump, attesting

the excellent crystal and optical quality of the as-grown nanostructures. These properties reveal the potential of these nanostructures to be used for various optoelectronic applications. The results presented in this work open up a pathway for low-cost synergy of III-V based optoelectronics with many technologies, e.g. TFT and nanofluidics, via poly-Si as a bridging platform.

Chapter 5 High-quality Growth of InP pillars on Silicon

In the last two chapters, we have discussed how the characteristic core-shell growth can bring about monolithic integration of high-quality InGaAs nanostructures on silicon and poly-silicon, in spite of the lattice mismatch and lack of long-range crystalline coherency. Electrical devices with promising performances are thereby realized. Obtaining excellent crystal quality is only the first step to achieve high-performance opto-electronic devices. Proper bandgap and refractive index engineering is crucial in optimizing the electrical and optical behaviors of the device. Arsenide material system alone simply cannot provide the capability for optimizations in all these dimensions. Therefore, it is highly desirable to extend the extraordinary growth mechanism to other III-V material systems.

Among all the III-V materials, InP is one of the most important building blocks for realizing hetero-junction devices. In fact, InP based alloys are widely used as growth templates, optical cladding layers, and active layers in long wavelength optoelectronic devices for silicon-transparent applications. Most importantly, InP has as much as 100 times lower surface recombination velocity than GaAs-based materials [90-91]. These unique properties make InP an ideal candidate for surface passivation as well as solar cell applications. Previously, InP nanowires grown on silicon have been reported using gold or indium as catalyst [19-20, 92]. However, high crystal phase purity can only be achieved when the nanowire diameter is smaller than a critical value of ~ 40 nm. The small size increases the surface-to-volume ratio, making the nanostructure more vulnerable to surface recombination. Hence, the growth of high-quality, micron-sized structures on silicon is of great importance.

In this chapter, we demonstrate the growth of high-quality InP-based nanostructures on silicon with base diameter approaching a micron. Unlike arsenide-based nanoneedles, InP nanopillars exhibit strong crystal phase dependence on growth temperature. The crystal phase evolves from a mixture of both wurtzite (WZ) and zincblende (ZB) to pure WZ as the growth temperature rises from 415 ^{o}C to 455 ^{o}C. This is attested by both direct crystal phase inspection with transmission electron microscopy (TEM) and the emergence of type-II emissions in photoluminescence (PL). The InP/Si hetero-interface is examined with high-resolution TEM (HRTEM) to study how InP nucleates on Si. Interestingly, InP nanopillars do not possess any inverse tapering at the base because of the absence of polycrystalline InP film. The 8% lattice mismatch is relaxed via the formation of periodic misfit dislocations at the hetero-interface. The bulk material well above the hetero-interface is of excellent crystalline quality. Lasing action is observed in as-grown InP nanopillars on Si under optical pump. To achieve long-wavelength emission, InP hetero-structures with InGaAs multiple quantum wells are synthesized. Clear core-shell architecture can be seen under high angle annular dark field (HAADF) imaging. Since there is no inverse tapering at the base, the entire heterostructure is in contact with the substrate. To remove the shunt path which would otherwise short out the diode, a two-step regrowth process is developed to isolate the shell from the substrate. Excellent diode

behavior is observed with devices fabricated from the re-grown structures. Finally, we studied the possibility of controlling the site of InP nanopillar nucleation. The synergy of phosphides and arsenides on silicon promises new functionalities and design capabilities that can never be attained by individual material systems.

5.1 Synthesis of InP Nanostructures on Silicon

InP nanopillars are grown on (111) Si substrate with low temperature metalorganic chemical vapor deposition (MOCVD). Similar to the growth of InGaAs nanopillars, surface roughening is of ultimate importance for nucleation. In the growth of InP pillars, conventional mechanical roughening was first utilized to create natural oxide on the freshly exposed silicon surface. The nanostructure density, however, is far worse than the case of InGaAs, probably due to the much higher indium adatom mobility than gallium. Another technique is therefore developed to increase the density. Instead of random oxidation, silicon dioxide is deposited and patterned on the substrate using photolithography. The substrate is then dipped into tetramethylammonium hydroxide (TMAH) for anisotropic etch. At temperatures above 85 ^{o}C, TMAH roughens silicon surface nanoscopically, creating silicon terraces on the surface [93]. The substrate is then cleaned with acetone and methanol to remove any organic contaminants. A short dip in buffered oxide etchant (BOE) is applied to remove any native oxide on top of the exposed silicon area. The growth is carried out in an Emcore D75 MOCVD system, at growth temperatures varying from 415 ^{o}C to 455 ^{o}C. Tertiary-butyl phosphine (TBP) and Trimethylindium (TMIn) are used as the precursors for phosphorus and indium, respectively. TBP is pre-flown into the reactor during temperature ramp-up. Upon temperature stabilization, TMIn is introduced into the chamber to start the growth. With a constant total flow rate of 12 SLM, the mole fractions of TBP and TMIn are held at 5.9×10^{-4} and 4.73×10^{-6}, respectively. Unless otherwise specified, the growth duration is kept constant at 15 minutes.

Figure 5-1 displays scanning electron microscope (SEM) images of InP nanostructures grown at 415 ^{o}C. Instead of upright nanoneedles or nanopillars, InP grows into nanowires that ‘crawl’ on the substrate surface. In particular, the nanowires possess weird shapes and do not exhibit specific crystal facets, as seen in Figure 5-1(b). We believe the growth assumes a vapor-liquid-solid (VLS) mechanism in which indium droplets act as catalysts for the nanowire growth. At elevated temperature, the indium catalysts diffuse along random routes on the substrate, resulting in the curly appearance of the nanowires. This VLS growth comes as a consequence of very low phosphorus partial pressure inside the chamber. At 415 ^{o}C, the cracking efficiency of TBP into active phosphorus radicals can be as low as 10% [94]. Such low phosphorus supply favors the formation of indium metal droplets for VLS growth.

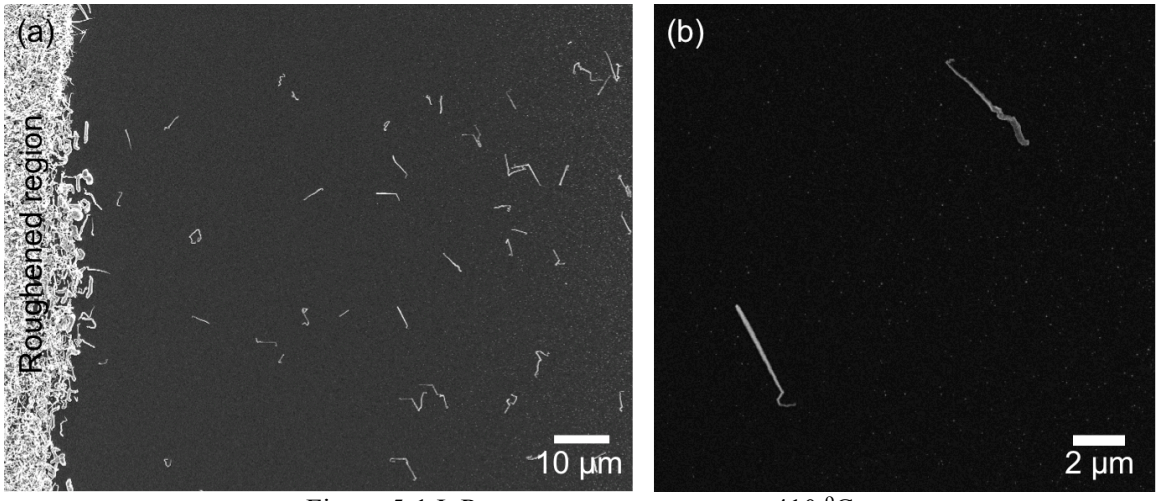

Figure 5-1 InP nanostructures grown at 410 ^{o}C

As the growth temperature increases, InP evolves into nanoneedles with clear hexagonal facets. Figure 5-2 show some typical nanostructures grown at 425 ^{o}C, 435 ^{o}C and 455 ^{o}C. We note that the nanoneedle grown at 425 ^{o}C is much longer and has a smaller taper angle than the other two. Since the cracking efficiency of TBP is still low at 425 ^{o}C, the growth is still in phosphorus deficient regime. A low group V condition favors diffusion of indium towards the tip, resulting in ultra-fast vertical growth. This leads to the observed small tapering and long length in nanoneedles grown at 425 ^{o}C.

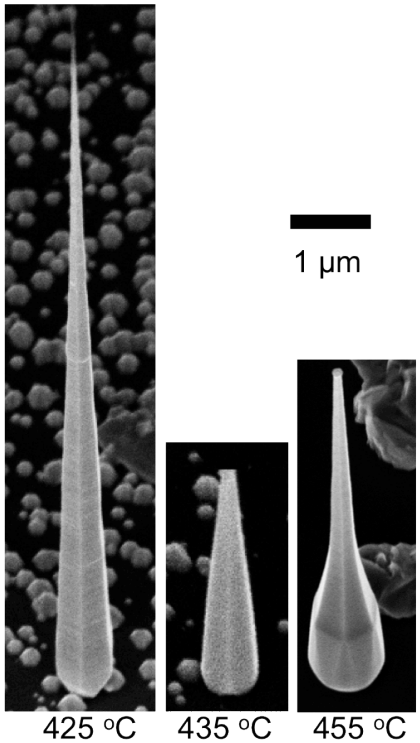

Figure 5-2 InP nanostructures grown at various temperatures

This extremely fast growth rate along [0001], however, results in 'wrinkles' on the needle sidewall, which are likely related to defects. The surface roughness disappears as the growth temperature increases to 455 ^{o}C. Such observation suggests that a higher growth temperature gives rise to better crystalline quality, which is to be further confirmed with TEM analysis in the next session.

In the growth of arsenide-based nanostructure, a continuous poly-InGaAs film forms over the entire wafer as a by-product of the high-quality nanoneedle growth. The polycrystalline film confines the expansion of the base, leading to inverse tapering at the root. In the growth of InP, however, only isolated islands appear around the nanoneedles, as observed in Figure 5-2. This is probably due to the large lattice mismatch (~8%), which disfavors the wetting of InP on silicon. In a 15-minute growth, the base diameter of InP reaches ~ 800 nm, which is more than 4 times bigger than InGaAs nanoneedles grown for the same duration. This is a consequence of the high indium adatom mobility which facilitates ripening of sparsely distributed islands and nanoneedles rather than continuous film formation. Without the confinement from a poly-InP film, the entire InP nanoneedle is sitting on top of the substrate with a footprint as large as the base diameter. This geometry results in an alternative stress relaxing mechanism in InP nanoneedles/nanopillars, as will be discussed in the following sections.

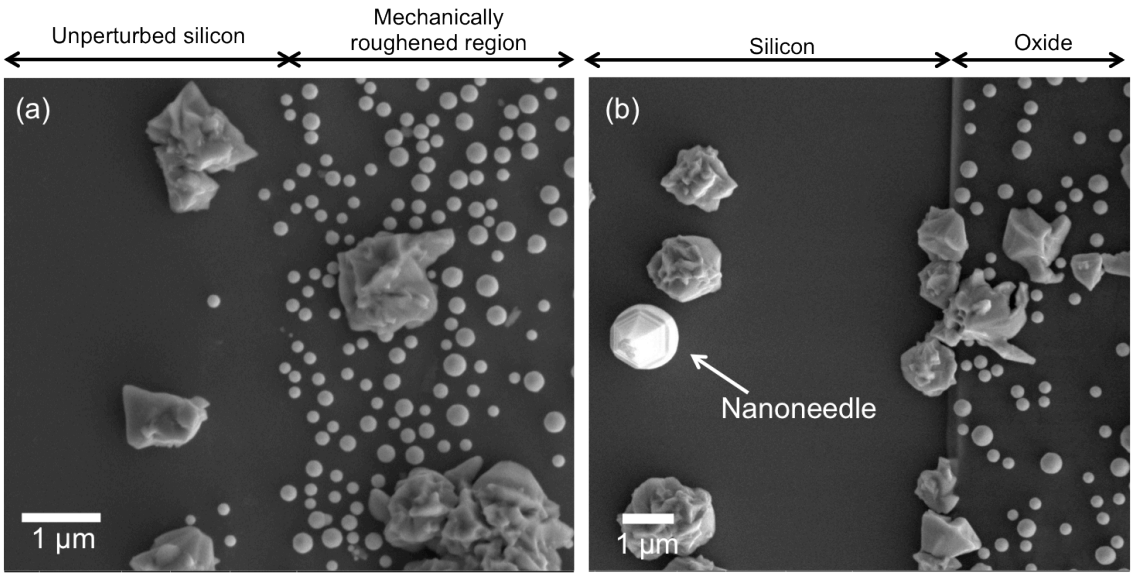

Figure 5-3 Presence of indium balls on (a) mechanically roughened region (b) patterned oxide region.

In Chapter 3, we observed from TEM and growth experiments that the nucleation of InGaAs nanoneedles is initiated by metal nano-clusters. However, there is no direct observation that metal clusters really form on the roughened region. This is because InGaAs wets silicon very well even if the surface is roughened. The growth of InP, on the other hand, shows a different behavior. Although conventional mechanical roughening cannot yield high density of InP nanoneedles, metal balls are clearly seen on the

roughened regions, as displayed in Figure 5-3(a). With the new surface-roughening scheme, the same metal droplets are observed as well on the oxide patterns (see Figure 5-3(b)). Energy dispersive spectroscopy (EDS) in Figure 5-4 confirms that the balls are indeed elemental indium instead of InP crystallites. Furthermore, InP needle density exhibits strong correlation with the abundance of indium balls on the oxide – decent needle density is usually found next to area with abundant indium balls, and vice versa (see Figure 5-5). These observations reveal that the formation of metal nano-clusters does play an important role in the nucleation of high-quality nanostructures.

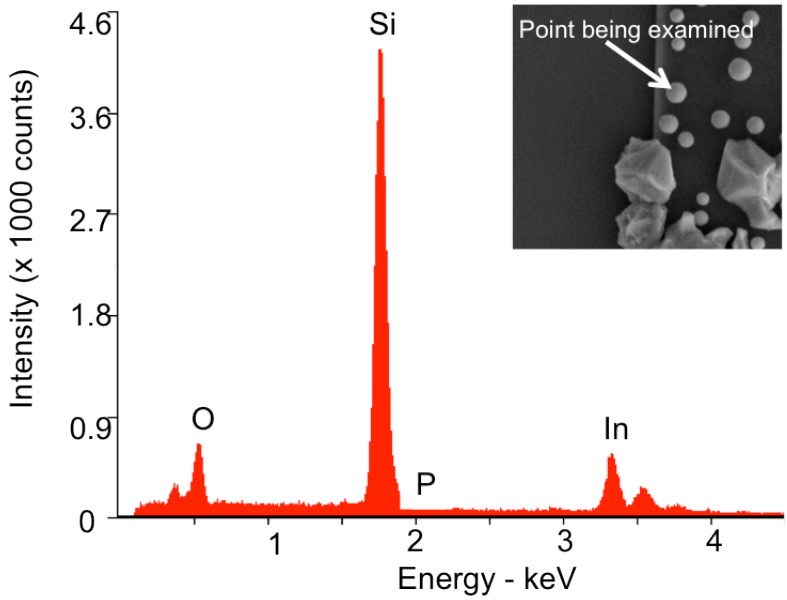

Figure 5-4 EDS spectra taken at a ball structure sitting on SiO_2. Signal from phosphorus is absent.

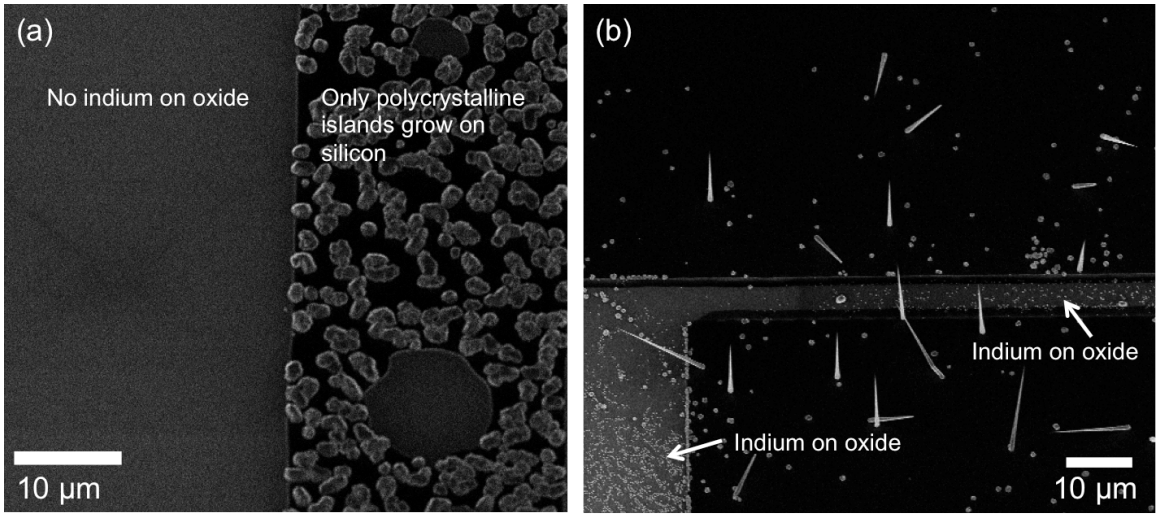

Figure 5-5 SEM images illustrating how the abundance of indium affects the nucleation of InP nanopillars

While both patterned oxide and mechanically roughened surface facilitates the formation of indium balls, only the former case can yield reasonable density of InP nanostructures. The reason for the discrepancy is the extra TMAH etch that is present only in the former case. TMAH etches silicon anisotropically and at the same time roughens the surface nanoscopically. We believe that the growth of InP starts with the formation of indium nano-clusters on the patterned oxide, followed by diffusion of these clusters onto the bare silicon surface. The terraces formed during TMAH etch trap the nano-clusters, which subsequently react with phosphorus to form InP. In fact, many nanopillars are observed to nucleate directly on a terrace, like the one shown in Figure 5-6. In the absence of surface roughness, indium balls can diffuse over long distance and aggregate to form big clusters. Once the size exceeds a certain value, indium clusters turn into poly-crystalline islands instead of single crystalline InP nanoneedle. This metal initiated growth is very similar to the nucleation of InGaAs nanopillars. We will show in section 5.3 that InP nanopillars indeed assume core-shell growth mode which is exactly the same as their InGaAs counterparts.

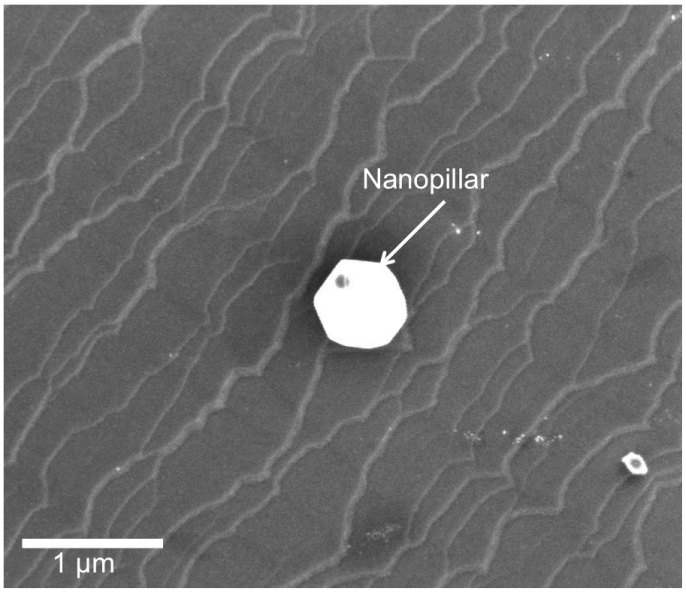

Figure 5-6 InP nanopillar growing on a silicon terrace

5.2 Crystal Phase Dependence on Growth Temperature

Crystal quality plays a very important role in the electrical and optical performances of the nanostructures. In this section, we study the crystal purity of InP nanoneedles grown at various temperatures with TEM. Sample preparation involves either direct 'wipe-down' of nanoneedles onto a TEM grid or lamella lift-out with the use of focused ion beam (FIB). Figure 5-7(a) shows a bright field (BF) TEM image of a wiped-down

nanoneedle grown at 425 °C. HRTEM image in Figure 5-7(b) shows that the lattice assumes an ABCA stacking, which is a signature of ZB lattice arrangement. The diffraction pattern along [1$\bar{1}$0] in Figure 5-7(c) further confirms the ZB nature of the crystal. Interestingly, the needle is growing along the [002] direction instead of [111]. Such uncommon growth is probably due to the low growth temperature and group V deficiency.

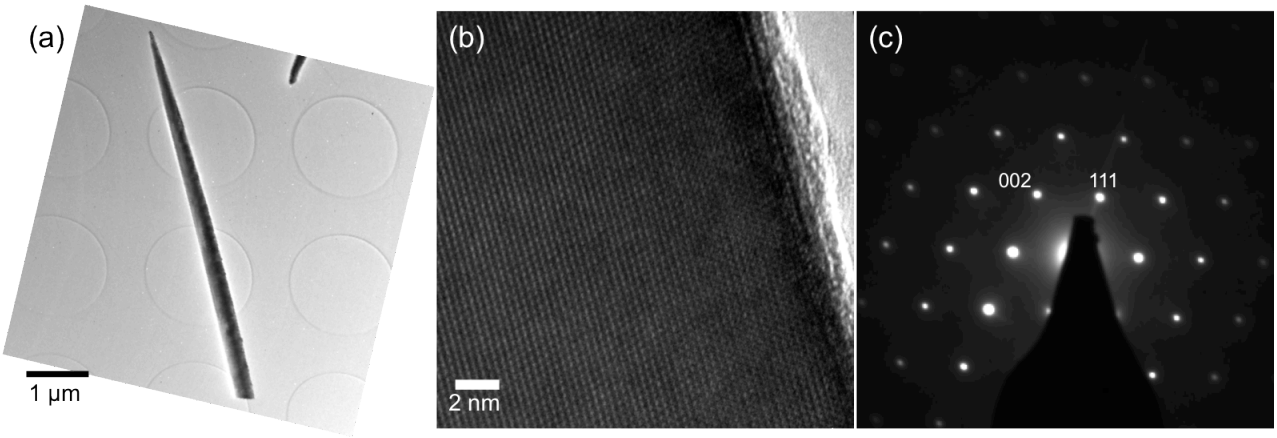

Figure 5-7 TEM images and diffraction pattern of a ZB nanoneedle grown at 425 °C

While some nanoneedles possess pure ZB phase and grow along [001] direction, most nanoneedles grown at 425 °C are polytypic. Figure 5-8(a) shows a HAADF image of an upright nanoneedle growing along Si [111] direction. The base diameter of this particular needle approaches a micron. As seen in Figure 5-2, upright nanoneedles grown at 425 °C have rather rough sidewalls, which is a first indication that there are defects in the structure. Indeed, high density of stacking disorders is present in the needle body, as observed in Figure 5-8(b). HRTEM image (see Figure 5-9(a)) shows that the crystal is composed of a mixture of WZ phase (~ 50%) and ZB phase with significant twinning. The polytypic nature can also be observed form the diffraction pattern. Diffraction pattern is a representation of the lattice in the spatial frequency domain. A single crystal always exhibits a single set of periodic spots that can be clearly discernable. A mis-stacked layer can be considered as an impulse function added onto the originally periodic lattice. According to Fourier transform theory, an impulse is represented by the superposition of all spatial frequencies with equal amplitudes. This translates to straight lines in the diffraction pattern that run along the direction perpendicular to the mis-stacked layer itself, i.e. along [0001]. In addition, the intensity of these streaky lines in the spatial frequency domain increases with more occurrences of mis-stacked layers. The clear streaky lines along [0001] on top of the WZ diffraction pattern in Figure 5-9(b) therefore show that high density of stacking disorders are present in the crystal. Stacking faults are known to cause carrier trapping and excess carrier scattering [95-96]. Hence, the corrupted crystal purity depreciates the usefulness of these nanostructures for opto-electronic applications.

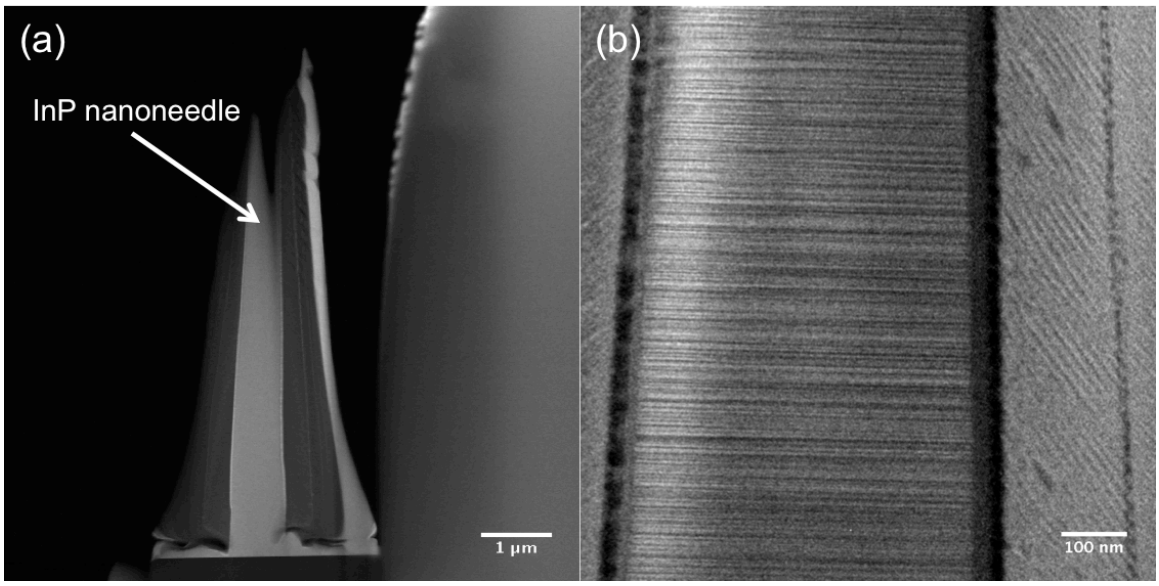

Figure 5-8 (a) HAADF image of an upright nanoneedle (b) BF-TEM showing high density of stacking faults in the body

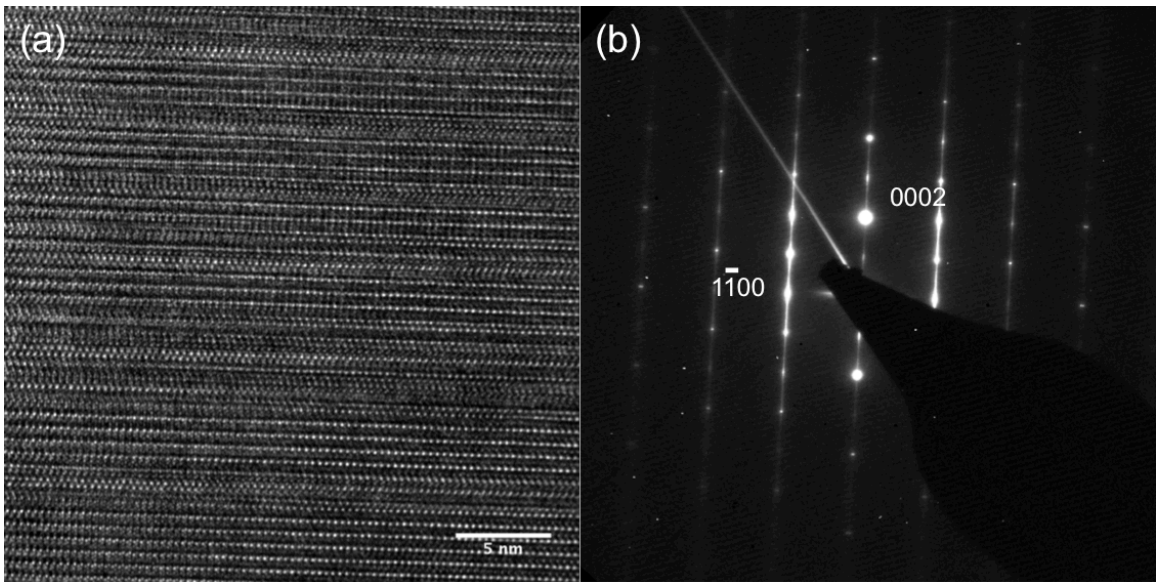

Figure 5-9 (a) HRTEM showing stacking disorders in the lattice (b) Diffraction pattern with streaky lines running along [0001] indicating significant polytypism

As the growth temperature increases to above 450 ^{o}C, InP nanopillars become pure WZ phase. Figure 5-10(a) shows a BF-TEM image of an InP nanopillar grown at 455 ^{o}C. The pillar is aligned such that the crystal is exactly on $[11\bar{2}0]$ zone axis. Under this condition, the nanostructure appears to be free of any stacking defects, as horizontal streaky lines are completely absent along the entire pillar. However, it is possible that the defects are masked by the thickness of the pillar, which can be over 800 nm. We therefore tilt the

pillar away from the exact [$11\bar{2}0$] zone axis along the [0001] direction. As observed in Figure 5-10(b), horizontally terminated stacking disorders do appear in the bulk of the pillar under the new alignment. However, the stacking fault density is much lower than that in nanoneedles grown at 425 ^{o}C. The clear diffraction pattern in Figure 5-10(c) and the characteristic ABAB lattice arrangement of the crystal displayed in Figure 5-10(d) further confirms the excellent WZ crystal phase purity of the pillar. With 8% lattice mismatch between InP and silicon, it is remarkable that the bulk of the nanopillar can remain single crystalline even when the base diameter approaches a micron. While the pillar body possesses brilliant crystal quality, the bottommost ~ 500 nm is populated with high density of stacking faults. This can be observed from the thick dark band at the pillar base in Figure 5-10(b). We attribute this to the ultra fast growth rate of the pillar during the early stage of the growth due to very long diffusion length of indium adatoms. In section 5.4, we will examine the base and the hetero-interface in details.

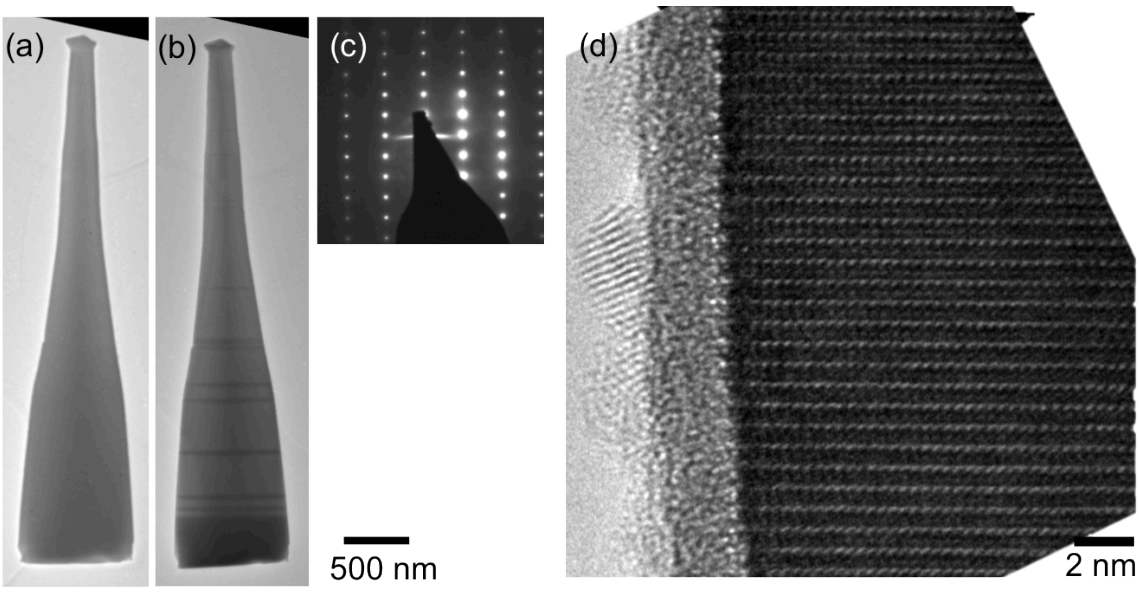

Figure 5-10 BF-TEM of an InP pillar aligned (a) on [$11\bar{2}0$] zone axis (b) slightly off [$11\bar{2}0$] zone axis. Wurtzite crystal phase is observed from (c) diffraction pattern and (d) ABAB stacking sequence in HRTEM image.

In addition to direct inspection with TEM, the crystal phase dependence on growth temperature can also be observed from optical characterization. Studies have shown that WZ-InP has a bandgap energy ~ 80 meV larger than that of ZB-InP despite the same chemical composition [97-98]. What makes it more interesting is that WZ- and ZB-InP exhibit a type-II band alignment, as illustrated in the schematic in Figure 5-11(a). Upon optical excitation, the barriers at the type-II junction effectively trap electrons and holes at the ZB- and WZ-InP, respectively. The spatially separated charge carriers create electric field that subsequently bends the energy bands at the junction, as shown in Figure 5-11(b). This energy band modification brings about blue-shift in the emission from this type-II configuration due to energy quantization effect [99]. We note that this band-

bending effect is very sensitive to the concentration of excited carriers, which in turn depends on pump power. Thus, type-II emission demonstrates significant blue shift with increasing pump power. This phenomenon can hence be used to estimate the stacking fault density in a nanostructure.

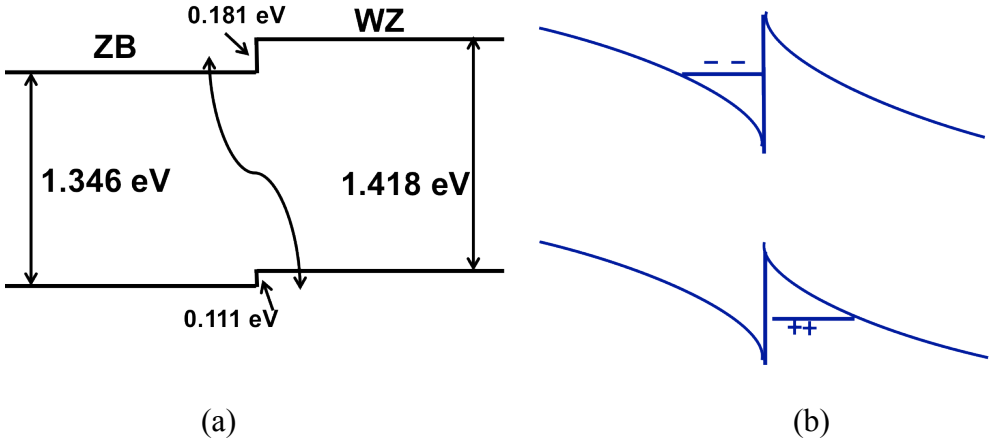

Figure 5-11 (a) Band diagram illustrating the type-II alignment between ZB- and WZ-InP at 0 K (b) Space charge creates E-field that bends the energy bands near the junction upon optical excitation.

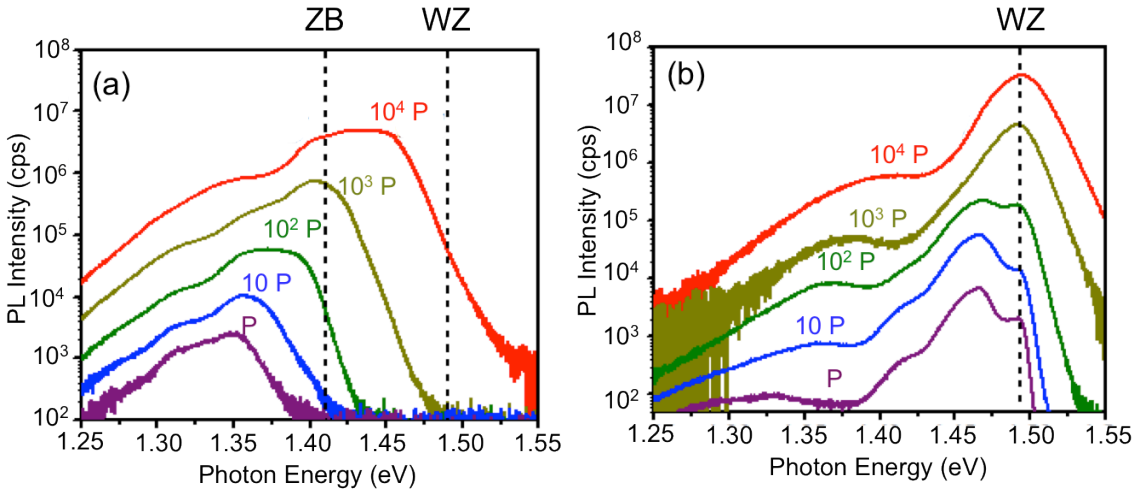

Figure 5-12 Emission spectra of InP nanostructures grown at (a) 425°C (b) 450°C, under various pump power levels

Figures 5-12(a) and (b) show some emission spectra obtained from typical InP nanostructures grown at 425 °C and 450 °C, respectively. Measurements were done at 4 K with a continuous wave (CW) pump diode laser operating at 660 nm to minimize wavelength shift due to band filling effect. We pumped the nanostructures at various

power levels, from P (318 mW/cm^2) to 10^4 P, to observe the change in their emission behaviors. As the pump level increases, the emission photon energy of the 425 ^{o}C-grown nanoneedle (Figure 5-12(a)) reveals a large blue shift of 110 meV. Such prominent blue shift originates from the type-II band alignment, attesting the high density of stacking disorders in the nanoneedle. On the other hand, 450 ^{o}C-grown nanoneedle shows a very stable peak emission energy at ~ 1.49 eV, i.e. the bandgap emission from WZ-InP, under the same power series. These results confirm that InP nanostructures indeed evolve from polytypic to pure WZ phase when the growth temperature increases to over 450 ^{o}C.

Although emissions from type-II architecture show an interesting pump power dependence, carrier trapping and excess carrier scattering due to stacking faults can be detrimental to the electrical properties of the nanostructure. Pure WZ-InP nanopillars grown above 450^{o}C, on the other hand, reveal great potential in the realization of high-performing opto-electronics devices on silicon. Therefore, we will focus on studying the growth of InP nanostructures at 455 ^{o}C in the following sections.

5.3 Core-Shell Growth of InP/InGaAs Multiple Quantum Wells

In the last two sections, we observed that the nucleation of InP nanostructures is initiated by trapping of indium nano-clusters diffusing from the oxide region. In addition, InP nanopillars grown at above 450 ^{o}C remain single crystalline even when the base diameter approaches a micron, which is over 20 times larger than the critical diameter for VLS nanowires. These extraordinary properties, which are also exhibited by InGaAs nanostructures, indicate that InP nanopillars evolve in the same characteristic core-shell growth mode. To prove that this is indeed the case, we synthesize InP/InGaAs/InP multiple quantum well (MQW) structures and examine the traverse cross-sections with HAADF imaging. The hetero-structure starts with an InP core with base diameter ~ 500 nm, followed by the MQW region and finally capped with 50 nm InP. The growth durations of each InGaAs well and InP barrier in the MQW were kept at 30 seconds, with growth temperature held constant at 455 ^{o}C for the entire structure. The alloy composition of each quantum well (QW) is designed to be around $In_{0.4}Ga_{0.6}As$ so that the emission wavelength would be close to 1310 nm, the regime for optical communication. After the growth, thin slices are cut horizontally to expose the (0001) facets, following the same procedures outlined in section 3-8.

Figures 5-13(a)-(c) shows three traverse cross-sections of nanopillars with 1, 2 and 5 quantum wells, respectively. Since arsenide has a much higher atomic number than phosphorus, InGaAs appears to be much brighter than InP in the HAADF images. The InGaAs QWs are found to be completely concentric in all three cross-sections. This 'tree-ring' growth clearly proves that InP nanopillars are truly evolving in a core-shell growth mechanism that is exactly the same as their InGaAs counterparts.

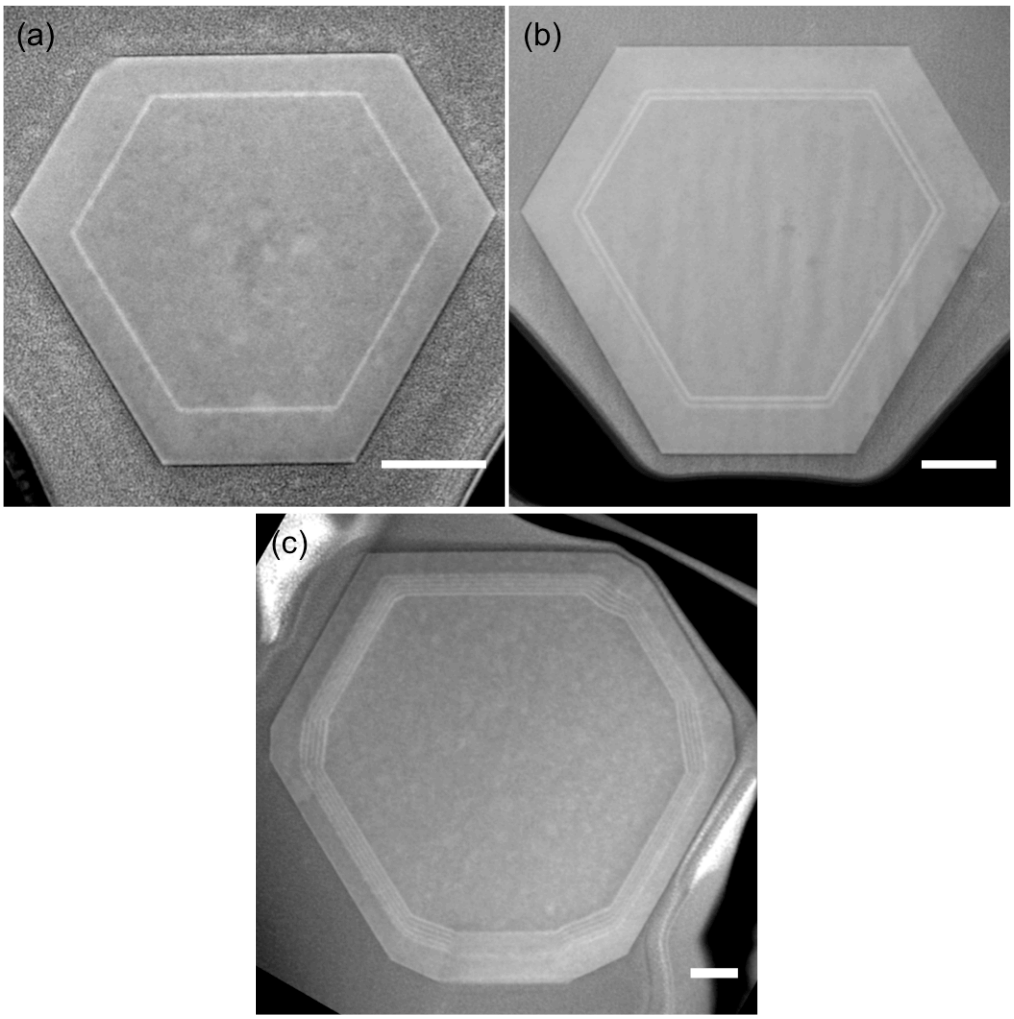

Figure 5-13 HAADF images of InP/InGaAs/InP structures with (a) 1 (b) 2 and (c) 5 quantum wells revealing the core-shell growth mode. Scale bars are 100 nm.

In addition to the concentric growth, one can observe that the cross sections have rather irregular shapes. We attribute this to the polytypic region at the nanopillar base. As mentioned before, the cracking efficiency of TBP is rather low at temperature ranging from 425~460 ^{o}C. The growth is therefore under a slightly phosphorus-deficient condition. In the polytypic region, ZB segments terminate as polar $\{\bar{2}11\}$ planes at the sidewalls. A low phosphorus environment disfavors the formation of phosphorus-rich $\{\bar{2}11\}$B planes. This results in an asymmetric hexagonal geometry at the base, with the three $\{\bar{2}11\}$A planes larger than the other three $\{\bar{2}11\}$B planes. This asymmetry propagates up to the pure WZ crystal in the pillar body, hence leading to the observed irregular shape in Figure 5-13. Further investigations are required to study how the shape of the InP nanopillars is affected by growth conditions.

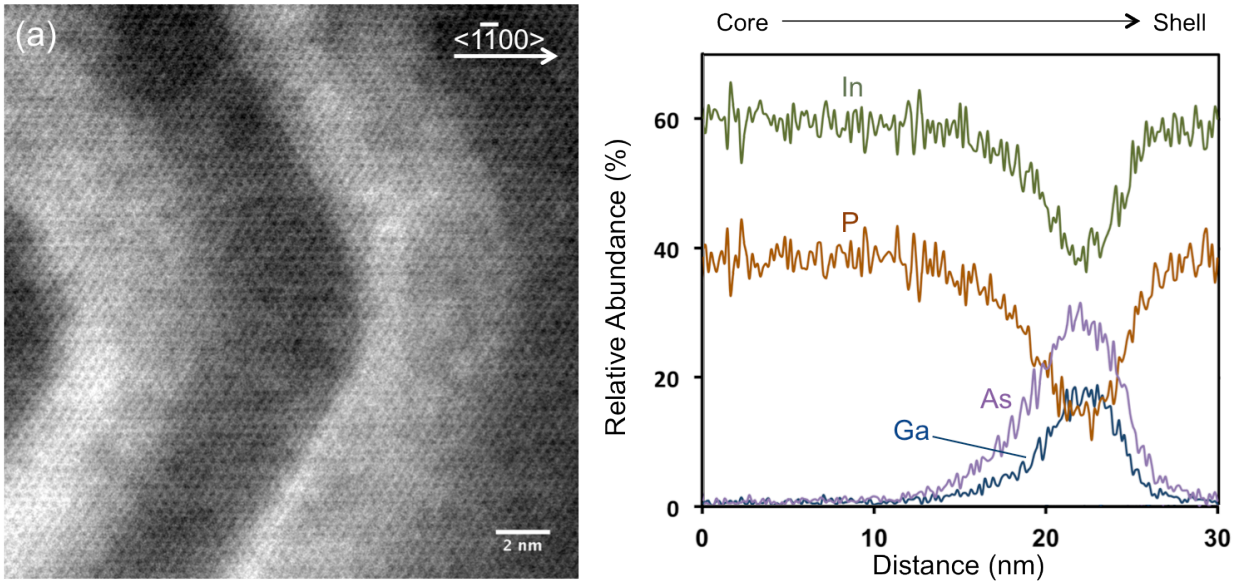

Figure 5-14 (a) HAADF image showing coherent lattice across the hetero-structure (b) EDS line scan profiles of elements of interest across an InP/InGaAs QW

InGaAs QW is used not only as a tag layer to study the growth mechanism, but also as the active region for light emission. Studying the crystal quality in the quantum well region is therefore of utmost importance. Figure 5-14(a) displays a high-resolution HAADF image taken at the right corner of the double QW structure depicted in Figure 5-13(b). Characteristic honeycomb lattice arrangement is seen to continue seamlessly throughout the InGaAs and InP layers. This observation indicates that the entire hetero-structure exhibits coherent WZ structure, which is crucial for efficient light emission. Unlike InGaAs nanopillars studied in Chapter 3, InGaAs QWs do not exhibit natural alloy composition ordering along <1$\bar{1}$00>, i.e. at the sharp corner in Figure 5-14(a). This is probably due to the surface energy of InP being different from InGaAs, thus perturbing the adatom diffusion behavior on the {1$\bar{1}$00} facets. However, we do observe a non-uniform intensity profile across the InGaAs QW along the radial growth direction. To be specific, the inner side of the QW (i.e. the InP→InGaAs interface) is brighter than the outer side (i.e. the InGaAs→InP interface) of the layer. This indicates a possible uneven distribution of alloy composition across the quantum well. Figure 5-14(b) shows an EDS line scan through a quantum well along the radial growth direction. While Ga and As are completely absent, the In/P ratio is 6:4 rather than the stoichiometric 1:1 in the InP barrier. We attribute this to the inaccuracy of the Cliff-Lorimer coefficients due to the large sample thickness [100]. Although the absolute value of the abundances may not be precise, the trends of the line-scans do reflect the actual elemental distribution profiles across the quantum well. One can observe that all elements exhibit asymmetric profile across the quantum well. Specifically, the downward transition of indium and phosphorus at the InP→InGaAs interface is much more gentle than the rising edge at the InGaAs→InP interface. The reverse tendency is observed in the Ga and As profiles – a slow rise followed by a sharp drop along the radial growth direction. In particular, the upswing of As is faster than that of Ga at the InP→InGaAs interface. This suggests that the InP→InGaAs side of the QW contains have higher arsenic composition than the other

interface. These observations agree well with the z-contrast image in which more heavy elements are present at the QW inner side. Such composition variation may be attributed to the inter-mixing of phosphide and arsenide at the InP→InGaAs interface. Since InP has a much lower decomposition temperature (~380 ^{o}C) than InGaAs (> 500 ^{o}C), arsenide has a strong tendency to replace phosphorus, but not the other way around [101-102]. On the other hand, group III elements are not as active in inter-diffusion as group V elements [103]. These factors lead to the strong inter-mixing profile and fast takeoff in the As profile at the InP→InGaAs interface, but a sharp transition at the InGaAs→InP interface.

In spite of inter-mixing at the interface, the InGaAs/InP MQW structure shows promising optical characteristics. Figure 5-15 displays a set of PL spectra obtained from a nanopillar with 5 QWs. The central emission wavelength is located at ~ 1310 nm, which is the frequency used for optical communications in industry. We note that the emission gets saturated quickly when the pump power increases to 10mW. With further optimization in quantum well composition and thickness, this InGaAs/InP MQW nanopillar structure shows great potential as long wavelength emitter monolithically integrated with silicon for optical communications.

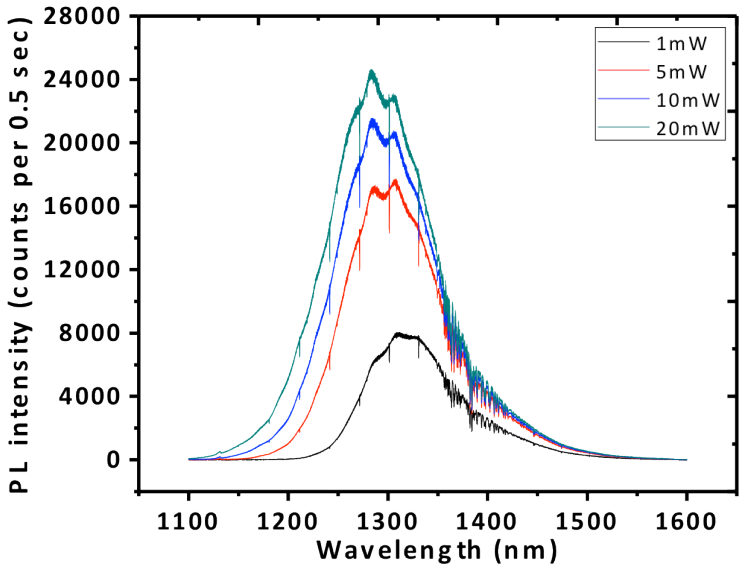

Figure 5-15 PL spectra of a 5-QW structure under various pump levels

5.4 High Resolution Studies of InP/Si interface

With the characteristic core-shell growth mode, InP nanostructures can be scaled up to micron size while maintaining pure WZ phase in the main body, similar to InGaAs nanoneedles. However, there is a distinct difference between the two – InP nanopillars do not possess an inversely tapered base. Without a continuous polycrystalline InP wrapping

around, the entire pillar base is stemming directly from the silicon substrate. With a lattice mismatch as high as 8% between InP and silicon, a large footprint implies a huge amount of elastic energy built up in the nanostructure. This section aims to study how the large stress can be relaxed to facilitate the high-quality growth in the bulk of InP nanopillars. In this study, we examine the hetero-interface of an InP pillar with diameter ~ 900 nm and length ~ 9 μm. With the use of FIB, the top part of the pillar was cut off such that only the bottommost ~ 400 nm remained. Pt was then deposited onto the frustum to passivate the InP/Si hetero-interface. These extra steps minimize curtaining effect that would have occurred if the full pillar were thinned down. The subsequent lift-out and thin-down procedures were the same as outlined in Chapter 2. The area close to the hetero-interface was then examined with HAADF imaging, using aberration corrected microscope TEAM I.

Figure 5-16(a) shows an SEM image of the pillar cross-section halfway through the milling process. We can observe that the entire pillar base, with a width of ~ 900 nm, is in direct contact with silicon without any inverse tapering. During the final thin-down, a large portion of InP is milled away, as revealed in the HAADF image in Figure 5-16(b). In addition, numerous bright dots are observed on the lamella. We believe that these are Ga droplets that deposit onto InP when the sample is bombarded with Ga^+ ions. In spite of these artifacts, one can clearly see that InP is stemming on top of silicon without any amorphous material in between.

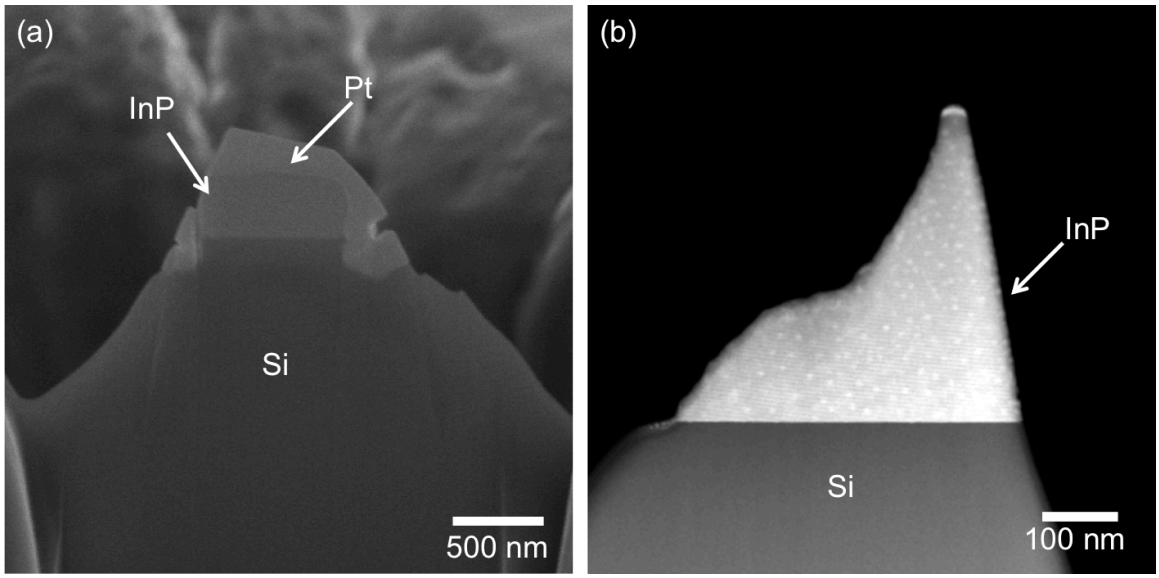

Figure 5-16 (a) SEM image of the InP/Si cross-section (b) HAADF image of the final lamella

To study how InP interfaces with silicon, we first tilt the sample to $[1\bar{1}00]$ zone axis. Since ZB $[\bar{2}11]$ looks exactly the same as WZ $[1\bar{1}00]$, any stacking faults would be invisible along this orientation. This faciliates the identification of any misfit defects that may appear at the interface. Figure 5-17(a) displays an HAADF image of the InP/Si interface. Since indium has a much larger atomic number than Si, InP appears to be much brighter than silicon in the z-contrast image. Ga droplets, which appear as random bright

patches, are present on the InP side. We note that the hetero-interface is a little blurry due to the nanoscopic roughness induced by TMAH etch prior to the growth. At higher magnification (see Figure 5-17(b)), we can observe that the lattice continues seamlessly from silicon to InP in spite of the blurriness at the interface. This shows that InP pillars do nucleate directly on silicon, similar to the high-quality mismatched growth of InGaAs nanostructures studied in Chapter 3.

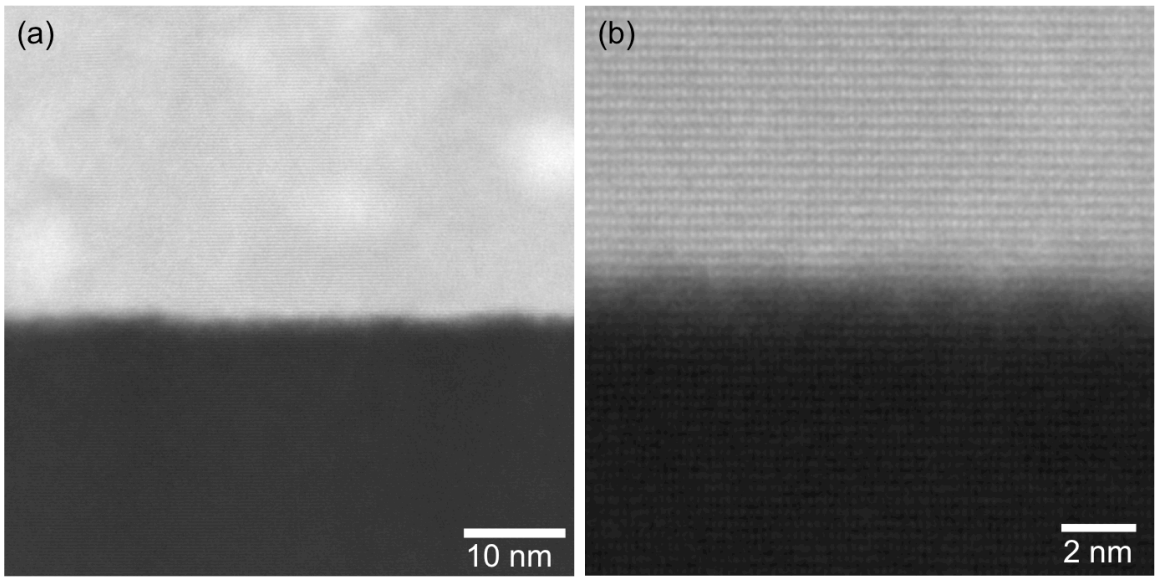

Figure 5-17 HAADF images of InP/Si interface at different magnifications

Although HAADF imaging can facilitate direct elucidation of chemical variance, the high contrast between InP and silicon makes interpretation of lattice positions very difficult. We can remove the step-wise contrast by filtering out the low frequency components of the image in its fast Fourier transform (FFT). The Matlab code for this operation can be found in Appendix I. The filtered image and its FFT are revealed in Figures 5-18(a) and (b), respectively. The lattices of both InP and Si can now be clearly seen at the same time. In particular, two sets of diffraction spots are present in the FFT. Diffractions from InP and silicon are registered with 4-digit Bravais-Miller indices and 3-digit Miller indices, respectively. The existence of two clearly discernable diffractions indicates that InP and Si are possibly relaxed to their own lattice spacing rather than strained to accommodate for the lattice mismatch elastically. The best way to verify this hypothesis is to study how the InP $(11\bar{2}0)$ planes stem from the Si $(02\bar{2})$ planes at the interface. This can be done by simple tracing of planes on both sides of the hetero-interface, i.e. the technique used in identifying misfit defects at poly-Si/InGaAs interface in Chapter 4. Alternatively, we can apply filtering in the spatial frequency domain so that only information of related planes remains in the image, i.e. only $11\bar{2}0$ and $02\bar{2}$ diffractions stay in the FFT (see Figure 5-18(d)). In the filtered image in Figure 5-18(c), most of the InP $(11\bar{2}0)$ planes (i.e. the vertical white lines) in the upper half are seen to continue seamlessly from the Si $(02\bar{2})$ planes below. However, there exist some locations at where one InP $(11\bar{2}0)$ is connected to two Si $(02\bar{2})$, as indicated by red arrows. These are in fact misfit dislocations that

propagate along the $[1\bar{1}00]$ direction. When connected together, the five misfit dislocations outline the contour of the silicon surface, attesting to the roughening effect of TMAH etch during sample preparation. Moreover, the planes in the vicinity of the misfit dislocations are considerably bent, revealing the presence of strain in these regions. Interestingly, these dislocations appear periodically in every 12th or 13th InP $(11\bar{2}0)$ planes. On average, 27 Si $(02\bar{2})$ planes are matched with 25 InP $(11\bar{2}0)$ planes in the presence of dislocations. The ratio of the two numbers, 1.08, accounts for exactly 8% lattice mismatch between Si and InP. We believe that these periodic misfit dislocations effectively relax the misfit stress between the two materials [104-105], leading to the high-quality growth in the bulk material of the pillar that is remote from the hetero-interface.

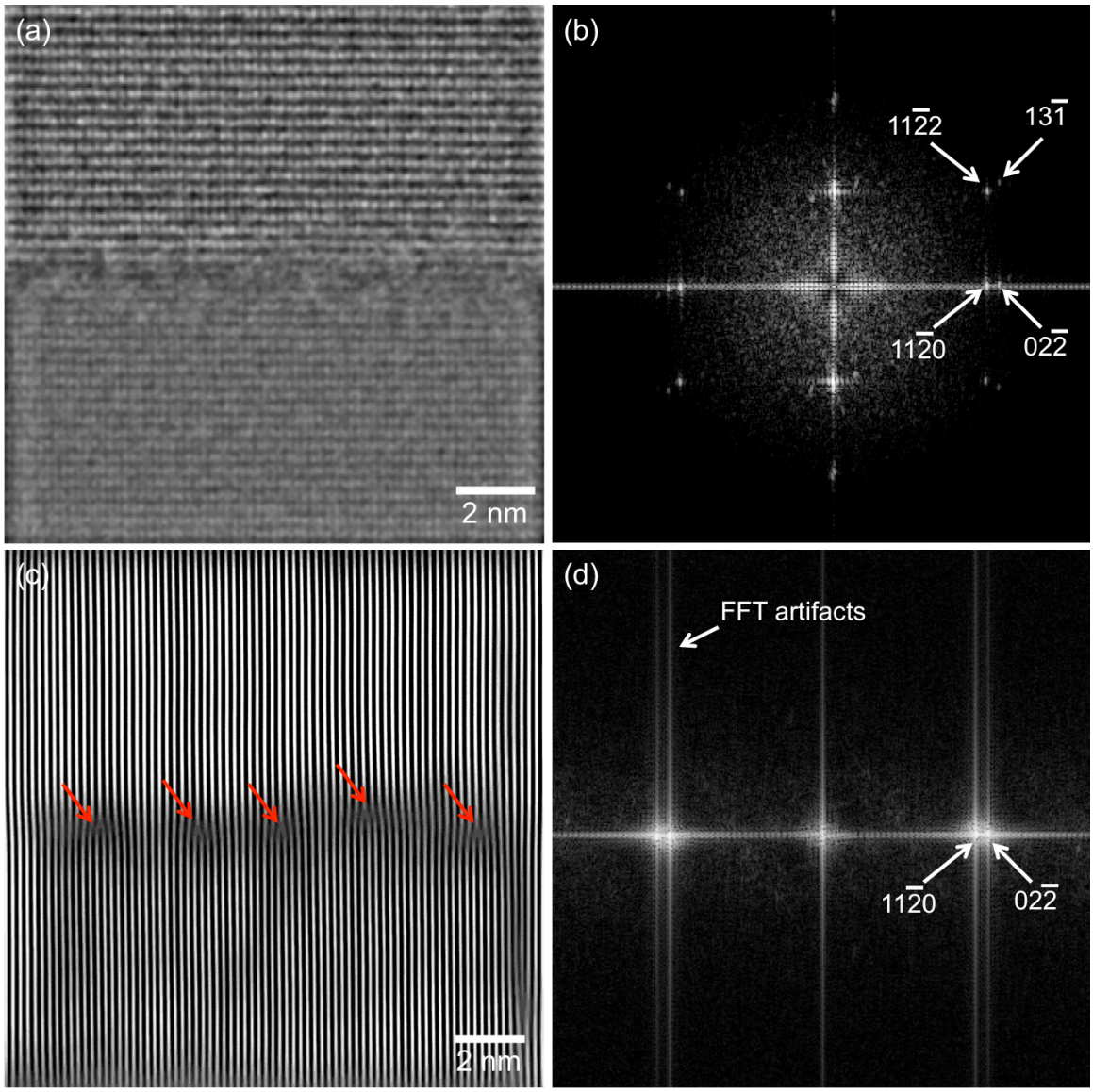

Figure 5-18 (a) & (c) Filtered HAADF images of the InP/Si interface and their FFTs in (b) and (d), respectively.

To observe the stacking sequence across the hetero-interface, we tilt the crystal to $[11\bar{2}0]$ zone axis, as observed in Figure 5-19(a). Immediately above the InP/Si interface is a transition region composed of ZB-phased crystal with stacking faults and twinnings. InP then stabilizes into WZ phase above this 4-nm transition region. Figure 5-19(b) shows the lattice of pure WZ InP under high resolution. The zig-zag arrangement is not as prominent as in WZ GaAs because of the size difference between In and P atoms. Nevertheless, one can still observe the polarity clearly from the highly asymmetric dumbbells – tiny phosphorus is sitting on top of gigantic indium in the lattice. This configuration, in which the top facet of the structure is terminated with group V, is exactly the same as InGaAs nanopillars. The observed polarity is consistent with the metal-initiated nucleation theory, which applies to both InP and InGaAs nanostructures.

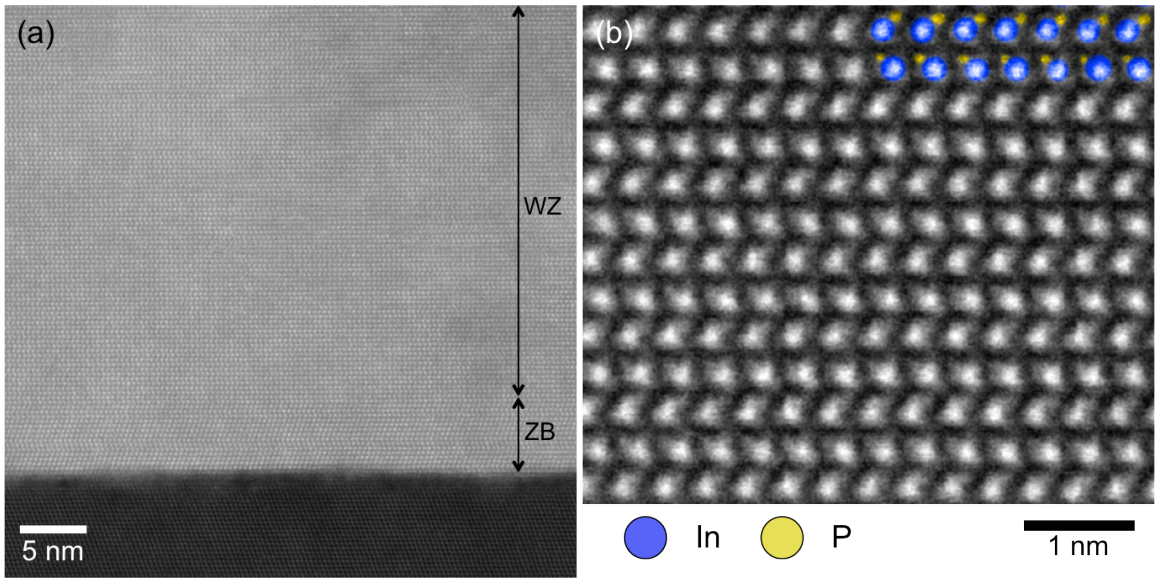

Figure 5-19 (a) InP/Si interface along $[11\bar{2}0]$ zone axis (b) High-resolution image of the pure WZ portion. Some dumbbells are colored for easier polarity interpretation.

Figure 5-20(a) displays the hetero-interface at high magnification, with the step-wise contrast between InP and Si filtered out. InP is observed to grow into ZB phase at the bottommost 4 nm. In spite of the blurriness at the exact interface due to silicon surface roughness, InP is observed to be in direct contact with silicon, with InP [0001] well aligned to Si [111]. This secures electrical conductivity across the hetero-interface. We note that the roughness of the silicon surface is limited to 1~2 monolayers. To visualize how the crystal planes are aligned at the exact interface, filtering is applied at the FFT so that only 111 diffractions of silicon and InP remain. The filtered image is then overlapped with its original form, as displayed in Figure 5-20(b). We can observe that most of the (111) planes of Si and InP are not very aligned to one another. The set of misalignment can be regarded as misfit dislocation networks which relax the stress bit by bit at the interface. Similar to the periodic dislocations observed along $[1\bar{1}00]$ zone axis, these dislocation networks propagate only horizontally without threading upward along the

[0001] direction. In other words, these defects are well confined close to the interface and accommodate for the 8% lattice mismatch between the two materials. InP can therefore evolve into pure WZ phase above the bottommost transition region, as observed in Figure 5-20.

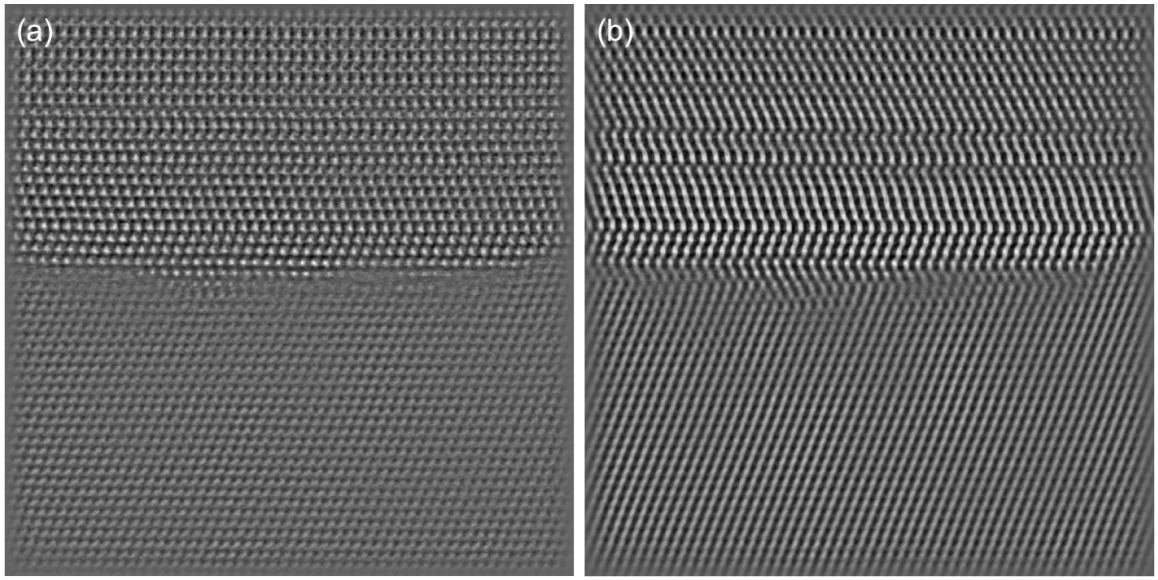

Figure 5-20 HAADF images at the InP/Si interface along $[11\bar{2}0]$ zone axis, (a) without and (b) with filtering in the frequency domain

In the presence of well-confined dislocation networks at the interface, one would expect that the bulk material of InP nanopillars should be almost free of stress. However, as seen in Figure 5-10, high density of stacking faults is still present at the base. We attribute this to the very fast deposition rate at the early phase of the growth. As discussed in section 5.2, InP exhibits poor wetting on silicon because of the large lattice mismatch and long diffusion lengths of indium adatoms. The non-wetting behavior creates a large indium diffusion flux that dominates the growth rate of InP nanopillars. We can consider the layer-by-layer deposition rate to be inversely proportional to pillar surface area. At the beginning of the growth, InP nanostructures have very small size and tiny surface area. The large diffusion flux thus dictates an ultra fast growth rate at the beginning. Too fast a vertical growth rate favors random stacking of monolayers along the [0001] direction, leading to the dense formation of stacking faults. This is similar to the growth of InP at 425 ^{o}C discussed in section 5.1. As growth time increases, pillar surface area increases quadratically. Indium supply due to diffusion flux is then more spread out over the entire pillar, thus slowing down the overall core-shell growth. This enables monolayers to stack in an ABAB sequence properly, leading to the formation of pure WZ phase well above the base. With better optimizations in growth rate at different stages, we may be able to eliminate the densely packed stacking disorders at the base. The advantage of well-confined interface defects can then be fully utilized for high-quality mismatched growth of InP structures on silicon.

5.5 As-grown InP Nanolaser on Silicon

To evaluate whether the InP nanostructures can be useful for optoelectronic applications, it is crucial to characterize their optical properties. We assess the internal quantum efficiency (IQE) of InP nanopillars grown at 450 ^{o}C by means of photoluminescence (PL). A continuous-wave (CW) semiconductor laser emitting at 660 nm was used as the pump source. The pump power is varied from 50 μW to 10 mW, with temperature ranging between 4 K and 298 K. We set the IQE to 100% at 20K since the emission intensity is the strongest at this temperature. The emission intensities at other temperatures are then normalized with this maximum intensity, yielding the IQE-temperature plot as shown in Figure 5-21. IQE is observed to drop slightly when temperature goes below 20K. This negative thermal quenching is probably due to the formation of intermediate energy states by impurities like hydrogen and carbon [106-107]. At temperatures above 20K, charge carriers possess higher kinetic energy such that they can diffuse to the surface and recombine irradiatively at the surface states. This leads to a sharp reduction in IQE with increasing temperature. At room temperature, InP nanopillars show an IQE of 15%. This number is surprisingly high when one takes into account that the nanopillars are not passivated with any high bandgap material. In fact, it is three times higher than the previous best reported IQE obtained from GaAs nanowire with InGaP passivation layer [108]. We attribute this amazing efficiency to the very low surface recombination velocity of InP. Moreover, the micron-sized InP nanostructure has a much lower surface-to-volume ratio than conventional nanowires, which usually have diameters of 100 nm or below. The combination of low surface-to-volume ratio and the superior material property of InP effectively suppress surface recombination, leading to the observed extraordinarily high IQE.

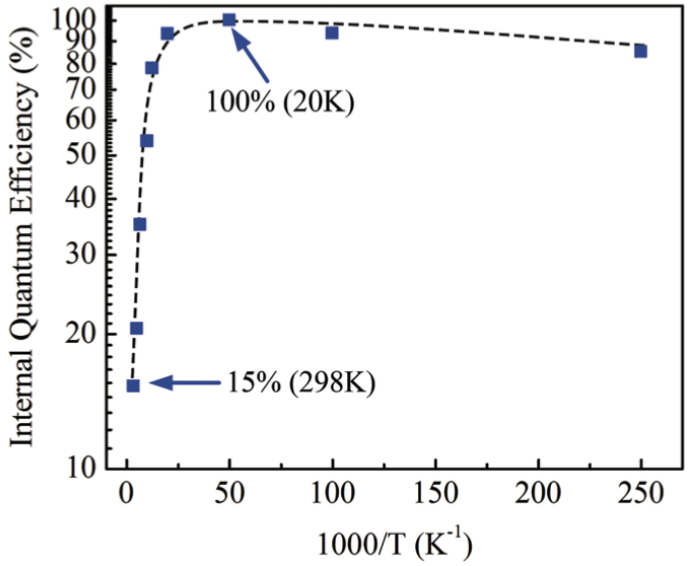

Figure 5-21 Dependence of IQE of InP nanopillars with temperature

Excellent emission efficiency gives rise to remarkable optical performances. Lasing action is achieved with as-grown, unpassivated InP nanopillars on silicon at 4K. A mode-locked Ti:sapphire laser delivering 140 fs pulses was used as the pump source. Figure 5-22(a) displays the emission spectra from a typical InP nanolaser below and above threshold. A sideband suppression ratio of 8.6 dB is observed. The dependences of light output power on input pump power, i.e. the light-light (L-L) curve, is plotted in Figure 5-22(b). Clear threshold behavior is observed. By fitting the L-L curve with gain model and rate equations, the cavity quality factor (Q) and spontaneous emission coupling factor (β) are estimated to be 126 and 0.021, respectively. Similar to InGaAs/GaAs nanolasers, the optical mode assumes a helical propagation in which light spirals up and down the well-faceted InP nanopillar. In addition, the emission linewidth reduces significantly above lasing threshold (see inset of Figure 5-22(b)), attesting to the coherence in emission frequency. These promising results demonstrate the potential of InP nanopillars monolithically grown on silicon for integration of optoelectronics with CMOS technologies.

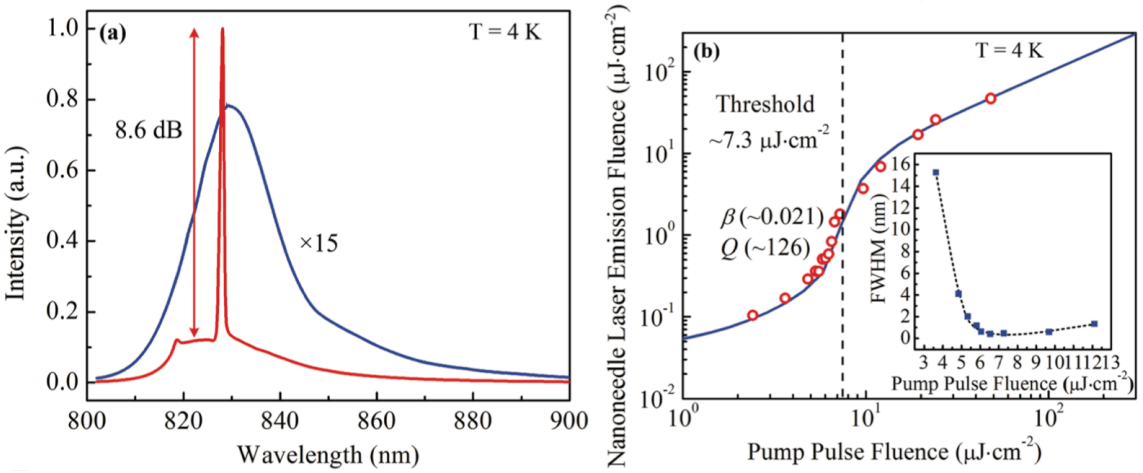

Figure 5-22 (a) Emission spectra below and above lasing threshold (b) L-L curve of as-grown InP nanolaser. Inset is linewidth dependence on pump power.

5.6 Regrowth of Diode Junction in InP Nanopillar Devices

With the excellent optical properties, InP nanopillars show great potential in realizing high-performance opto-electronic devices on top of silicon. P-n junction can be implemented within the nanopillar by adding dopants during different stages of the growth. N-core/p-shell or p-core/n-shell InP structures can then be easily achieved. However, there is a fundamental problem with the core-shell growth – both the core and shell would be in direct contact with the Si substrate, as illustrated in Figure 5-23(a). Ideally, current should flow from the shell through the core and finally down to the Si substrate. The direct contact between the shell and Si creates a shunt path which shorts out the p-n junction. A regrowth process is therefore developed to mitigate this problem. After growing the core, we take the sample out of the chamber and deposit an isolation

layer to cover up the entire surface. In this work, the isolation layer is either SiO_2 or SiO_2/amorphous Si (a-Si) bi-layer. Conformal deposition is enabled with the use of plasma enhanced chemical vapor deposition (PECVD). Photoresist is then spun onto the sample to cover up the base of the pillars. With photoresist as the mask, we etch away the isolation layer selectively and expose the top part of the nanopillar for secondary growth, i.e. regrowth. The regrown structure is schematically depicted in Figure 5-23(b). With the isolation layer, the shell is electrically disconnected from the substrate. P-n junction diode can then be fabricated easily with conventional means by contacting the shell and the silicon substrate with metal electrodes.

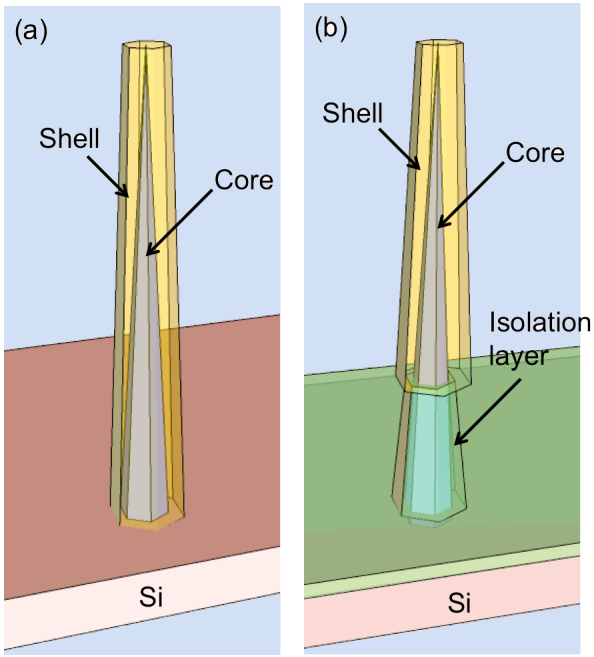

Figure 5-23 Schematic diagrams of core-shell structures synthesized by (a) single growth (b) re-growth

Regrowth was first carried out with SiO_2 as the isolation layer. All flow rates were kept the same as in normal InP nanopillar growth. Figure 5-24(a) shows a typical nanopillar after regrowth, viewed at 30^o tilt angle. Oxide is seen to cover the entire substrate surface as well as the nanopillar base. InP shows excellent growth selectivity such that InP islands cannot nucleate at all on the oxide layer. This significantly increases the diffusion length of indium adatoms, leading to the formation of indium balls on oxide, as observed in Figure 5-24(a). In fact, a lot of indium droplets are present at the oxide-wrapped nanopillar base. This is an indication of a tremendous indium diffusion flux towards the exposed InP. The excess supply of indium causes secondary nucleation of defective nanowires on the pillar surface in addition to the designed core-shell growth. To suppress undesired nucleation, we cut the indium flow to half the original value, i.e. from ~ 20 sccm to ~ 10 sccm. Although secondary nucleation becomes less pronounced, the shell grows into isolated patches rather than continuous layer on the core, as seen in Figure 5-

24(b). In addition, the dense indium droplets surrounding the InP nanostructure reveal indium supply still being too high. The ultra long diffusion length of indium adatoms on SiO_2 thus poses a fundamental limitation on this masked re-growth process.

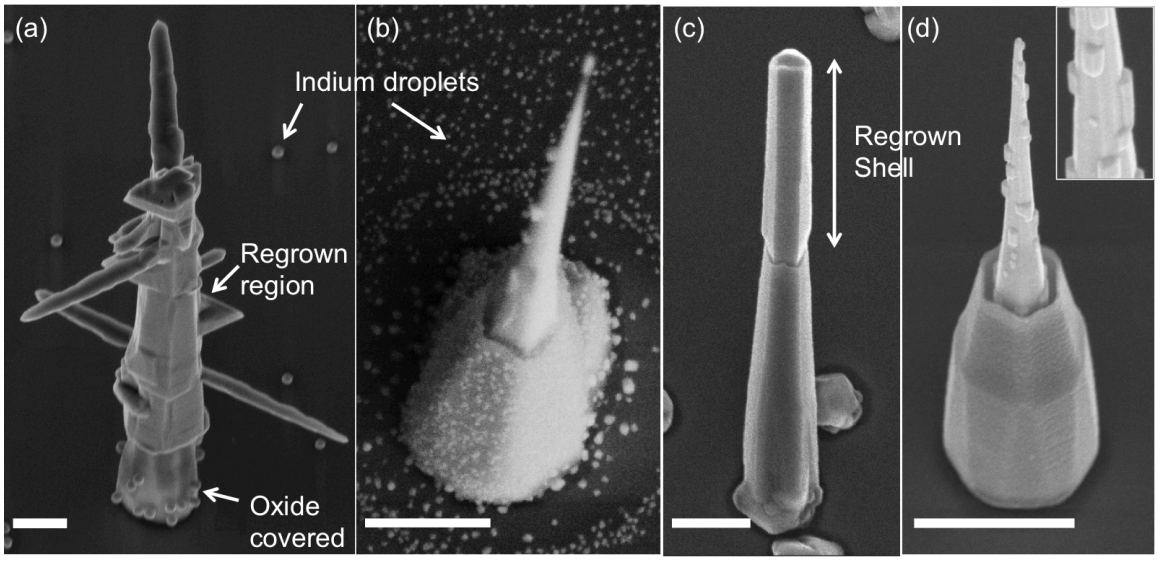

Figure 5-24 Nanopillars with shell regrown under different conditions (a) oxide mask and TMIn ~ 20 sccm (b) oxide mask and TMIn ~ 10 sccm (c) oxide/a-Si bilayer mask and TMIn ~ 5 sccm (d) oxide/a-Si bilayer mask and TMIn ~ 2.5 sccm. All scale bars indicate 1 μm.

To reduce the indium supply towards the exposed InP core, it is crucial to make the surface less favorable for indium diffusion. A possible solution is to change the surface properties by depositing an extra layer on top of the original SiO_2. a-Si is an ideal candidate because it has surface characteristics similar to crystalline Si. Furthermore, a-Si can be deposited at low temperature in the same PECVD chamber as SiO_2, and can be selectively etched away by XeF_2 gas. Figure 5-24(c) shows a regrown nanopillar with SiO_2/a-Si bilayer as isolation. In sharp contrast to the previous two cases, the shell layer grows smoothly on the core without any patches or secondary nucleation of nanowires. No indium balls are found on the a-Si surface, attesting the effectiveness of the amorphous layer to slow down indium diffusion. Interestingly, nucleation of new islands on a-Si is not observed during the second growth. This suggests that a-Si probably facilitates the re-evaporation of adatoms such that indium cannot accumulate on top. Notably, TMIn flow was reduced to ¼ of the original value during the regrowth. To see whether the regrowth deposition rate scales linearly with indium supply, we reduce TMIn flow further down to ~ 2.5 sccm. Surprisingly, rather than continuous thin film, the shell grows into small islands on the pillar (see Figure 5-24(d)). The magnified view in the inset shows that the islands are smooth and well faceted, suggesting that these are actually crystalline structures. With further optimization in size and alloy compositions, we may explore the synthesis of quantum dot devices with this special regrowth process. With the use of SiO_2/a-Si and an optimized TMIn flow rate, high-quality shell layer with perfect isolation from the substrate can be grown, enabling the fabrication of efficient p-n junction diodes.

The regrowth interface quality has significant impact on the device performance. Here, we study the interface by examining the cross-section of the regrown structure with TEM and HAADF imaging. Figure 5-25(a) shows the HAADF image of a full regrown structure and the corresponding schematic diagram. The bottom half of the pillar is well passivated by the isolation layer so that regrowth only happens in the upper half of the pillar. The shell layer is therefore perfectly isolated from the Si substrate, as designed. The regrown portion is then examined with BF-TEM, as displayed in Figure 5-25(b). The sample is mis-tilted a little away from exact $[11\bar{2}0]$ towards [0001] to facilitate the observation of stacking faults. Interestingly, the core-shell border can be clearly seen in the cross section displayed in Figure 5-25(b). The shell layer possesses a rather uniform thickness of ~ 250 nm over the entire regrown portion. Furthermore, laterally propagating stacking faults are present at the regrown homo-structure. While some of them penetrate through the whole structure, the majority is found to appear in the shell only and terminate at the core-shell interface. The termination of stacking faults at the border can be more readily observed in the zoom-in view (see Figure 5-26(a)). To find out the origin of these defects, we examine the interface in dark field. Figure 5-26(b) displays the core-shell interface that is immediately above the isolation mask. While the shell is populated with stacking faults, the core is almost free of any horizontal defects. In addition, numerous black spots with size ~ 5 nm are present along the core-shell interface. We attribute the nucleation of stacking faults to these dark patches at the interface. Notably, most of the stacking faults in the shell concentrate at regions close to the isolation mask. This phenomenon suggests that the dark spots are likely contaminants due to incomplete removal of the mask material, which usually prevails in regions adjacent to the mask. A better cleaning scheme can therefore help eliminating the stacking defects nucleating at the interface.

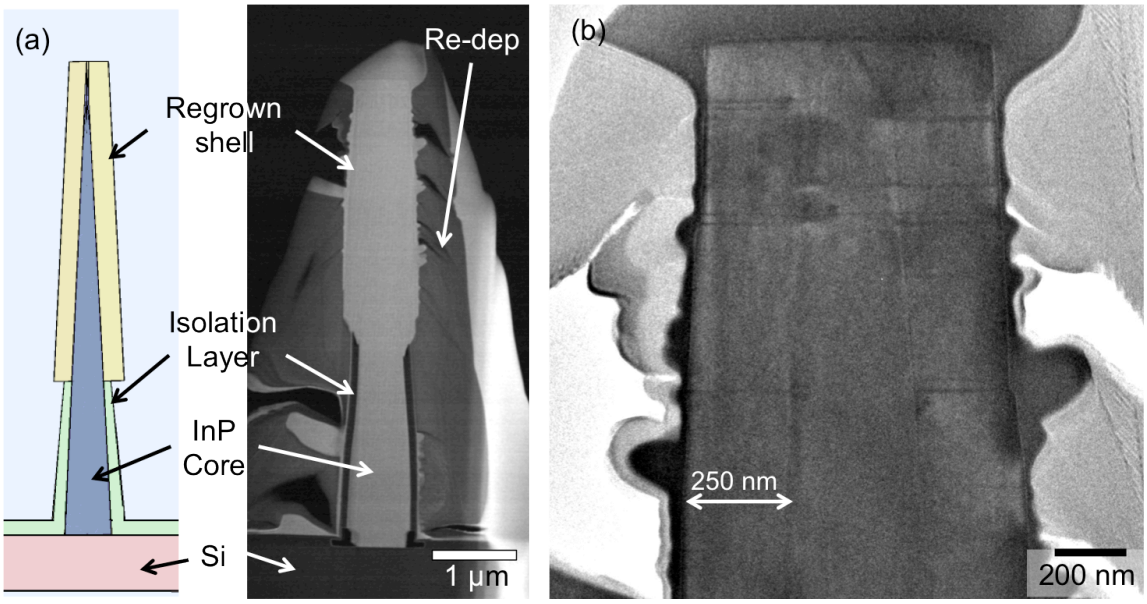

Figure 5-25 (a) Schematic and HAADF image of a full structure with regrown shell (b) BF-TEM of the tip. The core-shell border can be clearly seen.

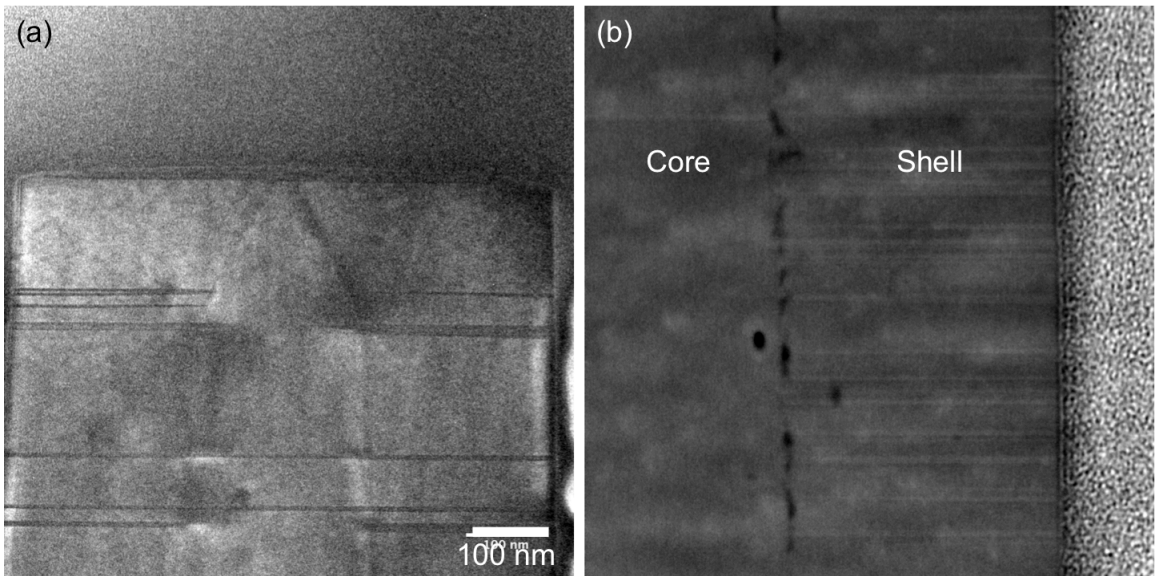

Figure 5-26 (a) Zoom-in view of the regrown pillar tip (b) DF-TEM of the core-shell border. Stacking faults are nucleating from the 'dark patches'.

Stacking faults that terminate midway are usually accompanied by dislocations. To see how dislocation is formed, we cut through the regrown portion horizontally and examine the core-shell structure along c-axis. Figure 5-27 shows HAADF image of a traverse cross-section with a small InP core and a large regrown shell with 5 InGaAs/InP QWs. Similar to the vertical cross-sections, a clear border can be observed at the core-shell boundary in this 'tree-ring' dissection. In addition, dislocations are found to nucleate at the core-shell border, as indicated by the arrows in the figure. These dislocations propagate radially and terminate at the sidewall of pillar. Notably, we do not observe any vertically threading dislocations in the cross-sections cut along the longitudinal direction, as illustrated in Figure 5-25 and 26. This is a direct proof, for the first time, that defects can only propagate laterally as a result of the unique core-shell growth mode.

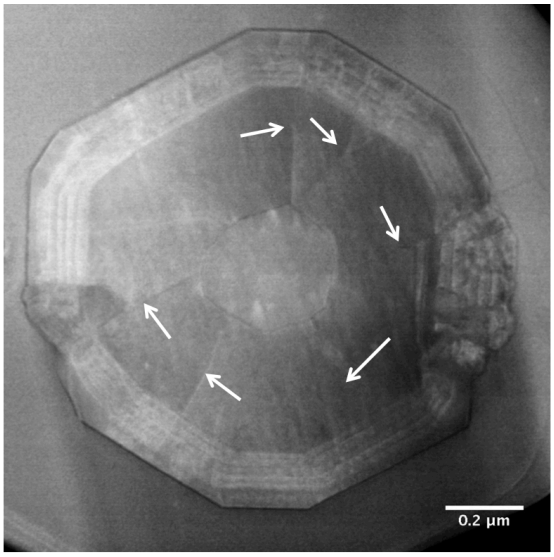

Figure 5-27 Traverse cross-section of a regrown core-shell homo-structure.

Homogeneous growth of a material on its native substrate should be perfectly seamless. In the case of InP regrowth, a dark border is observed at the homogeneous core-shell interface. To understand the origin, we examine the border at high resolution. Figure 5-28(a) displays an HAADF image of the homo-interface. The WZ lattice continues smoothly across the interface and the crystal is coherent even at the dark fringe that resembles the core-shell boundary. Contrast in HAADF image can come from either chemical or thickness variations. The extra contrast at the boundary is probably due to the presence of porous native oxide, which has lower atomic number than indium and phosphorus. Prior to loading into the MOCVD chamber, the sample was deoxidized with HCl [109]. However, there is a 3-minute time gap in between such that slight oxidation may have occurred on the surface during this short time. Another possibility is the presence of nano-roughness on the surface that comes as a result of mask fabrication process. The roughness induces formation of nano-voids which reduce the atomic density (or in other words, effective thickness) at the boundary. No matter what the origin is, a clearly observable boundary symbolizes an imperfect epitaxial regrowth. One possible way to tackle this problem is to include a high-temperature annealing step right before the growth. Annealing at elevated temperature not only removes native oxide but also allows reconstruction of the surface. Further optimization in process and growth is required.

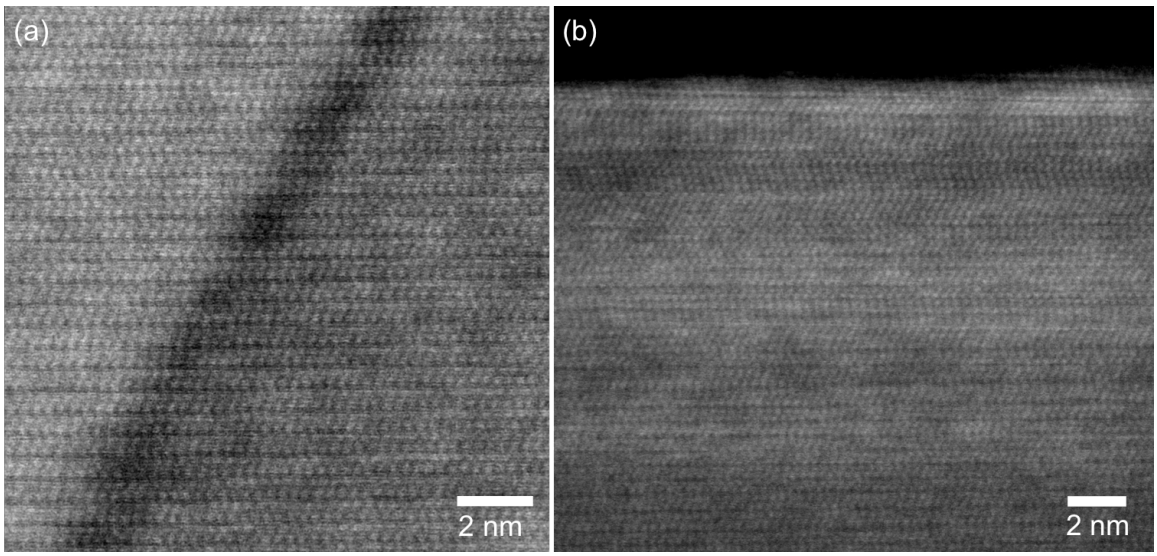

Figure 5-28(a) High-resolution HAADF image at the core-shell interface (b) HAADF image at the tip of the regrown pillar

In Figure 5-26(a), we can see that the core converges into a sharp apex at the tip of the structure. The regrowth, however, transforms the original sharp tip into blunt plateau. Figure 5-28(b) shows high-resolution HAADF image of regrown pillar tip. Instead of having WZ phase all the way, the tip is terminated with ZB crystal phase. This is exactly the same as what we observed in InGaAs nanopillars. This phase transformation is probably triggered by the many temperature ramping steps and chemical etching during the fabrication of isolation mask. In addition, the tip is observed to have a faster growth

rate than the base such that the sidewalls of the regrown portion almost become un-tapered. This may be attributed to the termination of growth along c-axis. In the absence of vertical growth, the adatom diffusion flux towards the tip can only contribute to the lateral growth, leading to the observed faster horizontal growth rate.

Although regrowth is not perfect, respectable electrical performance can still be obtained by proper device structure design. In a p-core/n-shell device synthesized by regrowth, 100 nm of p-InP was deposited on the p-core prior to the growth of n-shell. The depletion region, i.e. the area that is most vulnerable to defect-assisted Shockley-Reed-Hall recombination [110], can thus stay away from the exact core-shell boundary. This minimizes the impact of core-shell boundary defects to the I-V characteristics. Figure 5-29(a) shows the I-V curves of three typical p-core/n-shell devices. Dark currents lower than 10 pA are achieved at a reverse bias of -2V, which is an excellent value even in epitaxial devices. On the contrary, devices fabricated from core-shell pillars without regrowth (i.e. the structure in Figure 5-23(a)) exhibit dark current 10^5 times higher than the regrown devices, as revealed in Figure 5-29(b). The very high reverse current is likely due to leakage from the shell to the silicon substrate. The perfect electrical isolation in regrowth is therefore crucial to the electrical performance. At forward bias, the regrowth devices show an ideality factor close to 2, which is a typical value obtained from high-quality planar diode with efficient radiative recombination. In addition, prominent photovoltaic effect is observed with the regrowth devices. Under an illumination of ~ 10 mW/cm^2 (i.e. 1/10 solar intensity), the I-V curve shifts downwards, showing an open-circuit voltage of ~ 0.3V (see Figure 5-30). These exciting preliminary results underscore the potential for these nanostructures to be used for photovoltaic applications. With further improvements in device structure design and growth conditions, InP nanopillars can become important building blocks for the integration of optoelectronics with silicon CMOS technology.

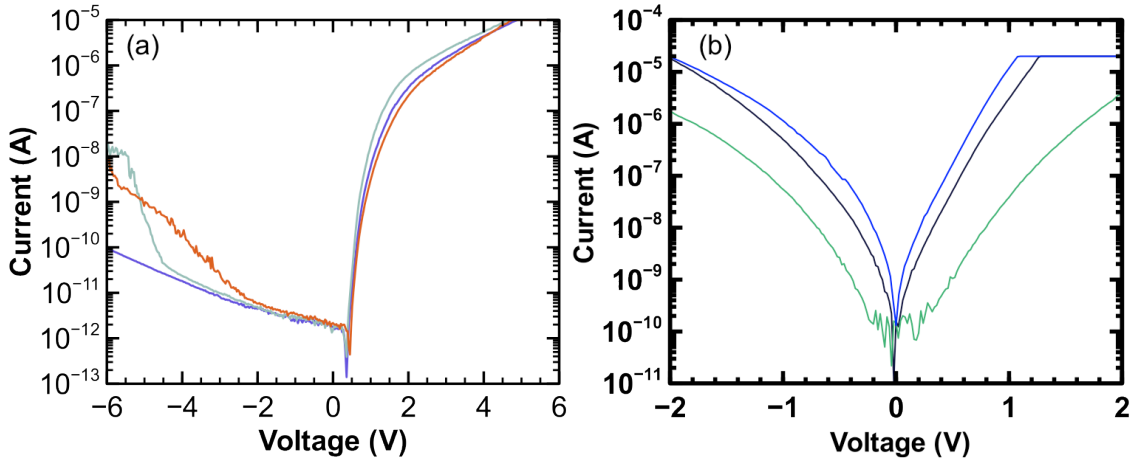

Figure 5-29 I-V characteristics of p-core/n-shell devices synthesized (a) with regrowth (b) without regrowthd

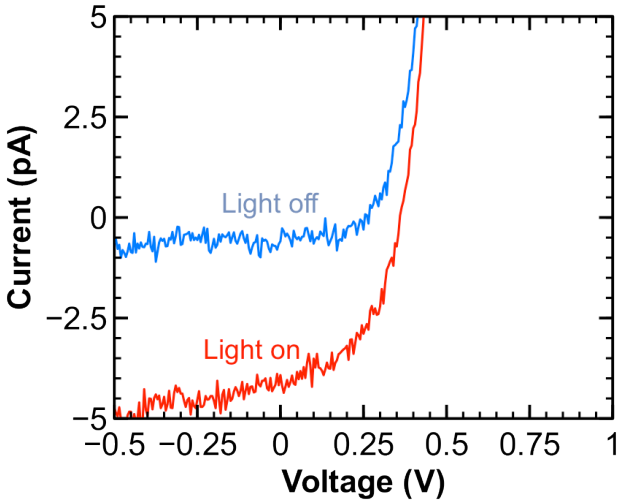

Figure 5-30 I-V curves showing prominent photovoltaic effect

5.7 Site-controlled growth of InP Nanopillars

While regrown InP nanostructures show great promise in achieving high-performance optoelectronic devices, they nucleate randomly over the Si surface, as observed in Figure 5-5. The lack of site controllability induces difficulties in the integration with other optical components like couplers and waveguides. The capability to 'plant' nanostructures at specific locations is therefore of utmost importance. Site-controlled growth of nanowires is usually implemented either by patterning of metal catalyst [111-112], or by selective area growth with the use of mask [113-114]. Since external catalyst is not used in InP nanopillar growth, we adopt the latter method, as schematically illustrated in Figure 5-31(a). The fabrication process starts with the deposition of SiO_2 onto (111)-Si substrate. Holes at selected locations are then opened up to expose bare silicon surface for pillar nucleation. The bare silicon surface is then roughened chemically with TMAH etch and subsequently deoxidized briefly with BOE. This patterned growth scheme not only enables precise control on the pillar location, but also facilitates *in situ* isolation of the shell layer from the substrate. After the opening is completely filled up, the crystal can only expand laterally above the SiO_2 mask, as illustrated in Figure 5-31(b). The materials grown above the oxide is therefore automatically disconnected from the substrate even without regrowth. Undesired defects and contaminants at the regrowth interface can then be avoided. With this masked growth scheme, high-quality core-shell nanopillars can be grown and subsequently fabricated into devices directly at well-defined locations on the silicon substrate.

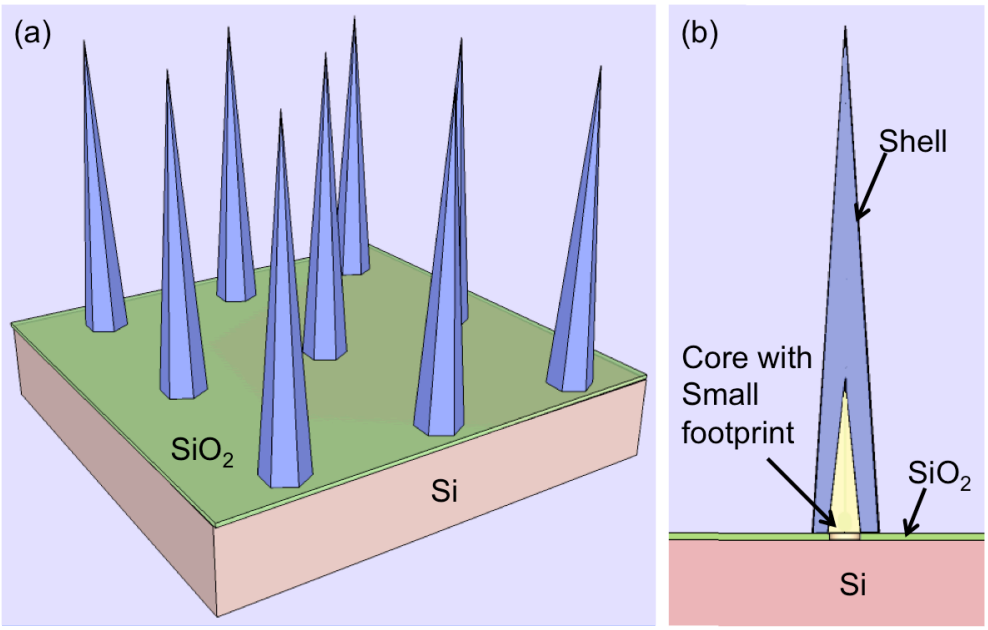

Figure 5-31 (a) Schematic diagram illustrating site controlled growth of InP nanostructures on Si (b) Cross-section of the nanostructure with the shell naturally disconnected from silicon

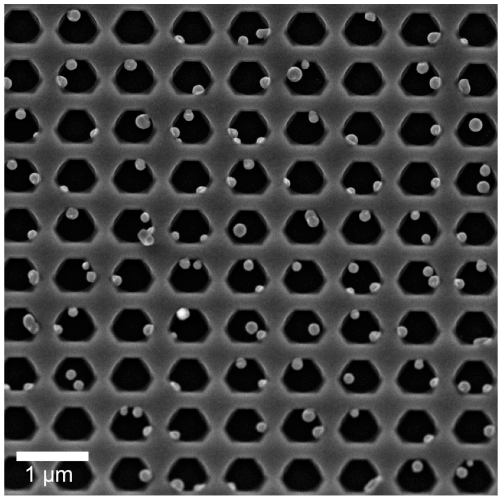

Figure 5-32 Formation of indium balls inside incompletely deoxided opening

The nucleation of InP nanostructures on the masked substrate exhibits strong dependence on the diameter of opening. Too large a hole size can cause multiple nucleations in the same hole and this potentially compromises the crystalline quality of the structure. However, a small hole size lowers the indium capturing cross-section and thus the nucleation probability. We observed that the optimum hole diameter lies between 360 nm and 400 nm. The yield rate, i.e. the percentage of holes filled with pillars, drops significantly when the hole diameter goes below 320 nm. The condition of the opened

silicon surface is also crucial to pillar nucleation. If the oxide within the opening is not completely removed, indium balls rather than InP structure would nucleate inside the hole, as revealed in Figure 5-32. In addition to the opening size, InP nanopillar growth also varies with the pitch, i.e. hole-to-hole separation. A densely packed array increases competition of adatoms among the nanopillars. Insufficient indium supply can result in poor nucleation and defective pillar growth. A large pitch, however, leads to a low pillar areal density, which can be a problem to applications like photovoltaics. A pitch of 800nm ~ 1500 nm gives the best compromise between yield rate and areal pillar density. Figure 5-33(a) displays an SEM image of a nanopillar array with hole and pitch size of 380 nm and 3000 nm, respectively. In this particular grid, the yield rate can be as high as 60%. When the pitch size lowers to 1000 nm, the yield rate drops down to 20%. However, with a pillar diameter approaching 1 micron, the areal fill ratio can become larger than 12%, as seen in Figure 5-33(b). We can see from the same figure that the pillars show fairly good uniformity within the grid, underscoring their potential to be used as ensemble devices. Further optimizations in mask design and growth conditions are needed to improve the yield rate and the run-to-run non-uniformity.

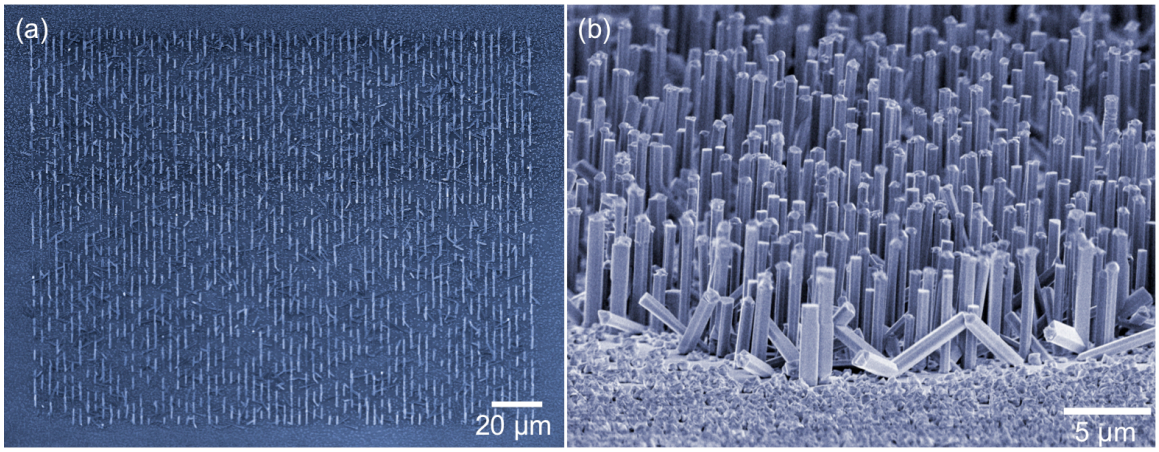

Figure 5-33 SEM images of nanopillar arrays with (a) Hole size = 380 nm, pitch size = 3000 nm (b) Hole size = 380 nm, pitch size = 1000 nm

To verify the crystalline quality of nanopillars obtained from the patterned growth, we examine the pillar cross-sections with TEM. Using FIB, we cut through the exact center of the pillar. Figure 5-34(a) shows an SEM image of the longitudinal cross section of a pillar halfway through the milling process. While the pillar base diameter is as large as 780 nm, its footprint on Si is only 380 nm in width, which is pre-defined by the opening size of the oxide mask. Above the oxide opening, the pillar grows laterally on top of the oxide layer. This follows exactly the proposed growth mechanism depicted in Figure 5-31(b). Figure 5-34(b) displays a BF-TEM image of the base of the same InP pillar. Although the left side was completely removed during the final ion mill, the 'mushroom' shaped root at the oxide mask opening can still be clearly visible. Moreover, only a few stacking faults are present at the base – the portion well above the oxide mask is free of any misfit defects. Similar to spontaneously grown nanopillars, InP synthesized with patterned growth is seen to stem directly from the Si substrate (see Figure 5-34(c)). Oxide

is completely absent at the hetero-interface. This implies that a thoroughly deoxidized silicon surface is crucial to the nucleation of nanopillars, which is coherent with the growth studies presented in Figure 5-32. InP evolves into pure WZ phase above the bottommost ~ 8nm polytypic transition layer, as revealed from the ABAB stacking sequence. Interestingly, the pillar core does not fill up the oxide opening completely. A small gap is observed between InP and Si, as indicated by an arrow in Figure 5-34(b). Rather than following the etched morphology of silicon, InP terminates itself with a well-defined sidewall at the root (see Figure 5-34(d)). The sidewall is likely composed of terraces formed by $\{1\bar{1}00\}$ and (0001), with the slope dictated by the ratio of vertical and lateral growths. These observations reveal high-quality growth of the pillar core inside the oxide opening similar to normal unpatterned growth.

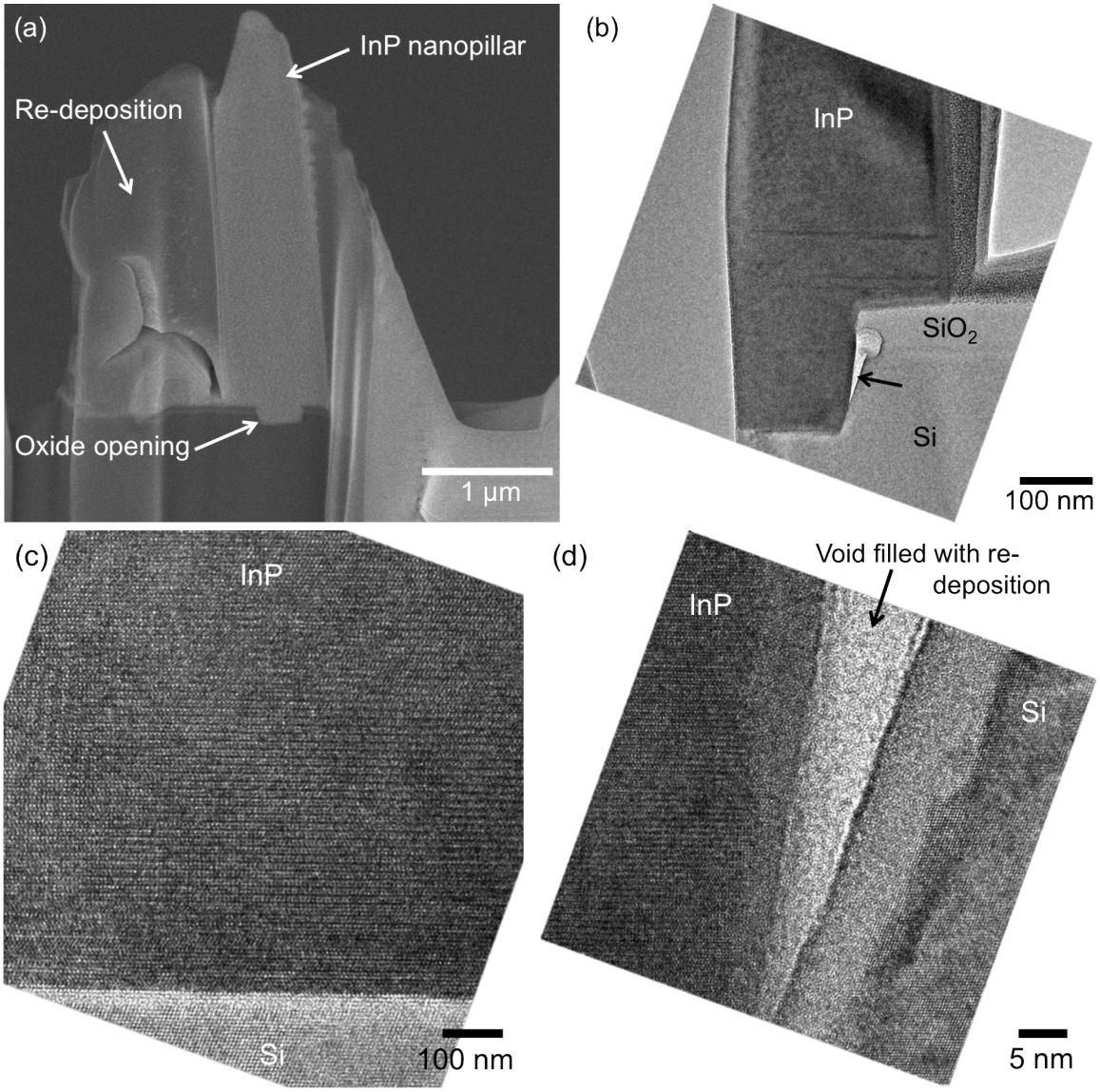

Figure 5-34 (a) Cross-sectional SEM of an InP pillar synthesized with patterned growth (b) BF-TEM image of the same pillar (c) InP/Si exact interface (d) The small gap between InP and Si at the pillar root.

In addition to the mushroom-shaped root, it is also important to examine the quality of crystal overgrown on top of the oxide layer. Figure 5-35(a) shows an HRTEM image at the InP/SiO_2 interface. Despite depositing on top of amorphous oxide, InP grows into WZ phase crystal with minimal stacking disorders. When examined at high magnifications (Figure 5-25(b)), InP is seen to be in tight contact with the oxide layer, similar to other work with epitaxial lateral overgrowth. This excellent crystal quality above oxide comes as a natural consequence of the characteristic core-shell growth mechanism. With proper doping and device structure optimization, high-performance ensemble InP pillar devices can potentially be realized directly on Si.

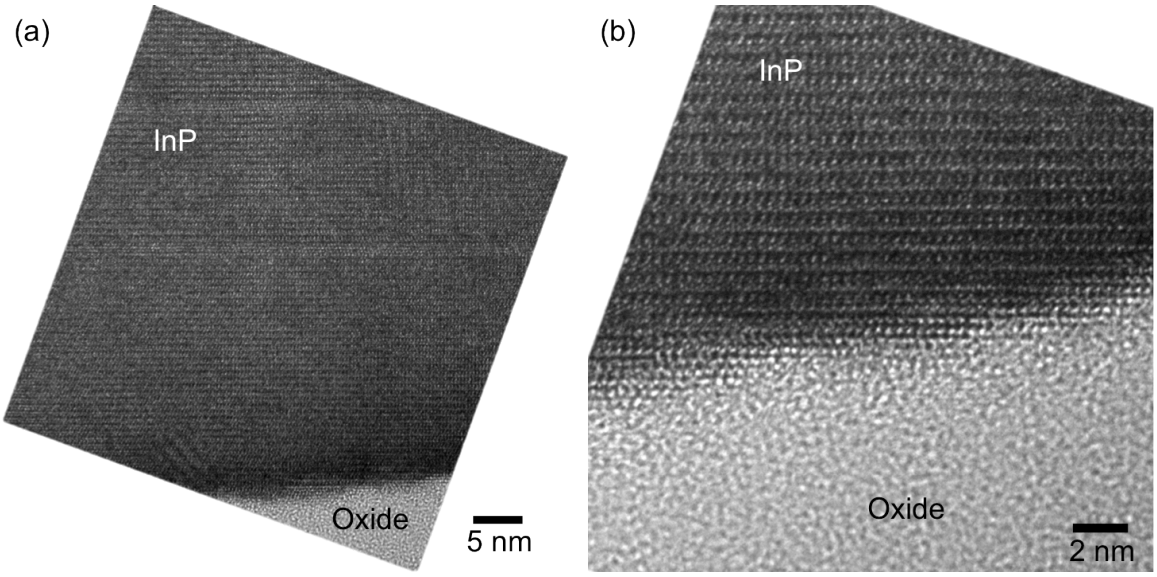

Figure 5-35 TEM images showing the InP/SiO_2 interface

5.8 Summary

In this chapter, we discussed the monolithic integration of InP nanopillars with silicon. High-quality InP nanostructures with diameters approaching a micron can be grown directly on top of silicon. Nanopillar nucleation is initiated by the diffusion of indium nano-clusters onto bare silicon surface at where indium reacts to yield InP structures. In particular, nucleation is facilitated by etching-induced surface nano-roughness, which effectively anchors the diffusive metal cluster for reaction. In addition, the crystal phase purity improves with increasing growth temperature. Specifically, pure wurtzite phase is obtained at growth temperature above 450 ^{o}C. The change in crystal phase is observed in both direct inspections with TEM as well as emission wavelength shift in photoluminescence. Similar to InGaAs-based nanostructures, high-quality growth of micron-sized InP nanopillars is enabled by the characteristic core-shell growth mode. InP/InGaAs/InP MQW structures that emit at ~ 1310 nm, i.e. the wavelength for optical communication, can therefore be synthesized in a core-shell manner. With extremely low

surface recombination velocity, lasing can be achieved in as-grown InP nanopillars even without any surface passivation. An internal quantum efficiency as high as 15% can be obtained with the bare nanostructures. To realize high-performing optoelectronic devices, however, excellent optical property alone is not sufficient. We therefore developed a regrowth scheme to eliminate the leakage path by electrically disconnecting the shell layer from the substrate. In spite of the presence of defects around the regrowth interface, p-n junction diodes with excellent diode behavior are demonstrated. To facilitate the subsequent integration with other optical components, patterned growth is developed to 'plant' nanopillars at specific locations. The overgrowth of the shell layer on the oxide mask also enables *in situ* electrical isolation between the shell and substrate even without regrowth. With further optimization in mask fabrication, growth conditions and run-to-run uniformity, ensemble pillars can be fabricated into devices on silicon for various functionalities like photovoltaic or sensing applications. This work presents a potential pathway for the integration of III-V with silicon, bridging optoelectronics with CMOS technology for many new technological opportunities.

Chapter 6 Conclusion

In this dissertation, we investigated the unconventional growth mechanism that enables high-quality mismatched growth of III-V nanostructures on dissimilar substrates. Firstly, we studied the synthesis of InGaAs nanopillars on silicon. Through HRTEM studies, the bulk material of the pillar is observed to be in pure wurtzite phase. *In situ* TEM experiment shows that the crystal can be transformed back into the energy-favorable zincblende phase upon high-energy dose. This attests to the meta-stability of the wurtzite phase lattice. InGaAs is found to nucleate directly on silicon without any amorphous material in between. Misfit strain between silicon and InGaAs is relaxed *via* an interesting inverted-cone shape tapering of the root, which reduces the footprint of the nanostructure and relax misfit strain partially through an elastic mechanism. The remaining stress is accommodated by horizontally terminated stacking disorders, which are well confined within the inverse-cone region. Polarity studies and growth experiments revealed that pillar nucleation was initiated by formation of metal nano-clusters, which subsequently diffuse onto flat silicon surface and react to form needle seeds for the following core-shell growth. The characteristic core-shell geometry facilitates elastic stress relaxation, enabling the mismatched growth of GaAs on $In_{0.2}Ga_{0.8}As$ with thickness 15 times over the critical value in thin-film case.

In addition to crystal quality, we also studied the alloy composition homogeneity of InGaAs-based nanopillars. Spontaneous alloy composition ordering was observed along the radial directions as a result of diffusion length difference of indium and gallium adatoms. Along the axial direction, on the other hand, InGaAs/GaAs nanopillars exhibit excellent composition coherency. With the extraordinary crystal quality and composition homogeneity, continuous wave operation of as-grown InGaAs nanolaser was achieved at 4K upon optical pump. Photodetector and light emitter are fabricated with nanopillars as-grown on silicon, using conventional lithography and etching processes. The devices reveal extremely low dark current and ideality factor close to 2, which are comparable to decent thin film diodes. Clear amplified spontaneous emissions are observed in pillars embedded in metal-optic cavity. With further improvements in device structure and cavity design, electrically pumped nanolasers can be realized with InGaAs based nanopillars monolithically grown on top of silicon at a CMOS-compatible temperature.

High quality InGaAs nanopillars can be grown not only on single crystalline substrate, but also on polycrystalline silicon. The pillar base diameter could scale up to a micron, which is far greater than the substrate crystal grain size (~ 100 nm). With the inverse tapering at the base, the effective footprint of the nanostructure is reduced to below 40 nm in diameter. The small contact area prevents the III-V crystal from nucleating on top of multiple grains in the substrate and minimizes stress in the system due to lattice mismatch. The special crystal alignment between InGaAs and Si facilitates formation of misfit dislocations at the interface, thus allowing the growth of stacking fault free III-V crystal on poly-Si. Although asymmetry is observed in the core-shell configuration, the lattice is highly coherent across the hetero-interface. In addition, EDS shows that the hetero-interface has an abrupt composition profile, which is crucial to carrier confinement

in the structure. Lasing is demonstrated upon optical pump, attesting the excellent crystal and optical quality of the as-grown nanostructures.

With the success in the synthesis of arsenide-based nanostructure devices on silicon, we extended the unique core-shell growth mechanism to another III-V material system, InP. High-quality InP nanostructures with diameters approaching a micron could be grown directly on top of silicon. Nanopillar nucleation is initiated by the diffusion of indium nano-clusters onto bare silicon surface at where indium reacts to yield InP structures. In particular, nucleation is facilitated by etching-induced surface nano-roughness, which effectively anchors the diffusive metal cluster for reaction. In addition, the crystal phase purity improves with increasing growth temperature. InP/InGaAs/InP MQW structures that emit at ~ 1310 nm, i.e. the wavelength for optical communication, was synthesized via the characteristic core-shell growth. Unlike InGaAs nanostructures, InP nanopillars do not exhibit any tapering at the base. The huge elastic energy developed across the ~ 1 μm interface is relaxed via the formation of periodic misfit dislocations at the junction. The bulk material well above the interface is therefore free of stress. With extremely low surface recombination velocity, lasing can be achieved in as-grown InP nanopillars even without any surface passivation. An internal quantum efficiency as high as 15% can be obtained with the bare nanostructures. To realize high-performing optoelectronic devices, however, excellent optical property alone is not sufficient. We therefore developed a regrowth scheme to eliminate the leakage path by electrically disconnecting the shell layer from the substrate. In spite of the presence of defects around the regrowth interface, p-n junction diodes with excellent diode behavior are demonstrated. To facilitate the subsequent integration with other optical components, patterned growth is developed to 'plant' nanopillars at specific locations. The overgrowth of the shell layer on the oxide mask also enables *in situ* electrical isolation between the shell and substrate even without regrowth. With further optimization in mask fabrication, growth conditions and run-to-run uniformity, ensemble pillars can be fabricated into devices on silicon for various functionalities like photovoltaic or sensing applications.

In conclusions, the findings in this dissertation re-define the rules for heterogeneous integration of lattice-mismatched materials and their device structure design. The amazing optoelectronic device performances presented in this work underscore a potential pathway for the integration of III-V with single and poly-crystalline silicon, bridging optoelectronics with many other possible technologies such as CMOS circuits, TFT, nanofluidics, and so on.

Bibliography

1 Wang, G.; Leys, M.; Loo, R.; Richard, O.; Bender, H.; Brammertz, G.; Waldron, N.; Wang, W.; Dekoster, J.; Caymax, M.; Seefeldt, M.; Heyns, M.; Selective Area Growth of InP and Defect Elimination on Si (001) Substrates. *J. Electrochem. Soc.* **2011,** 118, H645-H650.

2 Krost, A.; Schnabel, R.F.; Heinrichsdorff, F.; Rossow, U.; Bimberg, D.; Cerva, H. Defect reduction in GaAs and InP grown on planar Si(111) and on patterned Si(001) substrates. *J. Cryst. Growth* **1994,** 145, 314-320.

3 Evers, N.; Vendier, O.; Chun, C.; Murti, MR.; Laskar, J.; Jokerst, NM.; Moise, TS.; Kao, Y-C. Thin film pseudomorphic AlAs/In0.53Ga0.47As/InAs resonant tunnelling diodes integrated onto Si substrates. *IEEE Electr. Device L.* **1996,** 17, p.443.

4 Schmidt, M. A. Wafer-to-wafer bonding for microstructure formation. *P. IEEE*, **1998,** 86, pp. 1575 –1585.

5 Goossen, K. W.; Walker, J. A.; D'Asaro, L. A; Hui, S. P.; Tseng, B.; Leibenguth, R.; Kossives, D.; Bacon, D. D.; Dahringer, D.; Chirovsky, L. M. F.; Lentine, A. L.; Miller, D. A. B. GaAs MQW modulators integrated with silicon CMOS. *IEEE Photonic. Tech. L.* **1995,** 7, pp. 360 –362.

6 Matijasevic, G. S.; Wang, C. Y.; Lee, C. C. Void free bonding of large silicon dice using gold-tin alloys. *IEEE T. Compon. Hybr.* **1990,** 13, pp. 1128 –1134.

7 Tsau, C. H.; Spearing, S. M.; Schmidt, M. A. Fabrication of wafer-level thermocompression bonds. *J. Microelectrom. S.* **2002,** 11, pp. 641 – 647.

8 Fan, A.; Rahman, A.; Reif, R. Copper Wafer Bonding. *Electrochem. Solid- State Lett.*, **1999,** 2, pp. 534–536.

9 Fang, A. W.; Park, H.; Cohen, O.; Jones, R.; Paniccia, M. J.; Bowers, J. E. Electrically Pumped Hybrid AlGaInAs–Silicon Evanescent Laser *Opt. Express* **2006**, 14, 9203–9210

10 Kunert, B.; Koch, J.; Torunski, T.; Volz, K.; Stolz, W. MOVPE growth experiments of the novel (GaIn)(NP)/GaP material system. *J. Crystal Growth* **2004,** 272, 753.

11 Kunert, B.; Volz, K.; Stolz, W. Properties and Laser Applications of the GaP-Based (GaNAsP)-Material System for Integration to Si Substrates. *Dilute III-V Nitride Semiconductors and Material SystemsMaterials Science*. **2008,** 105, pp 317-341.

12 Chuang, L. C.; Moewe, M.; Crankshaw, S.; Chang-Hasnain, C. J. Optical properties of InP nanowires on Si substrates with varied synthesis parameters. *Appl. Phys. Letts* **2008,** *92*, 13121.

13 Wu, Z. H.; Mei, X. Y; Kim, D.; Blumin, M.; Ruda, H. E. Growth of Au-catalyzed ordered GaAs nanowire arrays by molecular-beam epitaxy. *Appl. Phys. Letts* **2002,** 81, 5177-5179.

14 Bao, J.; Bell, D. C.; Capasso, F.; Wagner, J. B.; Mårtensson, T.; Trägårdh J.; Samuelson, L. Optical Properties of Rotationally Twinned InP Nanowire Heterostructures. *Nano Lett.,* **2008**, 8, pp 836–841.

15 Mohan, P.; Motohisa, J.; and Fukui, T. Fabrication of InP/InAs/InP core-multishell heterostructure nanowires by selective area metalorganic vapor phase epitaxy. *Appl. Phys. Lett.* **2006,** *88*, 133105.

16 Hertenberger, S.; Rudolph, D.; Bichler, M.; Finley, J. J.; Abstreiter, G.; Koblmüller, G. Growth kinetics in position-controlled and catalyst-free InAs nanowire arrays on Si(111) grown by selective area molecular beam epitaxy. *J. Appl. Phys.* **2010,** *108*, 114316.

17 Tomioka, K.; Tanaka, T.; Hara, S.; Hiruma, K.; Fukui, T. III–V Nanowires on Si Substrate: Selective-Area Growth and Device Applications. *IEEE J. Quantum Elect.* **2011,** 17, pp.1112-1129.

18 Renard, V. T.; Jublot, M.; Gergaud, P.; Cherns, P.; Rouchon, D.; Chabli, A.; Jousseaume, V. Catalyst preparation for CMOS-compatible silicon nanowire synthesis. *Nat. Nanotechno.* **2009,** 4, 654 – 657.

19 Chuang, L. C.; Moewe, M.; Chase, C.; Kobayashi, N. P.; Chang-Hasnain, C. J.; Crankshaw, S. Critical Diameter for III-V Nanowires Grown on Lattice-Mismatched Substrates. *Appl. Phys. Lett.* **2007,** 90, 043115.

20 Cirlin, G. E.; Dubrovskii, V. G.; Soshnikov, I. P.; Sibirev, N. V.; Samsonenko, Y. B.; Bouravleuv, A. D.; Harmand, J. C. ; Glas, F. Critical Diameters and Temperature Domains for MBE growth of III–V Nanowires on Lattice Mismatched Substrates. *Phys. Status Solidi-R.* **2009,** 3, 112–114.

21 Moewe, M.; Chuang, L. C.; Crankshaw, S.; Ng, K. W.; Chang-Hasnain, C. J. Core-Shell InGaAs/GaAs Quantum Well Nanoneedles Grown on Silicon with Silicon-Transparent Emission. *Opt. Express* **2009,** 17, 7831-7836.

22 Chuang, L. C.; Sedgwick, F. G.; Chen, R.; Ko, W. S.; Moewe, M.; Ng, K. W.; Tran, T. T. D.; Chang-Hasnain, C. J. GaAs-Based Nanoneedle Light Emitting Diode and

Avalanche Photodiode Monolithically Integrated on a Silicon Substrate. *Nano Lett.* **2011**, 11, 385-390.

23 Chen, R.; Tran, T. T. D.; Ng, K. W.; Ko, W. S.; Chuang, L. C.; Sedgwick, F. G.; Chang-Hasnain, C. J. Nanolasers Grown on Silicon. *Nat. Photonics* **2011**, 5, 170-175.

24 Chuang, L. C.; Moewe, M.; Ng, K. W.; Tran, T. T. D.; Crankshaw, S.; Chen, R.; Ko, W. S.; Chang-Hasnain, C. J. GaAs Nanoneedles Grown on Sapphire. *Appl. Phys. Lett.* **2011,** 98, 123101.

25 Yu, E. T.; Dang, X. Z.; Asbeck, P. M.; Lau, S. S.; Sullivan, G. J. Spontaneous and piezoelectric polarization effects in III–V nitride heterostructures. *J. Vac. Sci. Technol. B* **1999,** 17, 1742.

26 Mishra, A.; Titova, L. V.; Hoang, T. B.; Jackson, H. E.; Smith, L. M.; Yarrison-Rice, J. M.; Kim, Y.; Joyce, H. J.; Gao, Q.; Tan, H. H.; Jagadish, C. Polarization and temperature dependence of photoluminescence from zincblende and wurtzite InP nanowires. *Appl. Phys. Lett.* **2007,** 91, 263104.

27 Chen, R.; Crankshaw, S.; Tran, T.; Chuang, L. C.; Moewe, M.; Chang-Hasnain, C. Second-harmonic generation from a single wurtzite GaAs nanoneedle. *Appl. Phys. Lett.* **2010,** 96, 051110.

28 Lawaetz, P. Stability of the Wurtzite Structure *Phys. Rev. B* **1972,** 5 4039-4045.

29 Yeh, C. Y.; Lu, Z. W.; Froyen, S.; Zunger, A. Zinc-blende-wurtzite polytypism in semiconductors. *Phys. Rev. B* **1992,** 46, 10086-10097.

30 Dubrovskii, V.G.; Sibirev, N.V. Growth thermodynamics of nanowires and its application to polytypism of zinc blende III-V nanowires. *Phys. Rev. B* **2008,** 77, 035414-8.

31 Kisielowski, C.; Hetherington, C.J.D.; Wang, Y.C.; Kilaas, R.; O'Keefe, M.A.; Thust, A. Imaging columns of the light elements carbon, nitrogen and oxygen with sub Ångstrom resolution. *Ultramicroscopy* **2001,** 89, 243-263.

32 http://www.cryotem.com/about/RST/Polymer_Films.html

33 Bals, S.; Kabius, B.; Haider, M.; Radmilovic, V.; Kisielowski, C. Annular dark field imaging in a TEM. *Solid State Commun.* **2004,** 130, 675-680.

34 Larsson, M. W.; Wagner, J. B.; Wallin, M.; Håkansson, P.; Fröberg, L. E.; Samuelson, L. Strain mapping in free-standing heterostructured wurtzite InAs/InP nanowires. *Nanotechno.* **2007,** 18, 015504.

35 Joseph Goldstein (2003). Scanning Electron Microscopy and X-Ray Microanalysis. Springer. ISBN 978-0-306-47292-3.

36 http://cime.epfl.ch/webdav/site/cime2/shared/Files/Teaching/Doctoral%20School%202009/Chapter%2013%20-%20EDX.pdf

37 Cliff-Lorimer Ratio Method for EDS Measurements - Practical Electron Microscopy and Database - An Online Book - http://www.globalsino.com/EM/page4643.html

38 Moewe, M.; Chuang, L. C.; Dubrovskii, V. G.; Chang-Hasnain, C. J. Growth Mechanisms and Crystallographic Structure of InP Nanowires on Lattice-Mismatched Substrates. *J. Appl. Phys.* **2008** 104, 044313-044313-4.

39 Duan, X.; Huang, Y.; Agarwal, R.; Lieber, C. M. Single-Nanowire Electrically Driven Lasers. *Nature* **2003,** 421, 241-245.

40 Mårtensson, T; Svensson, C. P. T. ; Wacaser, B.A.; Larsson, M. W.; Seifert, W.; Deppert, K.; Gustafsson, A.; Wallenberg, L. R.; Samuelson, L.; Epitaxial III−V Nanowires on Silicon. *Nano Lett.* **2004,** 4, 1987–1990.

41 Lai, E.; Kim, W.; Yang, P. Vertical Nanowire Array-Based Light Emitting Diodes. *Nano Research* **2008**, 1, 123-128.

42 Sun, K.; Jing, Y.; Park, N.; Li, C.; Bando, Y.; Wang, D. Solution Synthesis of Large-Scale, High-Sensitivity ZnO/Si Hierarchical Nanoheterostructure Photodetectors *J. Am. Chem. Soc.* **2010,** 132, 15465–1546.

43 Atluri, V.; Herbots, N; Dagel, D; Bhagvat, S; Whaley, S. Hydrogen Passivation of Si(100) Wafers as Templates for Low Temperature (T < 600°C) Epitaxy. *Nucl Instrum Meth B*. **1996,** 118, 144–150.

44 Dubrovskii, V. G.; Nazarenko, M. V.; Chuang, L. C.; Ko, W. S.; Ng, K. W.; Chang-Hasnain, C. J. Growth Kinetics of GaAs Nanoneedles on Silicon and Sapphire Substrates. *Appl. Phys. Lett.* **2011,** 98, 153113.

45 Ertekin, E.; Greaney, P. A. ; Chrzan, D. C.; Sands, T. D. Equilibrium Limits of Coherency in Strained Nanowire Heterostructures. *J. Appl. Phys.* **2005,** 97, 114325.

46 Hiramatsu, K. ; Nishiyama, K. ; Motogaito, A.; Miyake, H. ; Iyechika, Y. ; Maeda T. Recent Progress in Selective Area Growth and Epitaxial Lateral Overgrowth of III-Nitrides: Effects of Reactor Pressure in MOVPE Growth. *Phys. Status Solidi A* **1999,** 176, 535-543.

47 Guo, W.; Zhang, M.; Bhattacharya, P.; Heo, J. Auger Recombination in III-Nitride Nanowires and Its Effect on Nanowire Light-Emitting Diode Characteristics. *Nano Lett.* **2011,** 11, 1434-1438.

48 Koblmüller, G.; Hertenberger, S.; Vizbaras, K. ; Bichler, M.; Bao, F.; Zhang, J. P.; Abstreiter, G. Self-Induced Growth of Vertical Free-Standing InAs Nanowires on Si(111) by Molecular Beam Epitaxy. *Nanotechno.* **2010,** 21, 365602.

49 Morral, A. F. i; Colombo, C. ; Arbiol, J. ; Morante, J.R.; Abstreiter, G. Nucleation Mechanism of Gallium-assisted Molecular Beam Epitaxy Growth of Gallium Arsenide Nanowires. *Appl. Phys. Lett.* **2008,** 92, 063112.

50 Chen, R.; Parekh, D.; Ng, K. W.; Chang-Hasnain, C. J. High-speed Avalanche Photodiodes Using III-V Nanopillars Monolithically Grown on Silicon. *Group IV Photonics (GFP), 2012 IEEE 9th International Conference* **2012,** 48-50.

51 Mitate, T.; Mizuno, S; Takahata, H.; Kakegawa, R.; Matsuoka, T.; Kuwano, N. InN polarity determination by convergent-beam electron diffraction. *Appl. Phys. Lett.* **2005,** 86, 134103.

52 Kim, Y.; Joyce, H. J.; Gao, Q.; Tan, H. H.; Jagadish, C.; Paladugu, M.; Zou, J.; Suvorova, A. A. Influence of Nanowire Density on the Shape and Optical Properties of Ternary InGaAs Nanowires. *Nano Lett*., **2006**, 6, 599–604.

53 Zimmermann, G. *et al*. Selective area MOVPE growth of InP, InGaAs and InGaAsP using TBAs and TBP at different growth conditions. *J. Cryst. Growth*, **1997**, 645-649.

54 Zou, J.; Cockayne, D.J.H.; Usher, B.F. Misfit Dislocations and Critical Thickness in InGaAs/GaAs Heterostructure Systems. *J. Appl. Phys.* **1993,** 73, 619-626.

55 Bower, A.F. *Applied Mechanics of Solids*, (CRC Press, New York, 2009).

56 Glas, F. Critical dimensions for the plastic relaxation of strained axial heterostructures in free-standing nanowires. *Phys. Rev. B* **2006,** 74, 121302(R).

57 Zhang, X.; Sibirev, N.V.; Dubrovskii, V. G.; Ren, X. Analytical Study of Elastic Relaxation and Plastic Deformation in Nanostructures on Lattice Mismatched Substrates. *Cryst. Growth Des*. **2011,** 11, 5441.

58 J. Dundurs and G. P. Sendeckyj, Edge dislocation inside a circular inclusion. *J. Mech. Phys. Solids* **1965,** 13, 141.

59 D. Hull and D. J. Bacon*, Introduction to Dislocations*. (Butterworth-Heinemann, Oxford, 2001).

60 Cliff-Lorimer Ratio Method for EDS Measurements - Practical Electron Microscopy and Database - An Online Book - http://www.globalsino.com/EM/page4643.html

61 http://nptel.iitm.ac.in/courses/103104045/pdf_version/lecture5.pdf

62 Rudulph, D.; Funk, S.; Doblinger, M.; Morkötter, S.; Hertenberger, S.; Schweickert, L.; Becker, J.; Matich, S.; Bichler, M.; Spirkoska, D.; Zardo, I.; Finley, J. J.; Abstreiter, G. and Koblmüller, G. Spontaneous Alloy Composition Ordering in GaAs-AlGaAs Core− Shell Nanowires. *Nano Lett.* 2013, 13, 1522.

63 http://www.unamur.be/services/microscopie/sme-documents/Energy-20table-20for-20EDS-20analysis-1.pdf

64 Joseph Goldstein et al. "Scanning Electron Microscopy and X-Ray Microanalysis".

65 Yu, K.; Lakhani, A.; Wu, M. C. Subwavelength Metal–optic Semiconductor Nanopatch Lasers. *Opt. Express* **2010,** 18, 8790–8799.

66 Hill, M. T. ; Oei, Y. S.; Smalbrugge, B.; Zhu, Y.; Vries, T.; Veldhoven, P. J.; Otten, F. W. M. ; Eijkemans, T. J. ; Turkiewicz, J. P. ; Waardt, H.; Geluk, E. J.; Kwon, S. H.; Lee, Y. H. ; Nötzel , R. ; Smit M. K. Lasing in Metallic-Coated Nanocavities. *Nature Photon.* **2007,** 1, 589–594.

67 Lu, C. Y. ; Chang, S. W.; Chuang, S. L. ; Germann, T. D. ; Bimberg, D. Metal-Cavity Surface-Emitting Microlaser at Room Temperature. *App. Phys. Lett.* **2010,** 96, 251101.

68 Lee, J. H.; Khajavikhan, M.; Simic, A.; Gu, Q.; Bondarenko, O.; Slutsky, B.; Nezhad, M. P.; Fainman, Y. Electrically Pumped Sub-Wavelength Metallo-Dielectric Pedestal Pillar Lasers. *Opt. Express* **2011,** 19, 21524-21531.

69 Scofield, A.; Kim, S. H.; Shapiro, J. N.; Lin, A.; Liang, B. L.; Scherer, A.; Huffaker, D. L. Room Temperature Continuous Wave Lasing in Nanopillar Photonic Crystal Cavities. *Conference on Lasers and Electro-Optics (CLEO)* **2012**, CTh4M.

70 Yu, K., Lakhani, A. & Wu, M. C. Subwavelength metal-optic semiconductor nanopatch lasers. *Opt. Express* **18,** 8790–8799 (2010).

71 Ding, K. *et al.* Electrical injection, continuous wave operation of subwavelength-metallic-cavity lasers at 260 K. *Appl. Phys. Lett.* **98,** 231108 (2011).

72 Lee, J. H. *et al.* Electrically pumped sub-wavelength metallo-dielectric pedestal pillar lasers. *Opt. Express* **19,** 21524–21531 (2011).

73 Xiong, Z.; Liu, H.; Zhu, C.; Sin, J.K.O. A new polysilicon CMOS self-aligned double-gate TFT technology. *IEEE T Electron Dev*. **2005**, *52*, 2629-2633.

74 Obermeier, E.; Kopystynski, P. Polysilicon As a Material for Microsensor Applications. *Sensor Actuat A-Phys*. **1992**, *30*, 149-155.

75 Kutchoukova, V.G.; Pakulaa, L.; Parikesitb, G.O.F.; Garinib, Y.; Nanvera, L.K.; Bosschea, A. Fabrication of nanofluidic devices in glass with polysilicon electrodes. *Sensor Actuat A-Phys*. **2005**, *123-124*, 602-607.

76 Stewart, M.; Howell, R.S.; Pires, L.; Hatalis, M.K. Polysilicon TFT technology for active matrix OLED displays. *IEEE T Electron Dev*. **2001**, *48*, 845-851.

77 Fossum, J.G.; Lindholm, F.A. Theory of grain-boundary and intragrain recombination currents in polysilicon p-n-junction solar cells. *IEEE T Electron Dev*. **1980**, *27*, 692-700.

78 Dhaka, V.; Haggren, T.; Jussila, H.; Jiang, H.; Kauppinen, E.; Huhtio, T.; Sopanen, M.; Lipsanen, H. High Quality GaAs Nanowires Grown on Glass Substrates. *Nano Lett.* **2012**, *12*, 1912–1918.

79 Ikejiri, K.; Ishizaka, F.; Tomioka, K.; Fukui, T. GaAs nanowire growth on polycrystalline silicon thin films using selective-area MOVPE. *Nanotechno.* **2013,** *24*, 115304.

80 Chandrasekarana, H.; Sunkara, M. K. Growth of Gallium Nitride Textured Films and Nanowires on Polycrystalline Substrates at sub-Atmospheric Pressures. *Mat. Res. Soc. Symp. Proc.* **2002,** *693*, I3.30.

81 Jacobs, R. N.; Salamanca-Riba, L.; He, M.; Harris, G. L.; Zhou, P.; Mohammad, S. N.; Halpern, J. B. Structural Characterization of GaN Nanowires Fabricated via Direct Reaction of Ga Vapor and Ammonia. *Mat. Res. Soc. Symp. Proc.* **2001,** *675*, W9.4.

82 Miller, O. D.; Yablonovitch, E.; Kurtz, S. R. Strong Internal and External Luminescence as Solar Cells Approach the Shockley–Queisser Limit. *IEEE Journal of Photovoltaics* **2012,** *2*, 303-311.

83 Moewe, M.; Chuang, L. C.; Crankshaw, S.; Chase, C.; Chang-Hasnain, C. J. Atomically sharp catalyst-free wurtzite GaAs/AlGaAs nanoneedles grown on silicon. *Appl. Phys. Lett.* **2008,** *93*, 23116.

84 Messmer , C.; Bilello, J. C. The surface energy of Si, GaAs, and GaP. *J. Appl. Phys.* **1981,** *52*, 4623.

85 Jallipalli, A.; Balakrishnan, G.; Huang, S. H.; Rotter, T. J.; Nunna, K.; Liang, B. L.; Dawson, L. R.; Huffaker, D. L. Structural Analysis of Highly Relaxed GaSb Grown on GaAs Substrates with Periodic Interfacial Array of 90° Misfit Dislocations. *Nanoscale Research Letters* **2009**, *4*, 1458-1462.

86 Nazarenko, M. V.; Sibirev, N. V.; Ng, K. W.; Ren, F.; Ko, W. S.; Dubrovskii, V. G.; Chang-Hasnain, C. J. Elastic energy relaxation and critical thickness for plastic deformation in the core-shell InGaAs/GaAs nanopillars. *J. Appl. Phys*. **2013,** *113*, 104311.

87 Yamashita, T.; Akiyama, T.; Nakamura, K.; Ito, T. Growth of side facets in InP nanowires: First-principles-based approach. *Surf. Sci.* **2013,** *609*, 207-214.

88 Liu, X. Y.; Shan, C. X.; Wang, S. P.; Zhang, Z. Z.; Shen, D. Z. Electrically pumped random lasers fabricated from ZnO nanowire arrays. *Nanoscale*, **2012**, *4*, 2843.

89 Chen, R.; Utama, M. I. B.; Peng, Z.; Peng, B.; Xiong, Q.; Sun H. Excitonic Properties and Near-Infrared Coherent Random Lasing in Vertically Aligned CdSe Nanowires. *Adv. Mater.* **2011,** *23*, 1404–1408.

90 Bothra, S.; Tyagi, S.; Chandhi, S. K.; Borrego, J. M. Surface recombination velocity and lifetime in InP. *Solid State Electron.* **1991** 34, 47.

91 Aspnes, D. E. Recombination at semiconductor surfaces and interfaces. *Surf. Sci.* **1983,** 132, 406.

92 Ertekin, E.; Greaney, P. A; Chrzan, D. C.; Sands, T. D. Equilibrium limits of coherency in strained nanowire heterostructures. *J. Appl. Phys.* **2005**, 97, 114325.

93 Shikida, M.; Masuda, T.; Uchikawa, D.; Sato, K. Surface roughness of single-crystal silicon etched by TMAH solution, *Sensor Actuat A-Physical* **2001,** 90, Pages 223-231.

94 Hill, C. W.; Stringfellow, G. B.; Sadwick, L. P. Pyrolysis of tertiarybutylphosphine at low pressure. *J.Electron Mater.* **1995**, 24, pp 731-734.

95 Stiles, M. D.; Hamann, D. R. Electron transmission through silicon stacking faults. *Phys. Rev. B* **1990,** 41, 5280–5282.

96 Bao, J M; Bell, D C; Capasso, F; Wagner, J B; T, Trägårdh, J; Samuelson, L. Optical Properties of Rotationally Twinned InP Nanowire Heterostructures. *Nano Lett.* **2008** 8, 836–41.

97 Murayama, M.; Nakayama, T. Chemical trend of band offsets at wurtzite/zinc-blende heterocrystalline semiconductor interfaces. *Phys. Rev. B*, **1994-I,** 49, 4710–4724.

98 Jancu, J. M.; Gauthron, K.; Largeau, L.; Patriarche, G.; Harmand, J.-C.; Voisin, P. Type II heterostructure fromed by zinc-blende inclusions in InP and GaAs wurtzite nanowires. *Appl.Phys.Lett.* **2010,** 97, 041910.

99 Liu, Q.; Derksen, S.; Lindner, A.; Scheffer, F.; Prost, W.; Tegude, F. ‐ J. Evidence of type-II band alignment at the ordered GaInP to GaAs heterointerface. *J. Appl. Phys.* **1995,** 77, 1154-1158.

100 Hoeft, H.; Schwarb, P. Investigations Towards Optimizing EDS Analysis by the Cliff-Lorimer Method in Scanning Transmission Electron Microscopy. *X-Ray Spectrom*. **1988,** 201-208.

101 Liu, Z.; Machuca, F.; Pianetta, P.; Spicer, W.E. Optimized cleaning method for producing device quality InP(100) surfaces. *J. Appl. Phys.* 97 , **2005,** 124902.

102 http://www.freiberger.com/images/PDF/Product-Information-Gallium-Arsenide-Rev-I.pdf

103 Chen, H.; Feenstra. R.M. Enchanced group V intermixing in InGaAs/InP quantum wells studied by cross-sectional scanning tunneling microscopy. *Appl. Phys. Lett.* **1999,** 75, 79.

104 Saylea, T. X. T.; Parkerb, S. C.; Sayle, D. C. Ionic conductivity in nano-scale CeO2/YSZ heterolayers. *J. Mater. Chem.* **2006**, 16, 1067-1081.

105 Huang, S. H.; Balakrishnan, G.; Khoshakhlagh, A.; Jallipalli, A.; Dawson, L. R.; Huffaker, D. L. Strain relief by periodic misfit arrays for low defect density GaSb on GaAs. *Appl. Phys. Lett.* **2006,** 88, 131911.

106 Shibata, H. Negative Thermal Quenching Curves in Photoluminescence of Solids *Jpn. J. Appl. Phys.* **1998,** 37, 550-553.

107 Watanabe, M.; Sakai, M.; Shibata, H.; Satou, C.; Satou, S.; Shibayama, T.; Tampo, H.; Yamada, A.; Matsubara, K.; Sakurai, K.; Ishizuka, S.; Niki, S.; Maeda, K.; Niikura, I. Negative thermal quenching of photoluminescence in ZnO, Physica B: Condensed Matter. Physica B **2006,** 376–377, pp. 711-714.

108 Schimper, H.-J.; Kollonitsch, Z.; Mo¨ller, K.; Seidel, U.; Bloeck, U.; Schwarzburg, K.; Willig, F.; Hannappel, T.; Material studies regarding InP-based high-efficiency solar cells. *J. Cryst. Growth* **2006,** 287, 642.

109 Sun, Y.; Liu, Z.; Pianetta, P. The dependence of the oxidation enhancement of InP(100) surface on the coverage of the adsorbed Cs. *J. Appl. Phys.* **2010,** 107, 124904.

110 Nash, G. R.; Ashley, T. Reduction in Shockley–Read–Hall generation-recombination in AlInSb light-emitting-diodes using spatial patterning of the depletion region. *Appl. Phys. Lett.* **2009,** 94, 213510.

111 Li, C. B.; Usami, K.; Mizuta, H.; Oda, S. Controlled Ge nanowires growth on patterned Au catalyst substrate. *Appl. Phys. Express* **2009,** *2, 015004.*

112 Boulanger, J P; LaPierre, R R. Patterned gold-assisted growth of GaP nanowires on Si. *Semicond. Sci. Technol.* **2012,** 27, 035002.

113 Schumann, T.; Gotschke, T; Limbach, F; Stoica, T; Calarco, R. Selective-area catalyst-free MBE growth of GaN nanowires using a patterned oxide layer. *Nanotechno.* **2011,** 22, 095603.

114 Goto, H.; Nosaki, K.; Tomioka, K.; Hara, S.; Hiruma, K.; Motohisa, J.; Fukui. T. Growth of Core–Shell InP Nanowires for Photovoltaic Application by Selective-Area Metal Organic Vapor Phase Epitaxy. *Appl. Phys. Express* **2009,** 2, 035004.

Appendix

The following is the matlab code for image processing by filtering the very high and very low frequency components in the fast Fourier transform (FFT).

```
function [Ifiltered] = highLowPassFFT(I)

% Apply high pass and low pass filtering to an image

% Define the characteristic frequency of our high pass filter

qHighPass = 0.0005;
qLowPass = 0.3;

% Get image size

Nxy = size(I)

% Make Fourier coordinate system

pSize = 1;
Lx = Nxy(1)*pSize;  % Length in nyquist units
Ly = Nxy(2)*pSize;
qx = circshift(((-Nxy(1)/2):(Nxy(1)/2-1))/Lx,[1 -Nxy(1)/2]);
qy = circshift(((-Nxy(2)/2):(Nxy(2)/2-1))/Ly,[1 -Nxy(2)/2]);
[qya, qxa] = meshgrid(qy,qx);
q2 = qxa.*qxa + qya.*qya;

% q1 = sqrt(q2);
% qxCoord = qxa(xDet,yDet);
% qyCoord = qxa(xDet,yDet);

% Create pass band filter

qLP = exp(-q2.*q2/2/qLowPass^4);
qHP = 1 - exp(-q2.*q2/2/qHighPass^4);
qFilter = qLP.*qHP;

%Apply Tukey window and Gaussian smooth to image

% Thickness of edge

r = 0.1;
% w2 = hanning(Nxy(1))*hanning(Nxy(2))';
w2 = tukeywin(Nxy(1),r)*tukeywin(Nxy(2),r)';
I = I / mean(I(:));
```

```
I = I.*w2 + 1*(1-w2);   %2nd term is to raise the edge values to approximately the same as center --> smoother edge

% Create and apply smoothing filter

smoothFilter = fspecial('gaussian',11,1);
I = I - 1;
I = conv2(I,smoothFilter,'same');
I = I + 1;

% Make filter guide image

Iplot = zeros(Nxy(1),Nxy(2),3);
Ifft = fft2(I);
I1 = fftshift(abs(Ifft));
I1 = I1 / max(I1(:));
I1 = log(I1);
I1 = (I1 + 12)/6;
I1(I1<0) = 0;
I1(I1>1) = 1;

Iplot(:,:,2) = I1.*fftshift(qFilter);
Iplot(:,:,3) = I1.*fftshift(qFilter);
% Iplot(:,:,2) = I1.*fftshift(qFilter);
% Iplot(:,:,2) = I1;%.*(1-fftshift(qFilter));
Iplot(:,:,1) = I1;

% Apply the filter

Ifft = Ifft.*qFilter;
Ifiltered = real(ifft2(Ifft));

% % apply a small Tukey window to fix edges
% r = (qHighPass / .5 / 1);
% w2 = tukeywin(Nxy(1),r)*tukeywin(Nxy(2),r)';
% % Ifiltered = Ifiltered - mean(Ifiltered(:));
% Ifiltered = Ifiltered.*w2 + 0*(1-w2);
figure(3)
clf
imagesc(I)
axis equal off
colormap(bone(256))
set(gca,'position',[0 0 1 1])
colorbar
```

```
figure(1)
clf
imagesc(Iplot)
axis equal off
colormap(gray(256))
set(gca,'position',[0 0 1 1])
colorbar

% figure(2)
% axes('FontSize',8);
% clf
% imagesc(log(Ifiltered+abs(min(Ifiltered(:)*1.01))))
% axis equal off
% colormap(hot(256))
% set(gca,'position',[0 0 1 1])
% colorbar

figure(4)
axes('FontSize',8);
clf
imagesc(Ifiltered)
axis equal off
colormap(gray(256))
set(gca,'position',[0 0 1 1])
colorbar




End
```